Available online at www.sciencedirect.com
SCIENCE DIRECT®
Physics Reports 427 (2006) 41–155
PHYSICS REPORTS
www.elsevier.com/locate/physrep

Relativistic high-power laser–matter interactions

Yousef I. Salamin[a,b], S.X. Hu[c], Karen Z. Hatsagortsyan[a,d], Christoph H. Keitel[a,*]

[a] *Max-Planck-Institute for Nuclear Physics, Saupfercheckweg 1, D-69117 Heidelberg, Germany*
[b] *Physics Department, American University of Sharjah, POB 26666, Sharjah, United Arab Emirates*
[c] *Group T-4, Theoretical Division, MS B283, Los Alamos National Laboratory, Los Alamos, NM 87545, USA*
[d] *Department of Quantum Electronics, Yerevan State University, A. Manoukian 1, Yerevan 375025, Armenia*

Accepted 11 January 2006
Available online 2 March 2006
editor: J. Eichler

Abstract

Recent advances in laser technology have pushed the frontier of maximum intensity achieved to about 10^{22} W/cm^2 and investigators currently believe even higher intensities may be reached in the near future. This, combined with other breakthroughs on the fronts of short pulse generation and high repetition rates, have stimulated considerable progress, theoretical as well as experimental, in the field of laser–matter interactions. It is now possible to laser-accelerate electrons to a few hundred MeV and laser-induced pair-production and nuclear physics experiments have made significant progress. This article is devoted to a review of the recent advances in the field and stresses quantum phenomena that require laser field intensities in excess of the relativistic threshold of $\sim 10^{18}$ W/cm^2. Interactions with free electrons, with highly-charged ions and with atoms and clusters, are reviewed. Electron laser acceleration, atomic quantum dynamics, high harmonic generation, quantum electrodynamical effects and nuclear interactions in plasmas and ions, are among the important topics covered in the article.
© 2006 Elsevier B.V. All rights reserved.

PACS: 42.65.−k; 52.40.Nk; 42.50.Vk; 52.75.Di

Contents

1. Introduction . . . 42
2. New technical advances . . . 43
   2.1. Experimental breakthroughs . . . 43
      2.1.1. Laser technology . . . 43
      2.1.2. Preparation of states of matter for laser–matter interactions . . . 47
   2.2. Theoretical advances . . . 47
      2.2.1. Analytical methods . . . 47
      2.2.2. Numerical techniques . . . 50
3. Relativistic laser–electron interactions . . . 53
   3.1. Classical analysis . . . 53
   3.2. Quantum mechanical analysis . . . 55
      3.2.1. Electron wave packet evolution . . . 55

* Corresponding author.
E-mail address: keitel@mpi-hd.mpg.de (C.H. Keitel).

0370-1573/$ - see front matter © 2006 Elsevier B.V. All rights reserved.
doi:10.1016/j.physrep.2006.01.002

3.2.2. Quantum interference . . . 55
3.2.3. Spin effects . . . 58
3.3. Ionized electrons in laser plus extra static fields . . . 60
4. Laser acceleration schemes . . . 64
4.1. Acceleration by a single laser beam . . . 66
4.2. Acceleration by crossed and two-color laser beams . . . 67
4.3. Acceleration by laser plus static electric and magnetic fields . . . 70
4.4. Acceleration of electrons from ions . . . 72
5. Relativistic laser–atom, and –ion interactions . . . 73
5.1. Ionization and stabilization . . . 73
5.2. Relativistic multi-photon and tunneling-recollision dynamics . . . 77
5.3. Spin–orbit coupling . . . 80
5.4. More complex systems . . . 82
5.4.1. Multi-electron systems . . . 82
5.4.2. Multi-atom systems . . . 89
6. Relativistic X-ray generation . . . 94
6.1. X-rays from multi-photon transitions . . . 95
6.2. Tunneling and re-collision harmonics . . . 96
6.3. Non-tunneling harmonics . . . 101
6.3.1. Plateau and surfing mechanism of non-tunneling harmonics . . . 102
6.3.2. High efficiency of non-tunneling harmonics . . . 106
6.4. Radiation of ionized electrons . . . 107
6.5. Positronium harmonics . . . 109
6.5.1. Recombination harmonics . . . 109
6.5.2. Radiation from laser-induced annihilation . . . 112
6.6. Multi-particle systems . . . 113
7. Towards high-energy laser physics . . . 117
7.1. Quantum electrodynamical effects . . . 117
7.1.1. Nonlinear Compton effect . . . 117
7.1.2. Radiation-reaction effects . . . 118
7.1.3. Electron–positron pair-production . . . 124
7.1.4. Light-by-light scattering . . . 127
7.2. Laser-induced nuclear reactions . . . 132
7.2.1. Nuclear reactions in plasmas . . . 132
7.2.2. Nuclear reactions with clusters . . . 135
7.2.3. Nuclear reactions with single atomic systems . . . 139
7.3. Laser-induced particle physics . . . 143
8. Conclusions and outlook . . . 144
Acknowledgments . . . 144
References . . . 145

1. Introduction

Almost 40 years after the invention of the laser, experimentalists have recently achieved laser intensities sufficient to accelerate particles close to the speed of light. The time scale of these laser pulses had initially been in the nanosecond range and thus were long enough to induce complex multi-particle dynamics with most quantum effects being washed out. As a consequence, most of the action in the physics of laser–matter interplay had been in relativistic laser–plasma interactions [1–5]. Excitement in this field has been directed, to a large extent, towards the investigation of collective multi-particle dynamics, fast-particle and high-frequency generation, as well as quantum electrodynamical, fission, fusion and other nuclear processes.

In recent years it has become possible to generate femtosecond laser pulses at relativistic intensities, with a clear perspective even for attosecond pulses [6–8]. The induced dynamics then becomes short enough such that quantum relativistic effects remain of significance [6,9–12]. Then quantum interferences, tunneling, spin and quantum electrodynamical effects are intrinsically involved on the microscopic scale and play an essential role in fast-particle and coherent high-frequency generation and novel physics beyond the Dirac theory. This review seeks to focus on relevant advances

in this direction, while attempting to place those developments within the whole field of ultra-intense laser–matter interactions.

Various aspects of the high-intensity laser–atom interactions have been the subject of a number of reviews in the past several years. The initial attempts in relativistic laser–atom physics were reviewed by Protopapas et al. [6] covering multi-photon ionization (MPI), tunneling ionization (TI), high harmonic generation (HHG), stabilization, controlled wavepacket dynamics, basic relativistic effects, as well as state-of-the-art laser systems and numerical approaches. Further developments in the theoretical investigation of MPI, HHG and laser-assisted electron-atom collisions were reviewed by Joachain [11] in 1999. Floquet and R-matrix Floquet theories were discussed, in particular, in addition to methods involving direct numerical integration of the time-dependent Schrödinger equation. A more extensive review of these topics was conducted in 2000 [12]. Further in 2000, the physics and technology of ultrashort-pulse lasers was the subject of a review by Brabec and Krausz [7]. Nonlinear effects that accompany interaction of matter with intense few-cycle laser fields were especially emphasized. Furthermore, the quantum-orbit approach for above-threshold ionization (ATI) and HHG has been reviewed recently [9] by Becker and his coworkers.

Developments in the quantum-mechanical study of the relativistic effects associated with high-intensity laser interactions with atoms, ions and molecules were discussed in more recent short reviews by Keitel [13] and Maquet and Grobe [14]. In [13], work based on solutions to the Dirac equation and involving multiply-charged ions and other more complex atomic systems is reviewed. In particular, relativistic tunneling, multi-photon resonances, and the effect of spin–orbit coupling on the radiation spectra are briefly described. In [14] several challenges in the relativistic domain, to be taken up as advances in laser technology continue to be made, are outlined. Those include the Klein paradox and pair-creation, Zitterbewegung, and the recently discovered bound-like system known as the *cycloatom*. Briefly discussed also in this article are the spin effects and quantum chaos in systems with a relativistically-induced nonlinearity.

2. New technical advances

In this section, we review the most recent advances in the techniques, experimental as well as theoretical, that are currently employed in the study of relativistic laser–matter interactions. The section is divided naturally into two subsections, one for the experimental breakthroughs and another for the theoretical advances and numerical techniques.

2.1. Experimental breakthroughs

2.1.1. Laser technology

The past few years have witnessed a number of significant advances in laser technology, raising the achievable intensity by a few orders of magnitude beyond the relativistic limit and reducing pulse duration to the attosecond regime.

The era of nonlinear relativistic optics began with the invention of the chirped pulse amplification (CPA) technique [15]. Nevertheless, one should remember that the drive to build powerful lasers was originally motivated by laser fusion research before the advent of CPA. The pioneer in this regard was the Lawrence-Livermore National Laboratory (LLNL), where a series of record-breaking powerful lasers have been built since the 1970s. Refinements in the technique have resulted in tremendous advancements; from a single laser beam of 10 J energy up to the National Ignition Facility (NIF) which will ultimately deliver 192 laser beams of the total energy of 1.8 MJ. Nd:glass lasers constitute the base for the construction of the NIF. Recent progress at NIF in the production of radiation pulses of nanosecond duration include 21 kJ single beam performance in the infrared, 11.4 kJ in the green and 10.5 kJ in the ultraviolet. Needless to say that it is a huge stadium-scale machine. Large-scale facilities of this type have also been built at CEA-Limeil in France (LMJ-Laser Megajoule), in the Rutherford Appleton Laboratory in the UK, and at the Institute of Laser Engineering at Osaka University. Typical parameters of these machines are: kJ energy in a single pulse of nanosecond duration, delivering already terawatt (TW) powers. While further compressing, a pulse of sub-picosecond duration and petawatt (PW) power may be generated without decreasing the pulse energy significantly. The petawatt regime has first been reached by the Nova laser in 1996 at LLNL (which was later dismantled to give way to the NIF). The Vulcan glass laser at the Rutherford Appleton laboratory is capable of delivering a nanosecond pulse of up to 2.6 kJ energy. It also achieved petawatt performance in 2004: 423 J in a 410 fs pulse of 1.03 PW power was focused to the intensity of 10^{21} W/cm^2

(for more on this system, see [16]). LIL facility at LMJ, France has showen operation of 9.5 kJ of UV light in 9 ns. The PW Gekko at Osaka University is capable to deliver (500 J/0.5 ps) pulses and will be upgraded up to 10 kJ. Other PW-class lasers are PHELIX in GSI, Darmstadt, Germany with (500 J/0.5 ps), LULI at Ecole Polithechnique, France with (400 J/0.4 ps) beam performance. A PW laser with (200 J/150 fs) and a high repetition rate of 0.1 Hz has been developing in Jena, Germany [17].

One of the most remarkable developments brought about by the invention of CPA was that it enabled construction of *table-top* terawatt lasers, employing high energy storage materials such as Ti:sapphire and Nd:glass, and leading to significant progress in the techniques of short pulse generation. Typical parameters of this class of machines are: hundreds of mJ energy in a single pulse of hundreds of femtosecond duration, delivering 1–100 terawatt peak power, which is enough to reach laser intensities of the order of 10^{20} W/cm^2 at focus. The repetition rate of these devices is about 10 Hz with the total number of shots about 10^5.

Due to the significant decrease in energy consumption compared with the megajoule facilities, these devices fit very well in university laboratories. They have been employed, since the late 1990s, in laser physics research at relativistic intensities.

Work in the field of relativistic-intensity laser–matter interactions is currently in progress, or is planned, at a number of places around the world. Chief among them are the following. HERCULES is a facility at the Center for Ultrafast Optical Sciences (CUOS) of the University of Michigan at Ann Arbor, where the power density record was recently broken by focusing a 45-TW laser beam [18]. Monoenergetic beams of electrons have been produced in plasma-based laser accelerators at three places recently: the Rutherford Appleton Laboratory in the UK, using the ASTRA laser of 40 fs duration and 500 mJ pulse energy [19], the Lawrence Berkeley National Laboratory in the USA using L'OASIS laser (4 TW, 7×10^{18} W/cm^2) [20], and the Laboratoire d'Optique Appliqée of the Ecole Polytechnique in France (the laser design parameters are: 100 TW, 25 fs, 10 Hz, 10^{20} W/cm^2) [21].

Laser-assisted fusion research is also carried out at some of the above-mentioned laboratories, in addition to the LLNL, Max-Planck-Institute for Plasma Physics (Garching, Germany), and Osaka University in Japan [22]. Moreover, high-intensity laser–matter interactions are studied also at many places using table-top laser devices of comparable parameters, of which the following are but a few examples: University of Texas at Austin in the USA (using the LLNL Jan USP laser: 100 fs, 10 J per pulse, a peak intensity of 2×10^{20} W/cm^2 [23]); The 100 TW facility of the LULI laboratory in Palaiseau, France (350 fs duration laser pulse delivering energy of up to 20 J, at a 1.057 μm wavelength and maximum intensity on target 2×10^{19} W/cm^2 [24]); Max–Born Institute in Berlin (10 Hz, 35 fs, maximum beam energy of 750 mJ, peak intensity 0.8×10^{19} W/cm^2 [25]); Jena University in Germany (10 Hz, 80 fs, 600 mJ, peak intensity 3×10^{19} W/cm^2 [26]); DSM/DRECAM at Saclay in France (SLIC facility: 600 mJ in 60 fs at 800 nm [27]); Advanced Photon Research Center (JAERI) in Kyoto, Japan (10 Hz, 30–500 fs, 320 mJ, peak intensity 10^{19} W/cm^2 [28]); and Max-Planck-Institute for Quantum Optics in Garching, Germany (laser parameters: 10 Hz, 150 fs, 230 mJ, peak intensity 5×10^{18} W/cm^2 [29]).

Further prominent advances in the strong field laser techniques have recently been achieved. Focusing over small spatial dimensions and reduction of pulse duration are key to reaching ultrahigh intensities at focus. Building on many years of improvements, scientists led by Mourou, using adaptive optics, have focused light from a Ti:Sapphire laser to a spot 0.8 μm across, thus reaching an intensity of $(6.6–8.5) \times 10^{21}$ W/cm^2 for the first time [18]. They have realized the so-called λ^3 *regime* of a laser pulse. When the laser pulse of a few cycles is focused down to a single wavelength spot size, the laser pulse energy is confined to a focal volume of λ^3. In the same regime, they have also produced the relativistic intensity of 10^{18} W/cm^2 at a kHz repetition rate with only mJ energy in the pulse [30].

A radially polarized laser beam has been focused by Dorn et al. [31] to a spot of area 0.06 μm^2, the spot size being defined as the area encircled by the contour line at half the intensity maximum. As is well known, focusing causes an asymmetric deformation of the focal spot [32]. What Dorn and his coworkers have done is take a linearly-polarized single-mode helium–neon laser beam, collimate it, and send it through an annular aperture followed by four half-wave plates. The resulting beam had a doughnut-shaped intensity pattern with a hole at the center. In the vicinity of the focus, the radially-polarized field developed a strong longitudinal electric field component containing almost three-quarters of the total beam power (see Fig. 1). The longitudinal electric field may be enhanced even further by increasing the numerical aperture of the focusing system.

Production of the shortest ever laser pulse at optical frequencies has recently been reported [33]. A train of single-cycle pulses of pulse width 1.6 fs, a pulse separation of 11 fs, and a peak power of 1 MW have been generated. Developments in compact ultrafast lasers have been reviewed recently by Keller [34].

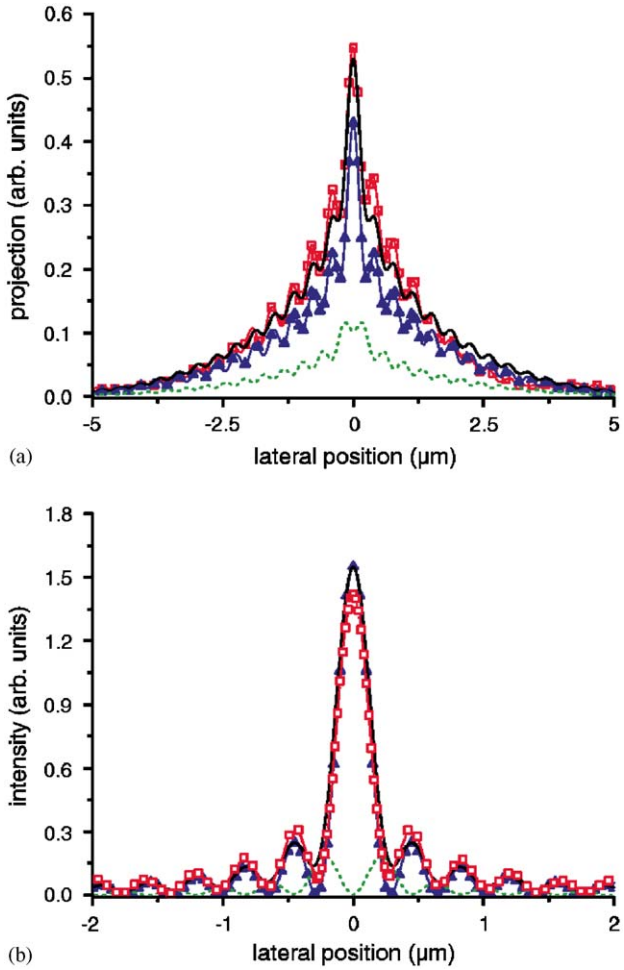

Fig. 1. (a) Measured projection of, and (b) cross section through, the tomographically reconstructed intensity distribution for a radially polarized input field focused using an annular aperture ($d_i = 3.3$ mm). The calculated power contained in the longitudinal field amounts to 72.8% of the total beam power. Open squares: experimental data; calculated curves: solid black line: total field; dashed line: transverse field; solid triangles: longitudinal field [31]. Reprinted with permission from [31]; Copyright 2003 by the American Physical Society.

Experimental advancements in strong field lasers have recently approached the limits of the CPA technique for table-top facilities. In fact, the CPA technique is applicable up to the threshold fluence of the Ti:sapphire (or analogue) crystal, i.e., no more than $1\,\mathrm{J/cm^2}$. Assuming that the radius of a laser beam in a table-top facility is 1 cm, the beam energy cannot exceed 1 J. Therefore, for a laser pulse of 10 fs duration, peak power cannot exceed 100 TW, the latter being focused to a spot of μm radius (of the order of magnitude of the radiation wavelength). This will deliver an intensity not exceeding $10^{22}\,\mathrm{W/cm^2}$. Tajima and Mourou [35] have proposed to extend capabilities of the CPA technique by allowing the use of large-scale components. Thus, if one increases the laser beam size to 1 m, then it can carry 10 kJ energy which, for a 10 fs pulse duration, delivers exawatt power ($\mathrm{EW} = 10^{18}$ W) and a $10^{26}\,\mathrm{W/cm^2}$ focused intensity. Meanwhile, if the laser beam size were to reach 10 m, the beam energy would be 1 MJ, the beam power would reach a zetawatt ($\mathrm{ZW} = 10^{21}$ W), and the intensity would climb to $10^{28}\,\mathrm{W/cm^2}$.

Another recent proposal of Mourou is aimed at building a 50 PW peak power laser operating at 15 kHz with average power of 20 MW. This proposal is based on fiber lasers. Using the maximal fluence of fiber lasers of $50\,\mathrm{J/cm^2}$, combining together 10^7 fibers and focusing the laser beam by a mirror of 1 m diameter, these amazing parameters of a laser beam may be achieved. Many problems, like synchronization, still remain to be solved if this proposal is to work.

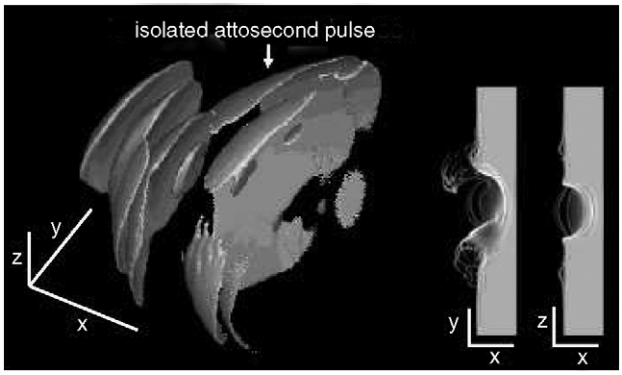

Fig. 2. 3D PIC simulation of isolated attosecond pulse generation. Isosurface of the electromagnetic energy density demonstrates efficient generation of isolated attosecond pulse (left). Electron density slices show anisotropic electron activity at the time of attosecond pulse generation (right) [37]. Reprinted with permission from [37]; Copyright 2005 by the Taylor & Francis Ltd.; web site: http://www.tandf.co.uk/journals.

Other new ideas have been put forward to go beyond CPA and achieve advances in laser intensity. A proposal has been advanced in [36] to generate a strong laser field from laser wave reflection from, and focusing by, the front of the electron density when an intense laser pulse propagates in a plasma in the wave-braking regime of the wakefield. Another idea has been proposed by the Mourou group. They have recently shown via numerical simulations that it would be possible to efficiently generate isolated attosecond pulses [37] (see Fig. 2) and electron bunches [38] in the relativistic interaction of an intense, very short, and tightly focused laser pulse (λ^3-regime) with an overdense plasma surface. The main idea is to use the relativistic nonlinearity of the plasma frequency dependence on the laser intensity and to extend the concept of the relativistic self-focusing from refraction to reflection and deflection. It is crucial to operate in the λ^3-regime because that allows to avoid the wave front distortion. Then, the electrons' initial collective response is used, and the complex, not coherent, dynamics in successive laser cycles are avoided. Besides, the narrow focus induces angular separation of attosecond (as) reflected pulses. Initial particle-in-cell simulations show that generation of a single 200 as pulse from a 5 fs laser pulse of $2 \times 10^{19}\,\mathrm{W/cm^2}$ with 10% efficiency is possible. Moreover, the scheme is scalable to higher energies. The intensity increases by two orders of magnitude, along with a plasma density increase by an order of magnitude, the same compression effect can be achieved. By this way the proposed technique can produce single attosecond pulses from mJ to the J level.

A concept close in spirit to this has recently been proposed [39]. It suggests employing high-order harmonic generation when a strong laser pulse is reflected from an overdense plasma. The calculations and simulations show that when the plasma surface is initially concave, it can focus the harmonics. Then extremely short electromagnetic pulses can be obtained with the field approaching the Schwinger intensity limit of $10^{29}\,\mathrm{W/cm^2}$. We have to mention though that these proposals are still speculative and far from being realized.

Tremendous progress has recently been made in the area of generation and characterization of attosecond pulses of extreme ultraviolet (XUV) radiation. This opens up a new field of attosecond spectroscopy for the time-resolved control and monitoring of atomic and molecular processes. The physics of attosecond light pulses has been the subject of a most recent and comprehensive reviews [40]. Theory of the attosecond pulses produced by exploiting high-harmonic generation or stimulated Raman scattering and their potential applications are all thoroughly discussed in these articles. Some of the significant achievements in this field will be alluded to here. In 2001 Krausz and his coworkers were able to track the motion of electrons around the nucleus of a krypton atom for the first time, using 650 attosecond X-ray pulses [41]. Further, 250 attosecond XUV pulses were generated and characterized by the same group for use in studying the relaxation dynamics of electronic shells [42]. The electric field variations in a few-cycle femtosecond pulse of visible laser light have been measured directly for the first time by means of attosecond pulses [43]. The emerging techniques of generation and characterization of attosecond light point to a very promising potential in advancing towards ever intense radiation fields via increasing the pulse energy and improving focusing in the XUV spectral range.

Efforts to develop coherent short wavelength radiation sources are currently spearheaded by super-large-scale projects. Construction and operation of X-ray free-electron laser (X-FEL) facilities are currently in progress at DESY (TESLA) and Stanford (LCLS) as part of a super-conducting electron–positron linear collider [44,45]. In 2000

radiation at a wavelength of 109 nm was generated for the first time in a free-electron laser (FEL) utilizing the process of self-amplified spontaneous emission (SASE) [46]. The radiation pulse shows significant fluctuations which is inherent in the SASE process. A pulse of picosecond duration had coherence time of only 28 fs. The efforts of TESLA and LCLS projects aim at the generation of extreme ultraviolet (XUV) and hard X-ray radiation, in the wavelength range of 0.1–100 nm, for applications in basic as well as applied sciences [47]. Particularly, hopes are high that X-FEL will achieve stronger fields, provided the parameters for focusing short-wavelength radiation could be improved. For example, in Ref. [48] the following parameters of coherent radiation are indicated as a goal for X-FEL: wavelength of 0.15 nm, peak power of 5 TW, and coherent spike length of 0.08 ps. All that yields a peak intensity of 7×10^{27} W/cm^2, which is only one order of magnitude below the Schwinger limit. Advances in the development of high-frequency and attosecond lasers is likely to leave a lasting mark on the physics of ultra-high intensity laser–matter interactions, as well as open up new areas thereof.

2.1.2. Preparation of states of matter for laser–matter interactions

In general, intense laser–matter interactions are studied using gases of atoms or plasmas. Clusters of various types are also testing grounds for many applications in the field, especially laser-fusion experiments. But ions are also very promising as they allow for semi-bound single electron interactions. The strong Coulomb field of highly charged ions can be comparable with that of the driving laser field, thus leading to a very interesting and promising regime of interaction (see discussion in Sections 6.2 and 6.3). Multiply-charged ions of arbitrary charge and excellent purity can be routinely produced by sending them through thin foils [49]. Another, albeit much less controllable, method of producing highly charged ions employs strong lasers. When neutral atoms are subjected to ultraintense laser fields, many of their electrons get stripped from them very quickly during interaction with the rising portion of a short pulse. This photoionization process results in the production of highly charged ions (HCI) and very energetic electrons [50,51]. Furthermore, photoionization studies of HCIs currently rely on radiative electron capture, the time-reversed photoionization process occurring in ion-atom collisions [52].

There are plenty of developments in the preparation of matter in very specialized states that promise interesting future laser–matter interactions. A wide range of high-precision physics experiments involving HCIs, produced in so-called electron beam ion traps (EBITs), are currently conducted at a number of laboratories. The first EBIT was designed and operated at Lawrence Livermore National Laboratory (LLNL) in the USA. Other EBITs, based on this design are now in operation at the National Institute of Standards and Technology (NIST) in Gaithersburg (USA), at Oxford in the UK, in Berlin and Heidelberg (Germany), and in Tokyo (Japan). Using super-EBIT, a high-energy modification of the facility, scientists at LLNL have produced bare uranium (U^{92+}) for the first time without the need for a high-energy accelerator [53]. The Heidelberg EBIT facility at the Max-Planck-Institute for Nuclear Physics in Heidelberg (Germany) is also capable of producing up to bare uranium ions and keeping them trapped at velocities as low as $10^{-4}c$. Work on the construction of two new EBITs is currently underway in Heidelberg. One of them is intended for use in experiments at the VUV free-electron laser facility at TESLA (Hamburg), while the other will be used for the charge breeding of short-lived radioactive isotopes at the TRIUMF ISAC facility [54].

Currently under construction at the GSI accelerator complex (in Darmstadt, Germany) is HITRAP, a novel facility for the production, trapping and cooling of highly charged ions [55]. The ions are stripped to the desired charge state by sending them through foils.

2.2. Theoretical advances

In what follows theoretical advances will be discussed which have served both for quantitatively describing and intuitively understanding the interaction of matter with super-intense laser pulses. For pedagogical reasons, we start with the Schrödinger dynamics before the fully relativistic quantum dynamics is addressed in more detail based on the Dirac equation. We note also that the Schrödinger equation beyond the dipole approximation and with the addition of leading relativistic terms, such as the mass shift, may be employed to describe the intermediate weakly relativistic regime, being also of interest to us in this review.

2.2.1. Analytical methods

Analytical investigations of super-strong laser–atom interactions have seen much progress over the past two decades. The first impetus in this field is connected with Keldysh's seminal work [56]. It has been developed into a successful

theoretical framework for studying strong-field phenomena—the Keldysh–Faisal–Reiss (KFR) theory [56–58], also known as the strong-field approximation (SFA). The core of the SFA theory for laser-induced ionization processes is to neglect the influence of the Coulomb field of the residual atomic core on the ionized electron state, and the influence of the laser field on the bound state. Correspondingly, the final state of the ionized electron is represented by the Gordon–Volkov state [59] which describes a free electron moving in a laser field. This is a reasonable approximation for regimes of interaction when the intense laser field dominates the ionized electron dynamics. With this method, the qualitative features of above-threshold ionization (ATI) and high harmonic generation (HHG), such as the photon-energy-separated peaks, have been successfully accounted for [60].

Another development from the Keldysh work was the quasi-classical theory (quantum theory in the WKB approximation) of Perelomov, Popov and Terentyev (PPT) describing the strong field ionization of an electron bound in a short range potential [61,62]. Because of the employed WKB approximation, the applicability of this theory is restricted by the conditions

$$\hbar\omega \ll I_{\mathrm{p}} \quad \text{and} \quad E \ll E_a, \tag{1}$$

where E, and ω are the laser electric field strength and frequency, respectively, E_a is the atomic field, and I_{p} is the ionization potential. Both regimes of ionization, tunneling (the Keldysh parameter $\gamma < 1$) and multi-photon ionization ($\gamma > 1$), are well described by this theory. PPT theory allows to derive the pre-exponential coefficient in the Keldysh formula and to calculate the energy and momentum spectra of the photoelectrons. Moreover, the Coulomb interaction in the final state can be included in a quasi-classical (WKB) analysis yielding a more accurate description of the process [63,64]. The PPT theory is applicable for ionization from any atomic state excluding only the excited states of hydrogen. Later, PPT has been simplified and applied for analysis of experimental data (ADK theory) [65]. In the limit $\gamma \ll 1$, PPT theory has been simplified into the adiabatic approximation of Landau–Dykhne [66]. Based also on the same theory, the imaginary time method has been developed (ITM) which gives a formal procedure to derive the probability of ionization processes in the WKB approximation, using solution of the classical equations of motion of the electron with time variable allowed to have imaginary values during the electron motion under the barrier [64,67]. While the SFA yields closed-form analytical results for strong field ionization, the expressions for the transition probabilities are complex and contain sums over all multi-photon processes. Then, physical implications can only be deduced after the numerical calculations have been performed. In contrast to that, the ITM provides simple analytical expressions for the process of direct ionization. Ionization in ultra-short laser pulses has been investigated by this method [67].

New theoretical methods dealing with the strong-field ionization of atoms, based on the original SFA theory, have been developed in the 1990s [68]. To improve on the fact that the original SFA theory completely neglects the influence of the atomic core on the ionized electron, some authors proposed to modify the final Gordon–Volkov state by some means [69]. This approximation stems from the early work of Jain and Tzoar [70] in which a product of a Coulomb scattering state with the standard Volkov time-dependent factor has been proposed to be used instead of the Volkov state as the final state. Further modifications of this approximation have been done by Krainov and co-workers [71] and by Faisal and his collaborators [72]. Other versions of improved Coulomb–Volkov states have been proposed [73]. Some problems in the derivation of Coulomb–Volkov states have been pointed out in [74]. With such modifications to the final state of the ionized electron incorporated, improvements on the quantitative agreement with the experimental measurement of strong field ionization could be achieved [75].

Since its first observation [76], the ATI spectrum has been extensively investigated in experiments. As mentioned above, the original Keldysh-type theories successfully explained its low-energy parts. However, in the mid 1990s, experimental observation of an ATI plateau [77], in which all ATI peaks have almost equal amplitude, challenged the existing SFA theories. As the original SFA theory neglects interaction of the ionized electron with the residual atomic core, it cannot shed any light on the mechanism leading to such an ATI plateau.

Meanwhile, the three-step simple-man model [78,79] proposed the idea of re-scattering which proved very fruitful for explanation of, not only the ATI plateau but, HHG and non-sequential ionization as well. Soon after the observation of the plateau behavior in ATI, Becker and co-workers [80] proposed a theory that attributes the appearance of the high-energy ATI plateau to the (re)scattering of the ionized electron (driven back by the intense laser field) on the atomic core. Alternatively, expanding the time-dependent wave function in terms of ground and continuum states, Lewenstein and co-workers formulated the re-scattering model for intense laser–atom interactions [81]. A more elegant formalism, using the short-range atomic potential, was derived in a series of publications by Becker and co-workers [82]. Most interestingly, with this formalism, one can semiclassically decompose the total ATI probability amplitude into a series of

free-electron trajectories in the laser field (*quantum orbits*) [83]. In other words, one may write the total ATI probability amplitude in the form

$$M = \sum_n a_n e^{iS[\mathbf{r}_n(t)]/\hbar}, \tag{2}$$

where a_n is an amplitude and $S[\mathbf{r}_n(t)]$ denotes the action calculated along the quantum orbit. The amplitude is determined by summing over three steps of the ATI process: (1) tunneling ionization; (2) free electron evolution in the laser field only; and (3) re-scattering on the atomic core at a later time. Eq. (2) corresponds indeed to a Feynman path integral [84]. With this formalism one can also study high-order harmonic generation (HHG), which is a companion of the process of ATI.

Most of these analytical theories of intense laser–atom interactions treat the re-scattering as a perturbation. In this respect, the more accurate consideration of the *Coulomb focusing* effect has shown enhancement of re-scattering [71,85].

Different types of theories for non-sequential ionization employing the idea of re-scattering have been developed including intense-field-many-body *S*-matrix theory [86], a fully classical theory [87], SFA [88], and a time-dependent density-functional theory [89]. These analytical theories, though having employed approximations, have been successfully used to obtain qualitative results in good agreement with the experiments. They have the advantage of offering more explicit explanations of the physics exhibited in intense laser–atom interactions in the non-relativistic regime [9].

We have to mention that, in the theory of strong field ionization, an exactly-solvable model exists which is described by the Schrödinger equation for an electron state decaying in a zero-range potential and a laser field of circular polarization [90]. It allows to investigate the transition from the tunneling regime to the multi-photon regime, in detail, and to check validity of the quasi-classical description (for more details on this study, see recent reviews by Manakov and his collaborators [91]).

Meanwhile, technological advancements in laser physics rendered the realization of relativistic laser–atom interactions possible, thus promoting theoretical investigations in this field. The relativistic version of SFA based on the Klein–Gordon [92] and Dirac [93] equations has been formulated, giving rise to further theoretical investigations in the relativistic regime. Rates for the direct ionization of hydrogen-like ions in strong laser fields of circular as well as linear polarization [94] have been calculated by means of the relativistic version of SFA. The spin effects in the direct ionization of an atom via SFA based on the Dirac equation have also been studied recently [95].

The quasi-classical (WKB approximation) description proves fruitful for the strong-field ionization problem in the relativistic regime as well [96]. The ITM has been extended to the relativistic regime and developed further [97,98]. The ionization rate of the *s* atomic level in the relativistic regime has been calculated taking into account the Coulomb and *spin* corrections in the case of low frequency laser radiation [99]. A relativistic theory of ATI of a quasi-classical nature has been developed in [100] which takes into account the influence of the Coulomb field on the ionized electron. In this work, the SFA approach is applied for the Dirac equation. The state of the ionized electron is described by the so-called generalized eikonal wave function [101], instead of the Volkov wave function as in the SFA. Nevertheless, expressions in closed form for the transition amplitude are restricted to the Born approximation for the Coulomb field of the ionic core. Finally, in the theory of relativistic direct strong field ionization we should mention also an exact solvable model of a Klein–Gordon particle in a separable short-range potential [102].

The existing theories of direct strong field ionization in the relativistic regime give a rather complete quantitative picture of the process. Meanwhile, the high-order ATI with re-scattering and HHG in the relativistic regime have not been investigated sufficiently. A relativistic SFA theory for HHG via solution of the Klein–Gordon equation with a short range potential has been proposed [103]. To investigate relativistic signatures in the "re-collision" model in the weakly relativistic regime, the SFA based on the Schrödinger equation with non-dipole treatment of the laser field has been developed for HHG [104–107] as well as for ATI [108]. Although the basic ideas of the three-step-model and the quantum trajectory approach remain mostly valid in the non-relativistic domain, relativistic effects can significantly modify the process. Particularly, the magnetic field component of the laser field induces a substantial drift in the laser propagation direction, prevents the electron from exactly revisiting the ionic core, and thus decreases essentially the electron re-scattering probability. This effect, for non-sequential double ionization, has been pointed out in [109,110]. An analogous non-dipole treatment has recently been applied to study HHG from intense laser-driven positronium [111]. The result indicates that the damping influence of the relativistic drift on the HHG probability is absent for that system.

As one may expect, non-dipole effects on both the ATI and HHG emission spectra will be significant and may possibly be observed in experiments with the laser intensities currently available. However, since most experiments are being carried out in the non-relativistic regime, the relativistic theories are yet to be widely applied.

2.2.2. Numerical techniques

In addition to the analytical methods mentioned above, more accurate investigations of intense laser interactions with matter rely on numerical solutions to the time-dependent Schrödinger-type equation (TDSE). These methods retain the time-dependent *nonperturbative* term in the intense laser field coupling with the electron's motion. Comprehensive numerical simulations in strong-field physics have been pioneered by Kulander and his co-workers [112], Eberly and his collaborators [113], and many others [114]. In the early studies, three/five-points finite difference methods, with different algorithms such as the implicit Crank–Nicholson method, have been employed to discretize the time-dependent wave function in space, and to advance the time propagation of the wave function of the system [115]. Because the finite-difference method has low accuracy, one needs small grid and temporal steps for accurate calculations. Early simulations were therefore concerned with one-dimensional systems, mostly for linearly polarized intense laser fields [116]. Despite their simplicity, the numerical calculations stimulated research in the field which has resulted in the discovery of a number of exclusive phenomena characterizing intense laser physics in the late 1980s and the early 1990s. These novel features of intense laser–atom interactions include high harmonic generation [117], above threshold ionization [118], and stabilization [116], all of which have been elucidated in 1D calculations.

2.2.2.1. Split-operator algorithm. The split-operator algorithm was first introduced by Feit and coworker [119] to solve the time-independent Schrödinger equation for eigen-energies and eigen-states of a general potential. It was further used for the time-dependent Schrödinger equation by many others [120]. In particular, the split-operator algorithm has been extensively applied to investigate intense laser–atom interactions [121] and proved to be an efficient approach. Actually, the split-operator representation draws from the more general Lie-Trotter algebras [122]. We consider the following time-dependent Schrödinger-type equation

$$\mathrm{i}\frac{\partial}{\partial t}\psi(\mathbf{r},t)=\mathbf{H}(\mathbf{r},t)\psi(\mathbf{r},t), \tag{3}$$

with the time-dependent Hamiltonian $\mathbf{H}(\mathbf{r},t)$. In this section all symbols shown in bold type are operators, apart from the position vector $\mathbf{r}$. When the Hamiltonian is explicitly time-dependent, there is no simple general numerical technique to propagate the wave function from t to $t+\Delta t$. Most approaches assume that a power series in the time variable exists over the time domain, and then calculate the solution to the assumed order. The more sophisticated techniques adapt/adjust the time interval over which the power series is sufficiently accurate and, by a *divide and conquer* methodology, are able to calculate the solution to a predetermined accuracy over the Δt of interest. If we assume that the time interval is sufficiently small that the time-dependent interaction term may be treated as constant in time over the time step Δt, it is trivial to demonstrate that Eq. (3) has a solution given by

$$\psi(\mathbf{r},t+\Delta t)=\mathrm{e}^{-\mathrm{i}\mathbf{H}(\mathbf{r},t)\Delta t}\psi(\mathbf{r},t). \tag{4}$$

The total Hamiltonian may be broken up into two parts, that is, $\mathbf{H}(\mathbf{r},t)=\mathbf{T}+\mathbf{V}$, and $\mathbf{T}$ and $\mathbf{V}$ are the kinetic and potential energy components, respectively. Thus, the time-propagation of the wave function may be re-written as

$$\psi(\mathbf{r},t+\Delta t)=\mathrm{e}^{-\mathrm{i}(\mathbf{T}+\mathbf{V})\Delta t}\psi(\mathbf{r},t). \tag{5}$$

Successively more accurate approximations may be made to the exponential operator by taking higher-order symmetric products of the primitive operator $\mathbf{U}_1(\Delta t)$

$$\mathbf{U}_1(\Delta t)=\mathrm{e}^{-\mathrm{i}\mathbf{T}\Delta t}\times\mathrm{e}^{-\mathrm{i}\mathbf{V}\Delta t}, \tag{6}$$

or

$$\mathbf{U}_1(\Delta t)=\mathrm{e}^{-\mathrm{i}\mathbf{V}\Delta t}\times\mathrm{e}^{-\mathrm{i}\mathbf{T}\Delta t}. \tag{7}$$

The exponential operator that is accurate to second-order in the time step has the following form

$$\mathrm{e}^{-\mathrm{i}(\mathbf{T}+\mathbf{V})\Delta t} = \mathbf{U}_2(\Delta t) + O((\Delta t)^3), \tag{8}$$

with $\mathbf{U}_2(\Delta t) = \mathbf{U}_1((\Delta t)/2) \times \mathbf{U}_1((\Delta t)/2)$. Combining the inner exponential terms that depend on $\mathbf{T}$ or $\mathbf{V}$, produces the compact form of the second-order split-operator propagator,

$$\mathbf{U}_2(\Delta t) = \mathrm{e}^{-\mathrm{i}\mathbf{V}\Delta t/2} \times \mathrm{e}^{-\mathrm{i}\mathbf{T}\Delta t} \times \mathrm{e}^{-\mathrm{i}\mathbf{V}\Delta t/2}, \tag{9}$$

or

$$\mathbf{U}_2(\Delta t) = \mathrm{e}^{-\mathrm{i}\mathbf{T}\Delta t/2} \times \mathrm{e}^{-\mathrm{i}\mathbf{V}\Delta t} \times \mathrm{e}^{-\mathrm{i}\mathbf{T}\Delta t/2}. \tag{10}$$

Since the exponential kinetic energy operator $\mathrm{e}^{-\mathrm{i}\mathbf{T}\Delta t} = \mathrm{e}^{-\mathrm{i}\mathbf{p}^2\Delta t/2}$ can directly act on the momentum-space wave function, one may Fourier transform the spatial wave function into momentum space and take action of the exponential operator involving $\mathbf{T}$ on the wave function as a phase factor. However, because the potential term is expressed in terms of the space coordinates, the momentum-space wave function has to be transformed back to the coordinate space. Also, the exponential operator involving $\mathbf{V}$ acting on the coordinate-space wave function contributes only a phase shift. With the fast Fourier transformation (FFT) [123] of the wave function back and forth between the momentum and coordinate spaces, the split-operator approach can be efficiently implemented. It can be shown that the FFT approach reduces the N^2 operations to $N\log(N)$ ones. Similarly, one can get a higher-order splitting propagator, for example, by combining the second-order propagators to form an approximation accurate to fourth order, as in

$$\mathbf{U}_4(\Delta t) = \mathbf{U}_2(p\Delta t)\mathbf{U}_2(p\Delta t)\mathbf{U}_2(q\Delta t)\mathbf{U}_2(p\Delta t)\mathbf{U}_2(p\Delta t), \tag{11}$$

where $p = 1/(4 - 4^{1/3})$ and $q = 1 - 4p$. The optimal choice of the splitting parameters p and q derives from the particular Lie–Trotter algebra [122].

When one has to deal with the Schrödinger-type Hamiltonian beyond the usual dipole approximation, the normal split-operator algorithm can be modified for solving the time-dependent Schrödinger equation in the non-dipole and relativistic cases. For example, to implement the split-operator algorithm for the non-dipole interaction term "$p_x A_x(z, t)$", we may Fourier transform only the x-component of the coordinate wave function and leave the z-component unchanged. Therefore, its exponential action can be carried out in such a mixed form.

If the split-operator algorithm is employed to solve the fully relativistic Dirac equation, this minor complication does not occur, since the Dirac equation is linear in the momentum, and mixed terms do not appear. Apart from this advantage of formal simplicity, the Dirac equation also includes the particle's spin without the need of additional terms. It is suitable for both particles and antiparticles, and, to some extent, it can even be employed to model pair-creation processes. Both the particle's spin and its sign of energy are typically encoded via a matrix formalism. In this case, the Hamiltonian itself is a four by four matrix.

We write the Dirac equation in the same form as the Schrödinger equation

$$\mathrm{i}\hbar\,\frac{\partial\psi}{\partial t} = \mathbf{H}\psi. \tag{12}$$

The Dirac Hamiltonian for a fermionic particle with charge q and rest mass m then reads as follows

$$\begin{aligned}\mathbf{H} &= -\mathrm{i}\hbar c\alpha^i\frac{\partial}{\partial x^i} + \beta mc^2 + q(A_0(\vec{x}) + \alpha^i A_i(\vec{x})) \\ &= \mathbf{H}_{\vec{\partial}} + \mathbf{H}_{\vec{x}},\end{aligned} \tag{13}$$

and can be split into a position-dependent and a derivative-dependent part, as indicated above. Here, α^i and β represent the usual Dirac matrices with $i \in \{1, 2, 3\}$. As in the Schrödinger case, we consider the short-time propagation of a wave function at time t

$$\psi_{(t+\Delta t)} = \mathrm{e}^{-(\mathrm{i}\Delta t/\hbar)\,\mathbf{H}}\psi_t. \tag{14}$$

The split-operator approximation then reads as follows [125]

$$\psi_{(t+\Delta t)}(\vec{x}) \approx \exp\left(-\frac{\mathrm{i}}{\hbar}\frac{\Delta t}{2}\mathbf{H}_{\vec{\partial}}\right)\exp\left(-\frac{\mathrm{i}}{\hbar}\Delta t\,\mathbf{H}_{(t+\frac{\Delta t}{2},\vec{x})}\right)\exp\left(-\frac{\mathrm{i}}{\hbar}\frac{\Delta t}{2}\mathbf{H}_{\vec{\partial}}\right)\psi_t(\vec{x}) + O(\Delta t^3). \tag{15}$$

Again, just as in the Schrödinger case, fast Fourier transforms are an appropriate means to evaluate the action of the exponential momentum space operator that contains $\mathbf{H}_{\vec{\partial}}$. In addition, the matrix character has to be taken care of. This is most conveniently accomplished with the help of a series expansion. The result can be written as follows

$$\exp\left(-\frac{\mathrm{i}}{\hbar}\frac{\Delta t}{2}\mathbf{H}_{\vec{\partial}}\right) = \mathbf{F}^{-1}\left(\cos(\phi) - \mathrm{i}\,\sin(\phi)\frac{\beta\frac{mc}{\hbar} - \alpha^i k_i}{\sqrt{\left(\frac{mc}{\hbar}\right)^2 + \vec{k}^2}}\right)\mathbf{F}; \quad \phi = \frac{c\Delta t}{2}\sqrt{\left(\frac{mc}{\hbar}\right)^2 + \vec{k}^2}, \tag{16}$$

where $\mathbf{F}$ indicates the Fourier transform and $\mathbf{F}^{-1}$ its inverse . Similarly, one obtains

$$\begin{aligned}\exp\left(-\frac{\mathrm{i}}{\hbar}\Delta t\,\mathbf{H}_{(t+\frac{\Delta t}{2},\vec{x})}\right) = &\left(\cos\left(\frac{qA_0}{\hbar}\Delta t\right) - \mathrm{i}\,\sin\left(\frac{qA_0}{\hbar}\Delta t\right)\right)\\ &\times\left(\cos\left(\frac{q|\vec{A}|}{\hbar}\Delta t\right) - \mathrm{i}\,\sin\left(\frac{q|\vec{A}|}{\hbar}\Delta t\right)\frac{\alpha^i A_i}{|\vec{A}|}\right).\end{aligned} \tag{17}$$

The major drawback of the Dirac treatment is the temporal step size $\Delta t \lesssim \hbar/E$ required, which has to be significantly smaller than for Schrödinger treatments, because of the large rest mass energy mc^2 that is contained in the particle's total energy E.

To fully explore the relativistic super-strong laser–matter interactions, Maquet et al. have numerically solved the Klein–Gordon equation [126]. Also, the Pauli equation [127] and the four-spinor Dirac equation [128] have already been used in intense laser physics. Besides the fully quantum mechanical treatments, semiclassical and classical methods, such as the semiclassical relativistic Monte-Carlo method [129] and particle-in-cell (PIC) simulations [130], have been employed in investigating the strong-field interactions.

2.2.2.2. Adaptive-grid and parallel schemes. For the algorithms described above the spatial grids are generally discretized equally in space. This is too demanding, especially for 2D or 3D calculations. In fact, it is more reasonable to discretize the spatial grids unequally according to the potential configuration. For example, one may distribute more grid points in the region where the potential has a larger gradient (i.e., near the nucleus), and less points for the flat potential parts. This technique has been adopted for solving TDSE of intense laser–atom interactions [131]. It has been proven extremely useful for large-scale simulations. In addition, parallel schemes of either using the general MPI or applying OpenMP would have substantial potential to save CPU times, particularly for many-electron systems driven by intense laser fields [132].

Most recently, Mocken and Keitel have developed an advanced algorithm to numerically solve the Dirac equation [133] in two dimensions following the method laid out in subsection (a). To reduce the computing times, they employ the following two techniques. First, in position space, the calculation is not actually carried out for the whole region of interest, but only in a much smaller area that is always kept centered around the wave packet—a so called "moving-grid" approach. Second, the grid size, too, is dynamically adapted to the problem: even a freely-evolving wave packet spreads as time goes by and, e.g., a scattered one does so even more. As the simulation has to cover times where the packet is still quite small, it is possible to save a lot of CPU time, because one of the most demanding operations, the two-dimensional fast Fourier transform, scales as $O(N^2 \log N)$, where $N \times N$ equals the grid size. This so-called "growing-grid" approach is also a pragmatic solution to the well-known boundary problem [134,135] in Dirac calculations: a damping function is applied to the wave function to simulate an absorbing boundary around the edge of the numerical grid, knowing that this is an insufficient solution. However, this damping effectively only comes into play after the grid has reached its maximum size (which is given by practical considerations such as memory and time requirements). Prior to this situation, there is no boundary problem simply because the wave packet is far away from the boundary. By dynamically adjusting the boundary position, it is possible to maintain this favorable condition for

at least a while. The main difference between this approach and the one discussed before is that the grid resolution (number of grid points per physical unit length) is constant in space. This is a tribute to the Fourier Transform, which requires a well-defined momentum space, and therefore equally spaced grid points.

Other methods to solve the Dirac equation that rely on finite-difference techniques rather than Fourier transforms typically suffer from a problem called *fermion doubling* [136,137]. However, they are more suitable for distributed parallel programming techniques than any codes that rely on Fast Fourier transforms. The latter can at least benefit from SMP (symmetric multiprocessing) environments, where all grids can be kept in one contiguous memory space. In this case, use of a multi-threaded FFT implementation such as the one provided by the FFTW library [138] is beneficial. For the special momentum and position space grid operations given by Eqs. (16) (leaving out the Fourier Transforms) and (17), a parallel implementation is possible as well. These operations are local ones, therefore it is possible to split the grid into slices and feed each slice to one particular CPU.

More precisely, if N is the number of grid rows and n the number of CPUs available, then the following formula ensures optimum distribution of grid rows among the units

$$p = N \operatorname{div} n \quad r = N \bmod n, \tag{18}$$

$$\min_i = \begin{cases} i(p+1), & i \le r, \\ r(p+1) + (i-r)p, & i > r. \end{cases} \quad \max_i = \begin{cases} \min_{(i+1)} - 1, & i < n-1, \\ N-1, & i = n-1. \end{cases} \tag{19}$$

By "div" and "mod" in Eq. (18) we mean the usual integer operations for division and modulus. The index $i \in \{0, 1, \ldots, n-1\}$ in Eq. (19) enumerates the CPUs, and the set $\{\min_i, \min_i + 1, \ldots, \max_i\}$ represents the row numbers of the part of the grid that is assigned to the ith CPU. Eq. (19) ensures that for any N and n, the difference in size of the individual grid parts is always less or equal to a single row. Hence, the execution times of the separate threads are guaranteed to be almost equal, and waiting times for thread synchronization are minimized. This is especially important for size-adaptive grids and a large number of CPUs, where it becomes difficult (or at least inefficient) to maintain grid sizes that are divisible by n without a remainder for all times.

3. Relativistic laser–electron interactions

In a discussion of the interaction of a single electron with ultra-intense laser light, subject of the present section, the question arises often as to whether a quantum mechanical approach is mandatory. To shed some light on this issue, we consider first the classical mechanical description of the process which lays down a sound background for understanding interaction with strong laser fields. Particularly, as is well known, the main *coarse* features of the electron dynamics, such as the center-of-mass motion of the electron wave packet [139] and the electron threshold momenta at the ATI or cutoff frequency of HHG [9], are in general well described classically. Nevertheless, the quantum mechanical description reveals deviating *fine* features of the dynamics especially when it comes to interference and spin effects.

Thus, the first part of this section is devoted to a review of the classical relativistic laser–electron interaction, which will be sufficient for many situations such as laser acceleration. Next, intrinsically quantum effects are reviewed, including especially the spin and interference effects. Tunneling and QED effects are discussed in Sections 5 and 7. In the third subsection, interaction of electrons, born from ionization, with laser and other added static electromagnetic fields will be discussed.

3.1. Classical analysis

Motion of a single electron, of mass m and electric charge $-e$, in a low-intensity radiation field is influenced mainly by the electric field component of the wave. Typically, the electric force has a maximum $F_e \sim eE_0$, where E_0 is the peak-field strength. But the magnetic component has a peak value of $F_m \sim e\beta E_0$, where β is the velocity of the particle normalized by the speed of light c. As long as the electron speed stays small compared to the speed of light, i.e., $\beta = F_m/F_e \ll 1$, the magnetic component of the field force, may be neglected. For a sine-wave field, and under these conditions, Newton's second law of motion may be written as

$$m\frac{\mathrm{d}v}{\mathrm{d}t} = -eE_0 \sin\omega t, \tag{20}$$

where ω is the angular frequency of the electromagnetic wave. Note also that the term $\mathbf{k}\cdot\mathbf{r}$, where $\mathbf{k}$ is the wavevector and $\mathbf{r}$ is the position vector of the electron, has been ignored, a fairly acceptable procedure as long as the radiation wavelength is large compared to a characteristic length pertinent to the problem at hand. A single integration of Eq. (20) yields, in principle,

$$v(t) = v_m \cos\omega t; \quad v_m = \frac{eE_0}{m\omega}. \tag{21}$$

When conditions on the intensity render $v_m \sim c$ one must abandon the non-relativistic treatment, exemplified above, altogether and adopt a relativistic approach instead. In other words, relativity sets in whenever the dimensionless intensity parameter (see also Eq. (29) below)

$$q = \frac{eE_0}{m\omega c} \tag{22}$$

becomes comparable to or greater than unity. In terms of the laser field wavelength λ (in μm) and intensity I (in W/cm^2) one has

$$I\lambda^2 = \left(\frac{5\pi m^2 c^5}{e^2}\right) q^2 \sim 1.375\times 10^{18} q^2. \tag{23}$$

Our interest, in the present review, is in the kind of physics that may be done with laser systems capable of delivering field intensities in excess of the relativistic threshold ($q \sim 1$). For such systems, the fields may be treated classically and, hence, all information pertaining to the motion of a single particle, a *classical* electron to be definite, subsequent to injection into the laser beam, will be obtained from solutions to the Newton–Lorentz equations (with $\mathbf{E}$, the electric field strength and $\mathbf{B}$ the magnetic field strength, respectively, in Gaussian units)

$$\frac{\mathrm{d}\mathbf{p}}{\mathrm{d}t} = -e[\mathbf{E} + \boldsymbol{\beta}\times\mathbf{B}], \quad \frac{\mathrm{d}\mathscr{E}}{\mathrm{d}t} = -ec\boldsymbol{\beta}\cdot\mathbf{E}, \tag{24}$$

subject to initial conditions appropriate to the situation at hand. In Eqs. (24) the quantities have their usual definitions: the momentum $\mathbf{p} = \gamma mc\boldsymbol{\beta}$, the energy $\mathscr{E} = \gamma mc^2$, the Lorentz factor $\gamma = (1-\beta^2)^{-1/2}$, and the velocity, normalized by the speed of light c in vacuum, is $\boldsymbol{\beta}$.

Unfortunately, the equations of motion (24), or their covariant counterpart, admit analytic solutions only for plane-wave fields and under very specialized conditions [141–150]. For example, let the laser field be modeled by a vector potential $\mathbf{A}(\eta)$, where $\eta = \omega t - \mathbf{k}\cdot\mathbf{r}$, with t and $\mathbf{r}$ the time and space coordinates of the electron and $\mathbf{k}$ the wave vector of the laser field ($\omega = ck$). Then let an electron be incident from the point with a position vector $\mathbf{r}_0$, and sideways at an arbitrary angle θ_0 to the beam direction of propagation, with an arbitrary initial velocity $\boldsymbol{\beta}_0 = \mathbf{v}_0/c$. Then, its subsequent energy and momentum and position vectors, respectively, may be found from [148]

$$\mathscr{E}(\eta) = \gamma_0 mc^2\left[1 + \frac{\frac{1}{2}\left(\frac{e\mathbf{A}(\eta)}{\gamma_0 mc^2}\right)^2 + \left(\frac{e\mathbf{A}(\eta)}{\gamma_0 mc^2}\right)\cdot\boldsymbol{\beta}_0}{\left(1-\hat{\mathbf{k}}\cdot\boldsymbol{\beta}_0\right)}\right], \tag{25}$$

$$\mathbf{p}(\eta) = \frac{e}{c}\mathbf{A}(\eta) + \gamma_0 mc\boldsymbol{\beta}_0 + \hat{\mathbf{k}}\gamma_0 mc\left[\frac{\frac{1}{2}\left(\frac{e\mathbf{A}(\eta)}{\gamma_0 mc^2}\right)^2 + \left(\frac{e\mathbf{A}(\eta)}{\gamma_0 mc^2}\right)\cdot\boldsymbol{\beta}_0}{\left(1-\hat{\mathbf{k}}\cdot\boldsymbol{\beta}_0\right)}\right], \tag{26}$$

and

$$\mathbf{r}(\eta) = \mathbf{r}_0 + \frac{1}{k}\int_{\eta_0}^{\eta}\left[\frac{\boldsymbol{\beta}_0 + \frac{e\mathbf{A}(\eta')}{\gamma_0 mc^2}}{1-\hat{\mathbf{k}}\cdot\boldsymbol{\beta}_0}\right]\mathrm{d}\eta' + \frac{\mathbf{k}}{k^2}\int_{\eta_0}^{\eta}\left[\frac{\frac{1}{2}\left(\frac{e\mathbf{A}(\eta')}{\gamma_0 mc^2}\right)^2 + \left(\frac{e\mathbf{A}(\eta')}{\gamma_0 mc^2}\right)\cdot\boldsymbol{\beta}_0}{\left(1-\hat{\mathbf{k}}\cdot\boldsymbol{\beta}_0\right)^2}\right]\mathrm{d}\eta'. \tag{27}$$

Strictly speaking, Eqs. (25)–(27) have not been obtained directly from (20) but, rather, from a Hamilton–Jacobi construction [148]. With $\mathbf{A}(\eta)$ describing a plane-wave, one can easily see that the electron acquires a mass shift as a result of interaction with the radiation field. Note that, in the absence of the field, one has $(mc^2) = \mathscr{E}^2 - (c\mathbf{p})^2$, with m still the electron's rest mass. However, in the presence of the radiation field, the analog of this equation takes the form

$$(m_* c^2)^2 = \langle \mathscr{E} \rangle^2 - (c\langle \mathbf{p} \rangle)^2, \tag{28}$$

where m_* denotes an *effective mass* for the electron *dressed* by the radiation field, and $\langle \cdots \rangle$ stands for time-averaging. The effective mass is given by [142,143]

$$m_* = m\sqrt{1 + \frac{\bar{q}^2}{2}} \quad \text{where } \bar{q}^2 = \frac{2e^2\langle A^2 \rangle}{(mc^2)^2}. \tag{29}$$

The analytic solutions have been quite helpful in understanding the electron dynamics of some rather ideal configurations, and have helped in setting the stage for accurate numerical calculations involving realistic ones. The more complicated classical dynamics of an electron in the fields of a focused laser beam, as well as in the presence of additional static electric and magnetic fields, will be discussed in Section 4 in connection with the problem of laser acceleration.

3.2. Quantum mechanical analysis

Within a quantum mechanical approach, discussion of the interaction of a single electron with ultra-intense laser light portrays a number of interesting features. To begin with, the point particle model of an electron gives way to a wave packet description. Evolution of such an electron wave packet in the radiation field is considered next.

3.2.1. Electron wave packet evolution

We consider first the quantum evolution of a single electron wave-packet in a super-strong laser pulse. Such a wave packet undergoes distortion and shearing due to interaction with the oscillating electromagnetic fields of the laser (see Fig. 3), even at intensities below the relativistic threshold. This has recently been the subject of analytical investigation by solving the time-dependent Schrödinger equation for an electron in a plane-wave linearly-polarized laser field without resorting to the dipole approximation [151]. The distortions could, therefore, be attributed to the retention of the magnetic field effects in lowest order when the fields are derived from a vector potential $\mathbf{A} = \hat{\mathbf{x}}A(\phi) \approx \hat{\mathbf{x}}[A(\omega t) - kzA'(\omega t)]$, where $\phi = \omega t - kz$ and each prime on A stands for a single differentiation with respect to ϕ. In addition to the electric field $\mathbf{E} = -\hat{\mathbf{x}}(\omega/c)(A' - kzA'')$, this vector potential gives a magnetic field component $\mathbf{B} = -\hat{\mathbf{y}}kA'$. The latter is responsible for the squeezing and shearing of the wave packet via the $\mathbf{v} \times \mathbf{B}$ force.

At higher intensities, however, one must come to grips with the relativistic effects [139,140,153]. An appropriate representation ought to be in terms of relativistic wavepackets as investigated in [139]. Those wave packets may be described by a superposition of many relativistic Volkov states. Their evolution has been studied via numerical evaluation of the integral representing the time-dependent superposition

$$\Psi(\mathbf{x}, t) = \int \mathrm{d}^3 p \sum_r c_r(\mathbf{p}) \psi_{\mathbf{p}}^{(r)}(\mathbf{x}, t), \tag{30}$$

where the $\psi_{\mathbf{p}}^{(r)}(\mathbf{x}, t)$ are Volkov solutions with polarization r and momentum $\mathbf{p}$. The expansion coefficients $c_r(\mathbf{p})$ are derived from the initial condition that the wave packet is a Gaussian. In addition to a drift forward (in the laser propagation direction), the electron wave packet has been found to undergo distortion and squeezing. This is shown in Fig. 4.

3.2.2. Quantum interference

More recently, the quantum signatures of a free electron in interaction with such fields have been investigated using a Wigner-function approach [152]. As is well-known, the Wigner function is a phase space quasi-probability distribution which can assume negative values as a sign of departure from classicality of the system it describes. In Ref. [152] the Wigner function of a free electron modeled by a two-dimensional Gaussian wave packet and subjected to a plane-wave laser field has been investigated. The wave function of the system has first been calculated analytically in the

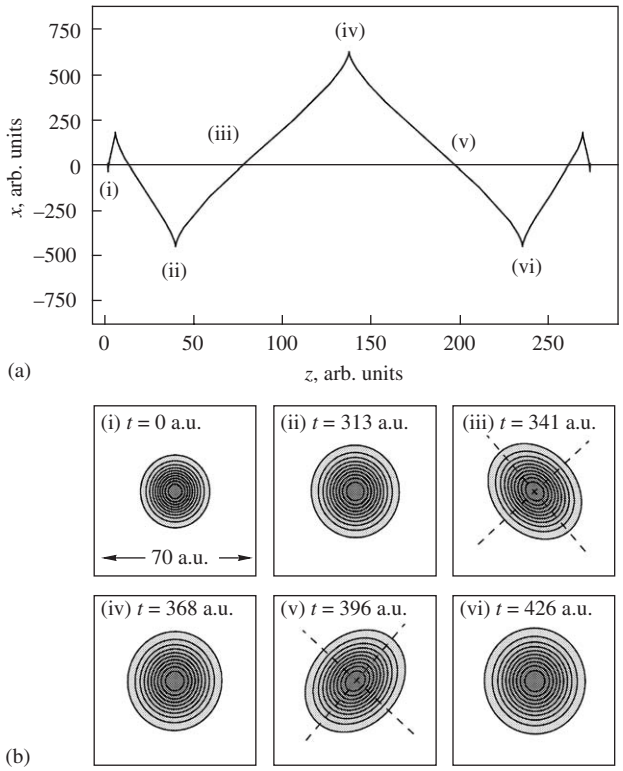

Fig. 3. Electron wave-packet dynamics: (a) the trajectory of the maximum of the wave packet. The labels (i)–(vi) mark the positions for which the wave packets are plotted in (b). The sides of each of the squares have a width of 70 a.u. In (iii) and (v), the principal axes of the wave packets are shown. The directions deviate from the diagonals by an angle of $A(t_{iii}/t_v)/(4c^2)$, where t_{iii}/t_v represent the times when the electron is at points (iii) and (v), respectively. The other wave packets in (b) are axially symmetric [151]. Reprinted with permission from [151]; Copyright 2005 by the Springer Science and Business Media.

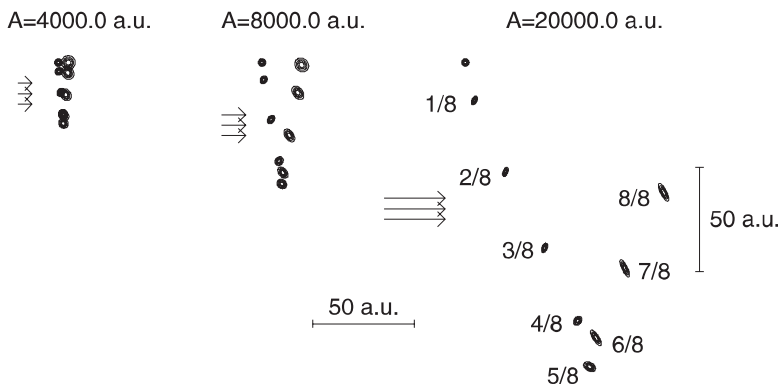

Fig. 4. Evolution of a free Dirac electron driven by an intense ultraviolet laser field of frequency equal to $\omega = 2$ a.u. (the photon energy of 54.4 eV) at three different laser intensities. Each trajectory is viewed using nine different plots, at intervals of an eighth of a period. The Schrödinger-like case (trajectory on the left) corresponds to $A = 4000$ a.u., where A is the amplitude of the laser field vector potential, (i.e. to an intensity of 1.2×10^{20} W/cm^2). Contour plots of the total probability density are drawn, using a linear scale for the contours. The horizontal axis is the propagation direction and the vertical axis is the electric field direction, meaning that the magnetic field is perpendicular to the paper. A relativistic case (trajectory in the center) corresponds to $A = 8000$ a.u. (i.e. to an intensity of 4.8×10^{20} W/cm^2). The trajectory for $A = 20000$ a.u. (i.e. an intensity of 3×10^{21} W/cm^2) corresponds to a strongly relativistic case (trajectory on the right) [139]. Reprinted with permission from [139]; Copyright 2000 by the IOP Publishing Limited.

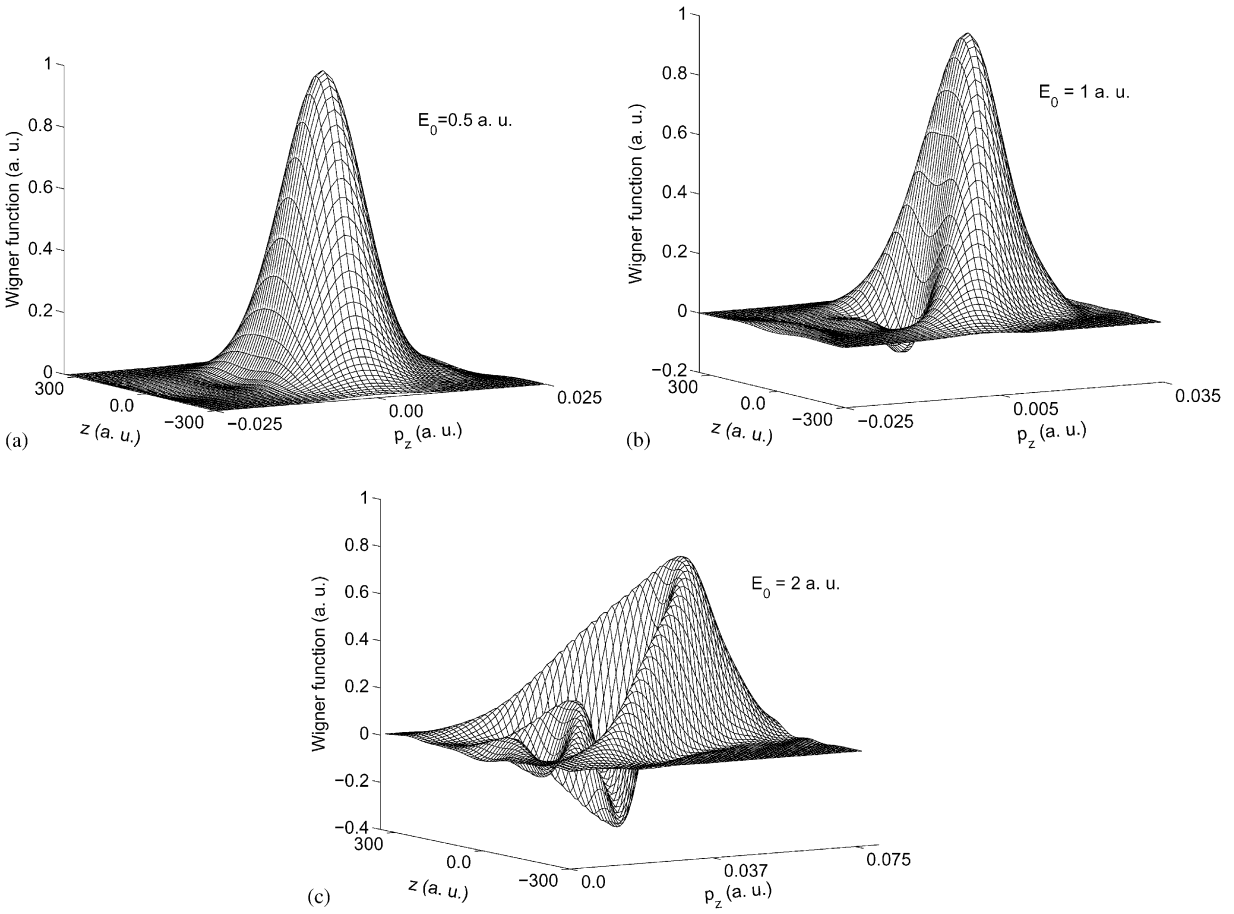

Fig. 5. The Wigner function of a free electron initially (at $t = 0$) at rest at the origin of coordinates and subsequently subjected to a plane-wave laser field. The plots are for a wave packet that has interacted with a field of frequency $\omega = 1$ a.u. for a time equal to 0.5 T, where T is a laser–field cycle. The snapshots correspond to $x = 0 = p_x$, and an initial wave packet modeled by a two-dimensional Gaussian of width equal to $a = 100$ a.u. in either spatial dimension. The dipole approximation has not been made [152]. Reprinted with permission from [152]; Copyright 2005 by the American Physical Society.

Kramer–Henneberger (KH) frame and then transformed to the lab frame. (The KH frame is a non-inertial reference frame in which the electron quiver motion in a laser field may be eliminated, exactly in the dipole approximation and approximately without it.) The Wigner function of the system has then been calculated numerically. Fig. 5 shows that the quasi-probability distribution exhibits negativities clearly when the dipole approximation (DA) is abandoned altogether. Furthermore, the distribution shows distortions and shearing as the wave packet evolves in time. Particularly interesting here is the interpretation of the distortions, due to the magnetic field of the laser in the non-dipole approximation (NDA) regime, in terms of quantum pathways (see Fig. 6). In Fig. 6, the arrows indicate both the forces acting on the electron as well as the free electron quantum pathways. Note that within the dipole approximation, Fig. 6(a), all parts of the wave packet (solid circle) are roughly subject to the same forces in both magnitude and direction. However, beyond the dipole approximation, Fig. 6(b), while at this stage a negligible ponderomotive force still acts, different parts of the wave packet may be subject to different forces at the same time. However, only beyond the dipole approximation, and with significant dynamics in the laser propagation direction, Fig. 6(c), may fractions of the wave packet move in both the polarization and propagation directions. Thus, there may be quantum pathway interferences leading to negativities in the Wigner function. Suppose, further, that measurement at some time, reveals that the free electron is roughly at point B in Fig. 6(c). Then, one would not be able to tell with reasonable certainty whether it was at A or at A′ at some earlier time.

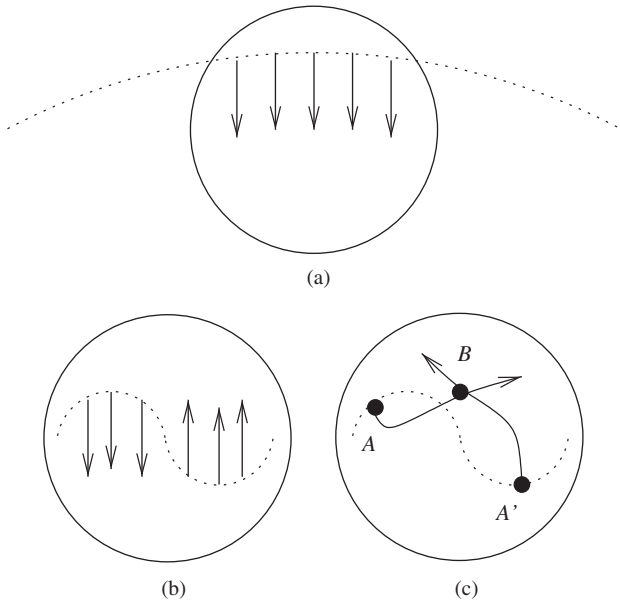

Fig. 6. A schematic of the interaction of a free electron wave packet (solid lines) with a laser wave (dotted lines). (a) In the dipole approximation (DA) ($\lambda \gg a$), where λ is the laser wavelength and a is the size of the wave packet, (b) In the non-dipole approximation (NDA), but in the regime in which the magnetic force ($\mathbf{v} \times \mathbf{B}$) is neglected, and (c) In the NDA case, where $\lambda \leq a$ and with the $\mathbf{v} \times \mathbf{B}$ force playing a significant role. The arrows indicate possible free electron quantum pathways [152]. Reprinted with permission from [152]; Copyright 2005 by the American Physical Society.

3.2.3. Spin effects

We now turn to the spin-induced dynamics and spin reaction of a free electron driven by weakly relativistic intense laser fields [154–156]. These were investigated in detail both semiclassically (simulating the quantum feature of spin classically) and fully quantum-mechanically. We review both approaches in what follows. A relativistic fully quantum description of this problem is still not available as far as we know.

3.2.3.1. Semiclassical spin dynamics. The non-relativistic equation of motion of a classical particle with charge $-e$, mass m and velocity $\mathbf{v} = (v_x, v_y, v_z)$, in a linearly polarized plane laser field, with polarization x, magnetic field oscillation along y and laser propagation axis z, reads

$$m \frac{\mathrm{d}\mathbf{v}}{\mathrm{d}t} = -e \left(\mathbf{E} + \frac{\mathbf{v}}{c} \times \mathbf{B} \right), \tag{31}$$

with the laser electric field denoted by $\mathbf{E} = (E_0 \cos(\omega t - kz), 0, 0)$, the laser magnetic field given by $\mathbf{B} = (0, E_0 \cos(\omega t - kz), 0)$, the angular frequency ω, $k = \omega/c$ and c is the speed of light. With the particle initially at rest at the origin of coordinates, the solution of Eq. (31) may be written as

$$v_x = v_0 \sin(\omega\tau), \tag{32}$$

$$v_y = 0, \tag{33}$$

$$v_z = c \left(1 - \sqrt{1 - \frac{v_0^2}{c^2} \sin(w\tau)^2} \right), \tag{34}$$

with $v_0 = eE_0/m\omega$ and the proper time parameter defined by $\tau := t - z/c$.

While the particle is in motion according to Eqs. (32)–(34), its spin changes. The starting point of a classical description of the spin dynamics is the equation of Larmor precession [141] of the magnetic moment $\mathbf{m} = \kappa \mathbf{s}$,

where $\kappa = e/mc$ for a particle with spin $\mathbf{s}$:

$$\frac{\mathrm{d}\mathbf{s}}{\mathrm{d}t} = \kappa \mathbf{s} \times \left(\mathbf{B} - \frac{\mathbf{v}}{c} \times \mathbf{E} \right), \quad \mathbf{s}^2 = \frac{\hbar^2}{4}. \tag{35}$$

Making the ansatz $\mathbf{s} = (s\cos\theta, 0, s\sin\theta)$, $s = \hbar/2$, the Larmor equation then leads to $\mathrm{d}\theta/\mathrm{d}\tau = \kappa E_0 \cos(\omega\tau)$ for the spin orientation θ. Finally, the change in spin orientation may be written as

$$\Delta\theta(\tau) = \theta(\tau) - \theta_0 = \frac{v_0}{c} \sin(\omega\tau), \tag{36}$$

where θ_0 denotes the initial orientation.

Now we turn to the spin signatures on the relativistic dynamics. A fully relativistic version of the classical spin dynamics follows from the

$$m \frac{\mathrm{d}\mathbf{u}}{\mathrm{d}t} = -e \left(\mathbf{E} + \frac{\mathbf{v}}{c} \times \mathbf{B} \right), \quad \frac{\mathrm{d}\mathscr{E}}{\mathrm{d}t} = q\mathbf{v} \cdot \mathbf{E}, \tag{37}$$

with the 3-velocity $\mathbf{u} = \gamma\mathbf{v}$, the energy $\mathscr{E} = \gamma mc^2$, and $\gamma = (1 - v^2/c^2)^{-1/2}$. With the electric and magnetic field components of the laser as prescribed in the non-relativistic case above, Eqs. (37) admit the following solution:

$$u_x(\tau) = v_0 \sin(\omega\tau), \tag{38}$$

$$u_y(\tau) = 0, \tag{39}$$

$$u_z(\tau) = \frac{1}{2} \frac{v_0^2}{c} \sin(\omega\tau)^2, \tag{40}$$

$$\gamma(\tau) = 1 + \frac{1}{2} \frac{v_0^2}{c^2} \sin(\omega\tau)^2. \tag{41}$$

The relativistic equation describing the spin precession is a generalization of (35), Thomas' equation [141]

$$\frac{\mathrm{d}\mathbf{s}}{\mathrm{d}t} = \kappa \mathbf{s} \times \left(\frac{\mathbf{B}}{\gamma} - \frac{1}{1+\gamma} \frac{\mathbf{v}}{c} \times \mathbf{E} \right). \tag{42}$$

Making again the ansatz $\mathbf{s} = (s\cos\theta, 0, s\sin\theta)$ one gets $\mathrm{d}\theta/\mathrm{d}\tau = \kappa[1 - u_z/c(1+\gamma)]E_0 \cos(\omega\tau)$, and

$$\Delta\theta(\tau) = \theta(\tau) - \theta_0 = 2 \arctan \left[\frac{1}{2} \frac{v_0}{c} \sin(\omega\tau) \right]. \tag{43}$$

Note that Eq. (43) reduces to (36) in the small velocity limit, $v_0/c \ll 1$.

3.2.3.2. The quantum approach to spin dynamics. We conclude this section by shortly addressing the quantum treatment of the electron spin dynamics. The non-relativistic Hamilton operator of the Schrödinger equation which describes the time evolution of the spin of a particle moving classically according to Eq. (35) reads

$$H = -\frac{\kappa\hbar}{2} \left(\mathbf{B} - \frac{\mathbf{v}}{c} \times \mathbf{E} \right) \cdot \boldsymbol{\sigma} \tag{44}$$

$$= -\frac{\kappa\hbar}{2} E_0 \cos(\omega\tau) \left(1 - \frac{v_z}{c} \right) \sigma_y, \tag{45}$$

where $\boldsymbol{\sigma} = (\sigma_x, \sigma_y, \sigma_z)$ denote the Pauli spin matrices. We denote the eigenvectors of σ_y by $|+\rangle_y$ and $|-\rangle_y$. Although this describes the spin degree of freedom within a conventional quantum treatment, the particle dynamics itself, including τ in the above equation, will be evaluated classically. The ansatz $\Psi = a|+\rangle_y + b|-\rangle_y$, $|a|^2 + |b|^2 = 1$ leads to

the equations

$$\frac{\mathrm{d}a}{\mathrm{d}\tau} = \mathrm{i}\frac{\kappa E_0}{2}\cos(\omega\tau)a, \tag{46}$$

$$\frac{\mathrm{d}b}{\mathrm{d}\tau} = -\mathrm{i}\frac{\kappa E_0}{2}\cos(\omega\tau)b, \tag{47}$$

with the solutions

$$a(\tau) = a_0 \exp\left[\mathrm{i}\,\frac{1}{2}\,\frac{v_0}{c}\,\sin(\omega\tau)\right], \tag{48}$$

$$b(\tau) = b_0 \exp\left[-\mathrm{i}\frac{1}{2}\,\frac{v_0}{c}\,\sin(\omega\tau)\right], \tag{49}$$

for all values of a_0 and b_0 that satisfy the normalization condition $|a_0|^2 + |b_0|^2 = 1$. With the time evolution of $\Psi(\tau)$ determined from (48) and (49), the expectation value of the spin operator follows from

$$\frac{\hbar}{2}\langle\Psi(\tau)|\boldsymbol{\sigma}|\Psi(\tau)\rangle = (s\cos\theta(\tau), 0, s\sin\theta(\tau)), \tag{50}$$

which reproduces the classical result. Detailed studies of the spin back reaction on the electron dynamics have been conducted in [154,155] generalizing for a laser field the approach developed for constant fields [157]. In particular, spin-induced dynamics have been found in the direction of the laser magnetic field. Such dynamics can, in principle, distort the center-of-mass motion of a free electron wavepacket. However, this is negligible for realistic present-day laser parameters.

There are certainly numerous interesting quantum effects associated with this situation. However, if one compares the motion of the wave-packet's center-of-mass with the classical motion of the corresponding point particle, one is likely to find the classical calculations to be reliable, as long as one is only interested in the center-of-mass motion. In addition, a relativistic classical Monte Carlo simulation is usually sufficient to mimic the evolution of the quantum wavepacket. While those simulations account for and demonstrate beautifully the shearing effects, interesting deviations occur when intrinsic quantum effects such as interferences and spin–orbit coupling are involved. With laser intensities increasing even further in the future, we anticipate that they may not be ignored anymore if a high accuracy is sought.

3.3. Ionized electrons in laser plus extra static fields

The non-relativistic counterparts of Eqs. (24), applicable when lasers of moderate intensity are used, have also been employed often to study the electron dynamics following laser-induced ionization. This constitutes the second step of the so-called "three-step model" which has been quite popular in explaining the main features of the process of high harmonic generation (HHG) in laser–atom physics. In the second step of the model the electron moves under the influence of the laser field alone.

The analysis of free electron motion in laser and external static fields is especially helpful for an intuitive understanding of the above-threshold ionization (ATI) and high harmonic generation (HHG) processes within atoms. Here we restrict ourselves to giving an example of HHG. HHG in the relativistic domain will be discussed in detail in Section 6. The applied external fields aim at controlling and optimizing HHG. A number of schemes have been suggested, including changing the laser field polarization [158,159], employing a two-color field [160], and adding static magnetic [161–163] and electric [164] fields.

An important feature of a typical HHG spectrum, from a practical point of view, is its efficiency, determined by the intensities of the different harmonics on the plateau. According to the three-step model, the electron ionizes, moves almost freely in the laser field and is finally brought back for re-collision with the core to which it was originally bound. Quantum-mechanically, however, a wave packet describing the evolution of the electron in this environment undergoes considerable spreading prior to re-collision, which results in substantial diminution in the emitted harmonic intensity. It has been suggested [161] that the spreading may be reduced using a strong static magnetic field.

While Zuo et al. have used a two-color field and a huge static magnetic field in their calculations, Milošević and Starace [163] have studied the effects of adding a magnetic field of strength achievable now or in the near future [165]. The

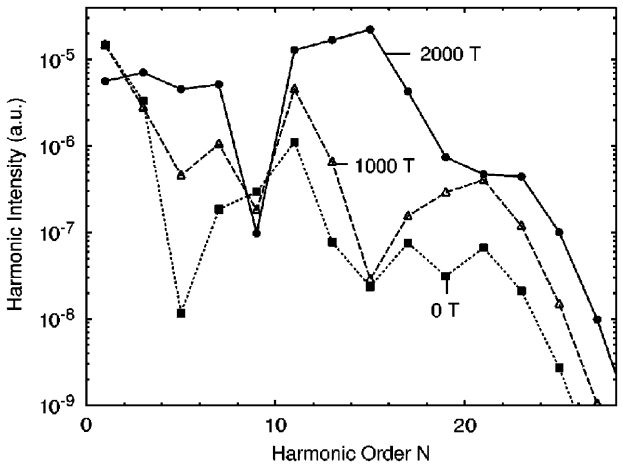

Fig. 7. Harmonic intensities as functions of the harmonic order N for the H^- ion in a CO_2 laser with intensity $I_L = 5 \times 10^{10}$ W/cm^2. The magnetic field induction is $B = 0$ T (squares), 1000 T (triangles), and 2000 T (circles) [163]. Reprinted with permission from [163]; Copyright 1999 by the American Physical Society.

system studied in Ref. [163] is a model H^- ion in a laser field of moderate intensity, and a magnetic field $B = 0$–8000 T, with the direction of B taken along the direction of laser polarization. Harmonic spectra are calculated then from the time-dependent quantum-mechanical matrix element of the dipole moment, within the strong-field approximation.

The harmonic intensity is shown to be clearly enhanced in the presence of a strong static magnetic field in Fig. 7, where only odd harmonics appear due to axial symmetry (even harmonics show up if the magnetic field is oriented perpendicular to the laser propagation direction [162]). Further evidence for enhancement is shown in Fig. 8. Note also the presence in Fig. 8 of pronounced intensity maxima corresponding to the values $B \approx 2000, 4000, 4000, 6000$ and 8000 T. What is remarkable is that a classical interpretation of the quantum-mechanical results displayed in Figs. 7 and 8, based on the three-step model, gives a qualitative explanation of the obtained results. According to that model, motion of the electron along the field polarization direction is governed by the laser field alone. Motion in the plane perpendicular to the B field, however, is controlled entirely by B. The pronounced enhancements in the harmonic intensities appear to result from a correlation between the period of cyclotron motion around the lines of B and the return times (of the electron to the atomic core after ionization).

Besides controlling the efficiency of HHG by suppression of the wave packet spreading, dynamics of an atomic electron in the presence of a moderate-intensity laser field and a strong static magnetic field has been shown recently to result in a peculiar bound-like system, called *the cycloatom* by its principal investigators [166,167]. An electronic charge distribution evolves from an initial atomic ground state into a ring, a Fig. 8 or a propeller-like structure in the presence of a laser field and a static magnetic field oriented parallel to the laser magnetic field component. Investigations so far indicate that the effect is purely relativistic in origin, despite the fact that the laser field intensities involved are orders of magnitude below the relativistic limit. What seems to happen is that the electron is launched from its ground state into cyclotron resonance with the laser field and gets swiftly accelerated by absorbing energy from the laser. The resonance condition in this case is $N\Omega = M\omega_L$, with $N, M = 1, 2, \ldots$, $\Omega = eB/mc$ the electron cyclotron frequency about the lines of B, and ω_L the laser frequency.

Investigation of the structure, and related features, stemmed originally from numerical simulations based on the classical relativistic Liouville equation

$$\frac{\partial \rho}{\partial t} = \{H, \rho\}_{\mathbf{r},\mathbf{p}}, \tag{51}$$

for the phase space density $\rho(\mathbf{r}, \mathbf{p}, t)$, where $H = \sqrt{c^4 + c^2[\mathbf{p} + \mathbf{A}/c]^2} + V(\mathbf{r})$ is the relativistic Hamiltonian, $\{\cdots\}_{\mathbf{r},\mathbf{p}}$ denote Poisson Brackets in the phase space variables, and atomic units are used. Furthermore, $\mathbf{A}(\mathbf{r}, t)$ is the vector potential modeling the laser plus static magnetic fields, and $V(\mathbf{r})$ is a Coulomb potential appropriate for the

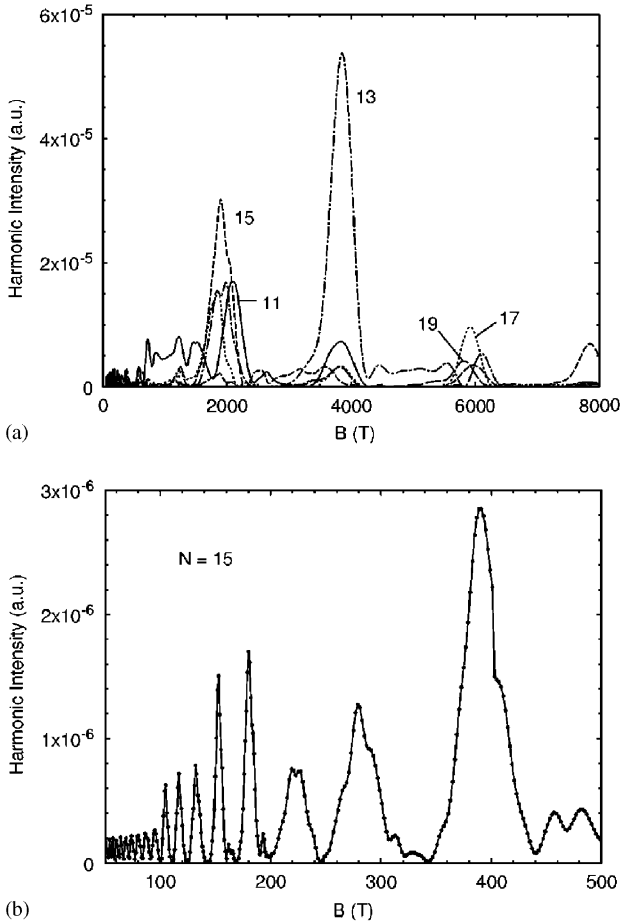

Fig. 8. Harmonic intensities vs. B for fixed harmonic order: $N = 11$ (solid line), 13 (dot-dashed line), 15 (dashed line), 17 (dotted line), and 19 (long-dashed line). The laser field and the H^- ion parameters are the same as in Fig. 7. (a) $0 \leq B \leq 8000$ T, and (b) $50 \leq B \leq 500$ T [163]. Reprinted with permission from [153]; Copyright 1999 by the American Physical Society.

numerical calculations of the system. Dynamics of the electron is then described by the classical probability distribution $P_{\rm cl} \equiv \int \rho \, \mathrm{d}^3 p$.

The classical picture emerging from the Liouville-equation-based numerical simulations has also been supported by quantum-mechanical calculations using solutions to the Dirac equation

$$\mathrm{i}\frac{\partial}{\partial t}\Psi = \left[c\boldsymbol{\alpha}\cdot\left(\mathbf{p}+\frac{\mathbf{A}}{c}\right)+\beta c^2+V\right]\Psi, \tag{52}$$

where $\boldsymbol{\alpha}$ and β are 4×4 Dirac matrices and $\Psi(\mathbf{r}, t)$ is a 4-component Dirac spinor. In place of the classical distribution $P_{\rm cl}$ one now has the quantum-mechanical probability density $P_{qm} \equiv \sum_{i=1}^{4} |\Psi_i|^2$.

Contours in snapshots of the ring-shaped distributions circulating the nucleus (at the origin of coordinates) are shown in Fig. 9 for a suitably-chosen parameter set. Agreement between the classical and quantum-mechanical pictures, as well as differences thereof, are quite obvious. Computer animations have also been produced to show the time-evolution of the *cycloatom* [168].

The classical analysis based on the *dephasing model*, alluded to briefly above, has recently been pushed a few steps forward [169]. Among the results stemming from the new refinements are the interesting S- and figure-8-shaped distributions. Furthermore, investigation has led to the realization of steady-state charge distributions in the form of a rotating triangle and a rotating 4-bladed propeller (see Fig. 10).

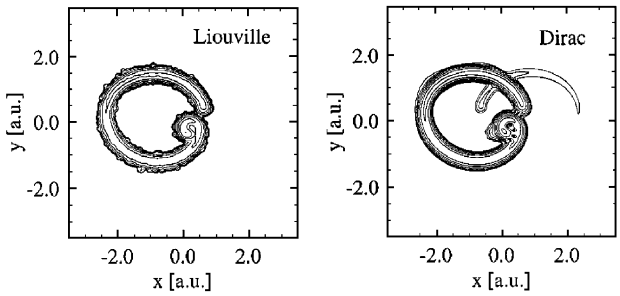

Fig. 9. Comparison of the spatial probability distributions predicted by classical and quantum mechanics. The nine contour lines are chosen at heights $10^{-n/2}$, where $n = -1, 0, 1, \ldots, 7$. The parameters are $E_0 = 800$, $\omega_L = 80$, $\Omega = 96$ and $T = 0.66$; all in a.u. [167]. Reprinted with permission from [167]; Copyright 2001 by the American Physical Society.

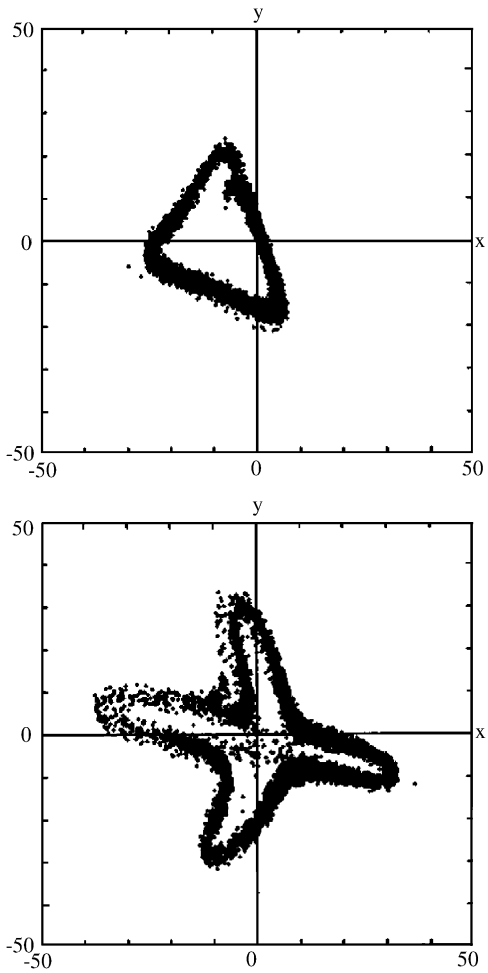

Fig. 10. Steady-state charge distributions. Top: the "triangular" spatial electron charge distribution with parameters: $E_0 = 150$, $\omega_L = 5$, $\Omega = 1.57$, and 10 000 quasiparticles with initial uncertainties $\Delta x = 0.5$, $\Delta v = 1$. Bottom: the "four-bladed propeller" spatial electron charge distribution with parameters: $E_0 = 150$, $\omega_L = 5$, $\Omega = 1.257$, and using the same number of quasiparticles and uncertainties as for the triangular case. All axes and parameter values are given in a.u. [169]. Reprinted with permission from [169]; Copyright 2002 by the American Physical Society.

4. Laser acceleration schemes

Advances in laser technology continue to draw attention to new ideas, and to revive old ones which have been simply not realizable with the less advanced systems. The idea of acceleration to high energy of charged particles using an electromagnetic wave is quite old, but has been lately gathering momentum. Laser systems currently in operation at a number of places around the world present a charged particle with huge electric and magnetic field strengths. Such fields can, in principle, be utilized for the purpose of accelerating an electron, for example, to GeV energies in some of the schemes we intend to review below. The need for such systems may be appreciated by noting that the conventional microwave electron accelerators are currently reaching their energy gradient limits of about 100 MeV/m. To get, say, 10 TeV at this gradient requires a 100 km long linear accelerator of the conventional type. On the other hand, laser accelerators have demonstrated gradients of 100 GeV/m, albeit over distances of the order of a millimeter [170]. To reach TeV energies, electrons must be accelerated in stages of ever increasing energy as has been recently demonstrated in experiments [171,172].

Work on plasma-based laser acceleration has recently made some significant progress, with three independent teams reporting on the production of monoenergetic electron beams of a few hundred MeV energy [19–21]. The three teams have succeeded in improving the beam quality of their accelerator systems, each in their own way. One group [19] utilized the non-linear broken-wave regime discovered by Pukhov and Meyer-ter-Vehn [173]. Another group [20] succeeded in trapping and accelerating the electrons by forming channels in the plasma. The third team [21] managed to achieve the same goal by forming bubbles in the plasma. We confine our attention in this part of the review to vacuum accelerator configurations, where no plasmas or boundaries are required, and comment only on the single-particle calculations. The plasma-based laser accelerators have recently been reviewed by Bingham and his coworkers [174] and by Pukhov [5]. Neither do we discuss here the vacuum accelerator schemes of the inverse-free-electron-laser type [175]. We mainly discuss less elaborate non-resonant schemes of laser acceleration that employ focused laser beams. Such schemes are probably easier to realize with present-day laser systems.

In the theoretical analysis aimed at demonstrating gain of energy by an electron from a laser field, the problem of representing the field plays a crucial role. A plane wave, by definition, has infinite space–time extension, thus the idea of injecting the particle into, and extracting it from, the field remains ill-defined. On the other hand, a plane-wave is highly symmetric and, as such, it presents the electron with a space–time environment in which it gains energy during interaction with one field half-cycle, only to lose it entirely during interaction with the following half-cycle. That an electron will come out with no net gain from interacting with a plane-wave field may be seen clearly from Eq. (25). Other considerations, embodied in what has been referred to for some time now as the Lawson–Woodward theorem [176–178], lead to the same conclusion. Besides all of that, to lead to MeV and GeV energy gain, the laser fields must be focused to micron-size spacial dimensions. The fields of such a laser system may be considered strictly planar only at the focus or too far away from it (see the Gaussian beam description below). Furthermore, focusing results in an enhanced axial electric field component which, in turn, plays the dominant role in accelerating the electron.

This is not to say that the idealistic plane-wave model is totally useless in this regard. Calculations employing the plane-wave description have been quite valuable in conducting intuitively clear analytical discussions which paved the way for the advancement of numerical analysis of the more realistic laboratory situations.

In the most recent investigations, a highly-accurate Gaussian description of a tightly-focused laser beam has been used [179–184]. In Fig. 11, we show the basic features of a Gaussian beam and display the essential parameters used in modeling its electric and magnetic fields. The beam has a stationary focus at O, propagates along $+z$ and is polarized along x. Its fields are derived from a vector potential whose amplitude is A_0 and frequency ω. Using the diffraction angle ε, to be introduced shortly, as a parameter of *smallness*, the electric field components of the beam may be written as [180–182,185]

$$E_x = E\left\{S_0 + \varepsilon^2\left[\xi^2 S_2 - \frac{\rho^4 S_3}{4}\right] + \varepsilon^4\left[\frac{S_2}{8} - \frac{\rho^2 S_3}{4} - \frac{\rho^2(\rho^2 - 16\xi^2)S_4}{16} - \frac{\rho^4(\rho^2 + 2\xi^2)S_5}{8} + \frac{\rho^8 S_6}{32}\right]\right\}, \quad (53)$$

$$E_y = E\xi\upsilon\left\{\varepsilon^2 S_2 + \varepsilon^4\left[\rho^2 S_4 - \frac{\rho^4 S_5}{4}\right]\right\}, \quad (54)$$

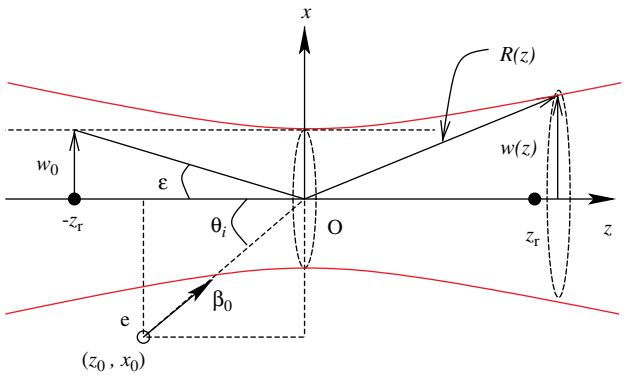

Fig. 11. The tightly-focused Gaussian-beam geometry and single-beam acceleration configuration. See the text for definitions [182]. Reprinted with permission from [182]; Copyright 2003 by the Springer Science and Business Media.

$$E_z = E\xi\left\{\varepsilon C_1 + \varepsilon^3\left[-\frac{C_2}{2} + \rho^2 C_3 - \frac{\rho^4 C_4}{4}\right] + \varepsilon^5\left[-\frac{3C_3}{8} - \frac{3\rho^2 C_4}{8} + \frac{17\rho^4 C_5}{16} - \frac{3\rho^6 C_6}{8} + \frac{\rho^8 C_7}{32}\right]\right\}. \tag{55}$$

Similarly, the magnetic field components are given by

$$B_x = 0, \tag{56}$$

$$B_y = E\left\{S_0 + \varepsilon^2\left[\frac{\rho^2 S_2}{2} - \frac{\rho^4 S_3}{4}\right] + \varepsilon^4\left[-\frac{S_2}{8} + \frac{\rho^2 S_3}{4} + \frac{5\rho^4 S_4}{16} - \frac{\rho^6 S_5}{4} + \frac{\rho^8 S_6}{32}\right]\right\}, \tag{57}$$

$$B_z = E\upsilon\left\{\varepsilon C_1 + \varepsilon^3\left[\frac{C_2}{2} + \frac{\rho^2 C_3}{2} - \frac{\rho^4 C_4}{4}\right] + \varepsilon^5\left[\frac{3C_3}{8} + \frac{3\rho^2 C_4}{8} + \frac{3\rho^4 C_5}{16} - \frac{\rho^6 C_6}{4} + \frac{\rho^8 C_7}{32}\right]\right\}. \tag{58}$$

A cross section through the beam focus is circular and has a radius w_0; a cross section through an arbitrary point z on axis is also circular with a radius given by $w(z) = w_0\sqrt{1 + (z/z_r)^2}$. With $k = 2\pi/\lambda$, the Rayleigh length is $z_r = kw_0^2/2$ and the diffraction angle is $\varepsilon = w_0/z_r$. In Eqs. (53)–(58), $\xi = x/w_0$, $\upsilon = y/w_0$, and

$$E = E_0\frac{w_0}{w}\exp\left[-\frac{r^2}{w^2}\right]; \quad E_0 = kA_0, \tag{59}$$

$$S_n = \left(\frac{w_0}{w}\right)^n \sin(\psi + n\psi_G); \quad n = 0, 1, 2, \ldots, \tag{60}$$

$$C_n = \left(\frac{w_0}{w}\right)^n \cos(\psi + n\psi_G). \tag{61}$$

Furthermore, $k = \omega/c$, $r^2 = x^2 + y^2$, and $\rho = r/w_0$. Also, $\psi = \psi_0 + \psi_P - \psi_R + \psi_G$, where ψ_0 is a constant phase, $\psi_P = \eta = \omega t - kz$ is the plane wave phase, $\psi_G = \tan^{-1}(z/z_r)$ is the Guoy phase associated with the fact that a Gaussian beam undergoes a total phase change of π as z changes from $-\infty$ to $+\infty$, $\psi_R = kr^2/(2R)$ is the phase associated with the curvature of the wave fronts, and $R(z) = z + z_r^2/z$ is the radius of curvature of a wave-front intersecting the beam axis at the coordinate z. The fields given above satisfy Maxwell's equations $\nabla\cdot\mathbf{E} = 0 = \nabla\cdot\mathbf{B}$, plus terms of order ε^6.

For the sake of completeness we also give here the laser power output (in terawatt) in terms of the expansion parameter ε

$$P[TW] = \frac{\pi w_0^2}{2} I_0\left[1 + \frac{\varepsilon^2}{4} + \frac{\varepsilon^4}{8}\right], \tag{62}$$

where $I_0 = cE_0^2/8\pi$ is the peak flux density at focus.

4.1. Acceleration by a single laser beam

Calculations using the above fields, and an injection geometry like the one shown in Fig. 11 above, have recently shown that an MeV energy electron may gain more than one GeV in the presence of a petawatt (PW) beam focused down to a few micron waist radius [179–182]. In a typical calculation, an electron is injected with some initial energy $\gamma_0 mc^2$ and the equations of motion are integrated over some period of time long in comparison to one laser period. The energy gain is then given by

$$\text{Gain} = mc^2(\gamma - \gamma_0), \tag{63}$$

where γ is the Lorentz factor at the end of integration. A scheme like this may obviously be used as a booster for particles already accelerated to MeV energies before they are submitted to the high-intensity focus of a laser beam. The initial injection energy and, hence, initial forward momentum, is required to allow the electron to penetrate the laser focus and reach regions of maximum intensity. It seems to acquire momentum from the field in the form of a small number of violent impulses, to get captured by the beam fields, and to travel slightly off of the beam axis. Otherwise, it would be reflected with little energy gain (or even loss).

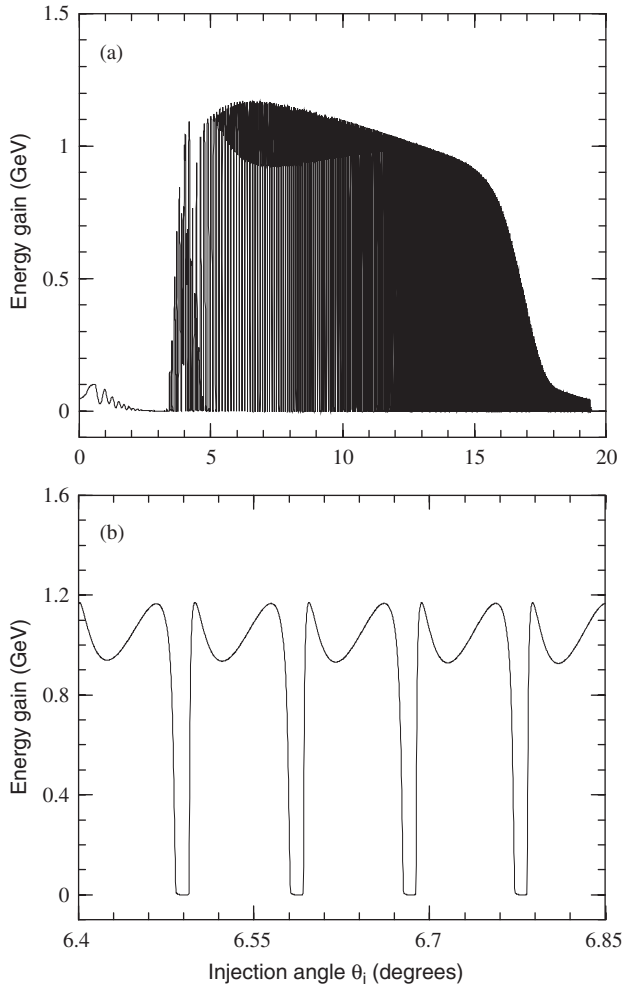

Fig. 12. Energy gain vs. the injection angle θ_i corresponding to a scaled injection energy $\gamma_0 = 10$, $z_0 = -5$ mm, and an initial phase constant $\psi_0 = 3°$. The remaining parameters are: power $P = 10$ PW, wavelength $\lambda = 1\,\mu$m, and waist radius $w_0 = 10\,\mu$m. Injection is into the laser focus and the interaction time, starting from injection at $t = 0$, is equivalent to $\Delta\eta = 10650\pi$, with $\eta = \omega(t - z/c)$. In (b) we only zoom on a small portion of (a) [182]. Reprinted with permission from [182]; Copyright 2003 by the Springer Science and Business Media.

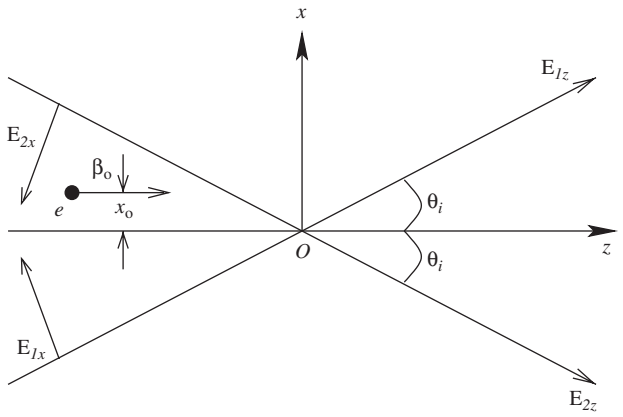

Fig. 13. A schematic diagram of electron injection into the region of overlap of two identical laser beams. Note that the coordinate axes of the individual beams are not marked explicitly. The understanding here, and elsewhere, is that E_{1x} points in the direction of $+x_1$, E_{2z} points in the direction of $+z_2$, and so on [182]. Reprinted with permission from [182]; Copyright 2003 by the Springer Science and Business Media.

It has recently been shown that, in the configuration discussed here, regions develop around the beam focus, due to the mechanism of focusing, over which the velocity of the electron is sub-luminous [186,187]. This lends support to the interpretation that the underlying mechanism of acceleration is most dominantly one of capture and violent acceleration [188,189]. The capture is mainly due to the transverse electric and longitudinal magnetic field components and the acceleration relies on the axial (longitudinal) electric field component.

Numerical calculations with low-order Gaussian beams have also been performed over the past several years [190], all supporting the conclusion that GeV energy gain may be achieved using a single beam arrangement. Some have also dealt with the question of interpretation of the mechanism of acceleration. It has, however, been demonstrated that focusing a beam to a waist radius of the order of the laser wavelength calls necessarily for representation of the fields by a Gaussian beam of higher order [179].

We conclude this subsection by noting that an order-of-magnitude estimate of the maximum energy gain may be arrived at from Eq. (25). Assuming that the vector potential is a sinusoidal function of the time, the following time-averaged value for the gain follows:

$$\langle \text{Gain} \rangle = \frac{q^2}{4} mc^2 \frac{\sqrt{1-\beta_0^2}}{1-\beta_0 \cos\theta_i}. \tag{64}$$

This obviously attains a maximum value of

$$\langle \text{Gain} \rangle_{\max} = \frac{q^2}{4} mc^2 \sqrt{\frac{1+\beta_0}{1-\beta_0}}, \tag{65}$$

corresponding to parallel injection, $\theta_i = 0$. A particle initially at rest, on the other hand, would gain a maximum energy equal to $mc^2 q^2/4$ during interaction with the radiation field. Employing a laser system of present-day maximum intensity, corresponding to $q^2 = 10^4$, this roughly amounts to a maximum gain of 1.3 GeV. The results of Fig. 12 are obviously consistent with this conclusion.

4.2. Acceleration by crossed and two-color laser beams

The crossed-beam accelerator scheme, shown schematically in Fig. 13, was suggested about ten years ago [191,192], in which the electron may be injected through the intersection point of two laser beams crossing at an angle. Experimental proposals for multi-stage crossed-beam, vacuum-based and dielectric-based accelerator structures, have also been put forth [193,194].

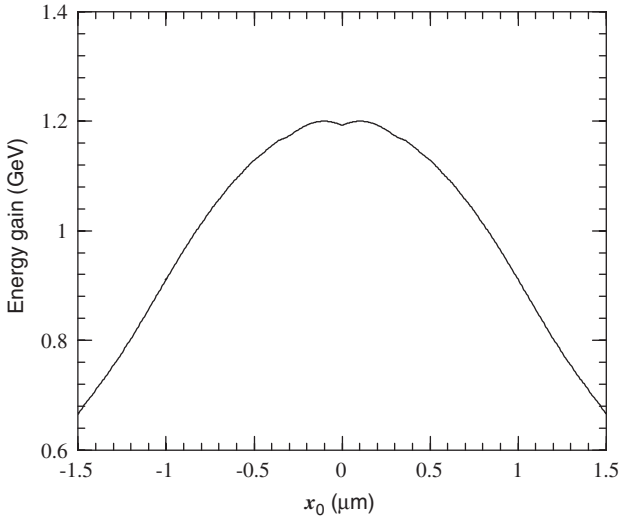

Fig. 14. Electron energy gain vs. the off-axis injection distance x_0, as a result of interaction with two identical beams. The injection energy is $\gamma_0 = 10$, the crossing half-angle is $\theta_i = 6.5°$, $z_0 = -5\,\mu m$, and the initial phase constant $\psi_0 = 3°$. The remaining parameters and initial conditions are the same as in Fig. 12. The integration has been carried out over a time equivalent to 10^4 laser periods [182]. Reprinted with permission from [182]; Copyright 2003 by the Springer Science and Business Media.

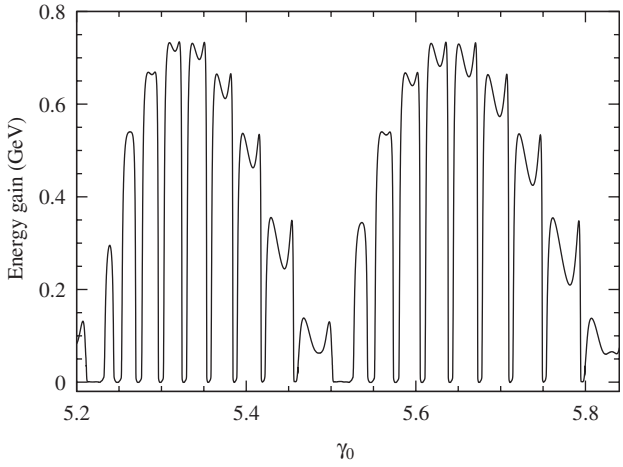

Fig. 15. Electron energy gain in a vacuum beat wave laser accelerator as a function of the initial scaled injection energy. The two beams copropagate along $+z$, 127° out of phase. The other parameters are: $\lambda_1 = 1\,\mu m$, $\lambda_2 = \lambda_1/1.1$, laser power = 1 PW, $w_{01} = w_{02} = 6\,\mu m$, injection is sideways at an angle $\theta_i = 10°$ with the propagation direction and from a point in the polarization plane with a $z_0 = -5$ mm coordinate, and integration is taken over a time equal to 10^5 laser periods [183]. Reprinted with permission from [183]; Copyright 2005 by the Elsevier.

Lowest-order Gaussian beams [191,192] were employed in the initial proposals and a preliminary plane-wave investigation was carried out later [195]. Recently, however, tightly-focused (high-order) Gaussian beams of the type discussed above have been used in detailed numerical calculations [181,182]. The general configuration of injection parallel to the bisector of the crossing angle between the two beams has been discussed (see Figs. 13 and 14).

Another scheme, the vacuum beat wave laser accelerator (VBWLA), has also been suggested [192,196–198] for accelerating electrons in vacuum using a double-beam arrangement. As is the case in all wave phenomena, when two waves differing slightly in frequency are co-propagated, they constitute a beat structure. The beat-wave not only breaks the symmetry of the individual waves but it also offers the electron an overall field amplitude that can be twice as large as that of one of the beams alone, assuming they are of the same amplitude. This leads to an intensity four times as

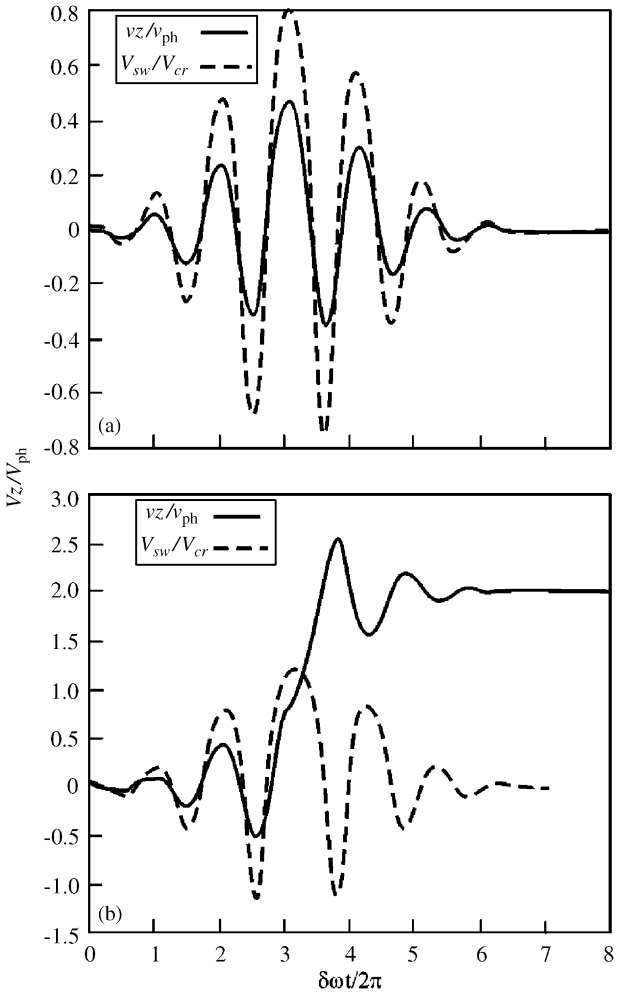

Fig. 16. The solid curves display temporal evolution of the atom scaled velocity. The dashed curves show variation of the scaled ponderomotive potential sensed by the atom along its trajectory: (a) the laser intensity is below the critical value: $V_0 = 0.8\,V_{cr}$, and (b) above the critical value: $V_0 = 1.3\,V_{cr}$. The initial velocity of the atom is zero. $\delta\omega = \omega_1 - \omega_2$, ω_1 and ω_2 are the frequencies of the counter-propagating laser waves, $(\omega_1 - \omega_2)\tau = 10$, with τ the pulse duration [202]. Reprinted with permission from [202]; Copyright 2003 by the Springer Science and Business Media.

large as the intensity of one beam. Thus far, only plane-wave fields [196] and low-order Gaussian and Bessel beams [192,197,198] have been employed in the theoretical calculations. Numerical work with high-order Gaussian beams has recently been carried out [183,184] and some of its results are shown in Fig. 15. Plasma-based beat wave acceleration has received a lot more attention, theoretical as well as experimental [174].

Finally, we mention a nonlinear mechanism for laser acceleration based on electron reflection from the moving ponderomotive barrier formed by two counter-propagating laser waves of different frequencies, known since the early investigations of the nonlinear dynamics associated with the free electron laser [199]. This effect has been also proposed for the coherent X-ray generation due to the quantum reflection of an electron beam from a laser–field phase lattice [200] and for the monochromatization of charged-particle beams by a laser pulse [201]. It has recently been shown that this mechanism may be relevant for atom acceleration as well [202]. The process is strongly intensity-dependent in that the reflection from the barrier occurs only if the laser intensity exceeds some critical value. The latter depends on the initial atom velocity, see Fig. 16. The process is rooted in the stimulated multi-photon Compton scattering of laser radiation by the atomic bound electrons and in the coupling between the atomic translational and electronic degrees of freedom.

4.3. Acceleration by laser plus static electric and magnetic fields

Some ideas have been also suggested to achieve acceleration by breaking the plane-wave symmetry, and hence violating the Lawson–Woodward theorem, via the addition of extra static electric and magnetic fields. One proposal suggested adding a static electric field perpendicular to the laser propagation direction [204] more than a decade ago. The case of an electric field oriented anti-parallel to the propagation direction of the *plane-wave* laser beam has been

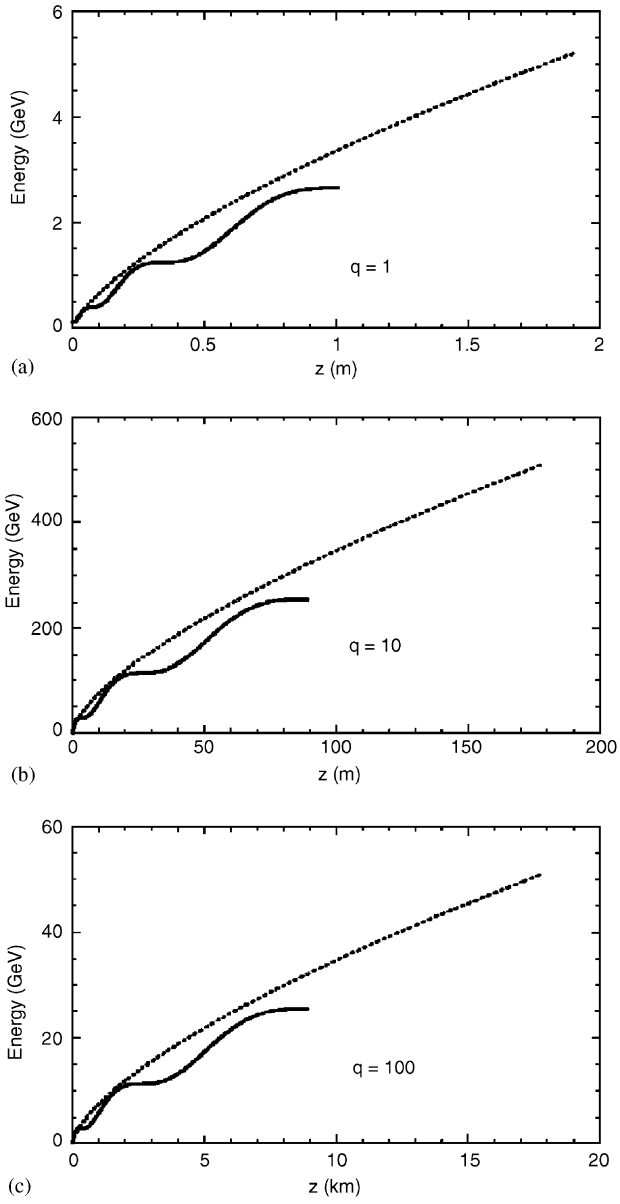

Fig. 17. Electron energy in a plane-wave laser field and a uniform magnetic field in the autoresonance laser acceleration regime vs. the forward distance over which interaction takes place. The continuous lines are linear polarization cases, and the dotted lines represent circular polarization. The parameters are wavelength $\lambda = 800\,\text{nm}$, number of field cycles 1.5, and $B_S = 30\,\text{T}$: (a) intensity $I \sim 10^{18}\,\text{W/cm}^2$ or $q = 1$; (b) $I = 10^{20}\,\text{W/cm}^2$ or $q = 10$; and (c) $I \sim 10^{22}\,\text{W/cm}^2$ or $q = 100$. Effectively, these are plots of $\mathscr{E}(\eta)$ vs. $z(\eta)$ parameterized by η. In other words, data for these plots have been produced by evaluating the functions $\mathscr{E}(\eta)$ and $z(\eta)$ over values ranging between 0 and 3π [150]. Reprinted with permission from [150]; Copyright 2000 by the American Physical Society.

discussed [205,206]. Unfortunately, the plane-wave discussions do not point conclusively to the plausibility of such a scheme, while a Gaussian-beam-based analysis remains to be done.

On the other hand, the auto-resonance laser accelerator scheme [207] has received more attention, mostly within a plane-wave plasma-based context [208–211]. In this scheme, a static magnetic field, B_s, is oriented along the laser propagation direction [149,212–214]. For the scheme to work, the electron injection energy and the angle, θ_i, at which it should be injected relative to the beam axis must conspire to make the electron cyclotron frequency the same as the Doppler-shifted laser frequency. This is the resonance condition

$$\frac{eB_s}{mc} = \omega\gamma_0(1 - \beta_0 \cos\theta_i), \tag{66}$$

from which the scheme derives its name. When this condition is met, the electron *rides* with the wave and continues to absorb energy from it. In other schemes, the electron may slip quickly behind the wave, a feature that places limits on the maximum energy gain achievable.

We show, in Fig. 17, the gain in energy as a function of the forward electron displacement during auto-resonance interaction with a few laser cycles. It is obvious that the huge gain in energy has a price in that the distance over which the gain occurs turns out to be large.

We stress here that the plane-wave-based discussions of the acceleration schemes using added static electric and magnetic fields have not led to the conclusion that such schemes might be plausible in the near future. However, the analytic work done in this area has been good in building an intuitive picture in each case. The equations may be quite useful in discussions involving configurations of the sort encountered in contexts different from acceleration per se, like atomic laser-induced ionization and control of the associated HHG. The equations have certainly some role to play in guiding the numerical analysis that must ultimately be resorted to in the study of laser acceleration employing tightly-focused beams.

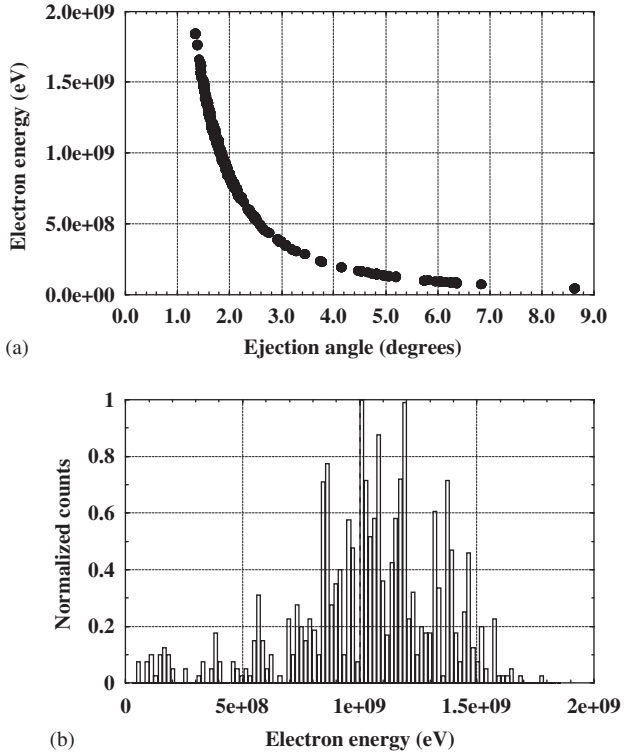

Fig. 18. Three-dimensional Monte Carlo simulation results for V^{22+} located at the center of the Gaussian laser beam of wavelength 1054 nm and a peak intensity of 8×10^{21} W/cm^2. The beam waist is assumed to be 10 μm, and its time envelope comprises a 5-cycle turn-on and turn-off, as well as a 5-cycle flat top with constant amplitude: (a) electron energies attained vs. the ejection angles with respect to the z axis; and (b) electron energy distribution normalized to the peak of the distribution [50]. Reprinted with permission from [50]; Copyright 2002 by the American Physical Society.

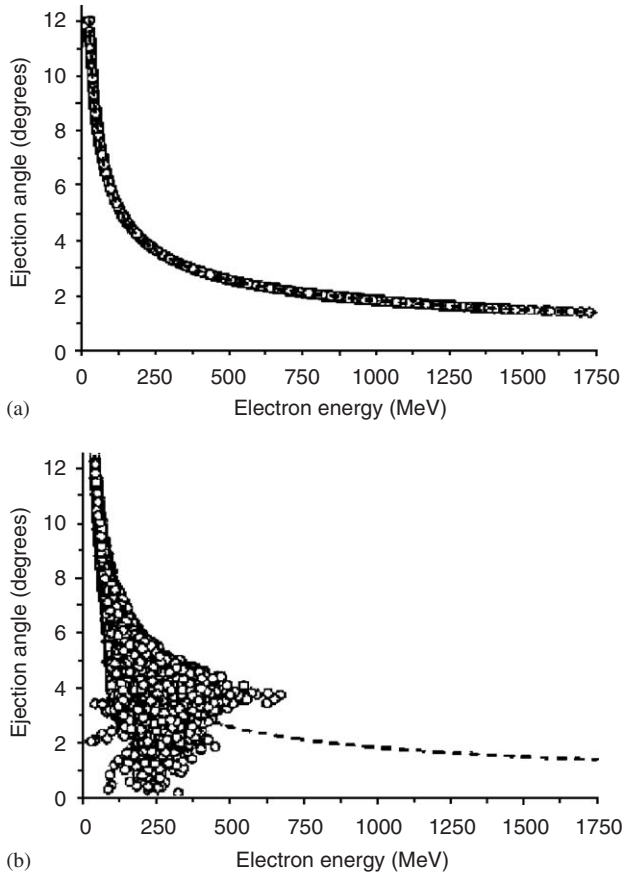

Fig. 19. Simulation results showing electron ejection angle as a function of electron energy for Ar^{17+} ionized with an 800 nm, 30 fs laser pulse at an intensity of 5×10^{21} W/cm^2. The dashed line shows the prediction of Eq. (1): (a) results when longitudinal fields are excluded from the calculation; and (b) results when longitudinal fields are included [51]. Reprinted with permission from [51]; Copyright 2003 by the American Physical Society.

Another shortcoming of some of the calculations cited above is the fact that they present single-particle results. A realistic situation involves an electron bunch of some sort. Study of the dynamics of such a bunch requires more sophisticated simulations [215–217]. More recently, a relativistic quantum theory of cyclotron resonance in a medium has been developed [218].

4.4. Acceleration of electrons from ions

Recent studies, based on three-dimensional Monte Carlo simulations, by Hu and Starace [50] have also shown that tunnel-ionized electrons, produced from interaction of highly-charged ions with ultraintense laser fields, may be accelerated to GeV energies. Because of strong binding, the electron survives the turn-on phase of the laser field and gets ionized when the laser attains its maximum amplitude. It may then be accelerated to relativistic velocities by *riding* on the laser wave. In those studies, the laser fields (taken as purely transverse to the propagation direction) are modeled by those of a Gaussian beam with a trapezoidal time-envelope. On the other hand, the ionic-core binding potential of the highly-charged hydrogen-like V^{22+} ion is taken as $V(r) = -23/r$. The resulting relativistic electron motion is then studied by integrating the classical Newton–Lorentz equations, in the laser plus Coulomb fields, numerically. In the simulations, an initial relativistic microcanonical ensemble corresponding to the quantum mechanical ground state, with ionization potential $I_p \simeq 7.2$ keV, has been employed. The results shown in Fig. 18 are for a laser wavelength of 1054 nm, an intensity of 8×10^{21} W/cm^2, and a beam waist of 10 μm.

Acceleration of tunnel-ionized electrons from highly-charged ions has also been the subject of a more recent, but similar, study by Maltsev and Ditmire [51]. In this study a more realistic Gaussian beam, one that has longitudinal as well as transverse field components, has been employed. Fig. 19 shows qualitative agreement with the work of Hu and Starace (Fig. 18) under the transverse-fields-only conditions. However, it displays significant deviations when the longitudinal field components are included.

Note that the fields employed by Maltsev and Ditmire [51] are the order ϵ terms of the Gaussian beam fields given in Eqs. (53)–(58). The full fields have recently been utilized [203] for the investigation of interesting correlations in the dynamics of a single-electron subjected to ultraintense laser fields. We close this section by drawing attention to the recent promising work of Plettner and coworkers [219–222] aimed at experimentally realizing electron acceleration by laser fields in a vacuum.

5. Relativistic laser–atom, and –ion interactions

When the laser intensity is high up to the order of $\sim 10^{18}\,\mathrm{W/cm^2}$, interaction with matter enters the relativistic regime, in which the electron, driven by the intense laser, moves with a velocity comparable to that of light, c. Technically, one needs to solve the Dirac equation for the relativistic dynamics. In contrast to the non-relativistic regime, important relativistic effects begin to appear and must be dealt with. We will give in this section a general review of the explorations of relativistic laser–atom and laser–ion interactions.

5.1. Ionization and stabilization

Ionization of atoms exposed to an oscillating electromagnetic field has been the subject of intense study ever since the invention of the laser. Non-perturbative treatment of laser-induced ionization can be traced back to the 1960s and 1970s [56–58,61–64]. The first experiment on intense laser ionization of atoms was done in 1979 [76], which showed that a ground state electron can absorb more than the number of photons that is necessary to ionize the atom. This phenomenon is the so-called above threshold ionization (ATI) (see the review in [223]). Typical ATI spectra consist of photoelectron peaks which are separated by integer numbers of the photon energy. For a moderately intense ($\sim 10^{13}$–$10^{16}\,\mathrm{W/cm^2}$), linearly polarized driving field, the ionized electrons are ejected mainly along the laser polarization direction. In a non-relativistic ATI spectrum, the photoelectron amplitude normally drops continuously down to a region of electron energy $\sim 2U_\mathrm{p}$ ($U_\mathrm{p} = e^2E_0^2/4m\omega^2$ is the ponderomotive potential, defined as the average electron oscillation energy in a plane-wave electric field of amplitude E_0 and frequency ω), the ATI amplitude then tends to be almost constant for a range of energies up to $\sim 10U_\mathrm{p}$ (the so-called plateau region). That is finally followed by a sharp cutoff in which the ATI peaks merge with the background. A typical measured ATI spectrum [224] is shown in Fig. 20, while Fig. 21 shows a calculated spectrum [225].

The whole feature of ATI is essentially complementary to the other intense-field process of high-order harmonic generation (HHG). The *direct* tunnelling/multi-photon ionization process (i.e., direct escaping from the atomic core) explains the first part of the ATI spectrum up to $2U_\mathrm{p}$; while the plateau has been attributed to the re-scattering of the returning electron on the atomic core. The re-scattering process results in two complementary consequences [79]: (a) the formation of an HHG plateau, if the returning electron recombines with its parent ion; and (b) the appearance of an ATI plateau, if the back-driven electron re-scatters off the atomic core (the re-scattering induces also non-sequential double ionization, see Section 5.4.1). The ATI plateau has first been observed experimentally by Paulus et al. [77]. These interpretations have been generally accepted. Moreover, experimental observation of the angular distribution of ATI spectra [227] has supported explanation of the re-scattering mechanism. In other words, the photoelectrons are distinctly found to be scattered away from the laser polarization axis in the ATI plateau region [227]. The energy gain through the re-scattering process can be significantly high (up to $\sim 10U_\mathrm{p}$), which may be viewed as a mechanism of hot electron generation in the intense laser ionization of atoms.

Non-relativistic above-threshold-ionization of atoms and molecules exposed to moderately intense laser fields has been extensively investigated over the past two decades. In [68] an extension of SFA for non-dipole non-relativistic laser–atom interactions has been developed and the region of applicability of the dipole approximation has been established. However, the relativistic ionization of atoms subjected to ultra-intense ($\geqslant 10^{18}\,\mathrm{W/cm^2}$) laser fields has only recently picked up momentum in strong-field physics, both theoretically and experimentally [92–100,228]. The

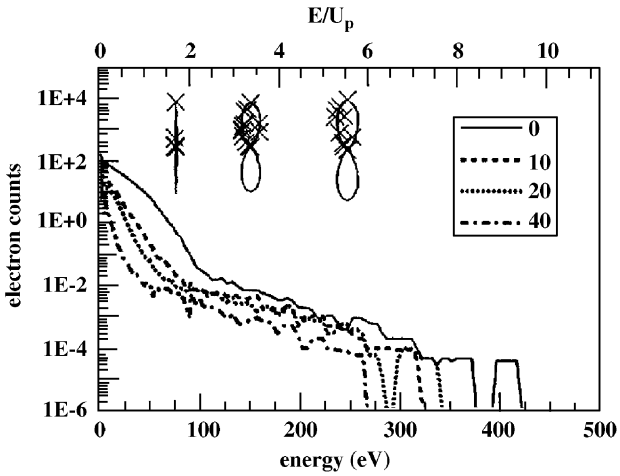

Fig. 20. Measured helium angular-resolved photoelectron spectrum for four different emission angles at the saturation intensity. The polar plots show the measured angular distributions (crosses) at the indicated energies and the solid lines are only to guide the reader [224]. Reprinted with permission from [224]; Copyright 1996 by the American Physical Society.

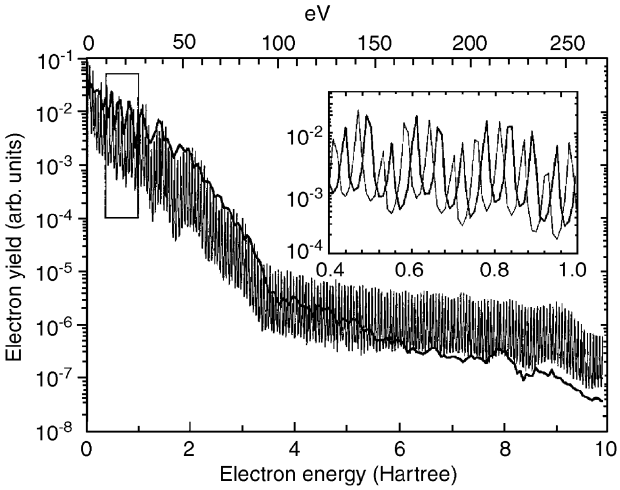

Fig. 21. Calculated ATI spectrum of helium for a 0.1291 a.u. field (585 TW/cm^2) at 800 nm, along the polarization vector. At this intensity there is a strong plateau between 4 and 8 hartree. The fat curve shows the spectrum at a slightly different field (0.1274 a.u.), which is nearly identical at low energy, but has a much weaker plateau. The inset is a blowup of the indicated region, revealing how the ATI peaks shift ponderomotively through a nearly constant envelope. For clarity the main plot shows only the envelope for the fat spectrum [225]. Reprinted with permission from [225]; Copyright 1999 by the American Physical Society.

first relativistic phenomenon predicted for ATI concerns the angular distribution of the ejected electrons. With the Lorentz force due to the laser magnetic field component imparting momentum to the ionized electrons along the laser propagation direction, the electron spectra get peaked around the laser propagation axis [92], in contrast to the non-relativistic case in which most electrons are ejected along the laser polarization direction. This is elucidated in Fig. 22. Such experiments have been done by Meyerhofer and his coworkers [229]. Furthermore, the magnetically-induced relativistic drift has been observed [230] by measuring the electron ejection angle with the laser propagation direction, during ionization of Ne up to 8+ and Kr up to 11+, that appeared to be smaller than 90°.

When ultra-intense laser fields are used, the neutral atoms are normally stripped of many electrons during the rising stage of a short laser pulse. The interactions result in the production of highly charged ions (HCIs) and energetic

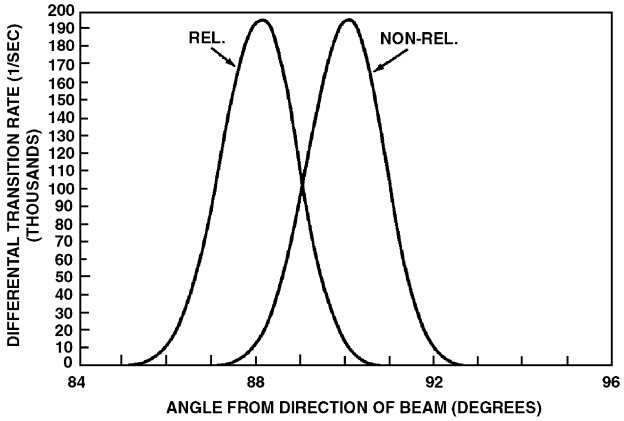

Fig. 22. Angular distribution of photoelectrons as measured from the direction of propagation of the circularly polarized field. The circularly polarized laser has a wavelength of 10.6 μm and an intensity of 1.1×10^{14} W/cm^2. The non-relativistic distribution is symmetric about 90°, and the relativistic distribution is displaced forward [92]. Reprinted with permission from [92]; Copyright 1990 by the American Physical Society.

electrons. Electron energies of hundreds of MeVs or even a few GeVs can be reached [50,51]. Usually, when an ultra-intense laser pulse blasts a solid target or a gas jet, a plasma consisting of HCIs and electrons is formed. Once a plasma is produced, the subsequent dynamics is governed by the laser–plasma interactions. Laser–plasma physics is well reviewed as one of the active branches of modern physics [231]. Since neutral targets may be quickly blasted, atomic physicists are interested in bringing the tightly-bound systems to interact with relativistic laser fields [98]. Highly charged ions are such systems in which the strongly-bound electrons may sustain the peak intensity of a super-strong laser pulse. HCIs can be generated either via many atomic collision processes [49] or directly by the super-strong laser pulse itself [233]. With the currently used techniques of producing HCIs one can generate any charge state of any atomic species [234]. Measuring a harmonic (radiation) spectrum requires a high-enough target density (10^{17}–10^{18} cm^{-3}). However, since the density of currently available HCIs is not high enough to allow for measurement of HHG radiation spectra from intense laser-driven ions, experiments with ions are suitable for the study of the relativistic tunneling ionization spectra [98,99].

The relativistic ionization of a highly charged ion subjected to an intense laser pulse is very interesting. Typically, one may divide the electron dynamics into inner-atomic and outer-barrier motions. Once an ion is irradiated by a super-strong laser pulse, the electronic wavepacket, tightly-bound by the ionic core, reacts to the external driving laser field. If the laser field is not strong enough to suppress the barrier under the energy-level of the ground state, most parts of the electronic wavepacket move dominantly inside the inner-atomic potential, in which case the strong Coulomb attraction makes the electron wavepacket move at a velocity fairly less than the speed of light. Therefore, relativistic effects have no room to be fully developed inside the inner-atomic potential. However, a small part of the electronic wavepacket can tunnel through the potential barrier suppressed by the intense laser field. The tunneled-out part of the electronic wavepacket looks like a quasi-free particle, thereby, driven to an extremely high velocity and requiring a relativistic treatment.

The inner-atomic dynamics of a strongly-bound electronic wavepacket has been investigated in the weakly relativistic regime [235,462] for the purpose of testing the effect of the laser magnetic field component on the wavepacket's motion, which can be viewed as a first-order relativistic effect. Beyond the usual dipole approximation, one can solve the following time-dependent Schrödinger equation (in atomic units)

$$\mathrm{i}\,\frac{\partial \Psi(\mathbf{r},t)}{\partial t} = \left[\frac{1}{2}\left(\mathbf{p} + \frac{\mathbf{A}(z,t)}{c}\right)^2 + V(\mathbf{r})\right]\Psi(\mathbf{r},t), \tag{67}$$

where the vector potential $\mathbf{A}(z,t)$ depends not only on the time but also on the coordinate z of the laser propagation direction which gives rise to a magnetic field via $\mathbf{B} = \nabla \times \mathbf{A}$. Recall that, using the dipole approximation, $\mathbf{A} = \mathbf{A}(t)$, and one may not determine what the laser magnetic field might do to the electronic wavepacket's motion. Fig. 23

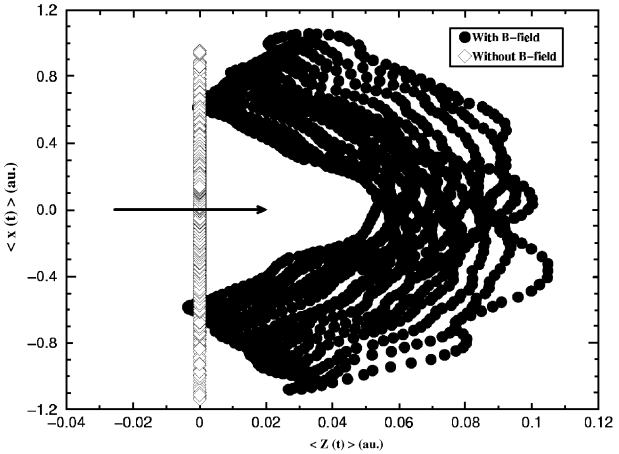

Fig. 23. The center-of-mass evolution of the electronic wave packet for the cases with B-field ("full circles") and without B-field ("open diamonds"). The laser parameters involve a wavelength of 248 nm, an intensity of 10^{17} W/cm^2, a three-cycle linear turn-on and a ten-cycle constant amplitude duration. A hole around the ionic core for Be^{3+} ($Z = 4$, $s = 1$, $k = 10.7$) as indicated by the arrow is clearly observable in the time-evolution of the center-of-mass of the electronic wave packet, when the B-field is considered [235]. Reprinted with permission from [235]; Copyright 1999 by the EDP Sciences.

elucidates the effect of the laser magnetic field component on the center-of-mass (c.m.) motion ($\langle x(t)\rangle$, $\langle z(t)\rangle$) of the wavepacket [235]. In Fig. 23, the c.m. position of the electronic wavepacket has been plotted in the plane spanned by the laser polarization x-axis and the laser propagation direction (z-axis), for continuous time steps during interaction with the laser pulse. The open diamonds show the CoM motion when the dipole approximation is employed. Apparently, the wavepacket just follows the laser electric field, along the polarization direction. However, when the magnetic field has been taken into account, we see that the electronic wavepacket follows a two-dimensional trajectory, indicated by the solid circles in Fig. 23, in the xz plane. When the wavepacket passes quickly by the nucleus, the Lorentz force $\mathbf{v} \times \mathbf{B}$ pointing along the laser propagation $+z$ axis, pushes it along that direction. Consequently, a *hole* is formed in the c.m. motion of the wavepacket.

Outside the atomic potential core, the tunneled-out electronic wavepacket can move at a relativistic velocity. The forward momentum imparted to the wavepacket by the Lorentz force (due to the laser magnetic field component) normally reduces the probability of the ionized electron re-colliding with the atomic core [236]. This causes the high harmonic generation to be less efficient [103]. However, the Lorentz force favors acceleration of the ionized electrons along the laser propagation direction [50,51].

Stabilization is one of a number of novel theoretical predictions in super-strong laser–atom interactions. In simple terms, stabilization refers to the tendency of the atomic ionization rate to decrease with increasing laser field intensity and/or frequency [237]. An example of stabilization is displayed in Fig. 24. Two types of stabilization effects have been found, often referred to as *field stabilization* and *interference stabilization*.

Pioneering work on intense laser–atom stabilization was done by Gavrila and co-workers [238], Su and Eberly [239], Fedorov and his collaborators [240], Reiss [241] and others [242]. Employing the Floquet theory, Gavrila et al. showed that when the applied laser frequency becomes much larger than the atomic binding energy, the electron sees virtually *two centers* for the atomic potential (the so-called phenomenon of *dichotomy*), and it tends to stabilize rather than be ionized [78,238]. Meanwhile, Su and Eberly [239] numerically solved the one-dimensional time-dependent Schrödinger equation for interactions of a laser pulse with atoms, and found that the ionization probability stays constant, or even decreases, when the applied laser intensity is increased. Calculations of Reiss based on SFA confirm the existence of the stabilization regime [241].

Interference stabilization in intense laser interactions with Rydberg atoms was extensively investigated by Fedorov and co-workers [240], Burnett and Knight and their collaborators [243], and Stroud et al. [244]. This kind of stabilization was explained by Raman interference, in which the Raman process occurs between the Rydberg state and the continuum. Currently, experimental demonstration of stabilization is carried out only for Rydberg atoms [245].

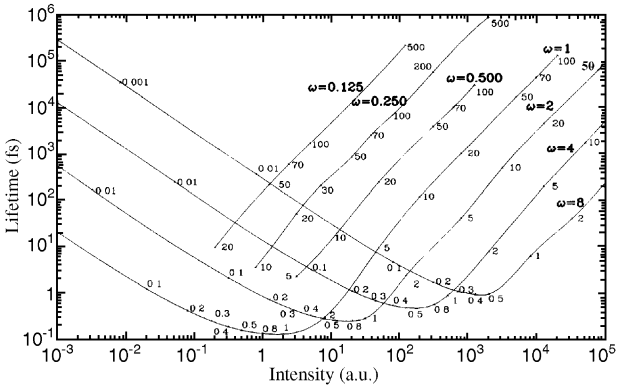

Fig. 24. Lifetime (in femtoseconds) of atomic hydrogen as a function of intensity (in a.u., $I_0 = 3.51 \times 10^{16}$ W/cm^2), for various ω (in a.u.). The numbers adjacent to the points give the corresponding value of a_0 (in a.u.) [237]. Reprinted with permission from [237]; Copyright 2002 by the IOP Publishing Limited.

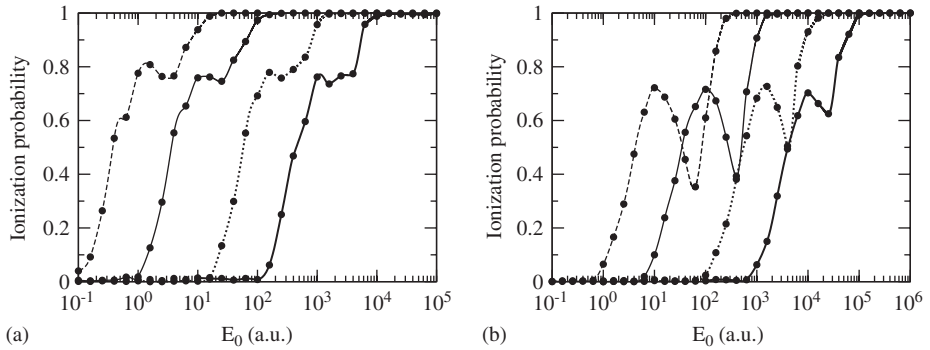

Fig. 25. Ionization probability as a function of electric-field strength for Coulombic hydrogen (dashed line), helium (+) (thin solid line), boron (4+) (dotted line), and neon (9+) (thick solid line). The laser pulses used were $\sin^2$ (3-4-3) type. In both graphs, the frequency has been scaled proportional to Z^2 in an attempt to reproduce the conditions necessary for stabilization to occur. In graph (a) $\omega = Z^2$ and in (b) $\omega = 5Z^2$ [248]. Reprinted with permission from [248]; Copyright 2002 by the American Physical Society.

A proposal to test ground-state hydrogen atoms has recently been advanced [246] employing intense high-frequency free-electron-laser light.

After the prediction of stabilization was made in the non-relativistic regime of intense laser–atom interactions, questions about possible relativistic corrections were, understandably, soon to be raised. Studies aimed at answering those questions have been made and the results showed that stabilization gets modified over a range of laser intensities, while its general feature still persists [94,247]. Most recently, stabilization has been also tested for ions in relativistically super-strong laser fields. Fig. 25 shows a comparison of atomic stabilization behavior in the non-relativistic and relativistic regimes [248]. Classical trajectory Monte-Carlo simulations indicate that stabilization can also occur in multiply charged ions, but for higher frequency and more intense fields. Besides being tested for single-electron systems, the stabilization phenomenon has also been investigated for many-electron systems in, for example, Refs. [249–251].

5.2. *Relativistic multi-photon and tunneling-recollision dynamics*

Ionization dynamics of atoms in intense laser fields generally falls into two categories: multi-photon ionization (MPI) and tunneling ionization (TI), depending on the laser intensity and the binding energy of the atomic system. The Keldysh parameter, defined as $\gamma = \sqrt{I_\mathrm{p}/2U_\mathrm{p}}$, where I_p is the ionization potential (binding energy) of the

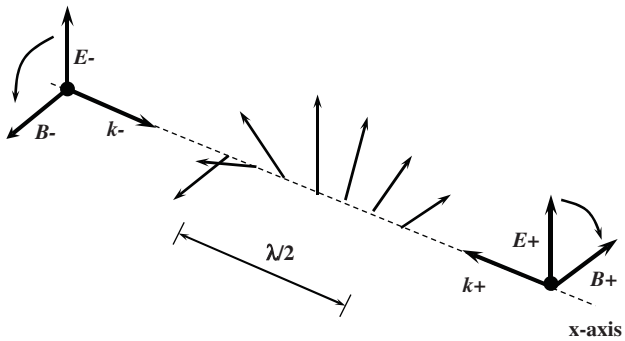

Fig. 26. Schematic of the laser setup consisting of two equal handed, circularly polarized, counter-propagating laser pulses with equal intensities. Electric and magnetic fields are parallel, point along the arrows, rotate in space along the propagation axis, and vary sinusoidal in time and 90° out of phase [256]. Reprinted with permission from [256]; Copyright 2004 by the American Physical Society.

atomic system and $U_p(\text{eV}) \simeq 9.33 \times 10^{-14} \times I(\text{W/cm}^2) \times \lambda^2(\mu\text{m})$ is the ponderomotive energy (see definition in Section 5.1), is customarily applied to characterize the ionization dynamics. Generally, atomic ionization is governed by the multi-photon process if the Keldysh parameter $\gamma \gg 1$, corresponding to low laser intensity, while tunneling ionization is dominant when $\gamma \ll 1$. The significant difference between MPI and TI lies in the fact that for multi-photon ionization the atomic intermediate states are important on the pathway of the bound electron escaping from the atomic potential, and multi-photon resonances within some bound states often show up in the final photoelectron spectra. However, in the case of tunneling ionization the atomic intermediate states play a minor role in the ionization dynamics. This is due to the fact that the higher laser intensity may have already suppressed the potential barrier far below all bound states except the ground state. Under this circumstance, the electron tends to tunnel through the potential barrier and to move subsequently in the laser field as a quasi-free particle. The laser field may bring the outgoing electron back to the atomic core, which results in either radiation of high-energy photons (harmonic generation) [79] (see Section 6.2) or scattering off the atomic core and, consequently, generating hot electrons in the tunneling and re-collision process [226]. Although the theoretical analysis of intense laser–atom ionization can be simplified into such two distinct processes, the two pictures are essentially mixed up in a realistic experiment using laser pulses. The laser pulse intensity rises up from zero to a peak value, a time interval during which the ionization dynamics sweeps from the multi-photon ionization region to the tunneling-dominated region.

The general description given above of MPI and TI applies specifically to non-relativistic intense laser–atom interactions. Now, the question arises as to whether the Keldysh parameter may still be available for characterizing the relativistic ionization dynamics of ultra-intense laser interactions with multiply- or even highly-charged ions. Since the relativistic motion of a free electron in a super-strong laser field is not exactly periodic, the strict definition of a relativistic ponderomotive energy is less meaningful in the strong relativistic interaction regime. Investigations of atomic ionization in the weakly relativistic regime have been carried out [103,252–254]. Assuming that the Keldysh parameter is approximately defined as usual, results [254] have shown that the intense laser interactions with multiply-charged ions are still dominated by the multi-photon ionization dynamics, even when $\gamma < 1$. This could be due to the fact the binding potential of a multiply-charged ion is so extremely narrow and deep that the potential barrier formed is too wide and high even in a moderately relativistic laser field, thereby reducing the tunneling probability of the tightly-bound electron [255].

Relativistic corrections to tunneling and re-collision dynamics have been investigated in recent studies [103,108,252]. The obvious modification is due to the laser magnetic field component: when the electron tunnels out of the laser-suppressed potential barrier, the Lorentz force ($\mathbf{v} \times \mathbf{B}$) will prevent the electron from returning back to the ionic core. This reduces the probability of recombination and, hence, the efficiency of relativistic harmonic generation [103]. A scheme of laser fields, in which the relativistic drift along the laser wave propagation direction is strongly suppressed, has recently been proposed [256]. The fields are those of two equal-intensity counter-propagating circularly polarized laser pulses of the same handedness (both left- or both right-circularly-polarized, see Fig. 26). In this field configuration,

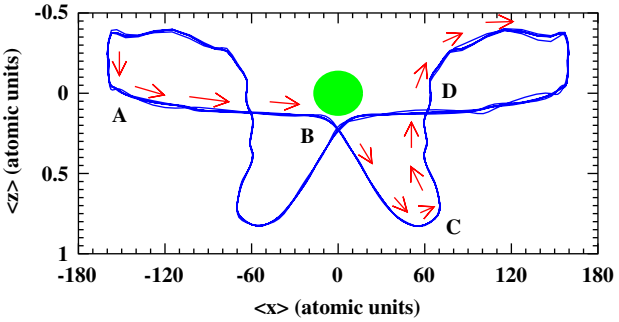

Fig. 27. Weakly relativistic motion of the center-of-mass of the tunneled electron wavepacket. $\langle x\rangle$ and $\langle z\rangle$ denote the center-of-mass in the laser polarization direction and the laser propagation direction, respectively. The arrows indicate the direction of motion of the center-of-mass of the electron wavepacket [252]. Reprinted with permission from [252]; Copyright 2002 by the American Institute of Physics.

the resultant electric and magnetic fields are parallel, which leads to focusing of the ionized electron wave packet during the excursion. This very interesting scheme has strong potential for relativistic HHG.

A subtle feature of the tunneling and re-collision dynamics has been recently investigated in detail for moderately relativistic laser–ion interactions [252]. In Ref. [252] expansion of the Dirac equation has been carried out up to fourth order in v/c. The laser parameters involve a wavelength of 248 nm (KrF laser), an intensity of $1.2\times10^{18}\,\mathrm{W/cm^2}$, a ten-cycle linear pulse turn-on and a ten-cycle duration at constant amplitude. The hydrogen-like nitrogen ions N^{6+} are employed as the targets. From the time-dependent wavefunction, one can trace the electron center-of-mass motion, as is shown in Fig. 27.

From Fig. 27 we see that the tunneled-out electron wavepacket starting its return to the nucleus (at point A) is merely scattered elastically at the nucleus (point B). Because of the electron's high velocity, its interaction with the nucleus is still rather small. Furthermore, with the laser magnetic field component acting, the returning electron is pushed in the laser propagation direction (point C). With changing laser phase and Coulomb focused by the ionic core, the center-of-mass of the wavepacket moves against the laser propagation towards the nucleus (at point D). The first re-collision at point B does not lead to immediate recombination to the ground state of the ionic core. The electron wavepacket is rather pushed first away from the vicinity of the nucleus, it then turns back and gets closer to the nucleus (from points C to D) due to the strong attraction of the multiply-charged ionic core. This dynamics is essentially different from that of the non-relativistic case. Most recently, Keitel and coworker studied the interference effects in relativistic collisions of an electron wavepacket with highly-charged ions, by numerically solving the Dirac equation [257]. This will be reviewed in Section 5.4.2 below.

Further work on the relativistic corrections to the weakly relativistic regime of ATI, taking re-scattering into account, has been carried out [108]. In the described region of parameters the re-scattering process still plays a role but relativistic signatures are clearly visible. Increase of the electron energy cutoff has been found, along with the expected results concerning the impact of the magnetic component of the laser field on the ATI process in the tunneling regime (drop in the plateau height and change of the angular distribution of the emitted electrons). It was shown that the relativistic mass shift reduces the final energy of the emitted electrons by almost the same amount as it is enhanced by the nondipole effects. The reason of this is that the parameter describing the impact of nondipole effects on the plateau damping, $\eta_1 = mc^2q^4/I_\mathrm{p}$, is of the same order of magnitude as the parameter describing the mass shift, $\eta_2 = q^2$.

The re-collision contribution to the ATI probability in the relativistic regime has also been investigated [100]. The strong field approximation is applied but, instead of the Volkov solution for the ionized electron, a wave function in the generalized eikonal approximation of a Dirac particle interacting with an arbitrary potential and radiation fields is used. The latter incorporates the free electron interaction with both the laser and the Coulomb fields [101]. Unfortunately, the derived formulae for the probability in the relativistic case are very unwieldy, even if the spin is neglected. Estimating terms in the probability expression due to re-scattering, a conclusion is drawn that they can have contributions comparable with the main terms.

Finally, we mention that multi-photon resonant excitation of atoms in strong laser fields that can be employed for the implementation of coherent superposition states has been investigated in [258].

5.3. Spin–orbit coupling

The laser magnetic-field-induced phenomena described above can be considered as first-order relativistic effects. Besides this, second-order relativistic effects, such as the relativistic correction to the kinetic energy and the spin–orbit coupling, have been investigated for intense laser–ion interactions [127,156,254,259,260].

In Ref. [260] the authors were interested in the weakly relativistic regime of optical laser intensities of up to $10^{17}\,\mathrm{Wcm}^{-2}$. For those parameters the Foldy–Wouthuysen expansion [261] of the Dirac equation in terms of the parameter $1/c$, is justified. The second order correction terms in the Pauli equation include the spin–orbit coupling as well as the leading relativistic mass shift term and Zitterbewegung. Under the weakly-relativistic approximation, higher order terms of $O(1/c^3)$ are neglected. The main advantage of using this equation, as opposed to the full Dirac equation [128], is the possible isolation of the influence of each of a number of physical mechanisms (e.g., spin–orbit coupling).

For circumstances involving the laser parameters described above, the Hamiltonian of a bound electron (binding provided by a multiply-charged core) in a strong laser field can be written (in atomic units) as

$$\mathbb{H} = \mathbb{H}_0 + \mathbb{H}_\mathrm{p} + \mathbb{H}_\mathrm{kin} + \mathbb{H}_\mathrm{D} + \mathbb{H}_\mathrm{so}, \tag{68}$$

where

$$\mathbb{H}_0 = \frac{(\mathbf{p} + \mathbf{A}(z,t)/c)^2}{2} + V(x,z), \tag{69}$$

$$\mathbb{H}_\mathrm{P} = \frac{\boldsymbol{\sigma}\cdot\mathbf{B}(z,t)}{2c}, \tag{70}$$

$$\mathbb{H}_\mathrm{kin} = -\frac{\mathbf{p}^4}{8c^2}, \tag{71}$$

$$\mathbb{H}_\mathrm{D} = \frac{\boldsymbol{\nabla}\cdot\mathbf{E}'(x,z,t)}{8c^2}, \tag{72}$$

$$\mathbb{H}_\mathrm{so} = \frac{\mathrm{i}\boldsymbol{\sigma}\cdot\boldsymbol{\nabla}\times\mathbf{E}'}{8c^2} + \frac{\boldsymbol{\sigma}\cdot\mathbf{E}'\times\mathbf{p}}{4c^2}. \tag{73}$$

Here $\mathbb{H}_0$ denotes the standard non-relativistic Hamiltonian in the Schrödinger form, where $\mathbf{p}$ is the momentum operator and $\mathbf{A}(z,t)$ is the time-dependent vector potential of the laser field, with an electric field component $E(z,t)$ linearly polarized along the x-axis and propagating in the $+z$-direction. For the vector potential, the authors include the magnetic field component and do not make the dipole approximation, in performing a two-dimensional numerical integration in the xz plane. They considered atoms in the single active electron approximation which are pre-ionized by the order of 10 electrons and, thus, are easily available today via lasers [233] or to highest accuracy via shooting the atoms through thin foils [49]. A soft-core potential [262] was used to model the Coulomb field experienced by the active electron of a multiply-charged ion, i.e., $V(x,z) = -k/\sqrt{s + x^2 + z^2}$. The parameters k and s are functions of the effective number of positive charges Z sensed by the electron. On the other hand, s compensates for the effect of possible inner electrons and reduced distances of the electronic wavepacket to the ionic core in two- rather than three-dimensional calculations. Also, k is adapted in such a way as to allow one to obtain the correct ionization energy of the system of interest with an effective charge Z on the ionic core. The static field of the ionic core is expressed by the gradient of the potential $-\boldsymbol{\nabla}V(x,z)$ and $\mathbf{E}'(x,z,t)$ stands for this field plus the laser field $\mathbf{E}(z,t)$. The following term $\mathbb{H}_\mathrm{P}$ in Eqs. (73) indicates the coupling of the laser magnetic field $\mathbf{B}$ to the electron spin as described by the Pauli matrix $\boldsymbol{\sigma}$. The sum $\mathbb{H}_0 + \mathbb{H}_\mathrm{P}$ gives the Hamiltonian in the well known Pauli equation. Further, in Eq. (73) $\mathbb{H}_\mathrm{kin}$ denotes the leading term for the relativistic mass increase, and $\mathbb{H}_\mathrm{D}$ is the well-known Darwin term. Finally the term in the Hamiltonian, of most interest here, is $\mathbb{H}_\mathrm{so}$, which stands for the spin–orbit coupling.

Considering the central potential, $V(x,z)$, the first term in $\mathbb{H}_\mathrm{so}$ in Eq. (73) disappears because $\boldsymbol{\nabla}\times(-\nabla V(x,z)) = 0$ and the contribution due to the laser field is of order $1/c^3$. Thus, the spin–orbit coupling term becomes

$$\mathbb{H}_\mathrm{so} = \frac{\boldsymbol{\sigma}\cdot\mathbf{E}'\times\mathbf{p}}{4c^2} = \frac{\boldsymbol{\sigma}\cdot\mathbf{E}\times\mathbf{p}}{4c^2} + f(x,z)\boldsymbol{\sigma}\cdot\mathbf{L}, \tag{74}$$

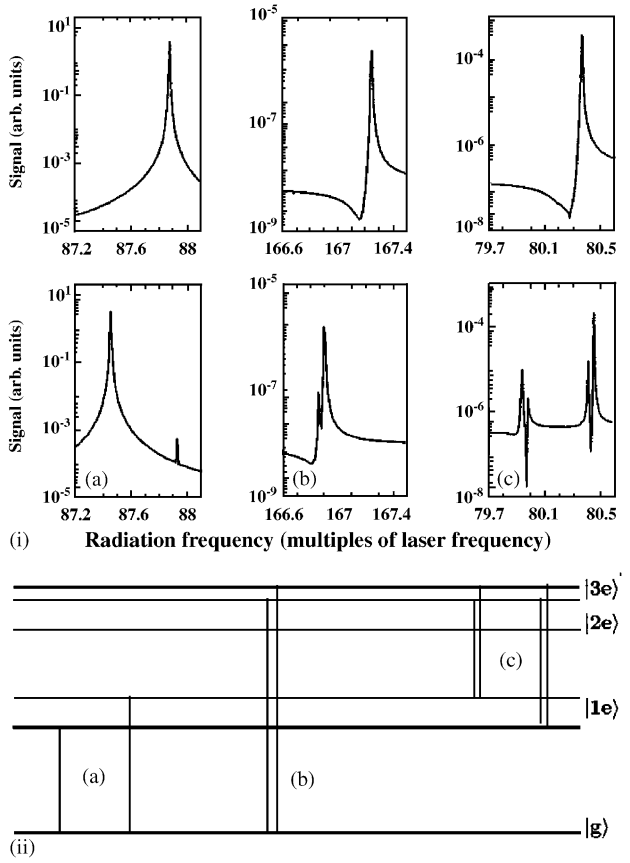

Fig. 28. (i) Radiation spectrum of the laser-driven ion close to its lowest resonances. The first row corresponds to the Pauli modeled system, and the second row is for the case where spin–orbit coupling including the relativistic mass shift and Zitterbewegung is taken into account. Figs. (a), (b) and (c) are associated, respectively, with transitions from $|1e\rangle$ to $|g\rangle$, $|3e\rangle$ to $|g\rangle$, and $|3e\rangle$ to $|1e\rangle$ (see also (ii)). The spectral lines split into doublets ((a) and (b)) and four-line structure (c) configurations due to the spin–orbit interaction. A line shift arising from the mass shift H_{kin} is also observable. The laser parameters involve a wavelength of 527 nm, an intensity of $7 \times 10^{16}\,\text{W/cm}^2$, a 5-cycle linear turn-on and a 100-cycle duration with constant amplitude. The parameters for the ionic core are $s = 1$, $k = 93.5$. (ii) The schematic diagram of state-splitting induced by the intense laser enhanced spin–orbit interaction. Note that non-symmetric states split as opposed to symmetric states. Transitions (a), (b) and (c) are associated with the corresponding spectral lines in (i) [254]. Reprinted with permission from [254]; Copyright 2001 by the American Physical Society.

with $f(x, z) = -k(s + x^2 + z^2)^{-3/2}/4c^2$, and where $\mathbf{L} = \mathbf{r} \times \mathbf{p} = (0, zp_x - xp_z, 0)$ is the orbital angular momentum, of which only the component along the y-direction is non-zero. The origin of spin–orbit coupling can alternatively be viewed as being due to the interaction between the magnetic moment of the electron and the magnetic field $\mathbf{B}'$ due to the motion of the positively charged core as sensed by the electron in its own rest frame. To demonstrate the spin–orbit effect, the authors chose specifically the potential parameters $s = 1$ and $k = 93.5$, which correspond to an ion with a ground state energy of -84.5 a.u. and a charge $Z - 1 = 12$. These parameters model the one electron ion Al^{12+}. They then used the split-operator algorithm [119] to investigate the evolution of the system under irradiation by an intense laser pulse consisting of a 5-cycle linear turn-on and 100-cycle duration with a constant amplitude. The laser parameters involve the wavelength 527 nm of a frequency-doubled Nd:glass laser and a peak intensity of $7 \times 10^{16}\,\text{W/cm}^2$.

The most significant qualitative features appear in the radiation spectrum as strongly laser-enhanced line splittings and shifts. Fig. 28 displays the spectrum of radiation emitted perpendicular to the plane spanned by the laser polarization and propagation directions and being polarized in the x-direction. The upper row describes the situation governed by the Pauli Hamiltonian, while the lower row involves the full second order Hamiltonian $\mathbb{H}$ in Eq. (73). Figs. 28(i)(a), 28(i)(b) and 28(i)(c) show the spectral segments corresponding to the resonances of the first excited state $|1e\rangle$ to the ground state $|g\rangle$, the third excited state $|3e\rangle$ with the ground state $|g\rangle$, and the third excited state $|3e\rangle$ to the

first excited state $|1e\rangle$, respectively. Comparing the upper and lower rows one notes the shifts and splittings of the spectral components into a doublet in (a) and (b) and a four-line structure in (c). The shifts are associated with the relativistic mass shift governed by $\mathbb{H}_{\rm kin}$ and may be considered as relativistic corrections to the Stark shift [254]. The Darwin term, $\mathbb{H}_{\rm D}$, is found to have no notable effect on this situation. The doublets and four-line structure, with the splitting of the antisymmetrical excited states $|1e\rangle$ and $|3e\rangle$, are due to the additional spin–orbit interaction as depicted in Fig. 28(ii), while the symmetrical states, possibly *s*-states, remain unchanged. The splitting increases with increasing laser intensity and/or charge of the ionic core. All transitions give rise to spectral features because the dipole selection rules do not apply in the parameter regime beyond the dipole approximation. The bound states in Fig. 28(ii) (thick lines) indicate which of the split states is more populated. This is explained by the relative heights of the spectral lines in Fig. 28(i).The amount of splitting is $\Delta E/\omega_L \simeq 0.51$ for the state $|1e\rangle$ and 0.05 for the state $|3e\rangle$ (here, $\omega_L = 0.0866$ a.u. is the applied laser frequency) so that the enhanced spin–orbit splitting should be easily measurable in experiments.

The spin effects in the direct ionization of an atom in the strongly relativistic regime have been studied recently [95]. The treatment has been done within the context of an SFA based on the Dirac equation. The rate of spin flip is calculated for a hydrogen atom in the laser field of $10^{20}\,\mathrm{W/cm^2}$. Intensity-dependent asymmetry between the spin-up and spin-down electron yield is found. The effect exists even when the retardation effects and the spin–orbit coupling are negligible. The mechanism responsible for the spin–flip is singled out to be the coupling to the spin of the motional magnetic field (i.e. magnetic field seen by the electron in its rest frame which arises from the Lorentz transformation of the laser electric field).

5.4. More complex systems

5.4.1. Multi-electron systems

5.4.1.1. Ionization processes. When a multi-electron atomic system is exposed to strong laser radiation, electron correlation effects can significantly modify the ionization and the high-order harmonic generation processes. The electron correlation effects are especially pronounced in the laser-induced double-ionization of atoms which has first been demonstrated in [263]. Experiments have demonstrated that the yield of double- and multiple-ionization in a strong laser field, below the saturation intensity, is many orders of magnitude higher than was predicted within a theory using one active electron at a time [264]. Several theories have been advanced to explain the discrepancy between the experimental results and the theory of sequential ionization in the double ionization process. The mechanisms of shake-off [265] and collective-tunneling [266] and the re-collision theories [79] clarify various aspects of the process. Physical essence of non-sequential ionization is currently well understood, at least in the non-relativistic limit (see, e.g., the review [267]). That is, one of the two electrons first tunnels out alone through the Coulomb barrier, then it returns, following a change of phase of the linearly-polarized laser field, towards the ionic core and ionizes the second electron in a re-collision process. A subtle structure of correlated electron dynamics during the non-sequential multiple ionization process has been investigated in a series of recent experiments using a "reaction microscope". The latter allows to calculate the full momentum vectors of the recoil ions and electrons from time-of-flight and position measurements on the detectors [268].

Present-day lasers, with power as high as 100 TW and intensities of over $10^{19}\,\mathrm{W/cm^2}$, allow for the study of the relativistic regime of ionization. Serious modification of the non-sequential ionization probability is expected in the relativistic regime. At relativistic laser intensities the first ionized electron will drift in the laser propagation direction, due to influence of the magnetic field of the laser radiation, in addition to the axial electric field component. This will cause it to miss the ionic core at the re-collision moment, which will result in a significant reduction of the non-sequential ionization probability. Experiments in the relativistic regime of non-sequential ionization are underway. For example, ion yield in Ar at relativistic intensities has been measured [269].

A first indirect evidence for the suppression of non-sequential ionization in the relativistic regime due to the relativistic drift has been observed [109], by measuring the multiple ionization yield of highly-charged states of Xe at relativistic intensities, but well below the saturation limit. The experiment used a laser beam of about 600 mJ pulse energy, 60 fs pulse-duration, and a maximum focused intensity of about $2 \times 10^{18}\,\mathrm{W/cm^2}$.

The integral ionization yield, for different ionic charged states, in this experiment is shown in Fig. 29 and compared with results of two different theoretical calculations. The first theoretical calculation assumes multiple-ionization is a sequential process, and calculates single ionization rates for $\mathrm{Xe}^{n+} \to \mathrm{Xe}^{(n+1)+}$ using probabilities of the ADK theory,

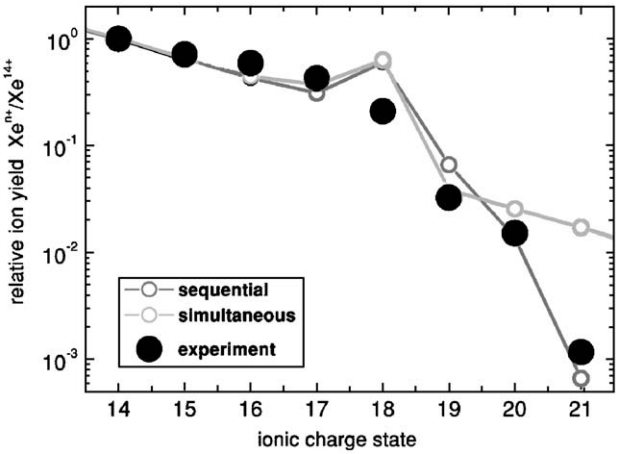

Fig. 29. Multiply charged ion yield for Xe at a laser intensity of about $10^{18}\,\mathrm{W/cm^2}$. The "simultaneous" results include contribution from non-sequential multiple-ionization, while the "sequential" do not [109]. Reprinted with permission from [109]; Copyright 2001 by the American Physical Society.

within the context of a single active-electron approach. The second theoretical calculation, termed "simultaneous", takes into account additional non-sequential processes via re-collision using an empirical formula [266,270]. Actually, for interpretation of the experimental results, an accurate formula for non-sequential ionization is not required. It suffices to use a formula that includes the strong enhancement of the non-sequential ionization probability, as long as the intensities involved are below saturation for a given charge state. The experimental and two theoretical calculations agree quite well up to the charge state 19^+ that is conditioned by saturation. The difference between sequential and non-sequential ionization is only evident if the lower charge state is not completely ionized. The applied laser intensity corresponds to the barrier suppression ionization of the state Xe^{19+}, and complete ionization of this state takes place. The principal result of this experiment is the ionization yield for Xe^{20+}, and especially for Xe^{21+} that indicates the suppression of non-sequential ionization at the applied intensities.

Furthermore, classical relativistic electron trajectory analysis has been done [109]. It supports a qualitative argument that the electron relativistic drift is responsible for the non-sequential ionization suppression. Electron trajectories were analyzed in the field of the laser pulse and the Coulomb field of the ionic core. The ionized electron returns to the parent ion within a given radius R_0 if it has a rather large initial negative momentum in the laser propagation direction. The radius R_0 is determined by the typical binding radius of the outer core electrons and, to a lesser extent, by the energy-dependent $(e, 2e)$ scattering cross section. The required initial negative momentum in the laser propagation direction depends significantly on the laser phase at the instant of ionization (see Fig. 30). The initial laser phase should not be far from zero to have significant ionization probability for the first electron. Besides, the requirement for the re-colliding electron to have sufficient energy for an $(e, 2e)$ process to proceed, imposes the condition that the electron initial negative momentum in the laser propagation direction should not be less than 0.4 times its peak value of 17.7 a.u. in the case of Xe^{19+}. The available initial electron momenta are determined by the tunneled wave packet. In particular, the size of the tunneled wave packet in the laser propagation direction, that is $a \simeq I_\mathrm{p}^{1/4}/E^{1/2}$, where I_p is the ionization potential and E is the laser (electric) filed strength, controls the maximum initial momentum of the ionized electron $\Delta p \simeq 1/a$. For the parameters used, $\Delta p = 0.94$ a.u. Therefore, the required electron momentum is larger, by a factor of 10, than the momenta available in the tunneled wave packet. That is expected to suppress exponentially the corresponding re-collision probability and, consequently, the probability of non-sequential ionization. Thus, suppression of non-sequential ionization arises in rather intense laser fields, where the magnetically-induced relativistic drift is large, and for highly-charged ionic species. That is because the available initial electron momentum in the laser propagation direction decreases with increasing ionization potential.

Accurate calculations are obviously needed in order to confirm the indirect evidence of the relativistic suppression of non-sequential ionization reported in [109]. Numerical calculations for the non-sequential ionization of helium in the relativistic regime has recently been carried out [110,271]. In both papers, the weakly-relativistic regime is considered

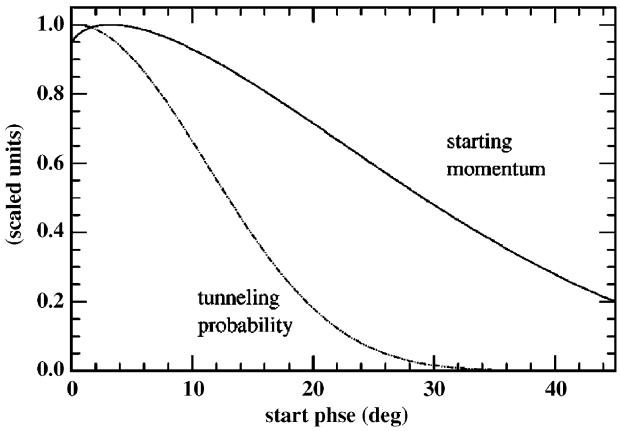

Fig. 30. Classical trajectory calculation results for the ionization probability of $Xe^{19+} \rightarrow Xe^{20+}$ (and return to the Xe^{20+} core) as a function of the initial phase of the field at the ionization time. The curves have been scaled to 1 at their peak values [109]. Reprinted with permission from [109]; Copyright 2001 by the American Physical Society.

in which the Schrödinger dynamics of the electron is still valid while the magnetic field of the laser radiation is fully taken into account without the dipole approximation. However, Ref. [110] deals with the tunneling regime while Ref. [271] takes up the barrier suppression regime of ionization. The ionization dynamics of a model helium atom in both references is considered based on the extended version of a model suggested in Ref. [274]. Electrons are assumed distinguishable in this model, exchange interaction is neglected, and a two-electron wavefunction is approximated by the product ansatz: $\Psi(\mathbf{r}_1, \mathbf{r}_2, t) = \phi_1(\mathbf{r}_1, t)\phi_2(\mathbf{r}_2, t)$, where the $\phi_i(\mathbf{r}_i, t)$ with $i = 1$ or 2, are the respective one-electron wavefunctions, and the antisymmetry requirement is neglected. In Ref. [110] the outer electron is modeled to move in a time-independent potential of the ionic core screened by the inner electron in its initial state, neglecting the polarization effect of the ionic core on the dynamics of the first-ionized outer electron. The inner electron is assumed to be influenced by the electron–electron interaction in order to describe the re-collision process. Thus, the Schrödinger equation for the tunneling dynamics during the non-sequential ionization in Ref. [110] reads (in atomic units)

$$\mathrm{i}\partial_t \Psi_2 = \left(H_0 + \frac{\langle \Psi_1^0 | V_{ee} | \Psi_1^0 \rangle}{\langle \Psi_1^0 | \Psi_1^0 \rangle} \right) \Psi_2, \tag{75}$$

$$\mathrm{i}\partial_t \Psi_1 = \left(H_0 + \frac{\langle \Psi_2 | V_{ee} | \Psi_2 \rangle}{\langle \Psi_2 | \Psi_2 \rangle} \right) \Psi_1, \tag{76}$$

where Ψ_2 and Ψ_1 are the outer and inner electron wavefunctions, respectively, Ψ_1^0 is the inner electron unperturbed wavefunction, and

$$H_0 = \frac{(\mathbf{p} + \mathbf{A}/c)^2}{2} + V_{ei}(\mathbf{r}), \tag{77}$$

is the single electron Hamiltonian. Furthermore, $\mathbf{p}$ is the electron momentum operator, $\mathbf{A} = \mathbf{A}(\omega t - \mathbf{k} \cdot \mathbf{r})$ is the laser vector-potential, $V_{ei}(\mathbf{r})$ is the electron interaction term with the atomic core, and $V_{ee}(|\mathbf{r}_1 - \mathbf{r}_2|)$ describes the electron–electron interactions. Finally, V_{ei} and V_{ee} are approximated by the soft core potential with free parameters chosen to reproduce the He^+ and He ground state energies. The dipole approximation is not employed, so that the magnetic field of the laser radiation is retained.

The Schrödinger equations (75) and (76) are numerically solved on a 2D grid using the split-operator method. In Fig. 31 the angular distribution of the total electron ionization yield during interaction with the laser pulse is shown. Due to the Lorentz force the ionization in (a) and (b) is favored in the direction of propagation of the laser field. In order to isolate the non-sequential yield of double ionization via re-collision from direct laser-induced ionization of the inner electron, the laser field force is switched off on the inner electron in (c) and (d). Figs. (c) and (d) indicate that non-sequential double ionization is less efficient when effect of the magnetic field is taken into account. In the short pulse

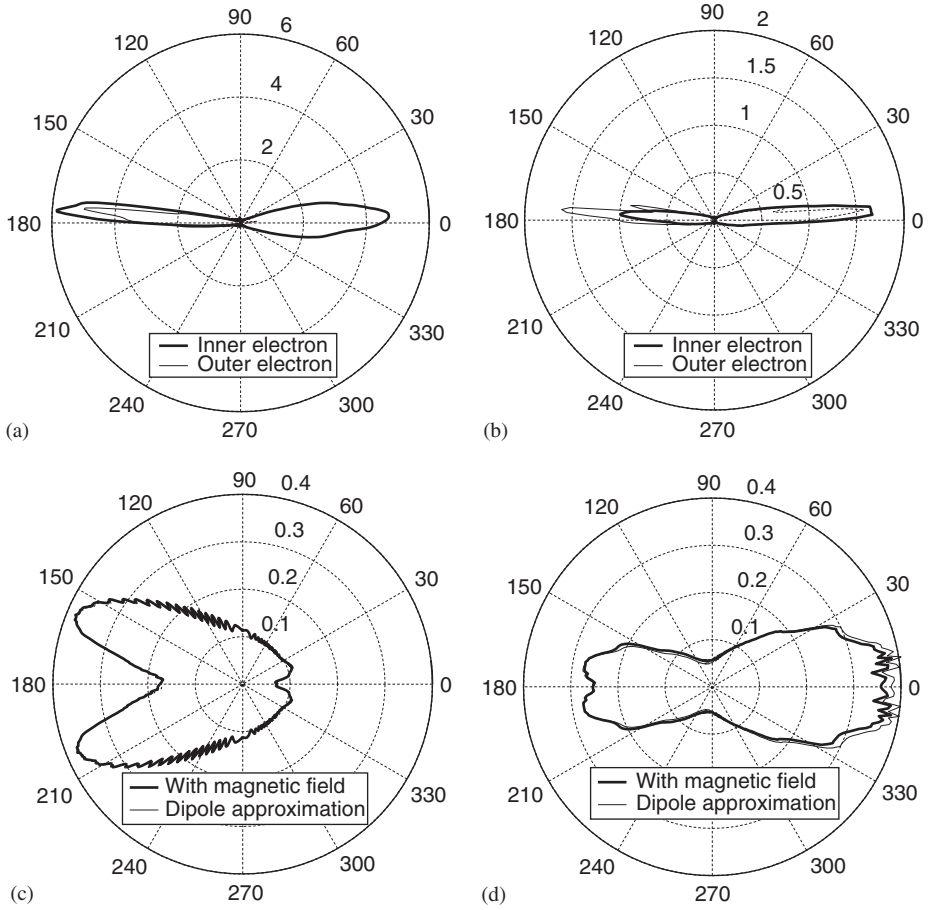

Fig. 31. (a) and (b) Angular distribution of the ionized inner and outer electrons including the influence of the magnetic field. (c) and (d) Angular distribution of the inner electron with and without the influence of the magnetic field while excluding the force of the laser field on the inner electron. The laser intensities used are $2.19 \times 10^{15}\,\mathrm{W/cm^2}$ (a), (c) and $1.4 \times 10^{15}\,\mathrm{W/cm^2}$ in (b), (d), respectively, with wavelength of 1053 nm and a 3-cycle pulse shape with a 1-cycle linear turn-on and turn-off in (a) and (c) and a 5-cycle $\sin^2$ pulse-shape in (b) and (d), respectively. The positive polarization and propagation directions are 0° and 90°, respectively. The total area has been normalized to one and the inner electron yield in (a) has been multiplied by four [110]. Reprinted with permission from [110]; Copyright 2002 by the IOP Publishing Limited.

case (c) one re-collision occurs prior to total ionization while in the longer pulse case (d) two re-collisions take place. That explains the asymmetry in (c) and the symmetry in (d). The splitting of the distribution in (c) and (d) perpendicular to the direction of collision is known in collision theory [273]. In Fig. 32 the inner electron ionization dynamics is depicted close to the return time of the outer electron to the ionic core. Rising of the probability density after 1.15 cycles in the polarization and propagation directions of the laser field indicates non-sequential ionization due to re-collision that makes an asymmetric contribution in the polarization direction and a symmetric contribution in the propagation direction. The magnetic field effect on the non-sequential ionization is most clearly displayed by the asymmetry in the non-sequential ionization probability in the propagation direction in Fig. 32(b). Note that 50.2% of the inner electron ionization yield is in the positive laser propagation direction. This number has been evaluated by integrating the probabilities in Fig. 32(b) in the negative and positive directions separately ignoring, in each case, the contribution between two arrows.

A smaller magnetic field effect is noticed on the probability in the polarization direction than in the propagation direction. Integrating the yield after 1.28 cycles between two arrows in Fig. 32(a) gives a 0.090% probability with the magnetic field included, and a 0.004% more probability when the dipole approximation is used.

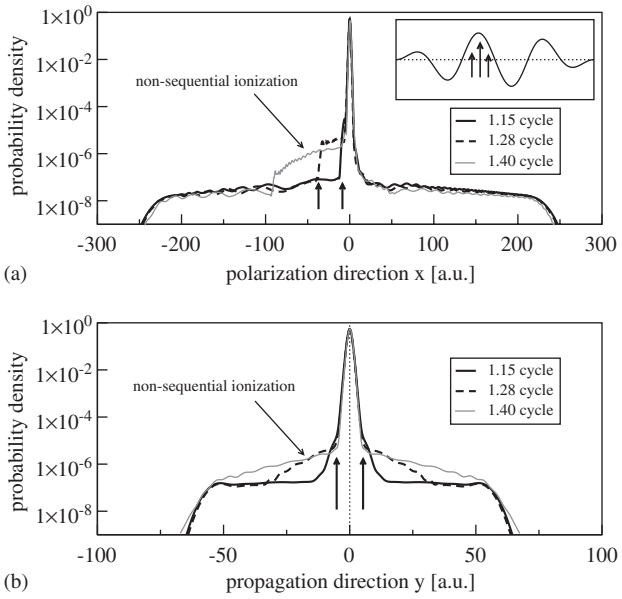

Fig. 32. Probability density of the inner electron. The inset depicts the three different observation times for the employed pulse shape of three cycles with one-cycle linear turn-on and turn-off each. The intensity used is $2.19 \times 10^{15}\,\mathrm{W/cm^2}$ and the wavelength is 1053 nm [110]. Reprinted with permission from [110]; Copyright 2002 by the IOP Publishing Limited.

Results of Ref. [110] show that the probability of non-sequential double ionization decreases with laser intensity towards the relativistic regime, due to the high electron velocities and the magnetically-induced displacement at re-collision. Clear magnetic field signatures appear in the total ionization yield and especially in the angular distribution.

In a super-intense laser field beyond the tunneling regime, re-collision-induced non-sequential double ionization does not play a significant role anymore, but the electron–electron correlation does. This question is investigated in Ref. [271] where the double ionization of a model helium atom with two active electrons in a super-intense high-frequency linearly-polarized laser pulse is considered in the over-the-barrier region without using the dipole approximation. It is assumed that the atom is initially transformed into an excited state, so that the electrons may be thought of as occupying different eigenstates. This makes it possible to distinguish between an inner and an outer electron and allows one to use an approach similar to the one of Ref. [110]. In this regime, the dynamics of the inner electron evolves remarkably in the laser field and, therefore, has significant impact on the outer electron. That is why in this case Eqs. (75) and (76) need to be modified. Instead of the initial state of the inner electron, in Eq. (75), its dynamical state has to be used. In Ref. [271] a 2D numerical integration of Schrödinger's equation is carried out for each electron. The dynamics of the two initially bound electrons in the laser field is given by their center-of-mass motion

$$\langle \mathbf{r}(t)\rangle_n = \int \phi_n^*(\mathbf{r}, t)\mathbf{r}\phi_n(\mathbf{r}, t)\,\mathrm{d}\mathbf{r}. \tag{78}$$

In Fig. 33, the center-of-mass of the inner and outer electrons, subjected to laser pulses with trapezoidal shapes, angular frequency $\omega = 1$ a.u. and electric field of peak amplitudes $E_0 = 5$ a.u. and $E_0 = 12$ a.u., are depicted. Due to the super-strong nature of the laser field, it dominates the electron dynamics almost entirely, thus the electrons leave the ion nearly at the same time. They follow trajectories very similar to the ones followed by free electrons in the laser field. This is particularly the case as far as the oscillation amplitude in the polarization direction is concerned. Only the magnetically-induced drift is less pronounced in the case of an ionized electron compared to the free-electron case due to attraction by the ionic core. On the other hand, mutual repulsion between the electrons is responsible for the electron trajectories being different, with the inner electrons driven farther away from the nucleus. That repulsion places the electrons in different laser phases, thus enhancing the difference between the trajectories. Simulations using the same parameters but without repulsion between the electrons leads almost to identical electron trajectories, as expected.

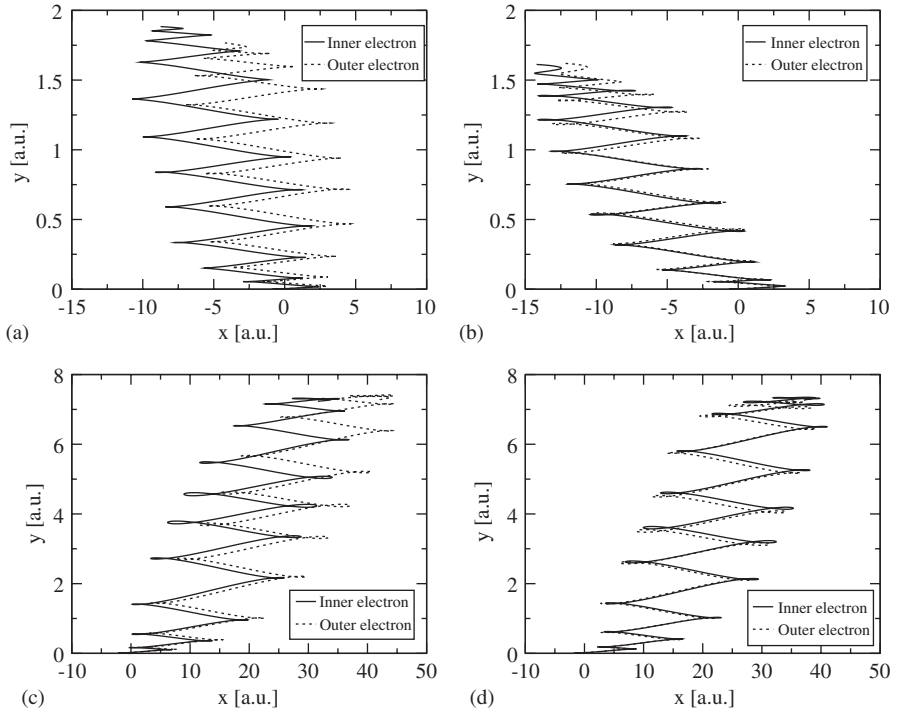

Fig. 33. Center-of-mass motion of the inner and outer electrons. In (a) and (c) the repulsion between two electrons is taken into account, while it is neglected in (b) and (d). The laser frequency is 1 a.u., the peak electric field strength 5 a.u. for (a) and (b), and 12 a.u. for (c) and (d) [271]. Reprinted with permission from [271]; Copyright 2003 by the EDP Sciences.

In Fig. 34, angular distributions of the ionized inner and outer electrons are shown for the same laser parameters as in Fig. 33. First of all, it is apparent that in contrast to results from calculations with the dipole approximation, symmetry of the angular distributions, with respect to the polarization axis, is broken. With interaction between the electrons taken into account, the angular distributions are almost symmetric with respect to the propagation direction. Ionization of the inner electron is higher by 10% than that of the outer electron. This has to do with the fact that the inner electron advances farther away from the nucleus than the outer one, due to their mutual repulsion. With increasing laser intensity (Fig. 33(c) and (d), $E_0 = 12$ a.u.) impact of the electron repulsion becomes more evident. The symmetry of the yield about the laser propagation direction depends strongly on the electron repulsion at the time of ionization. With repulsion taken into account, the ionization threshold is reached during interaction with one laser half-cycle, while in the case without repulsion both halves of one cycle contribute to the ionization.

Interaction between the electrons strongly enhances the ionization. Overall, the ionization probabilities are higher by a factor of two for both electrons when the electron–electron repulsion is included. Besides, ionization probability of the outer electron is higher than that of the inner electron if mutual interaction is included, while the probabilities are almost the same for non-interacting electrons. Thus, the main conclusion of Ref. [271] is that, by contrast to the tunneling ionization case in a super-strong laser field, the electrons leave the nucleus almost simultaneously and follow trajectories resembling those of the classical electrons in a laser field. The ionization angular yield is also strongly affected by the repulsive interaction between the electrons and differs substantially from the case of tunneling ionization.

5.4.1.2. High harmonic generation. Evidence of the electron correlation effects on harmonic generation has been observed [272]. Up to the 23rd harmonic, generated from helium atoms driven by a KrF laser, have been detected. For explanation of these experimental results, contribution to the harmonic emission from a He^+ ion due to the correlation effects, has been successfully invoked [275]. Furthermore, the two active electrons (TAE) approach for harmonic generation in the multi-photon regime, or at the beginning of the tunneling regime, has been investigated employing

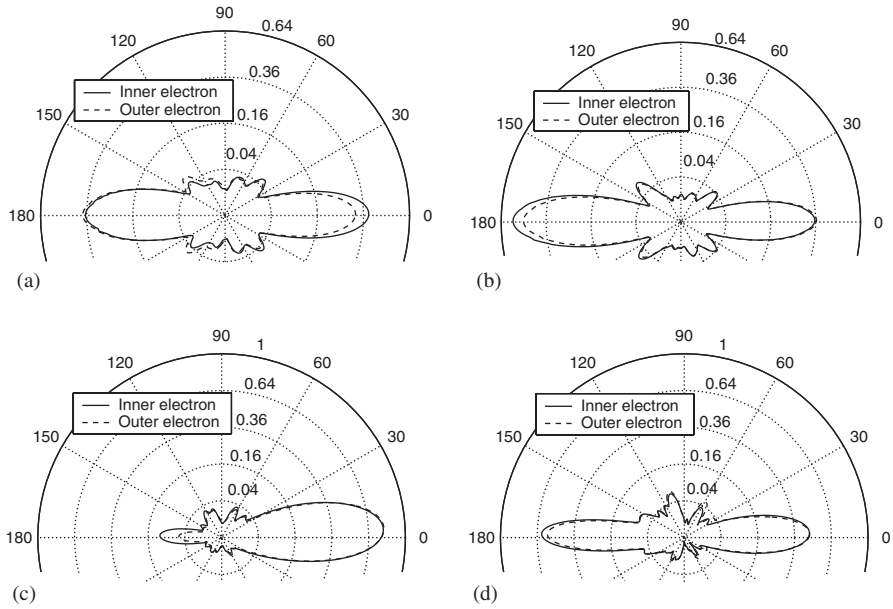

Fig. 34. Angular distribution of the ionized inner and outer electrons. The positive laser polarization direction is along 0°, the propagation direction 90°. In (a) and (c) the repulsion between two electrons is taken into account, while it is neglected in (b) and (d). The laser frequency is 1 a.u. and the peak electric field strength is 5 a.u. for (a) and (b), and 12 a.u. for (c) and (d). The total area of the sum of both angular distributions is normalized to unity for each picture [271]. Reprinted with permission from [271]; Copyright 2003 by the EDP Sciences.

density functional theories [276], fully correlated 1D treatments [277,278], as well as 3D benchmark simulations on a parallel supercomputer [279].

We stress that these treatments of HHG from helium, deal with the multi-photon regime (or with the beginning of the tunneling regime) and leave the emission of very high harmonics unexplored. This question is addressed in Ref. [280] where correlation effects within the TAE approach in the upper limit of the tunneling regime of very high harmonic generation in helium is considered without the dipole approximation. This regime is less elucidated, so we will consider it in more detail. In this regime the electron spends little time in the vicinity of both the nucleus and the second bound electron and, therefore, the electron correlation effects are expected to be small. Consider a helium atom submitted to laser radiation of intensity beyond 10^{15} W/cm^2 and a wavelength of 780 nm. Employing a Hartree–Fock approach to treat the two electron correlated dynamics, the helium atom wavefunction may be approximated by the product of doubly occupied orbitals $\Psi(\mathbf{r}_1, \mathbf{r}_2; t) = \phi(\mathbf{r}_1, t)\phi(\mathbf{r}_2, t)$, where $\mathbf{r}_1$ and $\mathbf{r}_2$ are the coordinates of the two electrons. The orbital ϕ follows from the Schrödinger equation

$$\mathrm{i}\partial_t \phi(\mathbf{r}, t) = \left(H_0 + \frac{\langle \phi | V_{ee} | \phi \rangle}{\langle \phi | \phi \rangle} \right) \phi(\mathbf{r}, t). \tag{79}$$

Here, too, the dipole approximation is not made in describing the laser field, so that account may be taken of the effects related to the magnetic field of the laser radiation. Harmonic yield may then be obtained from a numerical 2D solution of Eq. (79). In Fig. 35, the harmonic spectra are shown within the TAE and SAE approximations. Both spectra exhibit the principal features involving harmonics with plateaux and cutoffs. In the cutoff region intensity of the TAE spectrum is higher by a few orders of magnitude than that of the SAE spectrum. Furthermore, the cutoff frequency of the TAE spectrum occurs about eight harmonics higher than that of the SAE spectrum. These differences between the spectra are small but they clearly stem from introduction into the picture of the second electron. In TAE the effective potential sensed by the re-colliding electron is time-dependent due to motion of the inner electron. To investigate the origin of the cutoff frequency difference, the effective potential is calculated at the re-collision time corresponding to the cutoff frequencies. The re-collision time is obtained by employing a window function on the Fourier-transformed dipole acceleration that leaves only the cutoff frequency region. This is then followed by taking the inverse Fourier transform. The ground state energies of the effective potential at the re-collision time, found this way, are −1.03

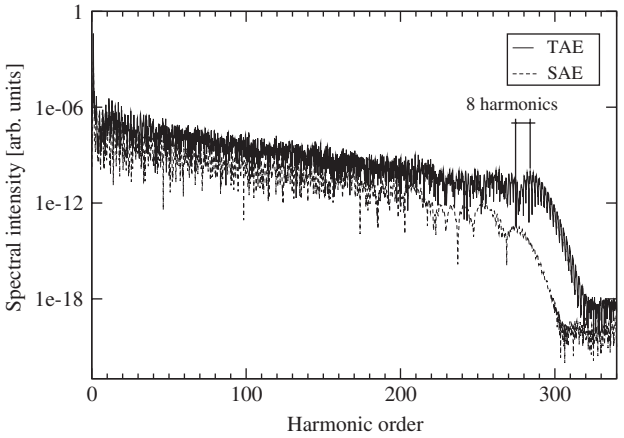

Fig. 35. Harmonic yield obtained with the single active electron (SAE) approximation and with two active electrons (TAE). The intensity employed is 2×10^{15} W/cm^2 at a laser wavelength of 798 nm [280]. Reprinted with permission from [280]; Copyright 2001 by the American Physical Society.

and -1.37 a.u. for the SAE and TAE cases, respectively. When dynamics of the second bound electron is taken into account, the effective potential is found to be stronger due to polarization of the atomic core. From the scaling law of the cutoff frequency, $I_p + 3.17U_p$, the difference obtained in I_p alone explains emission of 8 more harmonics within the TAE model. Furthermore, momentum distribution of the tunneled electron is calculated at the re-collision time to investigate the role played by the dynamical correlations.

5.4.2. Multi-atom systems

Quantum mechanical signatures, such as tunneling, spin effects, and quantum interference, play crucial roles in the single-particle dynamics in strong field atomic physics. This is because a characteristic size of the process, e.g., the size of an atom, is of the order of magnitude of the electron de Broglie wavelength. Meanwhile, for the many-particle collective dynamics in strong fields, as in laser-induced plasma physics, inter-particle distances are usually large by comparison to a particle's de Broglie wavelength. Hence, the quantum effects are suppressed in spite of the fact that the classical dynamics incorporates, as parameters, characteristics of some processes that have a single-particle nature, such as the cross-sections of ionization, recombination, scattering, and so on. In Ref. [257] the situation when the quantum effects are exhibited in the relativistic dynamics of a multi-particle system driven by a strong laser field is taken up. The relativistic electron wave packet evolution and its multiple-scattering by a system of highly charged ions in a super-strong laser field are considered. In an intense laser field modeled by a vector-potential $\mathbf{A}(t, \mathbf{r})$ and an ensemble of ions whose effect is modeled by a scalar potential $A_0(\mathbf{r})$, the Dirac equation for the spinor $\Psi(t, \mathbf{r})$ reads (in atomic units)

$$\mathrm{i}\partial_t \Psi = \left[c\boldsymbol{\alpha} \cdot (\mathbf{p} + \mathbf{A}/c) - A_0 + \beta c^2\right] \Psi, \tag{80}$$

where $\boldsymbol{\alpha}$ and β are the Dirac matrices.

The split-operator technique is used to propagate the wave packet, with the numerical error at the time step Δt being of order $(\Delta t)^3$. For $\Delta t \approx 2 \times 10^{-5}$ a.u. $< \hbar/2mc^2$, transitions between positive- and negative-energy states are resolved, that secures convergence even for $t \gtrsim 10$ a.u. A moving grid with a variable size is used in order to save numerical calculations with a fast-moving and spreading electronic wave packet. In Figs. 36 and 37, contour plots are presented that show time evolution and scattering of an initially Gaussian wave packet in the field of a four-cycle laser pulse with an amplitude $E_0 = 50$ a.u. ($I = 8.75 \times 10^{19}$ W/cm^2) and a frequency $\omega = 1$ a.u. The effect of the ions is modeled by a soft-core Coulomb-like potential, with an ion charge $Z = 50$ chosen to make it have a strength comparable with that of the laser field.

Fig. 36 illustrates the wave packet successive scattering from two highly-charged ions. Solid lines mark the center of mass motion of the wave packet. During the first 1.25 cycles, before encountering the ions, the observed motion of the wave packet can be modeled by a classical Monte-Carlo ensemble and is in agreement with known free wave

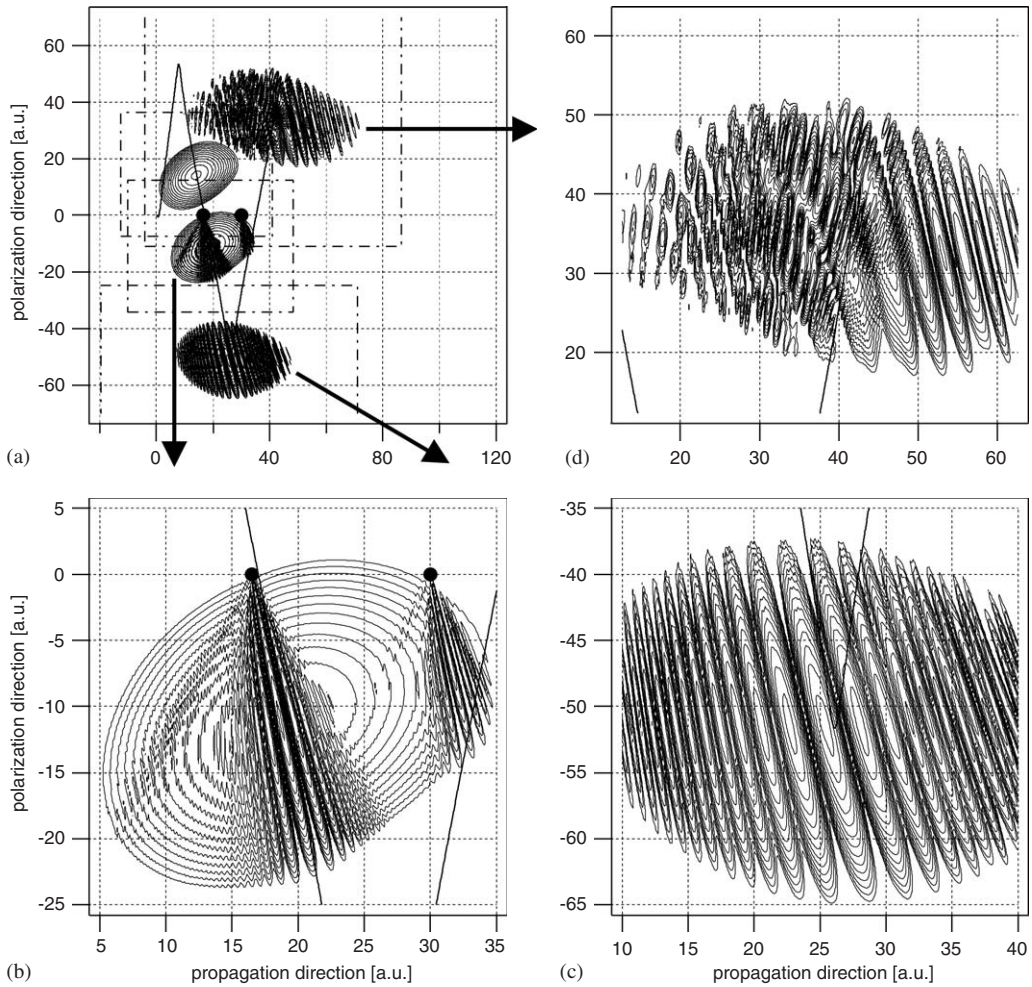

Fig. 36. (a) Overview: contour plots at $t = 7.645, 8.195, 9.495, 12.095$ a.u. corresponding to times before the first scattering, shortly after it, at the lower point of return, and after the second scattering, close to the upper point of return. The four dashed rectangles (some only partly visible) mark the dynamical grid boundaries for each of these situations. The thick dots indicate the positions of two Sn^{50+} ions, which are located right on the horizontal axis at positions 16.5 and 30.0 a.u. The solid line depicts the trajectory of the expectation value of the particle's spatial coordinate. We omit any enlarged view of the initially Gaussian packet at $t = 7.645$ a.u., but provide them for the other three cases as follows; (b) enlarged view at $t = 8.195$ a.u. showing single scattering fringes shortly after the scattering event; (c) enlarged view at $t = 9.495$ a.u. that depicts the same single scattering fringes somewhat later in order to illustrate the growth of the distance between any two fringes (compare with (b)); and (d) enlarged view at $t = 12.095$ a.u. which displays interference from two separate scattering events with crossed fringes on the left side and the unperturbed structure from single scattering at the first ion only on the right side. In all cases 20 contour lines are shown for $|\psi|^2$ with constant steps within $-1.15 \geqslant \log|\psi|^2 \geqslant -4$ [257]. Reprinted with permission from [257]; Copyright 2003 by the American Physical Society.

packet results [139], e.g., Lorentz-contraction of the wave packet and its rotation due to the phase difference sensed by its spatially separated parts. Furthermore, scattering with two ions generates interference fringes due to superposition of the incoming and scattered waves. The negative energy state probabilities are enhanced during the scattering events, although they remain well below 10^{-7} from then on. At the second scattering event with ions a new set of fringes, superimposed on the previous fringes, is created with a different orientation. Fig. 37 shows the same wave packet evolution after it has passed a collection of seven ions twice. Again, one can see interference structures that now are more complex and less clear than in the case of two ions. The code developed for solution of the Dirac equation [257] in the strong fields of a laser pulse and highly-charged ions can serve as an excellent instrument for further investigation of quantum dynamics in super strong fields.

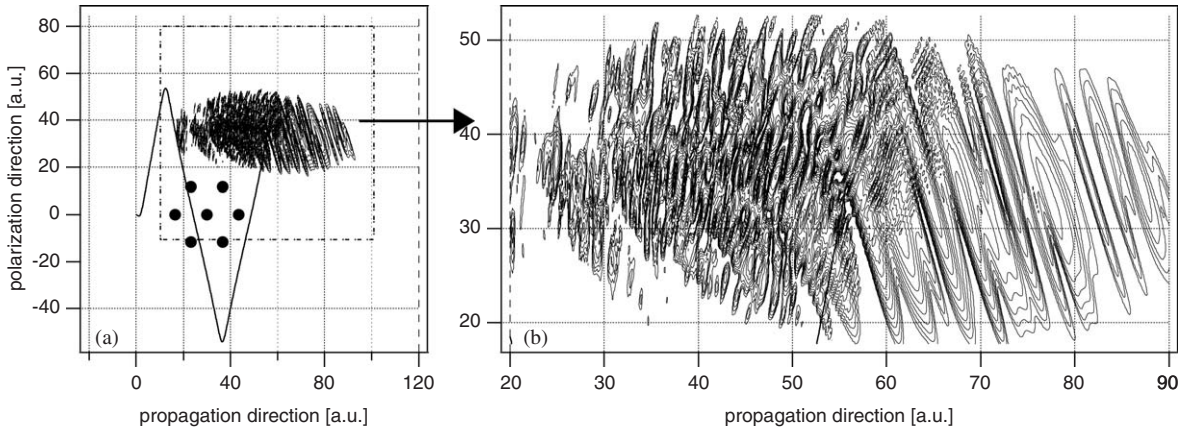

Fig. 37. (a) Overview: contour plots at time $t = 12.270$ a.u. after two scattering at an ensemble of six Sn^{50+} ions (thick dots) centered symmetrically around a further one at position (0,30) a.u. The dashed rectangle marks the grid boundary and the solid line depicts the trajectory of the expectation value of the electron's spatial coordinate; and (b) this enlarged view of the wave packet in (a) illustrates how the two scattering events at seven ions modify the regularity in the interference pattern. In both graphs, 20 contour lines are shown for $|\psi|^2$ with constant steps within $-1.15 > \log|\psi|^2 > -4$ [257]. Reprinted with permission from [257]; Copyright 2003 by the American Physical Society.

A lot of work has been done in the past two decades in the *non-relativistic* regime of intense laser interaction with more complex multi-atom systems. Examples include molecules [281–283], clusters [233,284–288], solids [289], underdense plasmas [2–5], and overdense plasmas [231,290]. In the past few years the field of *relativistic* laser–plasma interactions has seen rapid development [5,19,21,35–39,231], with a number of new phenomena discovered such as relativistic self-channeling and self-guiding, magnetic field self-generation, electron acceleration by wakefields in the bubble regime, ion acceleration via strong laser pulse interaction with thin foils, and nuclear reactions (the latter is discussed in Section 7.2). We do not intend to review the field of relativistic laser–plasma interactions here. Leaving that to the cited publications, we next review in this section a peculiar regime of laser-crystal-layer interaction.

Solid targets are important for studying the strong coupling of a laser field of relativistic intensity to a multi-atom system and the efficiency of laser energy deposition in the medium. The strong coupling increases efficiency of the coherent processes such as HHG but, at the same time, it increases the *incoherent* transformation of laser energy into energy of the nonlinear plasma excitations and into plasma heating. Competition between coherent and incoherent processes determines the overdense plasma dynamics, and efficiency and quality of HHG and other coherent processes at various intensities. However, very strong laser radiation is required, $I > 10^{20}\,\mathrm{W/cm^2}$, to generate harmonics of order $n \gg 100$. Laser radiation of such super-high intensity impinging on a solid surface excites plasma collective nonlinear instabilities such as ion shock waves [292], hole boring [293], and Rayleigh–Taylor surface rippling [290,291]. That substantially reduces the spatial coherence of the emitted harmonic radiation and, consequently, restricts the maximum achievable frequency of the coherent radiation generated by this mechanism. For incoherent X-ray generation laser–solid interaction is an efficient mechanism [294,295].

In Refs. [296–298] a new setup for laser–solid interaction is proposed where conditions are applied to reduce coupling of the laser field to the solid in order to reduce impact of the incoherent processes. As a result efficiency of the system in a single pass will be small, as only a small part of the laser energy will be converted into coherent short wavelength radiation (X-rays). Nevertheless, in this case, incoherent and collateral absorption will be small as well, making it possible to recuperate laser energy and improve the system's efficiency via multi-pass runs. The proposed setup is the following. A thin solid layer (or some other thin periodic ionic structure) is considered to interact with a short super-intense laser pulse propagating along the layer (see Fig. 38). The transverse width of the layer $L_\perp$, with respect to the laser beam propagation direction, is assumed to be substantially less than the waist size w_L of the laser beam

$$L_\perp \ll w_L. \tag{81}$$

Two regimes of interaction are considered depending upon which length prevails, the layer transverse size or the electron transverse oscillation amplitude in the laser field, $R_\perp$: a thin layer regime when $L_\perp \ll R_\perp$ and a thick layer

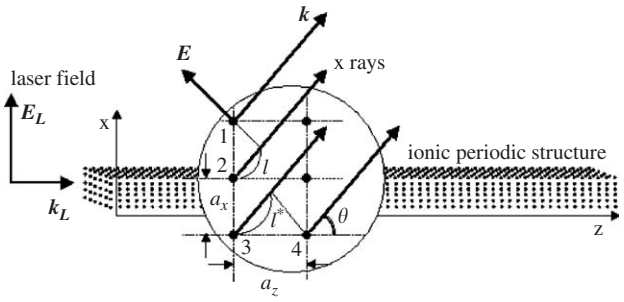

Fig. 38. Schematic diagram showing a thin layer in a strong laser field propagating parallel to its surface [297]. Reprinted with permission from [297]; Copyright 2002 by the IOP Publishing Limited.

regime whenever $R_\perp \ll L_\perp$. Usually, strong collective effects during laser–solid interaction arise due to the strong ponderomotive pressure of the laser pulse on the solid surface that launches a collisionless shock wave into the bulk of the medium and causes rippling and chaotic oscillations of the solid surface after the wave-breaking. Due to the applied condition (81) a transverse Gaussian distribution of the laser intensity has only a very small gradient in the vicinity of the layer that significantly reduces the ponderomotive forces. In fact, the ponderomotive force due to the laser pulse's transverse profile can be estimated to be $f_\perp^{(\mathrm{p})} \simeq ZU_\mathrm{p}/l_L$, with $U_\mathrm{p} = mc^2q^2/4$ the ponderomotive energy, Z the effective ion charge, and l_L a length determining the transverse gradient of the laser intensity, and q^2 is the dimensionless intensity parameter. In the case of the bulk medium it is equal to the laser waist size. In the case of a layer obeying condition (81) this length is much larger, $l_L = w_L^2/L_\perp$, and the gradient is much smaller. It causes ion displacements that may be determined from

$$l_\perp^{(\mathrm{p})} \simeq Zq^2 L_\perp \frac{m}{M}\left(\frac{c\tau_L}{2w_L}\right)^2, \tag{82}$$

during the brief interaction with the laser pulse of duration τ_L, M being the mass of an ion.

Longitudinal ponderomotive pressure due to the finite length of the laser pulse is negligible in the case of a thin layer as the bulk of the electrons leave the layer during transverse oscillations. For a thick layer regime the longitudinal ponderomotive force can be estimated from $f_\parallel^{(\mathrm{p})} \simeq Zmcq^2/(2\tau_L)$, as it imparts to the electron a momentum $mcq^2/2$ during the interaction time τ_L. Therefore, the ion displacement, $l_\parallel^{(\mathrm{i})} \simeq f_\parallel^{\mathrm{p}}/(M\omega_\mathrm{p})$, due to the longitudinal ponderomotive force, may be estimated from

$$l_\parallel^{(\mathrm{p})} \simeq \frac{Zq^3 m}{8\pi M n_e r_0 c\tau_L}, \tag{83}$$

where n_e is the electron density. It may be safely assumed that effect of the ponderomotive pressure will be damped in this setup if the ion displacement is negligible during interaction with the laser pulse, i.e.,

$$l_\parallel^{(\mathrm{p})} \ll L_\perp; \quad l_\perp^{(\mathrm{p})} \ll a. \tag{84}$$

In the thin layer regime electrons are extracted from the layer by the laser field assuming a minor role is played by the Coulomb forces compared to the laser field,

$$Zn_i r_0 L_\perp \lambda_L \ll 2q, \tag{85}$$

where Z is the ion charge, n_i is the ion density, and r_0 is the classical electron radius. The main destructive mechanism of the structure in this regime is not the ponderomotive pressure but the Coulomb explosion. The transverse and longitudinal ionic displacements due to the Coulomb repulsion, $l_\perp^{(\mathrm{C})}$ and $l_\parallel^{(\mathrm{C})}$, during the interaction

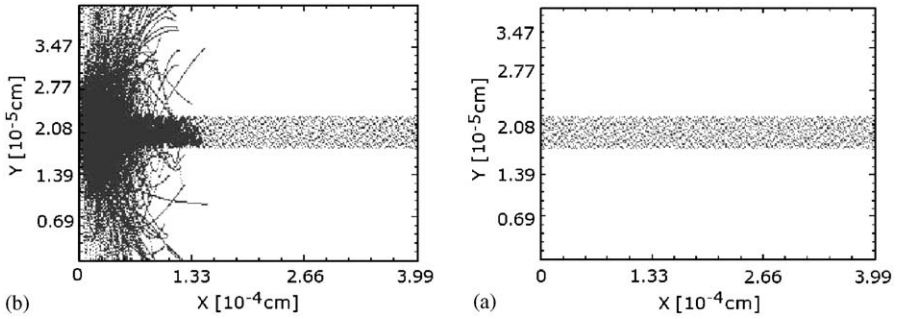

Fig. 39. The dynamics of the ions (a) and electrons (b) in propagation (X) and polarization direction (Y). In the considered thin layer regime of interaction, the transversal size of the electron oscillation amplitude exceeds the layer width. The electron and the ion trajectories are traced up to 6.3 fs after switching on the interaction with the laser pulse. The layer consists of a Pb sample with density $n_i = 3 \times 10^{22}\,\mathrm{cm}^{-3}$ and ion mass $M = 3.8 \times 10^5\,\mathrm{m}$. The layer width is $L_\perp = 5 \times 10^{-6}$ cm, and the length $L = 4 \times 10^{-4}$ cm. The laser radiation parameters are: wavelength $\lambda_L = 248$ nm (KrF), pulse duration $\tau_L = 10$ fs, intensity $I = 10^{21}\,\mathrm{W/cm}^2$. The electrons are extracted from the layer and oscillate with large amplitude while the motion of the ions is not noticeable [298]. Reprinted with permission from [298]; Copyright 2005 by the American Physical Society.

time can be estimated to be at most

$$l_\perp^{(\mathrm{C})} \simeq Z^2 n_i r_0 L_\perp (c\tau_L)^2 \frac{m}{M},$$
$$l_\parallel^{(\mathrm{C})} \simeq Z^2 n_i r_0 \frac{(L_\perp c\tau_L)^2}{L} \frac{m}{M}, \tag{86}$$

where L is the length of the solid layer. In the thin layer regime, the Coulomb explosion will not play a substantial role, as long as

$$l_\perp^{(\mathrm{C})} \ll L_\perp; \quad l_\parallel^{(\mathrm{C})} \ll a. \tag{87}$$

In the thick layer regime the role of the Coulomb explosion is minor in causing deterioration of the regular structure, as the electron transverse excursion in the laser field is of the order of the width of that layer. Estimates, that take into account the conditions (81), (84), (85) and (87) for a concrete parameter set to be given immediately, confirm the validity of the assumption on transient quasi-regularity of the ionic structure in the setup. Thus, for the thin layer regime in the case of a Pb sample with density $n_i \sim 10^{22}\,\mathrm{cm}^{-3}$, $a \sim 5$ Å, $M \sim 3.8 \times 10^5$ m, layer length $L_\perp \simeq 1.6 \times 10^{-6}$ cm, $L \sim 4 \times 10^{-4}$ cm, ion charge $Z \simeq 10$, laser pulse intensity $I \simeq 10^{21}\,\mathrm{W/cm}^2$, KrF wavelength $\lambda_L = 248$ nm, and a pulse-duration $\tau_L \sim 10$ fs, the above-mentioned conditions hold. In the thick layer regime, for a Ti:S laser with intensity $I = 5 \times 10^{21}\,\mathrm{W/cm}^2$ and a potassium crystal ($Z = 17$), one obtains $l_\perp^{(\mathrm{p})} \approx 0.2$ Å, and $l_\parallel^{(\mathrm{p})} \approx 1.7$ Å. These values are less than the lattice period $a = 4.5$ Å, so condition (84) holds. The conclusion, that the ionic structure is quasi-regular during the brief interaction with the laser pulse in the setup, has been confirmed also by particle-in-cell (PIC) simulations [298] based on the OOPIC code [299] as shown in Figs. 39–41.

Figs. 39 and 40 are for the thin layer regime, at an intermediate moment during the interaction and at a moment after the interaction, respectively. Electrons oscillate with amplitude exceeding the layer width while ions do not move noticeably. Fig. 41 is for a thin layer at an instant after the interaction. Electrons oscillate with amplitude within the layer width while ions, again, do not move noticeably.

Details of the laser wave propagation through the layer are clarified in Refs. [296–298]. In the case of a thin layer the strong laser field propagates along the layer, destroying it in the process. The collective properties of the medium, particularly refraction and plasma oscillation, are strongly suppressed during the interaction. This is so because the characteristic length of individual electron dynamics, that is the transverse oscillation amplitude ($R_\perp$) of the electron in the laser field, exceeds extent of the medium in transverse direction and the characteristic size $\delta = c/\omega_\mathrm{p}$ of the collective electron dynamics, i.e.,

$$\delta, \; L_\perp \ll R_\perp. \tag{88}$$

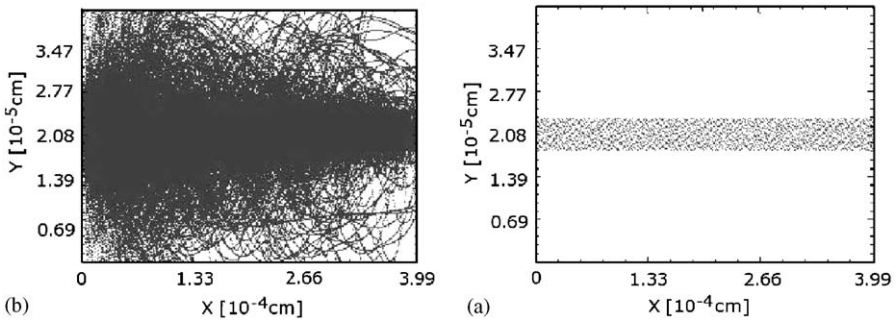

Fig. 40. Dynamics of the ion (a), and electron (b) for the same situation as in Fig. 39 but with tracing the trajectories for 20 fs after switching on the 10 fs laser pulse. The laser pulse has traveled up to the end of the layer and the ionic motion is still not noticeable [298]. Reprinted with permission from [298]; Copyright 2005 by the American Physical Society.

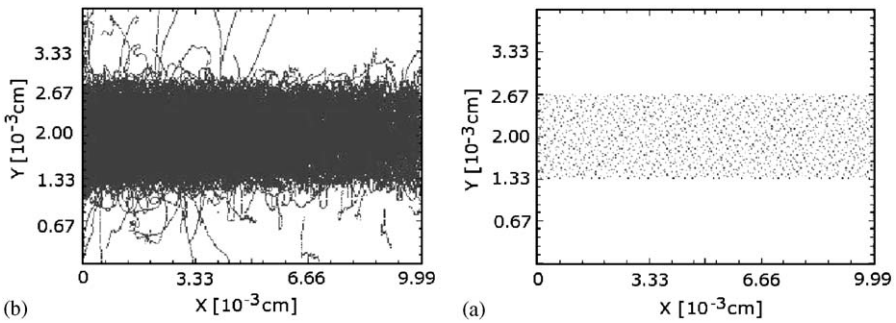

Fig. 41. The ion (a) and electron (b) dynamics in the thick layer regime. Here the layer width exceeds the transversal size of the electron oscillation amplitude. The electron and the ion trajectories are traced up to 143 fs after switching on the interaction with the laser pulse. The laser radiation parameters are: wavelength $\lambda_L = 800$ nm (Ti–Sapphire), pulse duration $\tau_L = 30$ fs, intensity $I = 5 \times 10^{21}$ W/cm^2. The layer is assumed to consist of a potassium sample with density $n_i = 1.3 \times 10^{22}$ cm^{-3}. The layer width is $L_\perp = 1.4 \times 10^{-3}$ cm, and the length $L = 10^{-2}$ cm. The electrons oscillate mainly within the layer while ionic motion is still not noticeable [298]. Reprinted with permission from [298]; Copyright 2005 by the American Physical Society.

Here ω_p denotes the relativistic plasma frequency. In the thick layer regime the layer maintains properties of an underdense plasma, $\omega_L > \omega_p$. That becomes particularly possible due to the relativistic increase in the electron effective mass in the laser field by a factor of $\sqrt{1+\bar{q}^2/2}$ and, hence, the intensity-dependent decrease in the plasma frequency $\omega_p^2 = 4\pi n_e^2/(m\sqrt{1+\bar{q}^2/2})$. The use of the setup discussed above for the laser–thin-solid-layer interaction at relativistic intensities for coherent X-ray generation is discussed in Section 6.6.

6. Relativistic X-ray generation

Coherent, short-wavelength radiation is essential for extremely high spatial- and time-resolved applications such as those encountered in the biological, chemical, and material sciences [300–303]. High-order harmonic generation (HHG) is one of a number of competitive ways to generate coherent X-rays, see e.g. [4,44,45,340]. HHG is a process in which an atom, exposed to an intense laser field, may emit radiation at a frequency that is an integer multiple of the driving laser frequency. Depending on the interaction parameters involved, the intense laser-driven radiation falls into the following categories: Radiation from multi-photon transitions, HHG from tunneling and re-collision dynamics, and non-tunneling harmonics. Recent investigations of intense laser-induced radiation processes will be reviewed below separately, with emphasis on radiation from the relativistic interactions.

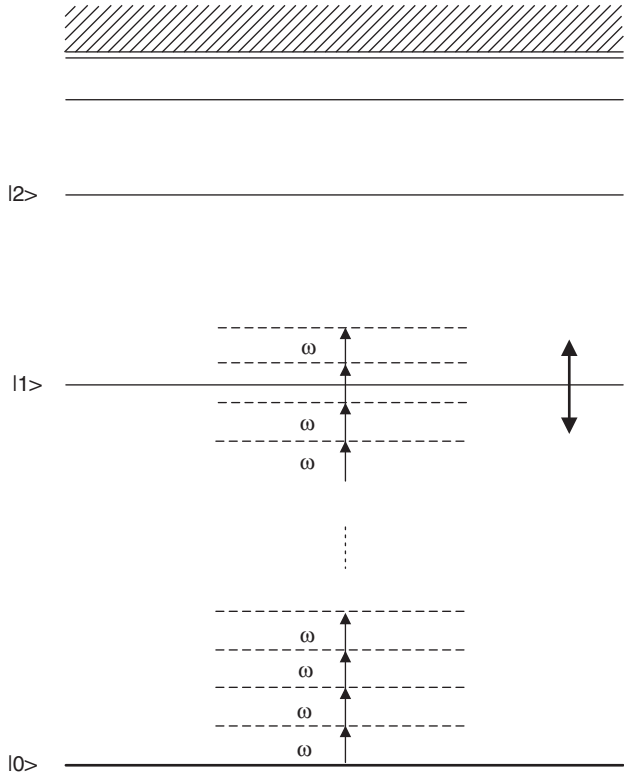

Fig. 42. The schematic picture depicting the resonant multi-photon absorption of a multiply charged ion (ground state $|0\rangle$ and excited states $|1\rangle$ and $|2\rangle$) in a super-strong laser field with angular frequency ω [253]. Reprinted with permission from [253]; Copyright 2002 by the EDP Sciences.

6.1. X-rays from multi-photon transitions

In this section we consider harmonic radiation from a laser-driven atomic system due to multi-photon bound-bound transitions. Because laser interactions with atoms and ions are dominated by the multi-photon dynamics, the emitted radiation from such interactions exhibits the main characteristics of multi-photon transitions. In the non-relativistic regime, this kind of radiation has been extensively studied [304]. Relativistic laser–ion interactions have recently been investigated, for moderately intense laser fields of $\sim 10^{16}$–10^{18} W/cm^2 [252–255]. X-rays can be emitted via resonant multi-photon transitions in such relativistic laser–ion interactions.

In Refs. [254,255] the weakly relativistic Schrödinger equation was numerically solved for multiply-charged ions exposed to intense laser pulses. The radiation spectra were explored for different laser intensities. Under the circumstance that the laser's action on the motion of the ground-state electron is less dominant with respect to the Coulomb force of the ionic core, the ground-state population can be partially transferred to the excited states via the so-called multi-photon resonance [253,255]. This is because the super-strong laser field can easily (ac-/dc-Stark) shift the loosely-bound excited states, although it is still a perturbation to the strongly-bound ground state. Once the energy gap between the excited states and the ground state is shifted to be equal to an integer multiple of the laser photon energy, the multi-photon resonance occurs, thereby excited states become populated. While those populated excited states are still under the laser-suppressed potential barrier, radiation may be emitted via transitions from temporally populated excited states back to the ground state. A schematic diagram shows the resonance mechanism in Fig. 42.

Thus, X-rays having specific energies can be generated in such interactions. Fig. 43 shows the radiation spectra from a model ion of O^{7+} interacting with 248 nm laser pulses having different intensities: (a) 10^{17} W/cm^2, (b) 5×10^{17} W/cm^2, and (c) 10^{18} W/cm^2. For the lowest intensity, we observe the radiation of multi-photon resonance between the first excited state $|1e\rangle$ and the ground state $|g\rangle$. The X-ray frequency is about $\sim 110\,\omega$, corresponding to the field-free energy gap between $|1e\rangle$ and $|g\rangle$. Besides this, there also exist other radiations from the second excited state to both the ground

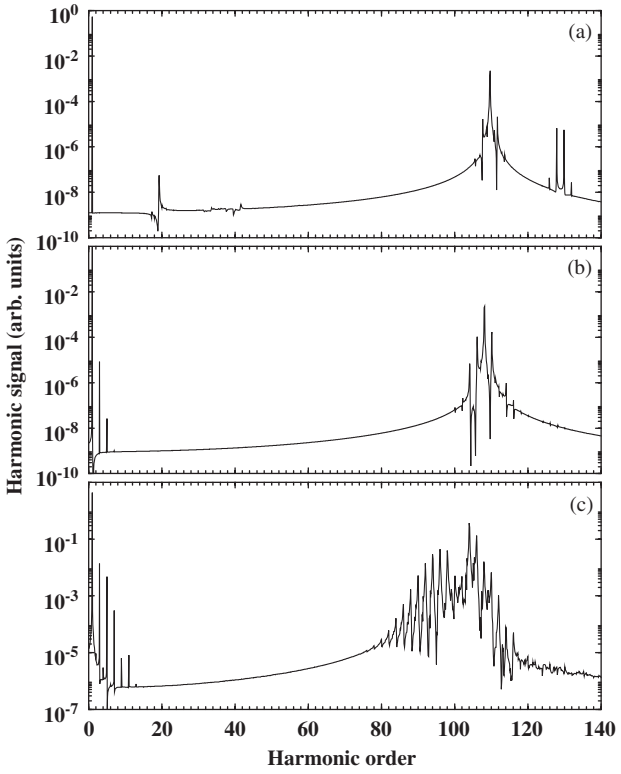

Fig. 43. The radiation spectra for a model ion of O^{7+} exposed to intense laser pulses. The laser wavelength is 248 nm and the intensities are: (a) $10^{17}\,\mathrm{W/cm^2}$; (b) $5\times10^{17}\,\mathrm{W/cm^2}$; and (c) $10^{18}\,\mathrm{W/cm^2}$. The laser pulse has a shape of a trapezoid with five-cycle turn-on and a flat section of ten cycles [255]. Reprinted with permission from [255]; Copyright 2002 by the IOP Publishing Limited.

state (at about $\sim 129.9\,\omega$) and the first excited state (at about $19.3\,\omega$). With increasing intensity, the excited–state $\rightarrow$ ground–state resonance moves to lower energy. At the same time, the effect of the second excited-state is no longer visible, since for higher intensities this state is above the classical barrier and ionizes very rapidly. Also, it is remarkable that the lowest intensity is not yet capable of producing any low-order harmonics, owing to the electron being so strongly bound.

By comparing the weakly relativistic calculations with the case of using the non-relativistic Schrödinger equation, we could explore the relativistic effects in X-ray generation via the multi-photon resonance. Specifically, it is of interest to know what happens to the radiation spectrum with and without the relativistic mass-shift term $-(\mathbf{p}+\mathbf{A}(z,t))^4/8c^2$. The result is plotted in Fig. 44. It shows that with the relativistic correction to the electron kinetic energy, a red-shift occurs to the multi-photon resonance radiation. A relativistic Stark shift has been introduced, in addition to the non-relativistic Stark shift for excited states in a super-strong laser field.

Furthermore, Casu and Keitel have recently extended the study of resonant multi-photon radiation by considering the extremely super-strong ($\sim 10^{22}\,\mathrm{W/cm^2}$) laser interactions with highly-charged ions such as Xe^{53+} and U^{91+} [253]. They found similar shifts to the radiation lines.

6.2. Tunneling and re-collision harmonics

Conventional tunneling and re-collision harmonic emission is explained by the so-called *three-step model* [79,305,306]. According to this model, under the laser field action the electron first tunnels through the potential barrier, and is then accelerated by the laser field in the continuum. Finally, when the laser field flips its sign, the electron is brought back to its parent ion and recombines to an atomic ground state, thereby emitting a high-energy photon. Typically, a spectrum of high-order harmonic generation exhibits a drop-off stage of low-order harmonics, and a plateau

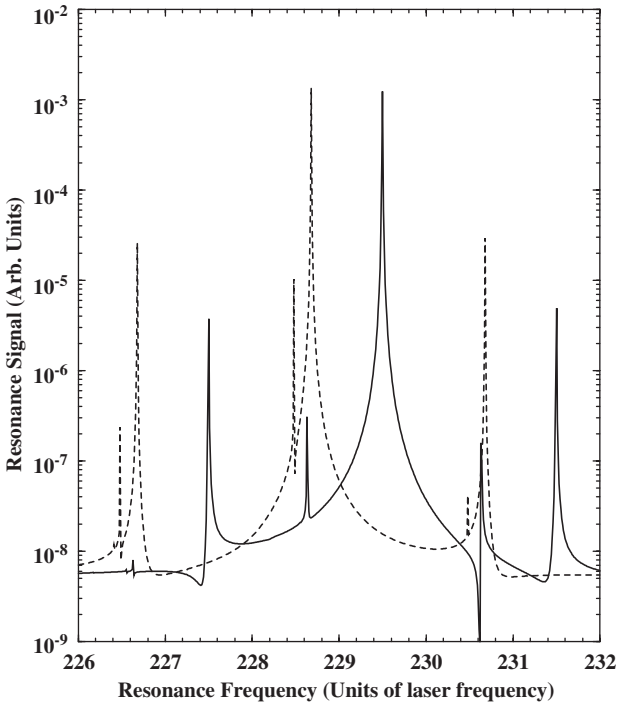

Fig. 44. The segment of the multi-photon spectrum from $Z = 12$ model ions which are exposed to an intense laser pulse of intensity 7×10^{16} W/cm^2 and the laser wavelength 527 nm. The laser pulse has a 5.25-cycle turn-on, followed by a 100-cycle period with constant amplitude. The segment shows the transition between the bound states $|4e\rangle \leftrightarrow |g\rangle$. The solid and dotted lines represent the cases without and with the leading relativistic correction, respectively. A large redshift of 0.82ω for this resonant transition is visible when the leading relativistic correction is taken into account. It can be attributed to the relativistic Stark shift of the energy levels of the ion [254]. Reprinted with permission from [254]; Copyright 2001 by the American Physical Society.

in which the overall harmonic amplitude is not changed very much, followed by a sharp cutoff. Since HHG was thought of as one of a number of competitive ways to produce coherent short-wavelength radiation [307,308] and attosecond pulses [8,41,309], it has been extensively explored both experimentally and theoretically. According to the *three-step model*, the maximum harmonic photon energy in the non-relativistic case is given by

$$\hbar\omega_{\max} = I_{\mathrm{p}} + 3.17U_{\mathrm{p}}, \tag{89}$$

in terms of the ionization potential I_{p} of the target and the ponderomotive energy $U_{\mathrm{p}}(\mathrm{eV}) \sim 9.33 \times 10^{-14} \times I\,(\mathrm{W/cm^2}) \times \lambda^2(\mu\mathrm{m})$ of a free electron in the driving laser field (see the definition of U_{p} in the beginning of Section 5.1). One goal of HHG studies is to generate the shortest wavelength coherent soft or even hard X-rays. Apparently, from the harmonic cutoff law given by Eq. (89) one needs both a high-I_{p} target and a higher intensity laser field (i.e., a larger U_{p}) for the generation of high-energy radiation. Multiply/highly-charged ions have higher ionization potentials than neutral atomic targets, so they can sustain super-strong laser pulses. Therefore, for extending HHG to the short-wavelength regimes, ions have recently been proposed and studied in detail [105–107,252,254,310–313]. In addition to that, the relativistic effects may be investigated in the study of harmonic generation from super-strong laser–ion interactions [103,104,314,315].

Let us see what kind of relationship between the laser intensity parameter q and the charge Z of a hydrogen-like ion should exist in order to have substantial HHG in the tunneling-recollision regime. First of all, the laser intensity must be large enough to operate in the tunneling regime ($\gamma < 1$), i.e., one must have

$$q > \sqrt{\frac{2I_{\mathrm{p}}}{mc^2}}, \tag{90}$$

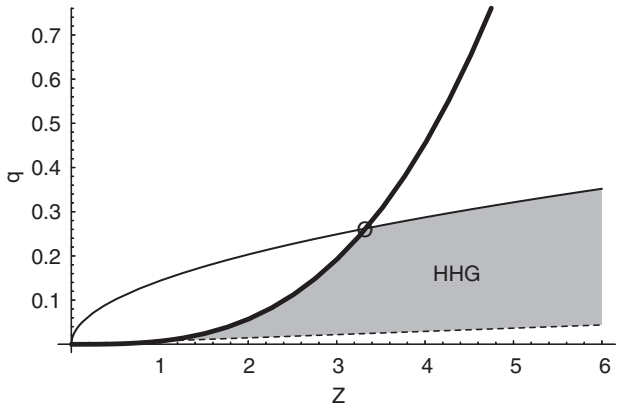

Fig. 45. The region of parameters q and Z where substantial HHG is possible using a hydrogen-like ion. The region above the dashed curve corresponds to the condition of Eq. (90), below the thick curve to the condition of Eq. (91), and below the thin curve to the condition of Eq. (92). Therefore, tunneling harmonics from a hydrogen-like ion will be generated in principle for those values of q and Z that belong to the shaded region. The HHG intensity is maximal near the thick curve. However, it is significantly damped away from this thick curve, i.e., with increasing Z. The maximal laser intensity when optimal HHG (i.e. in the region close to the OBI regime) is still possible, corresponds to the point marked by O.

where $I_p = mc^2(1-\sqrt{1-\alpha^2Z^2})$ is the ionization potential of the hydrogen-like ion and α is the fine structure constant. Then, the laser intensity must not be so large as to sweep the atomic electron over the barrier [316], which requires that

$$q < \frac{\lambda}{8\pi r_0 Z}\left(\frac{I_p}{mc^2}\right)^2, \tag{91}$$

where λ is the laser wavelength and r_0 is the classical radius of the electron. Finally, the relativistic drift of the ionized electron in the laser propagation direction ought to be negligible [104], demanding that

$$q < 2\left(\frac{I_p}{mc^2}\right)^{1/4}. \tag{92}$$

The range of parameter values allowed by q and Z that fulfil the conditions given by Eqs. (90)–(92) is shown in Fig. 45. HHG takes place for those values of q and Z that belong to the region indicated by grey shading in the figure (not too far from the thick curve). HHG will be optimal if the parameters are close to the over-the-barrier ionization (OBI) regime, i.e., close to the thick curve in Fig. 45; otherwise the tunneling probability becomes exponentially small. Therefore, we see that employing very highly charged ions for HHG is not optimal because at high Z the region of HHG is far from the thick curve. In other words, at high Z, when the laser intensity is so high that conditions are close to the OBI regime, the relativistic drift becomes very important and it damps HHG. The maximal laser intensity when optimal HHG is still possible via a hydrogen-like ion, corresponds to the point indicated in Fig. 45 by "O". Thus, for laser intensities up to the weakly relativistic regime ($q < 0.3$) the tunneling-recollision harmonic emission is possible using not so highly charged hydrogen-like ions ($Z < 4$).

Fast moving relativistic ions can be employed to increase the re-collision probability of the ionized electron and, therefore, the HHG yield in the relativistically-strong field of a counter-propagating laser pulse [317]. In the latter a new fast re-collision regime has been found (see Section 7.3.3). An analogous setup has been used in [107] where the increase of the re-collision probability is due to the decrease of the electron relativistic drift in the laser propagation direction, in the rest system of reference of the ion. This is because in that system of reference the ionized electron sees the laser radiation blue-shifted.

By solving the time-dependent Schrödinger equation for a model ion (such as He^+ or Li^{2+}), Casu et al. investigated HHG from ions interacting with an intense laser pulse [310]. They found that a small part of the electron wavepacket can still tunnel through the high Coulomb barrier for a sufficiently intense laser field (of intensity $10^{15}\,W/cm^2$ and higher). The numerical results showed that the periodic re-collisions of the tunneled wavepacket on the parent ion give rise to coherent X-ray radiation in the multiple keV regime. Similar model ions have also been studied by Potvliege and co-workers [312] employing few-cycle laser pulses. In particular, they investigated the magnetic and non-dipole effects

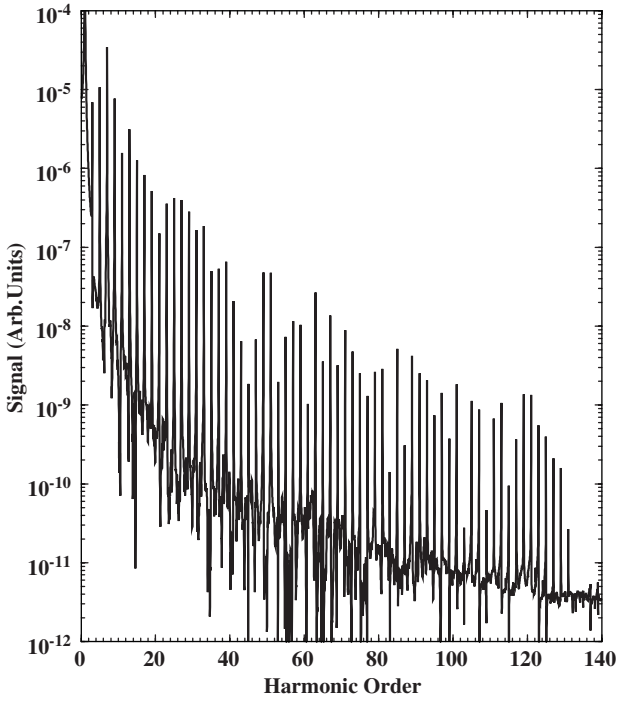

Fig. 46. The harmonic spectrum emitted from $Z = 3$ ions, with parameters $k = 6.48$ and $q_e = 1$ characterizing the potential (soft-core Coulomb). The laser intensity is $2.5 \times 10^{16}\,\mathrm{W/cm^2}$, and the KrF laser wavelength with 248 nm is applied. The laser pulse has a linear 10-cycle turn-on and is followed by a 10-cycle duration with constant amplitude. The 131st harmonic is visible in the cutoff frequency. For these laser parameters considered, the usual plateau range $3.17U_\mathrm{p}$ is equal to $\sim$ 32.8 keV [254]. Reprinted with permission from [254]; Copyright 2001 by the American Physical Society.

on HHG [105]. Their results indicated the existence of even-order harmonics polarized along the laser propagation direction, besides the dominant ones polarized along the polarization direction of the driving laser field. This was also seen in Ref. [255], and attributed to the magnetic dipole and quadrupole moments. Within the strong field approximation, the same topic has also been investigated beyond the dipole approximation [104,106,313,315]. As an example, HHG from Li^{2+} ions driven by a 248 nm laser is shown in Fig. 46. The laser intensity is equal to $2.5 \times 10^{16}\,\mathrm{W/cm^2}$. The laser pulse has a ten-cycle linear turn-on followed by a ten-cycle flat amplitude. It was shown that the highest (131st) harmonic is produced, which corresponds to an X-ray photon energy of 655 eV, far into the useful *water window* regime.

With a more intense laser pulse ($10^{17}\,\mathrm{W/cm^2}$) and a slightly higher charged ion, Be^{3+} (soft-core parameter $k = 10.7$ and $q_e = 1$), one could reach the coherent keV regime of HHG shown in Fig. 47. Evidently seen in the insert of Fig. 47 is the 427th harmonic, observable in spite of the low efficiency of 10^{-13}.

The relativistic effects on high-order harmonic generation have been elucidated in a number of recent studies [103,104,314,315]. Within the context of the strong-field approximation, the relativistic transition matrix element for emission of harmonics may be analytically written down as [103,314]

$$M_\mathrm{HHG} \simeq -\mathrm{i}\int \mathrm{d}^4x\,\mathrm{d}^4x'\Phi^*(x)V_\mathrm{H}G_L^{(+)}(x,x')V_\mathrm{L}\Phi(x'), \tag{93}$$

where $\Phi(x)$ is a solution to the Klein–Gordon equation in the presence of the binding potential only. It can be approximated by the non-relativistic wavefunction of the atomic ground state. V_L and V_H are the operators of the electron-interaction with the laser field and the harmonic field, respectively. In the velocity gauge, these may be written as

$$V_\mathrm{L} = 2\mathrm{i}e\mathbf{A}_L\cdot\boldsymbol{\nabla} + e^2\mathbf{A}_L^2, \tag{94}$$

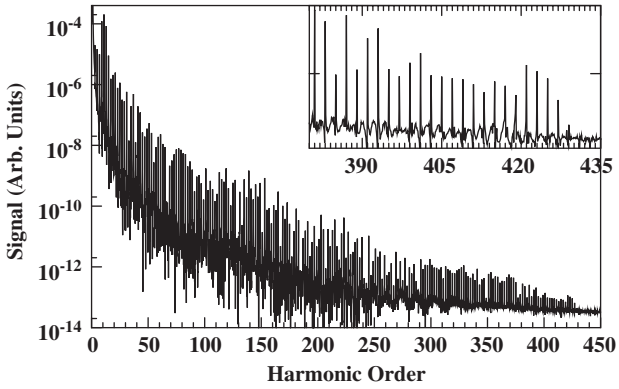

Fig. 47. The harmonic spectrum from intense laser-driven Be^{3+} (soft-core parameter $k = 10.7$ and $q_e = 1$) in a laser pulse of intensity 10^{17} W/cm^2 ions [254]. Reprinted with permission from [254]; Copyright 2001 by the American Physical Society.

and

$$V_{\rm H} = 2e\mathbf{A}_{\rm H} \cdot (\mathrm{i}\boldsymbol{\nabla} + e\mathbf{A}_L), \tag{95}$$

where $\mathbf{A}_L$ is the vector potential of the laser field. As in the treatment of the non-relativistic case, the full Green's function is approximated by the Klein–Gordon positive-energy Volkov propagator

$$G_L^{(+)}(x, x') = -\mathrm{i}\theta(t - t') \int \frac{\mathrm{d}^3 p}{2E_{\rm p} V} \exp\left\{-\mathrm{i}p \cdot (x - x') - \mathrm{i}\int_{u'}^{u} \frac{\mathrm{d}u''}{2k \cdot p}\left[2ep \cdot A_L(u'') - e^2 A_L^2(u'')\right]\right\}, \tag{96}$$

with $u = k \cdot x = \omega t - \mathbf{k} \cdot \mathbf{r}$, $p \cdot x = E_{\rm p} t - \mathbf{p} \cdot \mathbf{r}$, $k \cdot p = \omega E_{\rm p} - \mathbf{k} \cdot \mathbf{p}$, $E_{\rm p} = \sqrt{p^2 + m^2}$ and $\theta(t - t')$ is a step function. In fact, Eqs. (93) and (96) constitute the relativistic analog of the Lewenstein model [306]. A numerical example is shown in Fig. 48, which compares the harmonic emission rates as functions of the harmonic order for non-relativistic (blue) and relativistic (black) calculations.

From Fig. 48 one sees that, with increasing intensity, the relativistic effects become more important. This is evident in the following observations: (1) the wild fluctuations in the emission rates that span several orders of magnitude in the non-relativistic calculation are absent in the relativistic case. The spectrum turns out to be very smooth, with the exception of tiny frequency ranges preceding the various cutoffs; (2) the essentially flat non-relativistic plateau assumes a convex shape with a pronounced decrease towards high harmonic orders; (3) the multi-plateau structure appearing in the non-relativistic case is no longer identifiable; (4) the shift of the highest cutoff position to lower values of the harmonic order becomes visible; and (5) the relativistic harmonic yields are much lower than is suggested by the non-relativistic calculation, due to the laser magnetic field.

Although employing multiply-charged ions and higher-intensity lasers in the theoretical calculations leads to the conclusion that the cutoffs of relativistic HHG can be easily extended to the keV energy regime [254,310], or even to the sub-Angstrom hard X-rays [252], experimental production of such ultra-high harmonics is extremely challenging, because of the low density of the charged medium due to Coulomb repulsion. On the experimental side, one needs both high $I_{\rm p}$ targets and a high enough target density to produce measurable keV harmonic radiation. To fulfil this practical requirement, a proposal of using high Rydberg atoms as targets for keV-HHG has recently been made [318]. The idea is to exploit the stabilization effect of a high Rydberg atom in an intense laser field. In other words, one may apply an intense laser pulse to essentially drive the inner electron (having high $I_{\rm P}$) to emit keV-energy harmonics, while leaving the outer Rydberg electron stabilized. Interaction of neutral Rydberg gases exposed to an intense laser pulse proceed virtually like laser–ion interactions, while Rydberg gases can have a much higher density (10^{16}–10^{17}/cm^3 for $n = 10$ alklai Rydberg gases). Numerical simulations have demonstrated that keV harmonic generation with practical efficiency is possible with Rydberg lithium atoms ($n \sim 10$) [318].

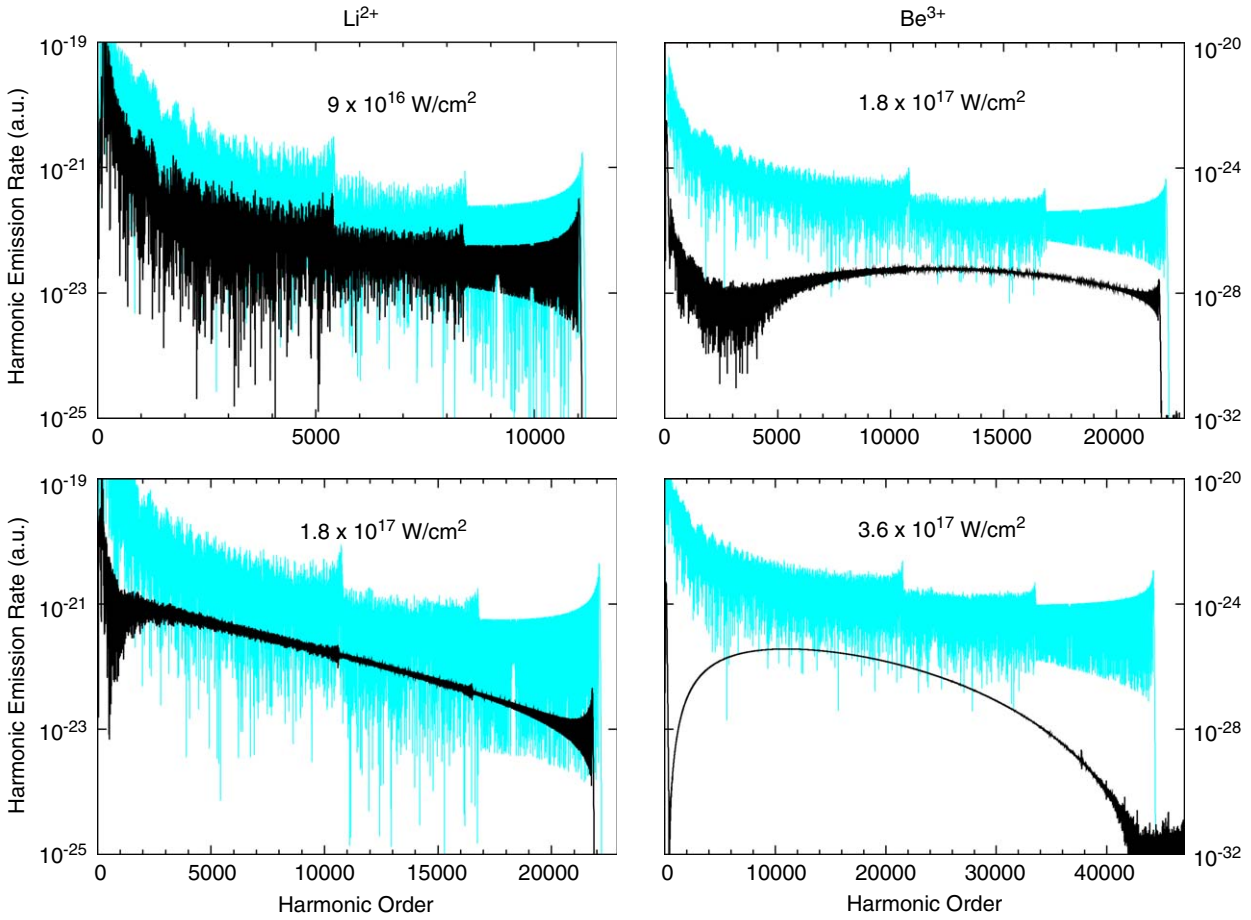

Fig. 48. Harmonic emission rates as functions of the harmonic order for Li^{2+} ($I_P = 122.45$ eV) and Be^{3+} ($I_P = 217.72$ eV) ions, exposed to a Ti:sapphire laser (800 nm) with the intensities given in each panel. The blue curves indicate the non-relativistic calculation for comparison, while the black curves represent the applicable relativistic results [314]. Reprinted with permission from [314]; Copyright 2002 by the Springer Science and Business Media.

6.3. Non-tunneling harmonics

In addition to the conventional tunneling and re-collision harmonics and the resonant multi-photon radiation, another mechanism of harmonic generation exists that is governed by the inner-atomic dynamics. Generally, the so-called *non-tunneling harmonics* result from intense laser interactions with multiply-charged ions. These interactions have been systematically investigated in [255,319]. In these references, hydrogen-like ions, such as N^{6+} and O^{7+}, were considered as targets exposed to ultra-intense fields, with intensities in the range of 10^{18} W/cm^2, so that if an electron were to move only under the influence of the laser field, it would obey relativistic kinematics. The pertinent ionization potentials easily reach hundreds of electron volts. As a consequence, the *low-energy* part of the harmonic spectrum defined by harmonic orders below I_p/ω, which for neutral atoms only includes a few harmonics, may now extend over hundreds of harmonics. For neutral atoms, this part is too short to develop any evident structure. For multiply- or highly-charged ions, this low-energy part of the HHG spectrum is extensive and exhibits its own characteristic structure.

In this case the HHG will be quite different from the standard situation, for several reasons. First, tunneling will play a lesser role because the tunneling rate decreases exponentially with Z^3 (Z is the charge of the ionic core) [320]. Second, any electron that does nevertheless tunnel out will be driven away from the ionic core by the Lorentz force via the magnetic-field component of the applied laser field (see Eqs. (90)–(92)). Third, for tightly bound systems some intermediate states remain bound when exposed to ultra-intense laser fields, and may play an important role in HHG.

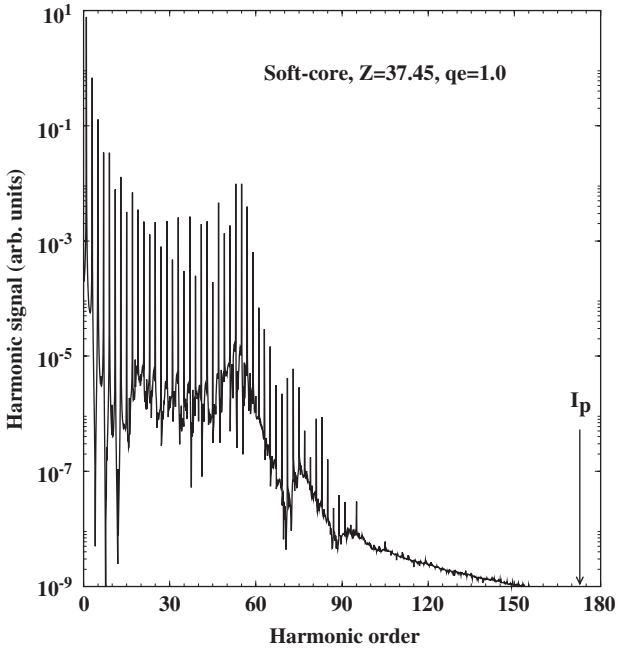

Fig. 49. The spectrum of the "non-tunneling harmonics" for an electron in the soft-core model potential ($V(x,z) = -k/\sqrt{q_e + x^2 + z^2}$), with $k = 37.45$ and $q_e = 1$, exposed to a laser with an intensity of $1.9 \times 10^{18}\,\mathrm{W/cm^2}$ ($q = 0.29$) and a wavelength $\lambda = 248\,\mathrm{nm}$. The arrow at the lower right marks the harmonic order having an energy equal to the ionization potential, $I_\mathrm{p} = 870.72\,\mathrm{eV}$, corresponding to that of hydrogen-like ion of O^{7+} [255]. Reprinted with permission from [255]; Copyright 2002 by the IOP Publishing Limited.

All three factors combine to reduce the role of the tunneling and re-combination mechanism for the case of multiply- and highly-charged ion targets in the low energy part of the HHG spectrum. By numerically solving the weakly relativistic, two-dimensional, time-dependent Schrödinger equation, Hu et al. investigated the plateau feature of the non-tunneling harmonic spectrum, and the effect of the shape of the binding potential on the non-tunneling harmonics [255,319].

6.3.1. Plateau and surfing mechanism of non-tunneling harmonics

First, we consider an active electron moving in the following soft-core potential, $V(x,z) = -k/\sqrt{q_e + x^2 + z^2}$, with a large smoothing parameter, that is, $k = 37.45$ and $q_e = 1$. It is exposed to a laser pulse with an intensity of $1.9 \times 10^{18}\,\mathrm{W/cm^2}$ and a wavelength $\lambda = 248\,\mathrm{nm}$. In Fig. 49, we present the corresponding harmonic spectrum. The harmonic order $I_\mathrm{p}/\omega = 174$ is marked by an arrow in the lower right of the figure. The plateau of Fig. 49 has basically the appearance of a common tunneling and re-combination plateau. It consists entirely of odd harmonics and has a well defined cutoff at about $n = 59$. Its physical origin, however, is completely different. If the extent of the spatial grid used in the numerical solution of the Schrödinger equation is reduced to about ten atomic units, the harmonics displayed in Fig. 49 hardly change. This proves that they cannot be due to the standard mechanism where the electron (having tunneled out of the atom) performs an excursion of about $\alpha = E/\omega^2$ (calculated here non-relativistically), whose value under our conditions is about 500 au. Hence, the origin of these harmonics is to be sought in the inner atomic dynamics. It has been suggested that they are produced when a laser-driven *bound* electronic wave packet sweeps over the center of the binding potential.

In Fig. 50, we plot the expectation value $\langle x \rangle$ of the electronic wave packet, obtained by using such a small box that the contribution from the tunneling part of the wave packet is excluded. The large-scale sinusoidal structure of $\langle x \rangle$ reflects the motion of the minimum of the effective binding potential,

$$V_\mathrm{eff}(x,t) = V(x,0) + xE(t), \tag{97}$$

as a function of the laser field. The little wiggles visible in Fig. 50 at those times when $\langle x \rangle$ goes through zero are related to the emission of the non-tunneling harmonics (see below). A very crude time-frequency analysis can be performed

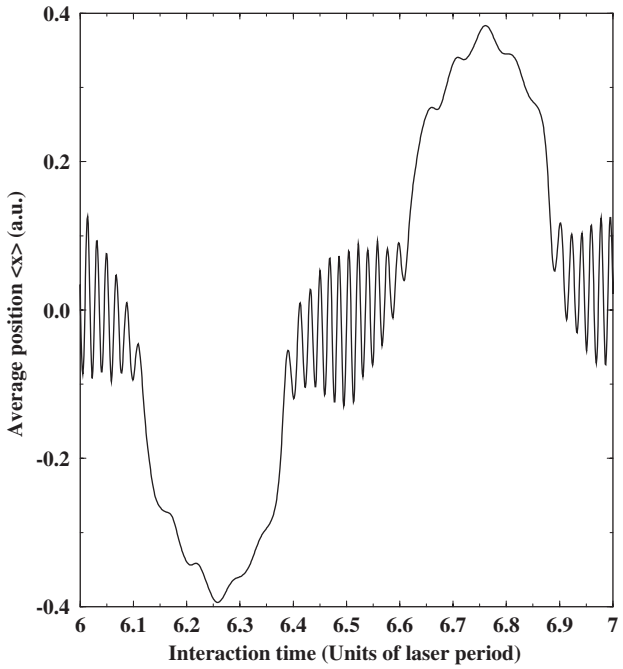

Fig. 50. The average position $\langle x\rangle$ of the bound electronic wave packet along the laser-polarization direction (x axis) as a function of the interaction time. The driving electric field is sinusoidal in time. The parameters are the same as in Fig. 49, but the calculation is for a small box in order to eliminate the effect of the ionized part of the wave function [255]. Reprinted with permission from [255]; Copyright 2002 by the IOP Publishing Limited.

by visual inspection of Fig. 50, determining the frequency by counting the number of small wiggles within the time interval $6.4T \sim 6.6T$, where T is the laser period. This yields a harmonic order of about 60, which agrees very well with the cutoff position of Fig. 49.

Fig. 51 displays the outcome, for selected harmonics, of a time-frequency analysis [159,321] of the electron acceleration $a_x(t) = \langle \ddot{x}(t)\rangle$ according to

$$a_x(t,\omega) = \int \mathrm{d}t' a_x(t') \mathrm{e}^{-\mathrm{i}\omega t'} \exp\left[-\frac{(t-t')^2}{\Delta t}\right], \tag{98}$$

with a time window of $\Delta t = 0.05T$, where T is the laser period and $\langle \ddot{x}(t)\rangle$ is the expectation value of the acceleration operator for the time-dependent wave packet. It shows that the harmonics within the plateau (H53 and H61) are emitted at two times during one optical cycle, around those times when the electric field goes through zero (note that the applied field is proportional to $\sin \omega t$, since $z \simeq 0$). Remarkably, for H61 we observe two peaks near each of those times, which is reminiscent of the emission times of the long and the short trajectories of the Lewenstein model [306]. In contrast, the harmonic H29, at the low end of the plateau, is emitted at times when the field is definitely nonzero.

The non-tunneling harmonics are amenable to a classical model description [319]. The effective potential (97) has a saddle point $x_s(t)$ obtained from $\partial V_{\mathrm{eff}}(x,t)/\partial x|_{x_s} = 0$. This is a saddle point in two dimensions. The classical modeling was restricted to one dimension (x, which is the polarization direction of the laser field). Then, for the one-dimensional effective potential (97), the saddle point is a maximum as a function of x. Classically, electrons released with zero velocity inside of this saddle point will tumble into the minimum of the effective potential, while those set free outside will move away from it. When the field decreases from its maximum to zero, the saddle point moves outward, and eventually goes to infinity. Fig. 52 displays the position and the total-energy gain $\Delta\mathscr{E}_{\mathrm{tot}}(t) = \mathscr{E}_{\mathrm{tot}}(t) - \mathscr{E}_{\mathrm{tot}}(t_0)$, where $\mathscr{E}_{\mathrm{tot}}(t) = V_{\mathrm{eff}}(x(t),t) + v_x(t)^2/2$ for an electron set free with zero velocity at the time $\omega t_0 = \pi/2$, at a position just outside the saddle point $x_s(t)$ when the electric field $E(t) = E_0 \sin \omega t$ of the laser is at its maximum. The precise value of the starting position was chosen as the maximal position that does not lead to immediate ionization. As the field

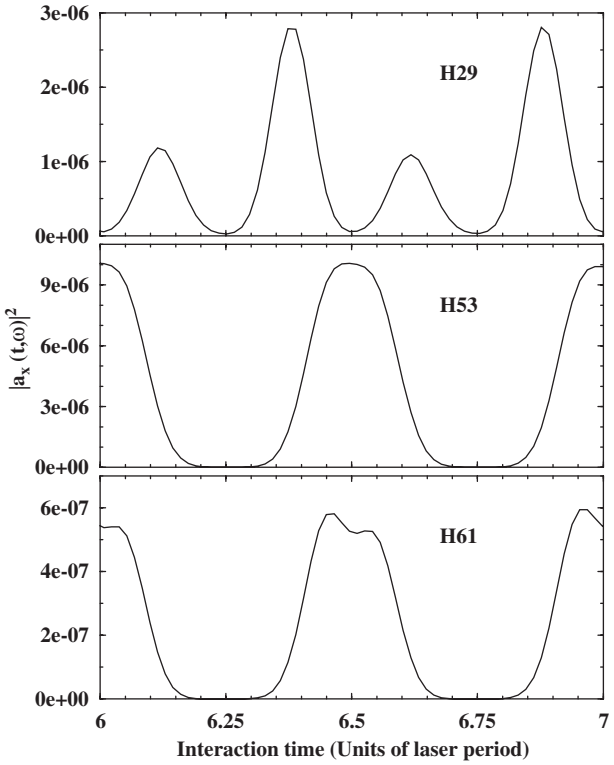

Fig. 51. Plot of the absolute square of the electron acceleration $a_x(t, \omega)$ (cf. Eq. (13) in [255]) vs. t for $6 \leq t \leq 7$ in units of the laser period T. The harmonic signal is proportional to the time-integration of $|a_x(t, \omega)|^2$. Results are shown for three of the harmonics: the 29th (upper panel), 53rd (middle panel) and 61st (lower panel) [255]. Reprinted with permission from [255]; Copyright 2002 by the IOP Publishing Limited.

strength decreases with time, the saddle point slowly moves outward and the electron moves with it, owing to the small outward-directed gradient of the effective potential. While the electron is in motion, riding on the saddle just outside of its maximum, it gains energy from the laser field as the effective potential increases. As the field decreases further, the outward motion of the saddle point accelerates while the net outward force on the electron decreases. At some point in time (to be denoted by t_1 which is $\approx 0.42\,T$ in the figure), the electron cannot keep up anymore and is drawn into the attractive region of the effective potential, where it oscillates back and forth a few times before it escapes from the binding potential when the field increases into its next half cycle. All of this is summarized in Fig. 53. Near the saddle point, the electron's energy gain is about $\Delta\mathscr{E}_{\rm tot} \approx V_{\rm eff}(x_{\rm s}(t_1)) - V_{\rm eff}(x_{\rm s}(t_0))$. This is the dominant part of its energy gain, but an additional smaller part is added during its ensuing oscillatory motion. Fig. 52(b) shows that this mechanism is able to explain the cutoff predicted by the quantum-mechanical calculation underlying Fig. 49.

The classical mechanism described above is the same as that by which a surfer first gains potential energy and then converts it into kinetic energy. Here, the electron surfs on the time-dependent effective potential (97).

A cutoff law of the form xE is reminiscent of the low-energy cutoff (in addition to the standard tunneling and re-collision cutoff) observed in calculations of harmonic generation in a diatomic molecule having a pair of charge-resonant states [322]. In the latter case, the electron gains energy by traveling the distance Δx from one atom to the other while the laser field is essentially constant. In the present case, the electron rides up in energy when the laser field decreases by ΔE while it essentially maintains its position x in space.

When the soft-core parameters k and q_e are decreased, the spectral features of harmonic emission change dramatically. In the upper panel of Fig. 54, we plot the harmonic spectrum for $k = 15.32$ and $q_e = 0.1$. The plateau of the non-tunneling harmonics is no longer the dominant feature of the spectrum. Rather, we observe a continuous decrease over six orders of magnitude from the lowest harmonics up to harmonic orders around 30. This part of the spectrum consists exclusively of odd harmonics of the laser frequency. There follows a resonance-like hump centered at an order just below 60.

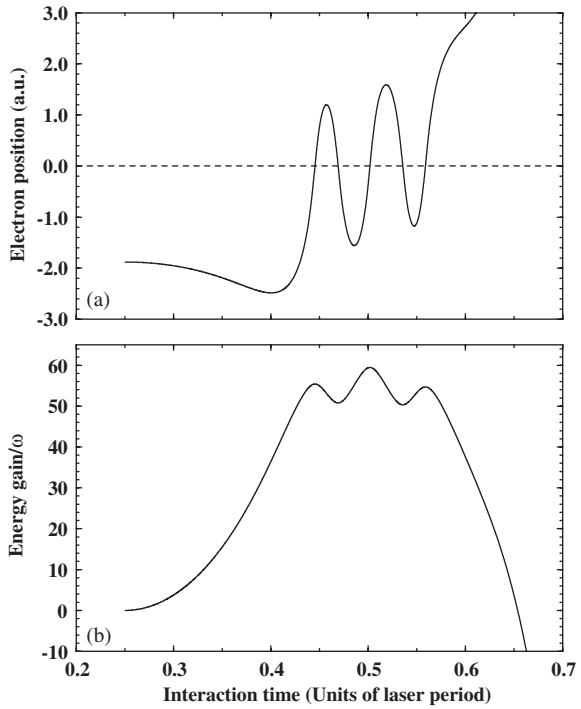

Fig. 52. Position (a) and total energy gain (b) of a classical electron as a function of time for the conditions of Fig. 49 with initial conditions as described in the text: namely, the electron starts just outside of the saddle point of the effective potential (97) at a time when the field is maximal [255]. Reprinted with permission from [255]; Copyright 2002 by the IOP Publishing Limited.

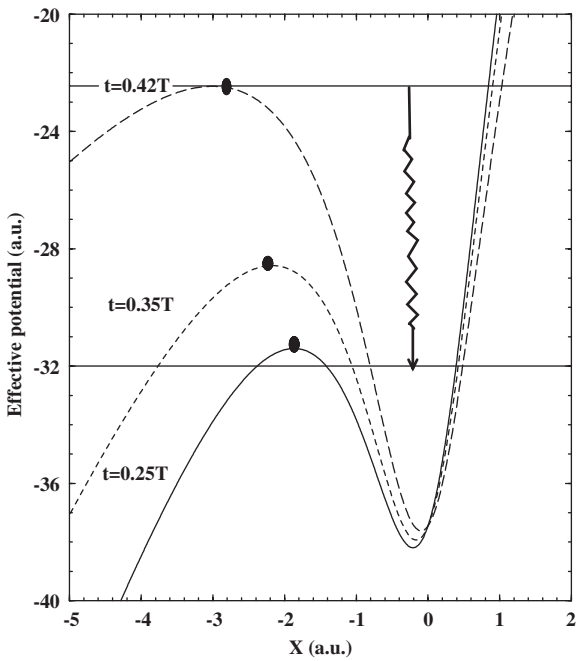

Fig. 53. Illustration of the surfing mechanism described in the text. The effective potential (97) is plotted for the parameters of Fig. 49 at three different times. The time $t = 0.25T$ corresponds to the maximum of the field. The solid dots represent the positions as a function of time of an electron that is released with zero velocity just outside of the effective potential saddle at the time $t = 0.25T$, whose orbit is depicted in Fig. 52. Notice how from $t = 0.25T = t_0$ to $t = 0.42T = t_1$ the electron moves from just outside to just inside the saddle point [255]. Reprinted with permission from [255]; Copyright 2002 by the IOP Publishing Limited.

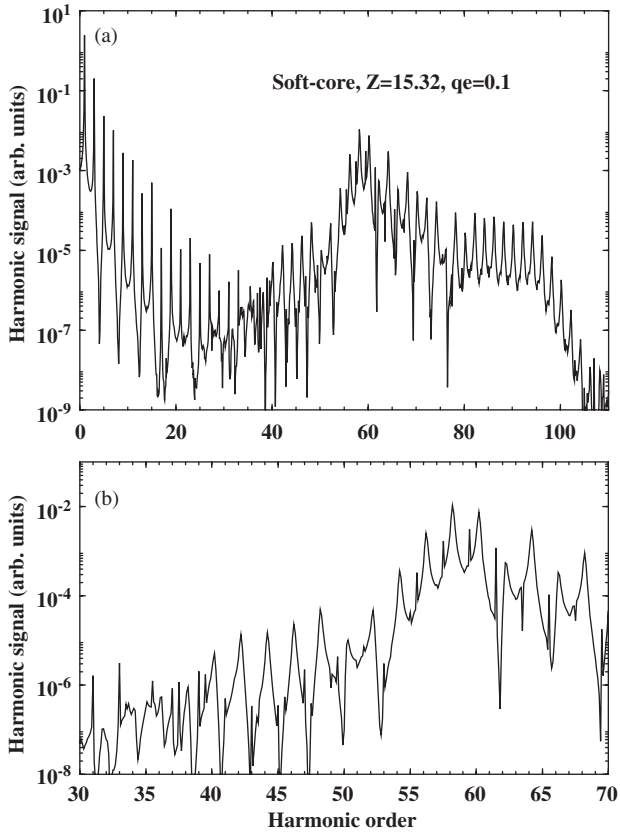

Fig. 54. Harmonic spectrum for the soft-core potential with $k = 15.32$ and $q_e = 0.1$. The lower panel shows a blow-up of the central part of the spectrum. It illuminates the transition from the purely odd harmonics of the low-energy part of the spectrum to the two series of harmonics characteristic of the upper part. The laser parameters are same as those of Fig. 49 [255]. Reprinted with permission from [255]; Copyright 2002 by the IOP Publishing Limited.

Note that, in the absence of the laser field, the energy separation between the ground state and the first excited state of the soft-core potential corresponds to about the 62nd harmonic, while the resonance-like hump shown in Fig. 54 has its maximum just below the order of 60. Above the order of 40, the odd harmonics have all but disappeared. In their place, two series of harmonics appear: one having broad spikes at energies approximately equal to $(2n + 0.2)\omega$, the other having very narrow spikes at about $(2n - 0.5)\omega$ that are less intense by one to two orders of magnitude. The lower panel of Fig. 54 displays an enlargement of the central part of the spectrum, which illustrates these statements. Starting at $n \approx 80$, a new plateau appears which extends up to a very pronounced cutoff at $n = 95$. This latter plateau consists almost entirely of the first series of broad spikes mentioned above.

The additional plateau above the hump, at harmonic orders between 75 and 95, is due to the classical *surfing* mechanism discussed in the preceding subsection. The energy of the saddle point of the effective potential for maximal field is now $V_{\text{eff}} = -21$ a.u., which is very close to the energy of the first excited field-free state, -20.4 a.u. Hence, an electron promoted into this excited state has an excellent chance of experiencing the energy-gain mechanism described above, the only difference being that now it starts from the excited state. Its maximal energy gain is about 35 a.u. Hence, assuming it makes a radiative transition back to the ground state, we obtain a cutoff near $n = 95$, in good agreement with the spectrum of Fig. 54.

6.3.2. High efficiency of non-tunneling harmonics

The high efficiency of non-tunneling harmonics is due to the fact that they are generated by the field-induced motion of that part of the electronic wave packet that stays inside the range of the binding potential. This is by far the dominant

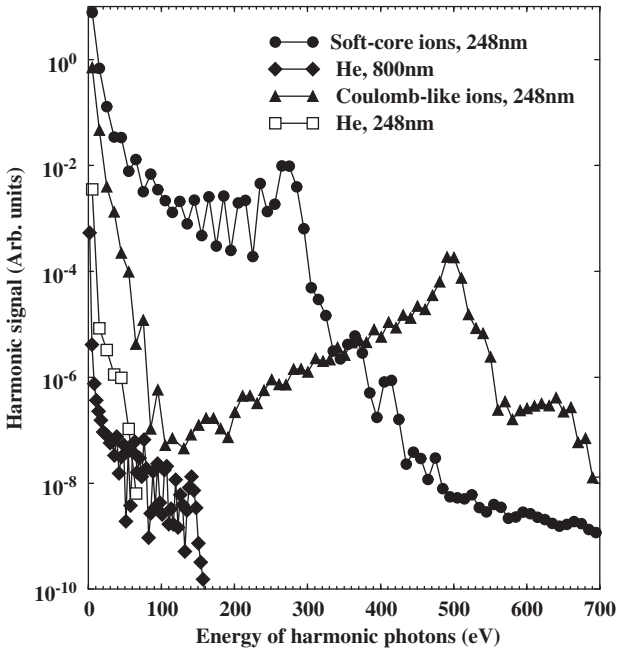

Fig. 55. Comparison of the harmonic spectrum of Fig. 49 (filled circles) to a standard (tunneling-recombination) harmonic spectrum in neutral helium for the same wavelength $\lambda = 248$ nm (open squares) as well as for the longer wavelength of 800 nm (filled diamonds), the latter two at intensities near saturation, 10^{15} W/cm^2 and 6×10^{14} W/cm^2, respectively. All spectra have been obtained by running the same code and are plotted on the same scale [255]. Reprinted with permission from [255]; Copyright 2002 by the IOP Publishing Limited.

part, as opposed to the continuum part that has tunneled out and is responsible for the standard tunneling and recombination harmonics [78,79,305,306]. In Fig. 55, we compare the intensities of the standard harmonics generated by a neutral atom and the non-tunneling harmonics generated by a highly charged ion, with each exposed to an ultra-intense field having an intensity close to that leading to saturation. In the figure, the results for the soft-core potential with $q_e = 1$ and $k = 37.45$ (Fig. 49) are reproduced. Reproduced are also the results for the Coulomb-like potential with $q_e = 0.0098$ and $k = 8$ (with both potentials having the same binding energy, which equals that of O^{7+}). These are compared to harmonic spectra calculated for helium near the saturation intensity. The plot was obtained by running the same code for all cases. The figure shows that the non-tunneling harmonics are radiated with an intensity that is higher by about four orders of magnitude for the low orders (and, of course, more than that once the harmonic order is above the cutoff in the atomic case). This very substantial harmonic yield may leave hope for an experimental observation, even though the density of an ion target will not be high.

We finally note that the relativistic effects are not significant for non-tunneling harmonic emission. In brief, in order to accelerate to relativistic velocities, the electron needs more space than is available within the range of the binding potential. Also for an electron in a hydrogenic ion such as O^{7+}, even a laser of intensity 10^{18} W/cm^2 has an electric field that is only 2% of that due to the nucleus. The lack of significant relativistic effects in these calculations thus lends added support for the proposed classic model of interpretation of non-tunneling harmonics.

6.4. Radiation of ionized electrons

We have seen that, for laser intensities up to the weakly relativistic regime ($q < 0.3$) and hydrogen-like ions with low charge state ($Z < 4$) the tunneling-recollision regime of harmonic emission works. In the case of more highly-charged ions ($Z \sim 8$) and relatively low laser intensity ($q \ll 1$) the regime of harmonic emission is via bound-bound multi-photon transitions. Meanwhile, with highly-charged ions ($Z \sim 8$) and relatively high laser intensity ($q \sim 1$) the regime of HHG is one of non-tunneling. In a relativistically strong laser field, the tunneling-recollision mechanism is not valid, because the re-collision of an ionized electron is strongly suppressed. The non-tunneling regime not valid either,

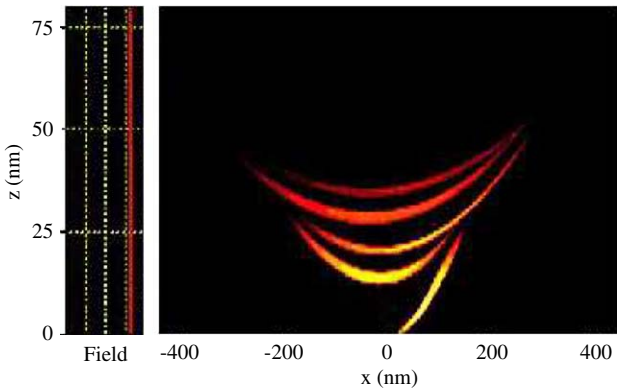

Fig. 56. The ionization wave function probability from Ne^{+7} ion at the center of a $\#f/1.5$ laper beam with intensity of $2 \times 10^{17}\,W/cm^2$ at peak focus and wavelength 800 nm ($q = 0.3$) [323]. Reprinted with permission from [323]; Copyright 2004 by the Optical Society of America.

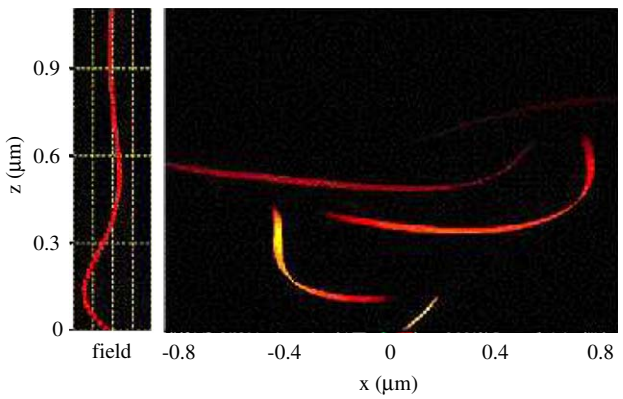

Fig. 57. The ionization wave function probability from Ar^{+15} ion at the center of an laser beam $\#f/1.5$, with intensity $1 \times 10^{19}\,W/cm^2$ at peak focus and wavelength 800 nm ($q = 2.15$). The x-axis extends to the e^{-2} beam radius and the z-axis to one Rayleigh length [323]. Reprinted with permission from [323]; Copyright 2004 by the Optical Society of America.

because in the very strong laser fields the ionized electron leaves the atom quickly without wiggling within an atomic radius. In this situation other mechanisms for the ionized electron radiation are more important [323,324]. Moreover, it has been pointed out that the ionized electron wavepacket, in this regime, carries the signature of coherence of the driving laser field. Namely, the electron wave is modulated with the laser frequency that can serve as a new source of the interference and coherence of the generated radiation.

The numerical investigation of radiation in the above-mentioned regime [323,324] incorporates three steps: (i) ionization according to the quantum tunneling theory of ADK; (ii) electron distribution propagation using a weighted ensemble of classical trajectories (according to the tunneled wave function); and (iii) superposition of the radiation across the interaction region. The modulation of the tunneled electron wave packet is shown in Figs. 56 and 57. Space distribution of the modulated electron density depends significantly on the laser intensity, which can serve as a clear indication of the relativistic effects.

A more interesting point in these calculations is that the interference effects play a significant role in the electron radiation (see Fig. 58). The Bremsstrahlung radiation of the ionized electron is considered in [323] and the Larmor radiation (multi-photon Thomson scattering of the laser radiation by the ionized electron) in [324]. Unfortunately in the considered setup, the interference effects decrease the radiation yield by an order of magnitude in comparison to point-electron calculations. Fig. 58(a) shows that the field of the Larmor radiation from each trajectory is an attosecond-duration burst, but when the contributions from all trajectories are added (see Fig. 58(b)), destructive interference suppresses the high-frequency region of the spectrum. Nevertheless, it is shown that the Larmor radiation from the

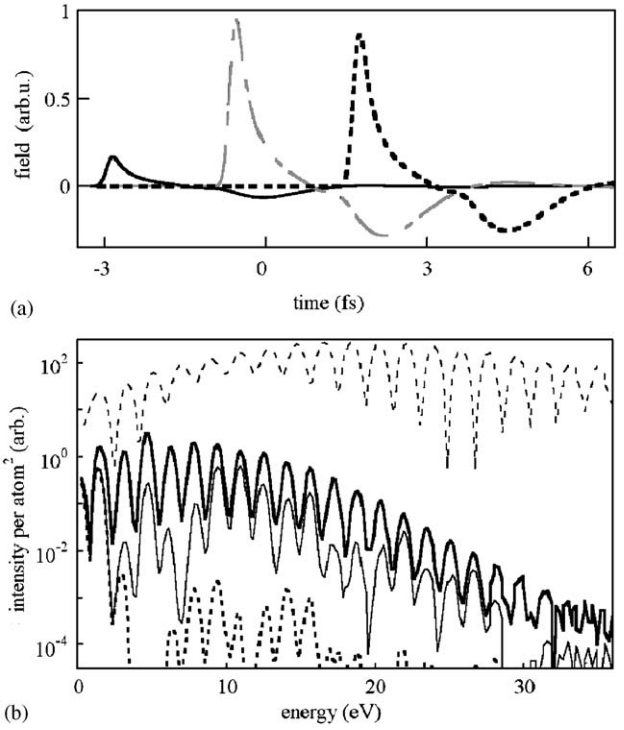

Fig. 58. The radiation field component along the laser polarization for three trajectories from ionization of Ar^{+15} at laser intensity of 10^{19} W/cm^2 and wavelength 800 nm ($q = 2.15$) in (a). In (b) the frequency-resolved power spectrum per atom^2 is shown for 1 classical electron (gray, dashed) and the ionization from 1 (solid), 10 (gray, solid), and 1000 (dotted) atoms along the laser propagation axis [324]. Reprinted with permission from [324]; Copyright 2005 by the IOP Publishing Limited.

ionized electrons is still highly directional. For the Bremsstrahlung radiation the azimuthal angular distribution becomes more isotropic with increasing intensity but the spectrum cutoff increases linearly with the laser intensity, reaching 10 MeV at 10^{20} W/cm^2.

6.5. Positronium harmonics

6.5.1. Recombination harmonics

The emission frequency that can be achieved in the high harmonic generation process (HHG) with atomic systems is determined mainly by the kinetic energy the ionized electron acquires from the laser field. A straightforward way for advancement in the frequency domain in HHG is increase of the driving laser intensity. However, once electrons reach velocities non-negligible by comparison to that of light, the magnetically-induced Lorentz force causes a separation of electrons and ionic core in the laser propagation direction which, in turn, results in a strong reduction in the high harmonic yields [104,109]. While highly-charged ions (see Sections 6.2 and 6.3) and crystals (see Section 6.6) have been studied to bring about a reduction in this effect [103,252,296,325], there is still a clear need for an efficient system, in which radiation pressure does not induce substantial ionization in the laser propagation direction. From this point of view positronium displays unique properties [111] in that, while tunnel-ionization of the electron and positron may occur almost oppositely on the laser polarization direction, both particles sense identical drifts due to their equal magnitudes of mass and charge (see Fig. 59). Therefore, periodic electron–positron re-collisions will occur automatically in spite of the influence of the Lorentz force, along with substantial high harmonic generation in the X-ray regime.

Positronium consists of an electron and a positron and is known to be unstable. While ortho-positronium annihilates into three photons with a lifetime of 1.4×10^{-7} s, para-positronium does so with two photons and a lifetime of 1.25×10^{-10} s [326]. The presence of a strong laser field may induce substantial reductions [327] or enhancements

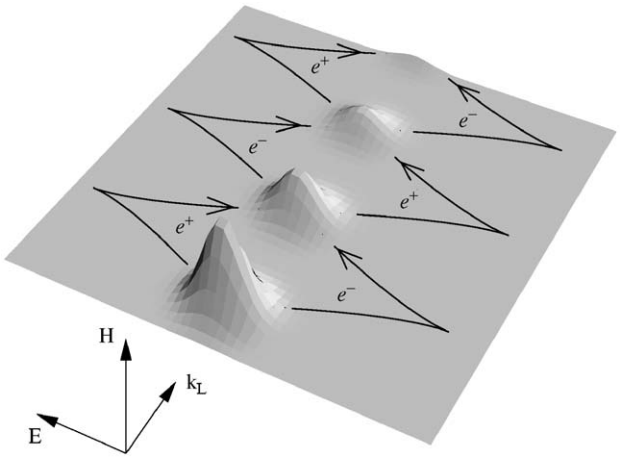

Fig. 59. Schematic diagram displaying positronium dynamics in an intense laser field. The bound system depicted by the density of its wave function may ionize in the laser field. Once free, both electron e^- and positron e^+ could be described as classical particles. Their trajectories are shown by the solid lines. The electric field **E** accelerates the particles in opposite directions while the Lorentz force, due to the magnetic field **H**, leads to an identical drift for both in the propagation direction $\mathbf{k}_L$. Without an initial center-of-mass motion these trajectories are symmetric and thus both particles overlap periodically giving rise to possible recombination and thus high-frequency light emission [111]. Reprinted with permission from [111]; Copyright 2004 by the American Physical Society.

[328,329] of the annihilation process into gamma photons. However, even the shorter lifetime of para-positronium is sufficient for the interaction with many cycles of a femtosecond laser pulse.

In Ref. [111] the dynamics and high harmonic generation of positronium are investigated in the tunneling regime using moderately intense laser field strengths. The investigations are based on a solution of the Schrödinger equation without using the dipole approximation for the laser field, and taking fully into account the Lorentz force due to the laser magnetic field component. The Schrödinger dynamics is governed by the following Hamiltonian (in atomic units)

$$H = \frac{1}{2}\left(-\mathrm{i}\nabla_{\mathbf{x}_-} + \frac{\mathbf{A}(t - z_-/c)}{c}\right)^2 + \frac{1}{2}\left(-\mathrm{i}\nabla_{\mathbf{x}_+} - \frac{\mathbf{A}(t - z_+/c)}{c}\right)^2 - \frac{1}{|\mathbf{x}_- - \mathbf{x}_+|}, \tag{99}$$

where, $\mathbf{x}_i$ and $-\mathrm{i}\nabla_{\mathbf{x}_i}$, $(i \in \{-, +\})$, are the coordinate and momentum operators of the electron and positron, respectively, and **A** is the vector potential of the laser field. A separation of the variables may be brought about by introducing the relative coordinates $\mathbf{r} = (x, y, z) = \mathbf{x}_- - \mathbf{x}_+$ and the center of mass coordinates $\mathbf{R} = (X, Y, Z) = (\mathbf{x}_- + \mathbf{x}_+)/2$, together with the running time $\tau = t - Z/c$. In the new variables, the system has three constants of the motion, namely, the center of mass transverse canonical momenta $-\mathrm{i}\partial_X$, $-\mathrm{i}\partial_Y$ and the quantity $\mathrm{i}(\partial_t + c\partial_Z)$, with the eigenvalues defined as P_x, P_y, and g, respectively. Thus the system's wavefunction now takes the form

$$\Phi(\mathbf{r}, \mathbf{R}, \tau) = \exp\left[\mathrm{i}\left(P_x X + P_y Y - \frac{g}{c} Z - \mathscr{E}\tau\right)\right] \phi(\mathbf{r}, \tau). \tag{100}$$

The equation governing the relative motion of particles is solved employing the SFA [306] and using a $1/c$-expansion of the vector potential as a function of the relative coordinates. Then the time-dependent wave function in the length gauge $\Psi = \exp(-\mathrm{i}\mathbf{A}(\tau) \cdot \mathbf{r}/c)\phi$ may be written as

$$|\Psi(\tau)\rangle = |0\rangle + \int \mathrm{d}^3\tilde{p}\, b(\tilde{\mathbf{p}}, \tau)|\tilde{\mathbf{p}}\rangle, \tag{101}$$

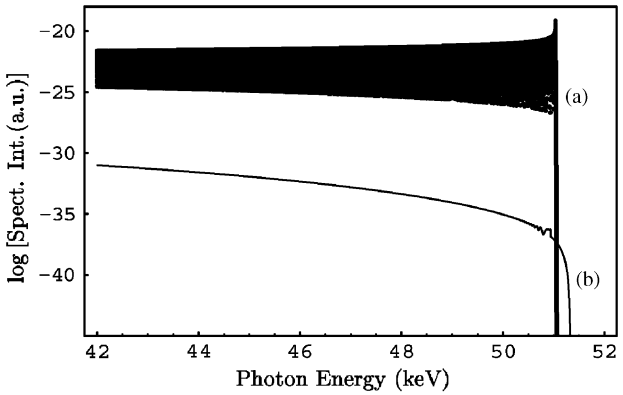

Fig. 60. Differential high-harmonic spectral intensities $(\mathrm{d}I_n/\mathrm{d}\Omega)\sin^{-2}\theta$ at odd harmonic numbers n as a function of the photon energy of the respective harmonic; θ being the harmonic emission angle with respect to the polarization direction: (a) displays the spectrum of a single positronium with ca. 4.1 million harmonics via a coherent field of intensity $I = 8.63 \times 10^{12}\,\mathrm{W/cm^2}$ at a wavelength of $\lambda = 100\,\mu\mathrm{m}$ close to that provided by the CLIO free-electron laser [330], $q = 0.25$ and positronium atom is initially at rest; and (b) displays the spectrum of an Ne^{7+} ion in an Nd:YAG laser field with $\lambda = 1054\,\mathrm{nm}$ at $I = 1.5 \times 10^{17}\,\mathrm{W/cm^2}$ $(q = 0.35)$. At those parameters both systems yield approximately the same cutoff frequency, though with a yield in the spectral intensity of the cutoff harmonics differing by about 15 orders of magnitude [111]. Reprinted with permission from [111]; Copyright 2004 by the American Physical Society.

where $|0\rangle$ is the ground state, and the coefficients are

$$b(\tilde{\mathbf{p}}, \tau) = -\frac{\mathrm{i}}{1 - B_z} \int_{-\infty}^{\tau} \left\langle \mathbf{p} - \frac{\mathbf{A}(\tau')}{c} - \mathbf{\Lambda}(\tau') | H_I(\tau') | 0 \right\rangle \mathrm{e}^{-\mathrm{i}S(\mathbf{p},\tau,\tau')}\,\mathrm{d}\tau'. \tag{102}$$

We have taken $H_I(\tau) = -E(\tau)x(1 - B_z) - B_x E(\tau)z$, with the electric field $\mathbf{E}(\tau) = -\partial_\tau \mathbf{A}/c$, the center of mass velocity $\mathbf{V} = \mathbf{P}/2$, the scaled center-of-mass velocity $\mathbf{B} = \mathbf{V}/c$, and $\mathbf{P} = (P_x, P_y, (\mathscr{E} - g)/c)$. Furthermore,

$$S(\mathbf{p}, \tau, \tau') = \int_{\tau'}^{\tau} \mathrm{d}\tau'' \frac{\left[\mathbf{p} - \dfrac{\mathbf{A}(\tau'')}{c} - \mathbf{\Lambda}(\tau'')\right]^2 + I_\mathrm{p}}{1 - B_z}, \tag{103}$$

is the quasi-classical action, with $\mathbf{p} = \tilde{\mathbf{p}} + \mathbf{A}(\tau)/c + \mathbf{\Lambda}(\tau)$. The wave function, in contrast to the dipole case [306], accounts for the magnetically-induced drift via the additional term

$$\mathbf{\Lambda}(\tau) = \Lambda(\tau)\boldsymbol{e}_z = \frac{B_x A(\tau)}{c(1 - B_z)}\,\boldsymbol{e}_z, \tag{104}$$

in the momentum.

The dipole moment responsible for HHG, calculated using the saddle-point method, displays essential differences from its counterpart in atomic HHG, especially in the real exponential factor

$$C := \exp\left[-\frac{2}{3} I_\mathrm{p}^{3/2} \frac{(1 + B_z)}{|E(\tau_0)|}\right]. \tag{105}$$

In the atomic HHG case [104] there is an additional difference (in place of I_p in C, one has $I_\mathrm{p}^a + c^2 q^4/4$) due to the drift in the laser propagation direction, which can strongly reduce the amplitude and, thus, the efficiency of HHG. Here, I_p^a denotes the atomic ionization potential. The expression for C, without the factor $1 + B_z$, coincides with the corresponding result within the dipole approximation for atoms. This means that for positronium, the magnetically-induced drift in the laser propagation direction has no diminishing impact on HHG.

Fig. 60 displays the hard X-ray harmonic spectrum of positronium obtained from the Fourier transform of its dipole moment via a five-fold $(\mathrm{d}\mathbf{p}, \mathrm{d}\tau, \mathrm{d}\tau')$ saddle-point integration versus Ne^{7+} ions. Ne^{7+} with $I_\mathrm{p}^a = 240.31\,\mathrm{eV}$ in the chosen laser field appears to be the currently most favorable choice for obtaining 50 keV X-rays at approximately the same

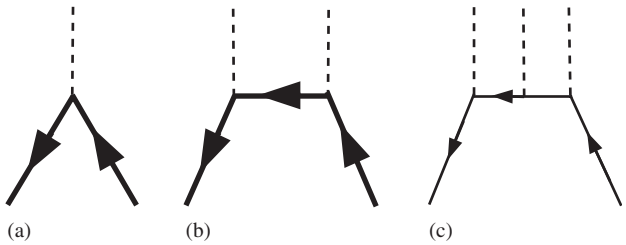

Fig. 61. Feynman diagrams displaying γ-photon emission via electron–positron annihilation: (a) multiphoton annihilation in super strong laser fields at $q \sim (m_*^2/\omega_L\Omega)^{1/3}$ with emission of $n \sim m_*^2/\omega_L\Omega$ laser photons, along with one γ-quantum; (b) annihilation in a laser field at $q \ll (m_*^2/\omega_L\Omega)^{1/3}$ with emission of laser photons, along with two γ-quanta; and (c) annihilation of ortho-positronium with emission of three photons without the laser field. The bold lines correspond to the electron (positron) Volkov states, i.e., involving a laser field, and the dashed lines correspond to the emitted photons [111]. Reprinted with permission from [111]; Copyright 2004 by the American Physical Society.

cutoff as for positronium. For Ne^{7+} the influence of the magnetic field component yields a very small re-collision probability so that the harmonic yield is about 15 orders of magnitude smaller than for positronium.

Assuming the high ion density of $10^{19}\,\mathrm{cm}^{-3}$, positronium density $3 \times 10^7\,\mathrm{cm}^{-3}$ such as demonstrated in a Penning trap [331], and a focal volume of $V_\mathrm{f} \simeq (10\lambda)^3$, with wavelength λ, only 6 out of the 15 orders of magnitude of the positronium versus ion yield in Fig. 60 will be lost. Thus hard X-ray harmonic yields from positronium should be substantially larger than from gaseous ions in comparable setups.

6.5.2. Radiation from laser-induced annihilation

It appears that positronium annihilation can be significantly modified in the laser field, causing emission of γ-radiation of a narrow bandwidth that clearly prevails over the spontaneous background [111]. Application of external radiation fields may transform the annihilation process [111,328,332]. Thus, coherent external γ-radiation with high frequencies of order $\omega_\mathrm{c} = mc^2/\hbar$ can induce a stimulated annihilation process [332]. Laser radiation also can have impact on the annihilation process. In the extremely intense laser fields, when $q \gg 1$, electron–positron annihilation can proceed via a new channel with emission of a single γ-photon along with a net emission of a large number of laser photons $n \sim m_*^2/(\omega_L\Omega)$, with the laser- and γ-photon frequencies ω_L and Ω, respectively. This process probability is not negligible if $q^3 \sim m_*^2/(\omega_L\Omega)$. At $\Omega \sim 10\,\mathrm{GeV}$, $q \sim 100$ is required, and the net number of emitted laser photons is $n \sim 10^6$ (Fig. 61a) [345] (see also Section 7.1.3). This new channel is closed if the laser intensity is not so high. There is still a way to influence the annihilation by the laser radiation. Let us discuss ortho-positronium annihilation. Without external laser fields, ortho-positronium annihilates spontaneously into three photons, with energies varying between zero and ω_c (Fig. 61(c)) [326]. There are annihilation channels that involve two γ's and a single low-frequency photon.Those channels may be enhanced by stimulating the low-frequency emission with the corresponding intense coherent fields. An analysis of these laser-induced processes in a weak laser field ($q \ll 1$) shows no enhancement of the laser-induced radiation over the background of annihilation radiation [328]. Nevertheless, in the feasible moderately intense ($q \sim 1$) low-frequency light, the laser radiation stimulates multiple emission of low-frequency photons and enhances, in this way, the probability of the corresponding annihilation channel with two γ photons (Fig. 61(b)) [111].

An estimate of the laser-induced annihilation probability of positronium via two γ-quanta has been made [111] by calculating the Feynman diagram in Fig. 61(b) (plus the same diagram with photon exchange). The intense laser field is included to all orders because electrons and positrons are dressed as Volkov states. The influence of the laser field on the propagator is assumed negligible as the laser frequency ω_L and the number s of photons involved is such that $s\omega_L \ll \omega_\mathrm{c}$. The differential probability of laser-induced annihilation with stimulated emission of s photons and spontaneous emission of two γ quanta with energies $\omega_{1,2} \approx \omega_\mathrm{c}$ and the first γ-quantum within the solid angle $\mathrm{d}\Omega$, then reads

$$\mathrm{d}W_\mathrm{s}^\mathrm{ind} \approx \frac{r_0^2}{2}\,\frac{\omega_1^2}{\omega_2\omega_\mathrm{c}}\,\rho c F_\mathrm{s}\,\mathrm{d}\Omega, \tag{106}$$

where

$$F_{\rm s} = \begin{cases} \left|1 - \dfrac{q^2}{2} - s\dfrac{\omega_L}{\omega_{\rm c}}\right| J^2_{\frac{s}{2}}(\zeta), & \text{for even } s \text{ (para)};\\ \dfrac{q^2}{2}[J^2_{\frac{s-1}{2}}(\zeta) + J^2_{\frac{s+1}{2}}(\zeta)], & \text{for odd } s \text{ (ortho)}. \end{cases} \tag{107}$$

In Eq. (107),

$$\zeta := \frac{q^2}{4}\,\frac{\omega_{\rm c}}{\omega_L}, \tag{108}$$

$J_n(\zeta)$ is an ordinary Bessel function, r_0 is the classical electron radius, and $\rho = a_{\rm B}^{-3}$ with the Bohr radius $a_{\rm B}$. In a weak laser field with $q \ll 1$ the formula for $\mathrm{d}W_{\rm s}^{\rm ind}$ given above matches the known result in Ref. [328]. The total probability of the laser induced annihilation for ortho-positronium is of the order of $W_{\rm o}^{\rm ind} = \sum_s W_{\rm s}^{\rm ind} \approx r_0^2 \rho c q^2$, and that of para-positronium is $W_{\rm p}^{\rm ind} \approx r_0^2 \rho c$. For the sake of comparison, we also invoke the corresponding spontaneous annihilation probabilities $W_{\rm o}^{\rm sp} \approx \alpha r_0^2 \rho c$ and $W_{\rm p}^{\rm sp} \approx \pi r_0^2 \rho c$, with the fine structure constant $\alpha = e^2/\hbar c$ [326]. The ratio of the ortho-positronium lifetime in the presence of a laser field to that without it is α/q^2. In laser fields with $q \lesssim 1$ of interest here, the ortho-positronium lifetime is of order 10^{-9} s (10^{-10} s for para-positronium), which makes it well suited for HHG.

Laser-induced annihilation according to Fig. 61(b) can be a source of high-frequency radiation. The spectrum is expected to be narrow and to be higher than the corresponding spontaneous radiation spectrum. In fact, the spectral bandwidth of the usual radiation from the spontaneous annihilation is $\omega_{\rm c}$. Let us estimate the bandwidth of the radiation due to the laser-induced annihilation. With annihilation being accompanied by stimulated emission of laser photons, energy and momentum conservation allow emission of γ quanta only at certain frequencies in each direction. The spectral bandwidth $\Delta\omega = \max\{\Delta\omega_{\rm D}, \Delta s \cdot \omega_L\}$ of the induced γ radiation due to annihilation is determined either by the laser Doppler line-width $\Delta\omega_{\rm D} \approx 10^{-4}$ at room temperature, or by the range of the harmonic order Δs of the involved stimulated photons. This leads to a bandwidth much narrower than that of the spontaneous process, $\Delta\omega \ll \omega_{\rm c}$. The ratio of stimulated to spontaneous γ radiation probabilities

$$\eta := \frac{1}{\Delta\omega}\,\frac{\mathrm{d}W^{\rm ind}/\mathrm{d}\Omega}{\mathrm{d}W^{\rm sp}/\mathrm{d}\Omega\,\mathrm{d}\omega}, \tag{109}$$

is largest for $\zeta \gg 1$. Then $s \approx \zeta$ is within the range $\Delta s \approx \zeta^{1/3}$, which, for ortho-positronium, yields

$$\eta \approx \frac{q^2}{\alpha}\,\frac{\omega_{\rm c}}{\Delta\omega} = \frac{q^{4/3}}{\alpha}\left(\frac{\omega_{\rm c}}{\omega_L}\right)^{2/3}. \tag{110}$$

This means large enhancement of the radiation from ortho-positronium, $\eta \approx 10^5$, even with a moderately intense laser field of $\xi = 10^{-1}$. For para-positronium, no enhancement is expected, $\eta \approx 1$ [111]. Thus, laser-induced γ radiation via positronium annihilation can exceed the spontaneous background in its narrow bandwidth. This is mainly because the stimulating laser radiation induces a concentration of the annihilation radiation within the narrow bandwidth.

We conclude this subsection by mentioning the proposals aimed at the design of a gamma-ray-laser (Graser) based mostly on the stimulated γ-radiation from excited nuclei [334].

6.6. Multi-particle systems

Other paths to HHG employ laser–cluster and laser–plasma interactions (nuclear reactions in laser–cluster and laser–plasma interactions are considered in Section 7.2). Both of these systems are highly nonlinear with good perspectives for high harmonics.

The laser–field interaction with an overdense plasma provides a strong coupling with the plasma which results in efficient HHG. At laser intensities up to $10^{19}\,\mathrm{W/cm^2}$, coherent HHG up to the 40th order has been achieved when a strong laser pulse is reflected from a solid surface [335]. The main mechanism behind this effect is the nonlinear oscillation of the critical surface of the plasma [336]. This mechanism of HHG has been reviewed in detail in [290],

and further developments have been reviewed in [231]. Therefore, we will not devote more attention to it here. A new development in this field has been observed in [29]. In addition to the HHG from the front side of a thin foil irradiated by an intense laser of intensity $10^{18}\,\mathrm{W/cm^2}$, harmonics up to the 10th order have been observed from the rear surface of the foil. The latter is due to a laser-driven resonant electron current flowing from the front surface into the foil.

The main problem hindering generation of more coherent high harmonics during the laser beam reflection from an overdense plasma is the excitation of nonlinear collective instabilities. Nevertheless, it appears that there is a way to circumvent this problem.

As has been mentioned in Section 5.4.2 a setup has been proposed [296–298] for laser–thin-solid-layer interactions at relativistic intensities that preserve the layer structure during the brief interaction time. This setup can be employed for X-ray generation.

X-ray generation in the thin-layer regime, when amplitude of the electron transverse oscillation with respect to the laser propagation direction is less than a layer thickness (see Eq. (81)), has been considered in Ref. [296]. In this regime, under the influence of the high-power laser pulse, the electrons are extracted almost instantaneously from the layer. The brief periodic interactions with the far slower moving, and thus still quasi-regular, ionic structure then produce high-frequency coherent Bremsstrahlung. Ref. [296] considers amplification of the probe X-ray due to *stimulated* coherent Bremsstrahlung. The radiation mechanism has some resemblance to the free-electron laser [337], as X-rays arise mainly due to stimulated radiation of essentially free electrons in a periodic (ionic quasi-regular) structure. However, in this case electrons are extracted from the laser-driven solid layer rather than being injected into the system. That substantially increases the number of electrons involved in the process and, consequently, increases the gain. Electrons in this regime are accelerated by the laser field as in the case of Thomson scattering [143], but the mean number of emitted harmonics is larger than in the Thomson scattering case. The reason is that the characteristic radiation length of the electron is different in the two mechanisms. For the Thomson scattering it is determined only by the laser parameters while in the regime at hand, the characteristic length is the spatial periodicity of the ionic structure. The mean number of emitted harmonics for Thomson scattering is $\tilde{n} \simeq q^3$ [143] while for the mechanism at hand, it is

$$\tilde{n} = \frac{q^2 \lambda_L}{2a}. \tag{111}$$

The expression for $\tilde{n}$ indicates that relativistic laser intensities and a small ion separation a are most favorable. For a KrF ($\lambda_L = 248\,\mathrm{nm}$) high power laser pulse with intensity $I \simeq 10^{21}\,\mathrm{W/cm^2}$, $q \simeq 6$ and $a \simeq 5\,\text{Å}$, the multi-photon parameter in the Thomson process is $\tilde{n} \simeq 200$, while for the proposed scheme $\tilde{n} \simeq 9 \times 10^3$. Enhancement of the multi-photon parameter above the Thomson scattering case may be attributed to the presence of sharp edges in the electron trajectories when they periodically penetrate the transient regular ionic structure.

The radiation mechanism in the thin-layer regime differs from the mechanism of radiation from the solid surface during laser-pulse reflection on it [290]. It is true that the radiators in both cases are the medium electrons which get accelerated in vacuum by the laser field and then emit HHG as they pass through the medium again. The difference, though, is in the medium condition. In the case of the solid surface the medium retains the properties of an underdense plasma, apart from a small skin layer. In the case of the thin layer, the strong laser field propagates along the layer and destroys it.

The small signal gain, G, of X-ray radiation for this scheme is calculated in Ref. [296]. The high power pump laser field is considered exactly while the scattering potential and the probe field of X-ray radiation are treated perturbatively to second order. A number of distinct regimes of amplification exist, depending on the characteristic width of the resonance of the process. The most favorable conditions for amplification of the probe are offered by the exponential instability (EI) regime. In this regime, the gain is large enough to allow the spectral width of the probe wave, due to its rapid increase in intensity, to prevail over the resonance width, due to the limited interaction time. Another condition is imposed by the momentum spread Δ of the electrons, $G \gg \max\{1/L,\ N\Delta/mc\lambda_L\}$, where L is the length of the layer. In the case of a strong laser field ($q \gg 1$) and, concentrating on the high harmonic regime ($n \gg 1$), the X-ray small signal gain is then given by the expression

$$G = \sqrt{3}\exp\left\{-\frac{4\pi^2 u^2}{3a^2}\right\}\left[\frac{\pi n_e n_i L_\perp^4 (1+\beta_0)^4}{4}\,\frac{Z^2 r_0^3 q^6 \lambda_L^2 \gamma_0^3 m^4 c^4}{n^2 a^4 \Lambda^4 R_\perp^2}\,I_{n-N}(\zeta)K_{n-N}(\zeta)\right]^{1/3}, \tag{112}$$

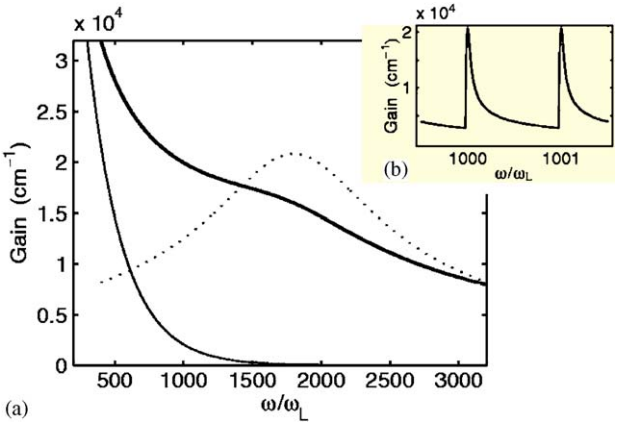

Fig. 62. (a) Gain in the EI regime according to Eq. (112) (thick line). The electron and ion densities are $n_e = 10n_i = 10^{23}\,\mathrm{cm}^{-3}$, the laser wavelength is $\lambda_L = 3.5 \times 10^{-6}$ cm, the laser intensity parameter is $q = 6$, the ion structure period $a = 3.5 \times 10^{-8}$ cm, the transversal size of the layer is $L_\perp = 7 \times 10^{-6}$ cm, $u/a = l_i/a = 0.087$ and the momentum spread of the electron beam is $\Delta/mc = 10^{-4}$. The thin line describes the corresponding gain for the multi-photon Compton radiation amplification in a plasma [338] for the same parameters. The dotted line depicts the function $I_{n-N}(\zeta) \cdot K_{n-N}(\zeta)$ multiplied by 2.5×10^7 which peaks at the multi-photon parameter $\tilde{n}$ in Eq. (111); and (b) a window of the fine structure of the gain corresponding to the thick line in (a) [296]. Reprinted with permission from [296]; Copyright 2001 by the American Physical Society.

where u is the mean deviation of electrons from the crystal knot points, r_0 is the classical radius of the electron, n_e and n_i are the electron and ion densities, respectively, γ_0 is the initial Lorentz factor of the electron, $\beta_0 = \upsilon_0/c$, υ_0 is the electron initial velocity, $\overline{\varepsilon_0} = \varepsilon_0 - c(mcq)^2/2\Lambda$ is the dressed energy of the electron in the laser field, $L_\perp$ is the transversal width of the layer, $R_\perp$ is the amplitude of the transversal oscillation of the electron, $n = \omega/\omega_L$ is the harmonic number, $N = \lambda_L q^2/2a$, $\zeta = \lambda_L q\gamma_0(1+\beta_0)/a$, and $I_n(\zeta)$ and $K_n(\zeta)$ are modified Bessel functions.

The gain dependence on the generated radiation frequency is shown in Fig. 62. This gain clearly dominates that due to the multi-photon Compton process in a plasma (see Fig. 62(a)). The multi-photon parameter $\bar{n}$ in this process corresponds to the number of harmonics at the peak of the function $I_{n-N}(\zeta)K_{n-N}(\zeta)$ in Eq. (112) (see Fig. 62(a), dotted line).

Let us make an order-of-magnitude estimate of the gain using Eq. (112). Consider the case of a KrF laser (wavelength $\lambda_L = 248$ nm and intensity $I \simeq 10^{21}\,\mathrm{W/cm}^2$) and a Pb crystal with $n_e \simeq 10n_i \simeq 10^{23}\,\mathrm{cm}^{-3}$, $a \simeq 4.95 \times 10^{-8}$ cm, $R_\perp \simeq 5.2 \times 10^{-6}$ cm, $L_\perp = 2.5 \times 10^{-5}$ cm, and $L = 4 \times 10^{-4}$ cm. Furthermore, take $Z \simeq 10$ and $\Delta/mc \simeq 3 \times 10^{-5}$. Then, the EI regime operates yielding very high gain, e.g., for the $n \approx 1000$th harmonic, $G \simeq 1.8 \times 10^4\,\mathrm{cm}^{-1}$. Compared to this, the multi-photon Compton effect gives rise to merely $\tilde{n} \simeq 200$ harmonics when the same parameters are used [338]. Still, for the chosen parameters, the gain via incoherent X-ray Bremsstrahlung in plasmas is very small, around $10^{-6}\,\mathrm{cm}^{-1}$ for the 1000th harmonic [339]. In our scheme, even for the very short interaction time of $\tau_{\mathrm{int}} \sim 10$ fs, the enhancement of radiation is substantial, as the gain-length product characterizing the lasing possibility at $\lambda = \lambda_L/n \sim 2.5$ Å, is $GL \simeq 7$. This gain-length product is somewhat less, but competitive with the gain-length of leading present-day and near-future X-ray lasers. Those include $GL \simeq 15$ at $\lambda = 13.9$ nm [340] and especially the ultimate of $GL \simeq 41$ at $\lambda = 1$ Å of X-FEL due to unprecedented long interaction lengths of $L = 95$ m currently under construction [45]. Temporal coherence of the emitted radiation is estimated to be $\delta\omega/\omega \sim cG/n\omega_L \sim 10^{-4}$, and spatial coherence $\delta\theta \sim \delta k_\perp/k \sim \lambda_L/2\pi n R_\perp \sim 8 \times 10^{-4}$. The scheme cannot, therefore, compete with leading schemes of X-ray lasers concerning coherence [340], where $\delta\omega/\omega \sim 10^{-5}$, $\delta k_\perp/k \sim 2.5 \times 10^{-5}$. However, the scheme does not require a large-scale facility and is still attractive for highly-efficient amplification of high harmonics.

Now we turn to the thick-layer regime (see Section 5.4.2). It seems to be possible [297] to attain phase matching in HHG in an environment abundant in free electrons, using the main features of the setup, namely that the layer periodic structure is quasi-preserved during interaction with the strong laser. In this work it is assumed that HHG from each atom arises due to the tunneling-recollision mechanism. Employing a potassium crystal, for example, 17 atomic electrons will be ionized on average by the laser pulse via the over-the-barrier process, and the last remaining 18th electron will generate the harmonics. At these intensities, the medium is highly-ionized, and the refractive index n_L seen by the

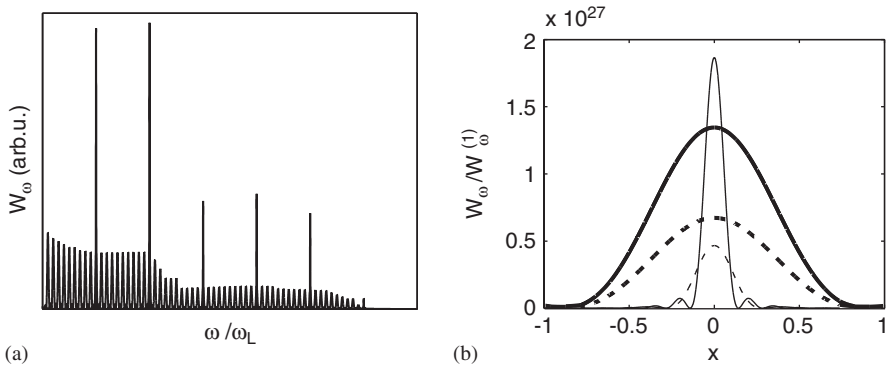

Fig. 63. (a) Sketch of a spectrum with periodic phase matching; and (b) HHG spectral intensity from a crystal layer $W_\omega = \mathrm{d}W/\mathrm{d}\omega\,\mathrm{d}\Omega$ scaled by the respective peak value for one ion $W_\omega^{(1)} = (\mathrm{d}W^{(1)}/\mathrm{d}\omega\,\mathrm{d}\Omega)_{\max}$, where $x = \omega/\omega_L - 10^6$. The narrow features (thin lines) correspond to the coherent HHG from the periodic structure, while the wide features (thick lines) correspond to the HHG from one ion multiplied by number of ions and magnified 3×10^{14} times, corresponding by intensity to the incoherent HHG from disordered ions. The solid lines correspond to $N_z = 2 \times 10^5$ and the dashed lines to $N_z = 10^5$. The parameters employed are: $L_x = L_y = 20\,\mu\mathrm{m}$, $\lambda_L = 800\,\mathrm{nm}$, $\tau_L = 30\,\mathrm{fs}$, $\theta = 0$, $a_x = a_y = a_z = 4.5\,\text{Å}$, $n - n_L = 0.057$ [297]. Reprinted with permission from [297]; Copyright 2002 by the IOP Publishing Limited.

laser wave is governed by the free electrons. Phase matching is achieved by imposing the Bragg condition between the fundamental and harmonic waves generated from various ions

$$|\omega t - \mathbf{k}\cdot\mathbf{l}| = 2\pi s; \quad s = 1, 2, \ldots, \tag{113}$$

where $\mathbf{l}$ is the displacement vector of the ions, ω and $\mathbf{k}$ are the frequency and wave vector, respectively, of the harmonic radiation, with $k = |\mathbf{k}| = n\omega/c$, and n the refractive index for harmonic radiation and t the time for the laser pulse to propagate the distance $\mathbf{l}$. With Eq. (113) and Fig. 38 the phase matching conditions become

$$ka_x \sin\theta = 2\pi s_1; \quad \text{and} \tag{114}$$

$$ka_z(n_L - n\cos\theta) = 2\pi s_2, \tag{115}$$

with $s_{1,2} = 0, \pm 1, \pm 2, \ldots$. The two most favorable directions of detection are along the laser propagation direction (first scheme: $\theta = 0$, $s_1 = 0$) and at a finite angle $\theta = \cos^{-1}(n_L/n)$ (second scheme: $\theta \neq 0$, $s_2 = 0$). The spectral intensity from the regular structure is calculated taking advantage of the fact that the electrons responsible for HHG ionize as well as evolve in the laser field similarly. Consequently, their trajectories are congruent, apart from translations in space by $\mathbf{l}$ and in time by t. Thus, to a good approximation, the total HHG spectral intensity of the crystal can be expressed via a coherent sum of the HHG spectral intensities arising from single ions (see Fig. 63). The peak spectral intensity of harmonic radiation at the coherence condition (113) is ideally proportional to $(N_x N_y N_z)^2$ and will thus in general significantly exceed the HHG spectral intensity of irregular systems. The spectral and angular line-widths are, respectively: $\delta\omega/\omega \approx a_z/sL_z$ and $\delta\theta \approx \lambda/L_x$; λ being the harmonic wavelength. Efficiency of the proposed X-ray radiation source is estimated by the spectral brightness of the radiation which, when expressed for convenience in units of photons/(s · mm^2 · mrad^2 · (0.1% bandwidth)), may be written as

$$\begin{aligned} B &= \frac{\mathrm{d}N}{\mathrm{d}t\,\mathrm{d}A\,\mathrm{d}\Omega\,\mathrm{d}\omega} \\ &= 3 \times 10^{15}\,\frac{N_x N_y N_z n_L |\boldsymbol{n} \times \boldsymbol{a}_\omega(a.u.)|^2}{a_x a_y a_z(\text{Å})}, \end{aligned} \tag{116}$$

where $\boldsymbol{n} = \mathbf{k}/k$, $\boldsymbol{a}_\omega = (\omega/e)\int \boldsymbol{j}_\omega^{(1)} \mathrm{e}^{-\mathrm{i}\mathbf{k}\cdot\mathbf{r}}\,\mathrm{d}V$, N is the number of emitted photons, A is the emitter area, and Ω is the solid angle about the emission direction. For a laser intensity $I = 5 \times 10^{21}\,\mathrm{W/cm^2}$, hard X-ray generation may be possible in principle with unprecedented coherence. For example, for 1.5 MeV photons, the spectral width becomes $\delta\omega/\omega \approx 1.4 \times 10^{-7}$, and the angular divergence of the emitted radiation is $\delta\theta \approx 4 \times 10^{-8}$ rad. No reliable estimates

are currently available for the single-ion-variable $\boldsymbol{a}_\omega$ entering into the expression for the total spectral brightness in Eq. (116), because of the favorable, but rather complex, situation that the tunneled wave packet may recombine with several ions on its journey through the crystal.

7. Towards high-energy laser physics

7.1. Quantum electrodynamical effects

In super-strong laser fields when an electron is stripped from an atom via the over-the-barrier ionization process, one essentially deals with a free electron interacting with the laser radiation from that point on. This field has been systematically and extensively investigated since the 1960s. The electron dynamics has been investigated both classically and quantum-mechanically [342,343]. The quantum-mechanical Volkov solution [59] (see Section 3.2.1) has been employed to treat multi-photon processes with free electrons in a strong laser field, such as multi-photon Compton scattering, pair-production in a laser field with absorption of a large number of photons, influence of a laser field on the decay of unstable particles, and vacuum polarization effects in a laser field [344,345]. Quantum electrodynamics in strong external fields has been also developed [346,347]. The closely related fields of free-electron laser and free-free transitions have been advanced (see also, e.g., [337,348–351]).

A large number of reviews and books devoted to this field are currently in existence, some of which are cited above. In this review we will touch only on a selected number of topics related to recent or near-future experimental realization of processes in nonlinear quantum electrodynamics. Here we should mention a remarkable experiment carried out in 1996–1997 at SLAC for observation of nonlinear effects in Compton scattering and electron–positron pair-production via light-by-light scattering [352,353]. We discuss also the radiation reaction effects, which can significantly modify the Compton scattering process, as well as light-by-light scattering and the vacuum polarization effects, which could be observable in the near future employing petawatt lasers.

7.1.1. Nonlinear Compton effect

Compton scattering (scattering of photons by free electrons) is one of the basic processes in which the quantum nature of the radiation field is exhibited. As the photon energy (in the rest frame of the electron) becomes comparable to the electron rest energy, photon recoil on the electron becomes considerable. That reflects particularly on the spectrum of the scattered electrons and photons. Photon recoil effects become more prominent in a multi-photon process, i.e., when the electron absorbs several photons from the laser field and spontaneously emits a single high-energy photon. This is a nonlinear Compton effect in a strong radiation field, sometimes referred to as *high-intensity Compton scattering* [333,354,355]. Relative contribution of the multi-photon process is determined by the relativistic invariant parameter of the laser field strength $q = eA_0/mc^2$, where A_0 is the amplitude of the laser field vector-potential. In particular, the mean number of photons involved in a nonlinear Compton process is $\tilde{n} \simeq q^3$. Therefore, multi-photon effects begin to play a role when the parameter q approaches unity. It should be noted that multi-photon Thomson scattering of strong laser radiation by an electron, describes the same process. This term is usually used when the photon recoil effects are negligible and the process is purely of a classical electrodynamical nature [143]. Furthermore, we are mainly concerned here with the nonlinear Compton effect; Thomson scattering, being very important for developing new brilliant short-wavelength radiation sources and for plasma diagnostics, has been considered in some recent reviews [231,232].

More recent developments also include the following. At LLNL experiments have been carried out on the laser radiation scattering by relativistic electrons (linear Compton scattering) to develop a tunable light source of high peak brightness (in the range of 10^{20}–10^{25} photons/(mm^2 × mrad^2 × s × 0.1% bandwidth)) in the 100 keV–10 MeV spectral region, for purposes of nuclear fluorescence spectroscopy, time-resolved positron annihilation spectroscopy, and MeV flash radiography [356]. A benchmark calculation using a three-dimensional time- and frequency-domain code has been carried out to analyze the experimental data. The peak brightness is found to scale quadratically with the electron energy, and inversely with the electron beam duration and the square of its normalized emittance [357]. This scaling emphasizes the importance of the electron beam quality for Compton-scattering radiation sources. Employing a laser pulse of a Joule energy and 5 ps duration, and a 50–250 MeV (relativistic) electron beam of a low normalized emittance (1 mm · mrad, 1 nC), the peak X-ray brightness of the scattered radiation can exceed

10^{23} photons/(mm^2 × mrad^2 × s × 0.1% bandwidth) near 1 MeV photon energy. It has been shown that the X-ray pulse temporal profile closely follows the electron beam pulse shape. An important finding is that, when the nonlinear effect of the laser intensity dependence on frequency of the scattered radiation is taken into account, the optimum of the impinging laser pulse duration is of the order of a few picoseconds, not femtoseconds as thought previously [357].

A new code and procedure to calculate radiation spectra of a laser-driven relativistic electron within a quantum mechanical description has been advanced in [153].

Observation of the nonlinear Compton effect, accompanied by a weak signal of second-harmonic radiation, has been reported in Ref. [358]. The unique angular distribution of the second and third harmonics, emitted from nonlinear Thomson scattering, has been reported in Ref. [359]. Refs. [360–362] are devoted to experimental investigation of nonlinear Thomson scattering in plasmas.

Nonlinear Compton scattering, in which up to four laser photons interact with a single electron, has been first observed at the Final Focus Test Beam facility at SLAC [352]. In this experiment, 46.6 GeV electrons were scattered in the strong laser field with intensity of 10^{18} W/cm^2. Infrared laser radiation of wavelength 1054 nm, as well as its second harmonic, were used. Parameters of the experiment correspond to the regime of nonlinear Compton scattering as the laser field strength parameter is $q \approx 0.6$ and photon energies in the electron rest frame are 211 and 421 keV, respectively, which are comparable to the electron rest mass.

When an ultra-relativistic electron (from a beam) of initial energy $\varepsilon_0 \gg mc^2$ absorbs n photons, each of energy $\hbar\omega \ll mc^2$, from a laser pulse that crosses the electron beam at the angle ϑ_0, the minimum energy of the scattered electron is

$$\varepsilon_{\min} = \frac{\varepsilon_0}{1 + (2n\varepsilon_0\omega_0/m_*^2c^4)(1 + \cos\vartheta_0)}, \tag{117}$$

where $m_* = m\sqrt{1 + q^2/2}$ is the effective mass of the electron in the laser field of linear polarization and frequency ω_0. We see that the minimum energy in the scattered electron spectrum depends on the number of photons absorbed from the laser field and, therefore, can serve as a signature of the nonlinear Compton effect [352,363].

For linear Compton scattering ($n = 1$) one obtains the scattered electron minimum energy $\varepsilon_{\min} = 25.6$ GeV, using parameters from the experiment ($\varepsilon_0 = 46.6$ GeV, $\vartheta_0 = 17°$, and $\lambda = 1054$ nm). But, for the two- and three-photon (nonlinear Compton effect) the electron spectrum threshold is found to be at 17.6 and 13.5 GeV, respectively. The experimental results are shown in Fig. 64, where the spectrum is normalized to the number of scattered electrons, with the latter deduced, in turn, from the number of scattered high energy photons. Furthermore, simulations have been performed using the theoretical results of Ref. [364]. In Fig. 64(a) the plateau at 19–21 GeV corresponds to two-photon processes and the drop at 17–18 GeV corresponds to their threshold. The threshold of the three-photon process is not distinct in Fig. 64(b) but the figure, nevertheless, shows electrons involved in four-photon processes. The dashed line displays contribution to the spectrum from successive linear ($n = 1$) scatterings. So, linear scattering alone does not account for the observed electron spectrum.

The electron spectrum from scattering green laser light, Fig. 64(c), shows a threshold for the two-photon process in a 34 mJ laser field, and for both two- and three-photon processes in a 220 mJ laser field. Dependence of the normalized yield on the laser intensity I fits an I^{n-1} law, where n is the absorbed photon number, which points to the perturbative character of the observed multi-photon processes in this experiment (for a theoretical description of the non-perturbative Compton effect, see [333,345,354]).

7.1.2. Radiation-reaction effects

Radiation-reaction effects can have a significant impact on the Compton (Thomson) scattering in strong laser fields of petawatt power [145,365]. These effects manifest themselves only in relativistic particle dynamics under the influence of extremely strong fields. Neither classical nor quantum electrodynamics are able to handle these effects rigorously, owing to the fact that these theories become inapplicable at the small distances involved. However, in some appropriate limits the strength of the radiation-reaction is restricted, which makes the problem treatable. Non-relativistic treatment of radiation-reaction within classical electrodynamics (Abraham–Lorentz model) has been put forward a hundred years ago [366–369]. Dirac generalized the classical radiation-reaction theory to include the relativistic domain [370] in what is known now as the Lorentz–Dirac model.

The radiation problem from an electron in classical electrodynamics assumes that the electron trajectory in the external fields is given, then the Lienard–Wiechert potentials are used to calculate the radiated fields. In this context,

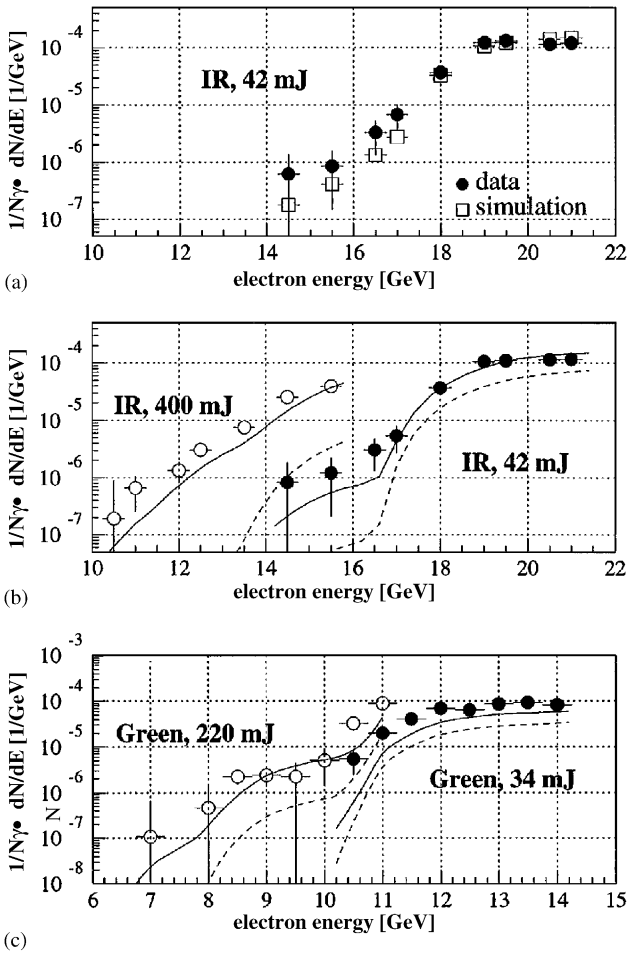

Fig. 64. Scattered electron energy spectra of the nonlinear Compton scattering experiment at the final focus test beam facility at SLAC. (a) Data and simulations for 42-mJ infrared laser pulses. (b) and (c) Data and simulations (solid curves) for infrared (b) and green (c) laser pulses, scaled to standard values of the interaction geometry. The dashed lines show the simulation for multiple linear Compton scattering only [352]. Reprinted with permission from [352]; Copyright 1996 by the American Physical Society.

the back-reaction of the radiated fields on the electron in classical electrodynamics can be tackled only by a perturbative approach, assuming the radiation-reaction force to be small in comparison with the Lorentz force. This approach results in the following equation of motion for the radiating electron in the non-relativistic limit [371]

$$m\frac{\mathrm{d}\mathbf{v}}{\mathrm{d}t} = e\mathbf{E} + \frac{e}{c}\mathbf{v}\times\mathbf{B} + \frac{2}{3}\frac{e^2}{c^3}\frac{\mathrm{d}^2\mathbf{v}}{\mathrm{d}t^2}. \tag{118}$$

The radiation-reaction force (the last term in Eq. (118)) may be expressed as

$$\mathbf{f}_{\mathrm{rad}} = \frac{2}{3}\frac{e^3}{mc^3}\frac{\mathrm{d}\mathbf{E}}{\mathrm{d}t} + \frac{2}{3}\left(\frac{e^2}{mc^2}\right)^2\mathbf{E}\times\mathbf{B}, \tag{119}$$

Then, the condition for the perturbative approach can be derived by comparing the radiation-reaction force with the Lorentz force (the first two terms). From this comparison we may see that the Abraham–Lorentz model is applicable in not-too-strong external fields, E, and at not-too-short distances [371], i.e.

$$E \ll \frac{m^2c^4}{e^3} = \frac{E_{\mathrm{c}}}{\alpha}; \quad \text{and} \quad \lambda \gg r_0, \tag{120}$$

where E_c is the Schwinger critical field (see Eq. (132) below), λ is the wavelength of the external field, α is the fine-structure constant, and $r_0 = e^2/mc^2$ is the classical electron radius. The relativistic Lorentz–Dirac model is based on the following relativistically covariant expression for the electron equation of motion which, in the rest frame of reference of the electron, coincides with the non-relativistic Eq. (118)

$$m\frac{\mathrm{d}u^i}{\mathrm{d}\tau} = \frac{e}{c}F^{ik}u_k + g^i; \quad g^i = \frac{2e^2}{3c^3}\left(\frac{\mathrm{d}^2u^i}{\mathrm{d}\tau^2} - u^i u^k \frac{\mathrm{d}^2u_k}{\mathrm{d}\tau^2}\right), \tag{121}$$

where g^i is the relativistic radiation-reaction 4-force, u^i is the 4-velocity, F^{ik} is the tensor of the electromagnetic field, and τ is the proper time. Correspondingly, the Lorentz–Dirac model will be applicable under the same conditions (120) taken in the rest frame of the radiating electron (then, E and λ are the field strength and the wavelength of the external field in the rest frame of electron, respectively). With the Compton wavelength $\lambda_c = \hbar/mc$ larger than r_0, and $m^2c^4/e^3 \gg E_c$, the Lorentz–Dirac model fails only when the quantum effects of photon recoil and vacuum instability enter into the picture.

In the non-relativistic domain, the above-mentioned conditions of the model imply that the radiation-reaction force is small compared to the Lorentz force. Therefore, the electron dynamics is not disturbed substantially due to the radiation-reaction. Meanwhile, in the ultra-relativistic domain, and due to the Lorentz boost, a situation may be reached [371] in which the radiation-reaction force becomes of the same order of magnitude as the Lorentz force but, nevertheless, the Lorentz–Dirac model is still applicable, because the model's validity conditions are still satisfied in the electron rest system. In fact, from Eq. (121) the component of the radiation-reaction force in the electron velocity direction is [371]

$$f_x = \frac{2e^4}{3m^2c^4}\left[(E_y - B_z)^2 + (E_z + B_y)^2\right]\gamma^2, \tag{122}$$

with γ the electron Lorentz factor. The first of the conditions in Eq. (120) of the Lorentz–Dirac model in the electron's rest frame reads

$$\gamma E \ll \frac{m^2c^4}{e^3}, \tag{123}$$

which does not mean that the ratio of the radiation-reaction force (122) to the Lorentz force

$$\eta_f \equiv \frac{e^3\gamma^2 E}{m^2c^4} = \frac{q\gamma^2 r_0\omega}{c}, \tag{124}$$

is small. The latter can have important implications, changing significantly the dynamics of the radiating electron and its radiation, when the parameter η_f approaches unity. Analogous criteria for the significance of the radiation-reaction effects has been proposed in [365], estimating the electron energy change, $\Delta\gamma$, due to the radiation reaction force by

$$\Delta\gamma \sim \frac{2\pi r_0 q^2\gamma_0\omega\Delta t}{\lambda + 2\pi r_0\gamma_0 q^2\omega\Delta t}, \tag{125}$$

where Δt is the interaction time, and γ_0 the electron initial γ-factor. The radiation-reaction effect becomes important when $\Delta\gamma$ reaches γ_0. The latter yields a parameter determining the significance of the radiation-reaction, namely

$$\eta_\varepsilon \equiv \frac{q^2\gamma_0 r_0\omega^2\Delta t}{c}. \tag{126}$$

When the electron energy loss due to radiation during one period of the external wave is comparable with its initial energy, one has

$$\tilde{\eta}_\varepsilon \equiv \frac{q^2\gamma_0 r_0\omega}{c} \gtrsim 1. \tag{127}$$

This has been called the radiation-dominant regime [365].

The first indication that nonlinear Compton scattering can be significantly modified by radiation-reaction has been discussed in Refs. [145]. The motion of an ultra-relativistic free electron of 50 GeV-energy in the field of strong laser radiation is considered based on the numerical solution of the Lorentz–Dirac equations. A scheme in which the

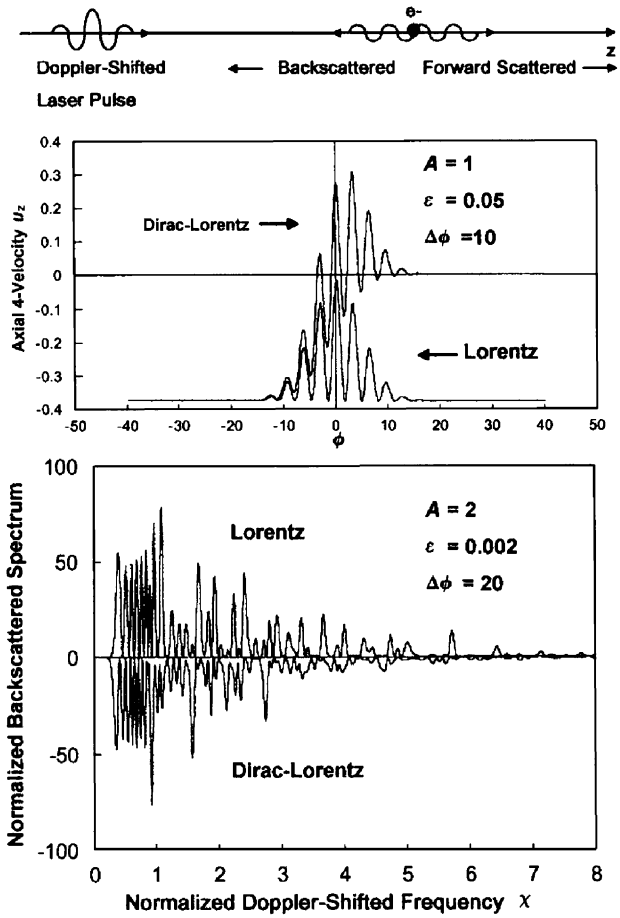

Fig. 65. Schematic diagram of the setup (top), Lorentz and Dirac–Lorentz electron dynamics (middle), and Lorentz and Dirac–Lorentz backscattered spectra (bottom). The parameters used in our notation reads $A \equiv q$, $\varepsilon \equiv \pi r_0/\lambda_0$, where λ_0 is the laser wavelength in the rest frame of electron, ϕ is the laser phase, and $\Delta\phi$ is the total phase change in the laser pulse, the electron energy is 48 GeV, laser wavelength 1 μm [145]. Reprinted with permission from [145]; Copyright 1996 by the American Physical Society.

electron counter-propagates with the laser pulse was considered and the backscattered radiation spectrum has been calculated (see Fig. 65). The parameters of Fig. 65 in our notation are $A \equiv q$, $\varepsilon \equiv \pi r_0/\lambda_0$, where λ_0 is the laser wavelength in the rest frame of the electron, ϕ is the laser phase, and $\Delta\phi$ is the total phase change in the laser pulse. The indicator parameters of the radiation-reaction strength in the considered case are: $\eta_f \gg 1$ and $\tilde{\eta}_\varepsilon \ll 1$, for the upper figure in Fig. 65 $\eta_\varepsilon = 1$, while for lower one $\eta_\varepsilon = 0.3$. This means that the radiation-reaction force is not negligible but the regime is not radiation-dominated. The radiation spectrum shows remarkable broadening and a frequency-shift attributable to the radiation reaction (see Fig. 65).

Another situation is considered in [373]. The electron is taken to be initially at rest before it is submitted to the laser field. Thus, in Ref. [373] influence of the radiation reaction on the dynamics and radiation of an initially bound electron ionized by the strong laser field is discussed. Laser intensities from 10^{19} up to 10^{22} W/cm^2 have been applied to a hydrogen atom in its ground state. At these intensity levels, a hydrogen atom undergoes fast over-the-barrier ionization during an atomic time-scale that is much less than the relaxation time of the atomic bound states. Therefore, the electron dynamics can be reasonably modeled by that of a free electron in a laser field with the initial conditions determined by a wave function of the hydrogen ground state. The approach employs a classical Monte Carlo simulation based on the Lorentz–Dirac equation. Averaging is done over a micro-canonical ensemble of initial electron positions and momenta which simulate the hydrogenic ground state [162,236,374]. In the case discussed, the radiation-reaction force is much less than the Lorentz force of the laser field. Nevertheless, the intensities used are high enough to see clear signatures of

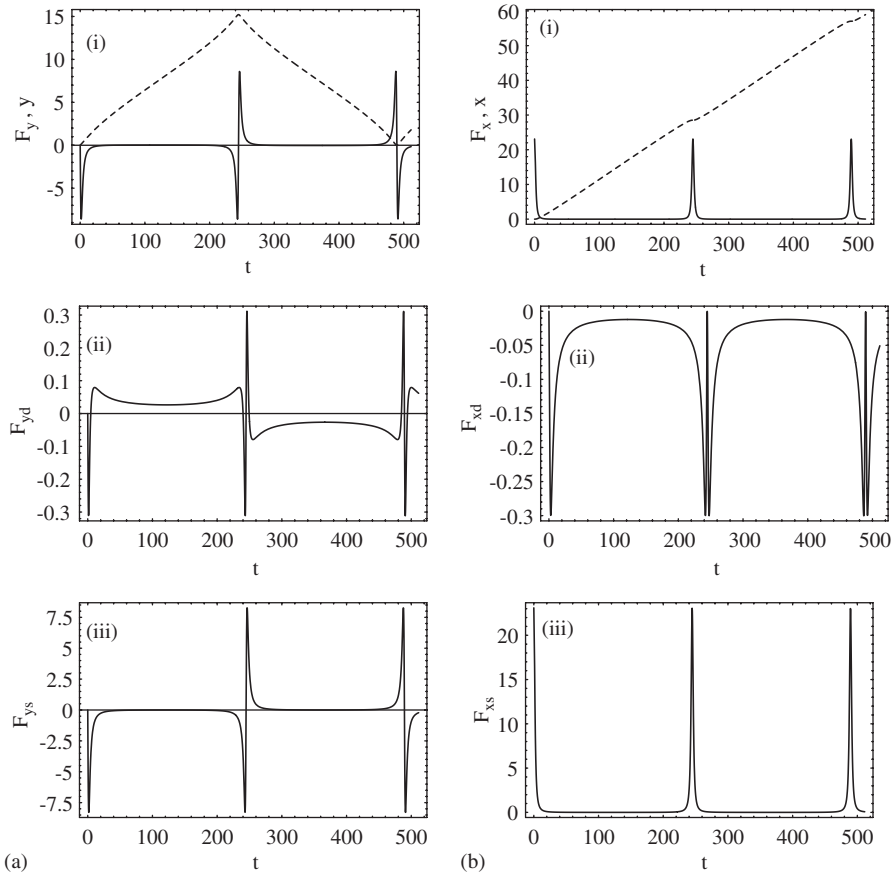

Fig. 66. (a)-left column: (i) The contribution $F_y(t)$ of the radiation-reaction force to the acceleration in the polarization direction of the laser field (y-direction) (full curve) and the corresponding evolution of the y component (broken curve) of the electron as a function of time t during interaction with a seven-cycle constant-amplitude laser pulse with intensity $10^{20}\,\mathrm{W/cm^2}$ and angular frequency $\omega = 0.086$ a.u. for arbitrary scaling. Parts (ii) and (iii) show the two contributions $F_{yd}(t)$ and $F_{ys}(t)$ to the acceleration in the y-direction from the radiation-reaction force in the same scaling as in (i) from the terms in the derivative of the laser field and the square of the laser field, respectively. (b)-right column: same as (a) with y replaced by x (propagation direction of the laser pulse) [373]. Reprinted with permission from [373]; Copyright 1998 by the IOP Publishing Limited.

radiation-reaction in the electron trajectories and the radiation spectrum. Furthermore, the simulations show a damping of the electron motion in the polarization direction of the laser field due to radiation-reaction, as is expected intuitively. More interesting, though, is the counterintuitive finding of a velocity boost in the propagation direction of the laser field and an increase in the red-shift of the electron oscillation frequency relative to that of the laser. Moreover, in Ref. [373] a detailed investigation of the influence of the different terms of the radiation-reaction force (a term proportional to the square of the field, denoted by $\boldsymbol{f}_\mathrm{s}$, and that proportional to the derivative of the field, denoted by $\boldsymbol{f}_\mathrm{d}$) on the electron dynamics is carried out. The force is written as

$$\boldsymbol{f} = \boldsymbol{f}_\mathrm{d} + \boldsymbol{f}_\mathrm{s}, \tag{128}$$

$$\boldsymbol{f}_\mathrm{d} = \gamma\tau_0 \left[\frac{\mathrm{d}\mathbf{E}}{\mathrm{d}t} + \frac{\mathbf{v}}{c} \times \frac{\mathrm{d}\mathbf{H}}{\mathrm{d}t}\right], \tag{129}$$

$$\boldsymbol{f}_\mathrm{s} = \frac{\tau_0}{c}\left[\mathbf{E}\times\mathbf{H} + \mathbf{H}\times\left(\mathbf{H}\times\frac{\mathbf{v}}{c}\right) + \mathbf{E}\left(\mathbf{E}\cdot\frac{\mathbf{v}}{c}\right)\right] - \frac{\tau_0\mathbf{v}\gamma}{c^2}\left[\left(\mathbf{E} + \frac{\mathbf{v}}{c}\times\mathbf{H}\right)^2 - \left(\frac{\mathbf{v}}{c}\cdot\mathbf{E}\right)^2\right], \tag{130}$$

where the d in $\boldsymbol{f}_\mathrm{d}$ and the s in $\boldsymbol{f}_\mathrm{s}$ stand for *derivative* and *square*, respectively, and $\tau_0 = r_0/c$.

Results from that investigation are displayed in Fig. 66. The total radiation-reaction force in the laser polarization direction is strongest at the turning points, where maximum acceleration occurs. It is also opposite the direction of

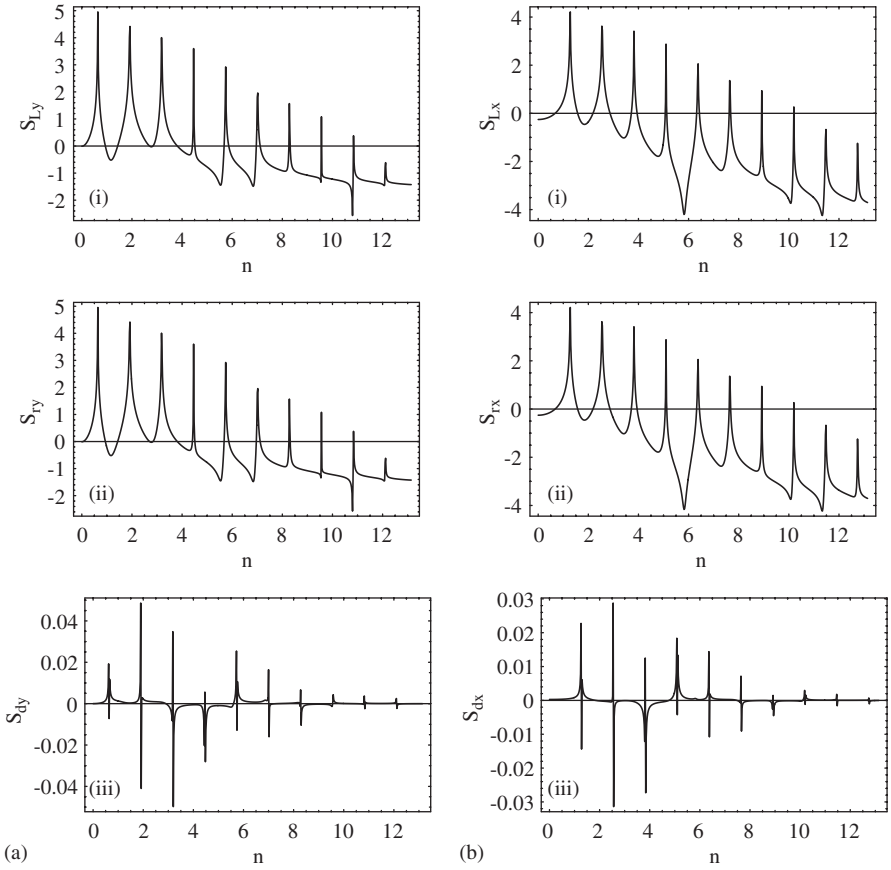

Fig. 67. The Monte Carlo radiation spectrum as a function of the multiple number n of the applied laser frequency ω_L ((i) S_{Ly}; S_{Lx} without radiation-reaction; (ii) S_{ry}; S_{rx} with radiation-reaction; and (iii) $S_{\mathrm{d}y}$; $S_{\mathrm{d}x}$ the difference, the latter minus the former, for a hydrogen atom in a laser field with 10^{19} W cm^{-2} intensity and $\omega = 0.086$ a.u. angular frequency. The initial state of hydrogen is simulated using a micro-canonical ensemble of 1000 members, while the time evolution is evaluated without the influence of the nucleus due to essentially instantaneous ionization. The spectrum is evaluated in the direction perpendicular to the polarization and propagation directions of the laser pulse, to show most clearly the effect on the red-shift. Part (a)-left column, shows the spectrum arising from the radiated electric field polarized along the polarization direction y of the laser field, while (b)-right column, considers the components polarized in the propagation direction x of the laser pulse [373]. Reprinted with permission from [373]; Copyright 1998 by the IOP Publishing Limited.

the transverse motion all the time, apart from a small positive acceleration between the turning points. The square contribution of the radiation-reaction force is essentially responsible for the damping, while the derivative term is responsible for the small positive acceleration between the turning points. The derivative term has a damping contribution near the turning points, as well. It is small in the ultra-relativistic limit but is believed to be the main damping contribution in the weakly-relativistic limit. The square term of the radiation-reaction force in the laser propagation direction is mainly responsible for the electron acceleration near the turning points of the transverse oscillation. The derivative term in the propagation direction has a small damping contribution in-between the turning points. The leading contribution to acceleration in the propagation direction comes from a term proportional to the Poynting vector, the pre-factor being proportional to $1/c^4$. Therefore, the damping is associated with the energy flux of the generated radiation. It also allows for a physical interpretation of the electron velocity boost in terms of the radiation-reaction, i.e., as a consequence of reabsorption of radiation in the laser propagation direction.

The most sensitive way of revealing the effect of radiation-reaction is observation of the electron radiation spectrum. Here, a substantial effect can be noted already for more moderate laser field intensities, e.g., 10^{19} W/cm^2 (see Fig. 67). The radiation-reaction damping causes a bigger red-shift in the emitted harmonics, resulting in a dispersion-like shape for the difference function.

Ref. [373] concludes that the effect of radiation-reaction is still rather small, even for intensities of the order of $10^{20}\,\mathrm{W/cm^2}$ and visible frequencies. However, clear signatures of it are noticeable in the radiation spectrum and electron trajectories.

In [365] nonlinear Thomson scattering in a regime approaching the radiation-dominated regime is considered. The equations of motion of a single electron taking into account the radiation-reaction force are numerically integrated, and the back-scattered radiation spectrum is calculated. An electron of 150 MeV energy is considered to counter-propagate with a laser pulse of wavelength 1 μm and duration 30 fs. The laser intensity parameter is varied from $q = 1$ up to $q = 100$. Notice that, for the given electron energy and laser wavelength, the region of the radiation-dominated regime begins from $q \approx 336$, according to the condition $\tilde{\eta}_\varepsilon = 1$. The calculation of the electron energy loss in [365] shows that the damping due to radiation-reaction becomes remarkable above $q = 10$. In the case of $q = 100$, the electron loses about 80% of its energy during interaction with the laser pulse. Significant modifications have been shown to occur in the radiation spectrum due to radiation-reaction. The first harmonic is down-shifted, and the overall spectral intensity of the radiation is significantly damped. For $q = 100$, the damping can reach an order of magnitude. The damping in the radiation intensity has been explained to be due to the energy loss of the electron, as the spectra are very sensitive to the electron energy ($\sim \gamma^6$).

The quantum electrodynamical corrections to the Dirac–Lorentz classical model of radiation-reaction are expected to be significant [365] when the characteristic photon energy of the Thomson radiation spectrum in the reference in which the electron is on average at rest (the R-frame), $\hbar\omega_{\mathrm{rad}} \sim \omega_R\gamma_R$, approaches the electron's effective mass, where $\omega_R \approx 2\omega\gamma_0/\sqrt{1+q^2}$ is the laser frequency and $\gamma_R = \sqrt{1+q^2}$ is the electron Lorentz factor in the R-frame. The latter condition reads

$$\gamma_0\sqrt{1+q^2} > \frac{mc^2}{\hbar\omega}. \tag{131}$$

From Eq. (131), when using initially relativistic electrons, $\gamma_0 = 300$, the quantum corrections may be significant starting at a laser intensity of the order of $10^{25}\,\mathrm{W/cm^2}$ (at $\lambda = 1\,\mu\mathrm{m}$).

7.1.3. Electron–positron pair-production

Although Compton scattering exhibits quantum features, it does not have an intrinsically quantum nature. By contrast, electron–positron pair-production is a process that has essentially a quantum nature. Nonlinear pair-production in a strong laser field has been observed for the first time at the final focus test beam facility at SLAC [353,363]. Particle production from the electromagnetic field, one of the amazing predictions of QED, is possible, at least in principle, in a static electric field [375], in a photon field [376], or in a combination of the two [377]. The first process requires a tremendous electric field

$$E_{\mathrm{c}} = \frac{m^2c^3}{e\hbar} = 1.3\times 10^{16}\,\mathrm{V/cm}, \tag{132}$$

equivalent to a laser intensity of $4.6\times 10^{29}\,\mathrm{W/cm^2}$ [375]. That intensity does not seem to be reachable in the near future, although there are proposals for experimental setups to achieve this fantastic goal [35–39,389]. Energy–momentum conservation rules out pair-production from a single photon. At least two photons are required for pair-creation. They have to counter-propagate in the center of mass (c.m.) of the created pair, and energy of each has to be equal to the electron rest mass at the process threshold. It means at least one of the photons in the Lab system has to be a γ-quantum $\hbar\omega \geqslant mc^2$. In a strong laser field, multiple laser photons can be involved in the pair-creation process. Again, the process is forbidden in a single laser wave by the conservation laws, but becomes possible if the process involves an additional γ-photon. Theoretically, pair-production in a strong laser field via absorption of a γ-photon along with multiple laser photons has been predicted in [329,333]. Multiple-photon absorption allows a process with a γ-quantum of lower energy. In fact, if the γ-quantum propagates counter to the laser photons then the c.m. equality $\omega' = n\omega'_L = m_*$, expressing energy–momentum conservation in the center-of-mass of the created electron and positron reads, in terms of the Lab system variables, as $\omega/2\gamma = 2\gamma n\omega_L = m_*$. Hence, $\omega = m_*^2/n\omega_L$, where ω', ω'_L are the γ- and laser–photon frequencies in the c.m., and ω and ω_L are the corresponding frequencies in the Lab frame, respectively, n is the number of laser photons involved in the process, and γ is the Lorentz-factor of the c.m. In the strong laser field, the mean number of photons involved in the pair-production process is $\overline{n} \simeq q^3$, as in multi-photon Thomson scattering [345]. For $q \geqslant 1$,

$n > 1$, and the minimum required energy of the γ-quantum decreases in comparison with the case of a one-laser–photon process, $n = 1$, in a weak laser field, $q \ll 1$. In Ref. [353] the electron–positron pair-production process

$$\omega + n\omega_L \to e^+e^-, \tag{133}$$

in a strong laser field has been observed. A laser pulse, of 650 mJ energy, a 527 nm wavelength, and a focused to intensity of $1.3 \times 10^{18}\,\mathrm{W/cm^2}$, has $q = 0.36$. The latter means that multi-photon processes will play a role, but with perturbative probabilities decreasing with n according to the power law q^{2n}. In the experiment, γ-photons of 29.2 GeV are derived by Compton back-scattering of the same laser pulse on the relativistic counter-propagating electron beam of energy 46.6 GeV. In this case, $n = 4$ laser photons are required to be absorbed in the elementary process of pair-creation. The probability of this process will be significant if the parameter

$$\kappa = \frac{\sqrt{(F_{\mu\nu}p^\nu)^2}}{mc^2E_c}, \tag{134}$$

is of the order of 1, where $F_{\mu\nu}$ is the laser field four-tensor, and p_ν is the 4-momentum of a particle which probes vacuum polarization [345]. For the process under consideration, p_ν is the γ-photon 4-momentum, yielding $\kappa = (2\hbar\omega/mc^2)(E_L/E_c) \simeq 1$. One can give an intuitive explanation to the parameter κ. The process will have significant probability if the number of photons of the threshold process, $n_{th} = m_*/\omega'_L$, is of the order of the mean number of photons involved, $\overline{n} = q^3$. With the given γ-quantum energy $\hbar\omega$, $\overline{n}/n_{th} = (\omega\omega_L/m_*^2)q^3$, which coincides with κ for $q \gg 1$. For the parameter values of the experiment discussed in Ref. [353], one has $\kappa = 0.2$.

There is a competing process of pair-production in this setup, namely, instead of the previously discussed two-step process (first γ-photon production via Compton scattering followed by pair-creation via γ-photon scattering on the laser photons) a pair can be created in one step via scattering of a virtual photon of the Coulomb field of the scattering electron on the laser photons (the trident process)

$$e + n\omega_L \to e'e^+e^-, \tag{135}$$

a variant of the Bethe–Heitler process [377]. Theoretically, electron–positron pair-production in a strong laser field impinging on the Coulomb field of a nucleus has been considered in [378–380]). Probability of the trident process may be characterized by the parameter $\chi = E'_L/E_c = 2\gamma E_L/E_c$; that is, the ratio of the laser electric field strength in the electron rest frame to the Schwinger field strength. For the case of Ref. [353], $\chi = 0.3$. Nevertheless, the experiment shows that contribution from the one-step process via a virtual photon is minor compared to the process of pair-production from real photons. Results of the experiment [353] are presented in Figs. 68 and 69. Fig. 68 shows the spectrum of the created positrons in comparison with the theoretical model calculation assuming it is a two-step process, using the formalism of Ref. [333]. Compton scattering on the positron is also taken into account. Reasonable agreement between the theoretical calculations and the experimental data is obtained. Restricting the data to events with high laser intensity, $q > 0.216$, improves the agreement of their momentum spectrum with the model calculation, as the momentum of the positrons at low laser intensity cannot be easily resolved from the possible residual background. Fig. 69 shows the yield of positrons per laser shot as a function of the laser intensity parameter q. The rate fits the power law $\propto q^{2n}$ with $n \approx 5$, which hints at the perturbative nonlinear character of the multi-photon process. The simulations show that, on average, 1.5 photons are absorbed from the laser in a Compton scattering process (first step) and 4.7 photons in the second step of pair-creation. However, simulation of the trident process (135) based on the Weizsäcker–Williams approximation shows that it does not account for the pair-production process of the experiment (see Fig. 69). Thus, the experiment [353] has reported observation of inelastic photon–photon scattering with real photons for the first time.This experiment remains to-date the only observation of the laser-induced electron–positron pair-production process.

An interesting variation of pair-production in the Coulomb and laser fields has been proposed in [381], where collision of a highly charged nucleus, moving at a relativistic velocity, with an intense laser field is considered. First of all, in the rest system of the nucleus the photon energy is Doppler-shifted, which decreases the number of photons required to drive the process. But what is more interesting, when the nucleus collides with a laser beam, is that production of a bound-free pair is possible along with free pairs. By this is meant that, during pair-creation, the electron is produced in a bound state while the positron in the continuum. For highly charged ions the energy of a bound state is very low-lying, thus decreasing the energy gap to be overcome by a multi-photon transition. The conclusion of the work [381] is that experimental observation of the process is feasible using future X-FEL and an ion accelerator.

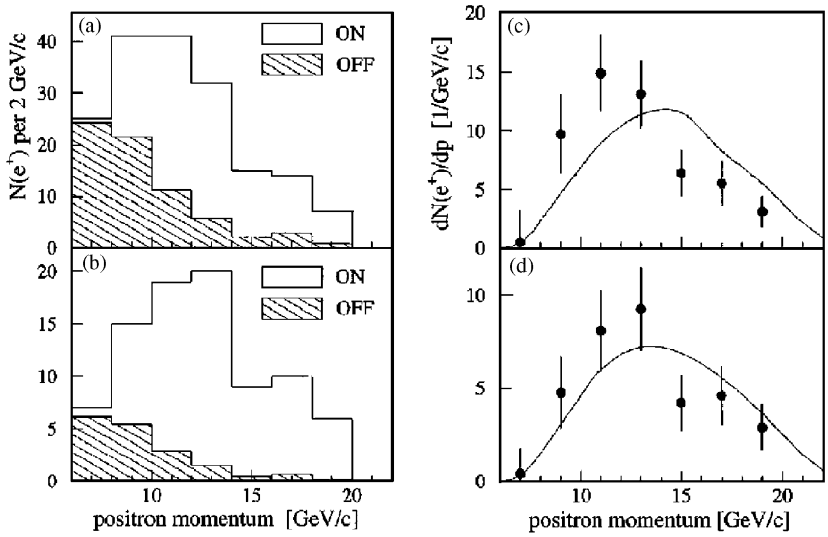

Fig. 68. (a) Number of positrons vs. momentum for laser-on and for laser-off pulses scaled to the laser-on pulses; (b) spectrum of signal positrons obtained by subtracting the laser-off from the laser-on distribution. The curve is the model calculation; and (c) and (d) are the same as (a) and (b) but choosing $q > 0.216$ data [353]. Reprinted with permission from [353]; Copyright 1997 by the American Physical Society.

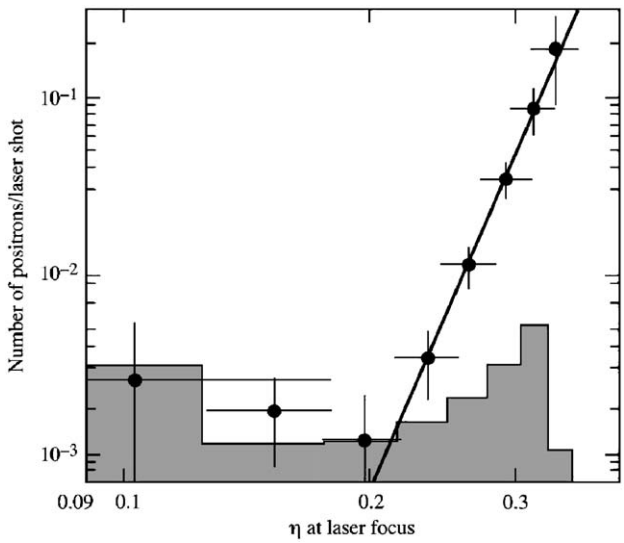

Fig. 69. Dependence of the positron rate on the field strength parameter q normalized to the number of Compton scatters. Lines are simulations for two-step processes (solid line) and trident processes (dashed line) [353]. Reprinted with permission from [353]; Copyright 1997 by the American Physical Society.

Energy–momentum conservation allows pair production also in the strong crossed laser beams, where absorption of a large number of low energy photons from both laser beams takes place. The case of two counter-propagating laser beams has first been investigated in [382], approximating the standing laser wave by an oscillating electric field and neglecting the magnetic field component. The quasi-classical treatment has been adopted for describing the process, making use of small parameters; as the laser field is small compared with the Schwinger field ($E \ll E_c$) and the laser photon energy is also small compared with the electron mass ($\hbar\omega \ll mc^2$). Later, the imaginary time method [383], the Bogolyubov transformation method [384], a resonance approximation [385], and the Fradkin representation for

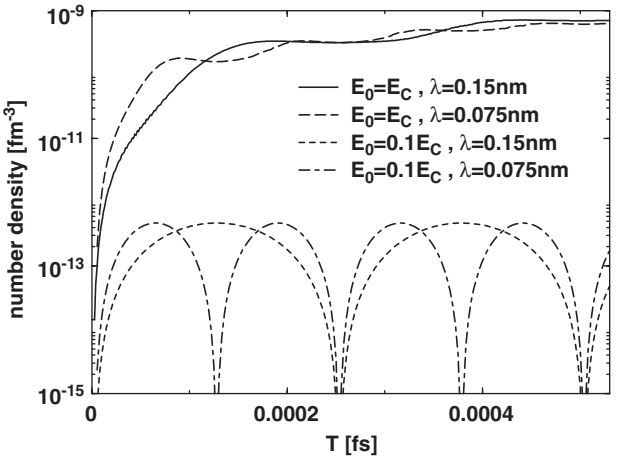

Fig. 70. Time evolution of the number density of pairs. In strong fields, particles accumulate, leading to the almost complete occupation of available momentum space. In weak fields, creation and annihilation occur in tune with the laser frequency [393]. Reprinted with permission from [393]; Copyright 2001 by the American Physical Society.

the logarithm of the fermion determinant [386], were applied in investigating this problem. A review of most of this work may be found in the book [387]. The short-pulse and focused-laser-beam effects in this process are considered in [388]. Conditions for experimental realization of this process are very demanding, with the feasibility analysis in [389] indicating that the best hopes are connected with X-FEL.

Another possibility for vacuum instability in laser fields is pair-production by a strong laser field in a plasma [390]. The plasma refraction makes one of two field invariants non-vanishing, namely, the invariant $\mathbf{E}^2 - \mathbf{B}^2 \neq 0$. Therefore, the nonlinear field Lagrangian, which depends on the field invariants only, does not vanish, making the vacuum unstable even in one laser wave. The back-reaction of the pair-production process on the propagation of the strong laser wave in the plasma has been investigated in [391]. The investigation has been based on the relativistic Boltzmann–Vlasov equation, which incorporates the pair-creation Schwinger rate as a source term. It has been shown that pair-production causes damping of the wave, a frequency upshift, and a change of polarization.

A quantum kinetic theory for pair-production in an oscillating electric field has been developed in a number of papers [392–394]. This theory allows for a self-consistent description of the pair-production process in the field, taking into account modification of the pair-creating field due to the field produced by the pairs themselves. The quantum kinetic equation is non-Markovian [392], which is important in the strong field of order of the Schwinger field. In [393] the quantum kinetic equation has been solved for parameters of a proposed X-FEL. It has been shown that the pair-creation rate is time dependent, in tune with the laser field oscillation. The particle peak-number is independent of the laser frequency. In strong fields, particles accumulate during many periods (see Fig. 70). As is shown in [394], particle accumulation changes qualitatively after $E > 0.25E_c$ (see Fig. 71). In [394], conditions to observe non-Markovian effects in the pair-production process have been found by solving the quantum kinetic equation, coupled with Maxwell's equations. With a 9 TW laser of 8.3 keV photon energy (reckoned achievable by X-FEL) a plasma of created electron–positron pairs is formed which exhibits non-Markovian features. This means that a new pair-creation is dependent of the pair-production history. Moreover, this demonstrates the possibility of plasma oscillations of the created pairs.

7.1.4. Light-by-light scattering

It has been mentioned in the previous subsection that observation of the vacuum instability effect in a strong laser field requires very demanding conditions. In this context, a question arises whether vacuum polarization effects could be observed in the strongest currently achievable laser fields. Vacuum of the electromagnetic field, even if it were stable, still can exhibit nonlinear properties due to the virtual electron–positron pair-creation. Nonlinearity of the field equations, in contrast to the Maxwell equations, arises because of nonlinear terms in the Lagrangian with respect to the two field invariants $\mathscr{G}_1 = \mathbf{E}^2 - \mathbf{B}^2$ and $\mathscr{G}_2 = \mathbf{E} \cdot \mathbf{B}$ [395]. In the electromagnetic field of a plane laser wave, vacuum is

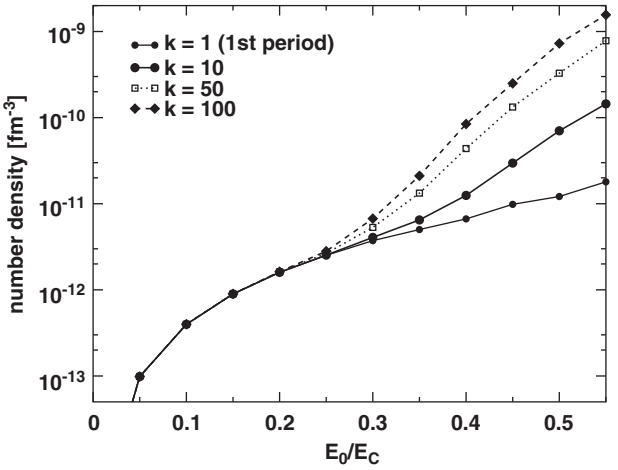

Fig. 71. Peak particle number density versus laser field strength. There is a striking qualitative change at $E_0 \approx 0.25E_c$, which marks the onset of particle accumulation [394]. Reprinted with permission from [394]; Copyright 2002 by the American Physical Society.

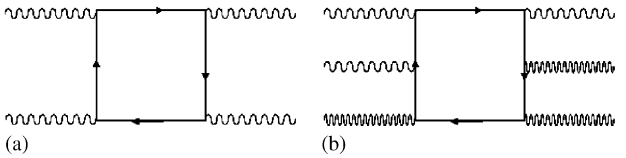

Fig. 72. Feynman diagrams for: (a) light-by-light scattering; and (b) photon splitting.

linear because both electromagnetic invariants are zero in this field. This is not the case if the field is no longer a plane wave. The nonlinearity of vacuum electrodynamics in the field of two photons, which is responsible, in lowest-order, for photon–photon scattering, has been known since Euler's seminal work [396]. Another effect of vacuum polarization, known since the early days of QED, is Delbrück scattering, that is the scattering of a photon in a Coulomb field [397]. Since then, a large number of light-by-light scattering processes have been considered (see the monographs [398] for an overview). One such process is photon splitting in a strong external field. The photon splitting process has first been considered in a strong constant magnetic field [399]. The same process, albeit in a laser field, has been studied in [400]. Furthermore, four-wave interaction in vacuum has been considered in [401], where three synchronized pump waves with frequencies ω_1, ω_2, and ω_3 have been employed to produce the combination mode with a frequency $\omega_1+\omega_2-\omega_3$.

Nonlinear effects in vacuum quantum electrodynamics are governed by two key parameters, namely, E/E_c and ω/m, where E_c is the characteristic Schwinger field (see Eq. (132)), and E and ω are the electric field strength and the frequency of the external field, respectively. In this section we use relativistic units, $\hbar = c = 1$. For small frequencies $\omega/m \ll 1$, the Heisenberg–Euler Lagrangian can be employed [402] yielding analytical results for arbitrarily strong fields [398]. In weak fields, $E/E_c \ll 1$, perturbative treatments of QED are applicable for any frequency. Actually, the experimentally accessible strongest laser fields are weak in a vacuum quantum electrodynamical context ($E/E_c \ll 1$). Therefore, the experimental feasibility analysis of specific vacuum processes can be done using Feynman graphs.

To get an order-of-magnitude estimate for the cross-section (σ) of light-by-light scattering, we resort to dimensional analysis, following [395]. In weak fields, $E \ll E_c$, light-by-light scattering is described by the *box* diagram of Fig. 72(a). According to the Feynman rules, each of the four vertices of the diagram introduces a coefficient α/ω in the cross-section (the factor of $1/\sqrt{\omega}$ in the transition amplitude is connected with normalization of the vector-potential of the vacuum field). The final phase space of the process, $d^3k_1 d^3k_2$, along with a four-dimensional δ-function for the 4-momentum conservation, gives a factor ω^2 (the estimate is done in the center-of-mass of the scattering photons with energy ω). Apart from these factors, the cross-section is proportional to the square of the scattering tensor $\sigma \sim |T|^2$. At $\omega \ll m$, the scattering tensor can be expanded in terms of ω. The first term of this expansion, corresponding to $\omega = 0$, vanishes

for the regularized scattering tensor. Therefore, the expansion begins with the term containing all four frequencies of the four photons of the *box* diagram, i.e., $T \sim \omega^4$. As a result, we have $\sigma \sim \alpha^4\omega^6$. The cross-section should have the dimensionality $(length)^2$. Then, the cross section of the light-by-light scattering is determined unequivocally by

$$\sigma \sim \alpha^4\left(\frac{\omega}{m}\right)^6 \lambda\!\!\!^{-2}_{c}, \tag{136}$$

with the Compton length $\lambda\!\!\!^{-}_{c}$. Exact calculation of the Feynman diagrams for light-by-light scattering gives the constant of proportionality in Eq. (136) to be equal to $139 \times 56/(4\pi^2 \times 5 \times 90^2) \approx 0.0049$ [395]. It should be remembered that Eq. (136) is valid for $E \ll E_c$ and $\omega \ll m$. The probability for light-by-light scattering per unit time, $W = \sigma \cdot j$, may be obtained by multiplying the cross-section by the impinging current density of the laser radiation $j = E^2/\omega$. The number of scattered photons $N = W \cdot N_2$, on the other hand, may be found by multiplying the probability by the number of impinging photons $N_2 = \varepsilon/\omega$, where ε is the energy of the second incident photon beam. Then, the estimated total number of scattered photons during the interaction time τ follows from

$$N \sim \alpha^3(\omega\tau)\left(\frac{\omega}{m}\right)^4\left(\frac{E}{E_c}\right)^2\left(\frac{\varepsilon}{\omega}\right). \tag{137}$$

The probability of light-by-light scattering can be increased by stimulating the process by a third laser beam [401]. Then the number of scattered photons $N^{(st)}$ in the stimulated process may be derived additionally by multiplying by the number of photons in the stimulating beam, $N_3 = \varepsilon/\omega$

$$N^{(st)} \sim \alpha^3(\omega\tau)\left(\frac{\omega}{m}\right)^4\left(\frac{E}{E_c}\right)^2\left(\frac{\varepsilon}{\omega}\right)^2. \tag{138}$$

In the case of scattering of a γ-photon by a laser field, we can use the cross-section formula (136) in the center-of-mass (c.m.) frame of reference of the scattering photons, replacing ω with the c.m. photon frequency ω'. The Lorentz-transformations require that

$$\omega' = \gamma\omega_L(1+\beta) = \gamma(1-\beta)\Omega, \tag{139}$$

where ω_L and Ω are the laser and γ-photon frequencies, respectively, and γ and β are the Lorentz factor and velocity of the center of mass. Eq. (139) gives $\omega' \approx 2\gamma\omega_L$ and $2\gamma \approx \sqrt{\Omega/\omega} \gg 1$. Therefore, the cross-section of a γ-photon scattering by a laser field reads

$$\sigma_\gamma \sim \alpha^4\left(\frac{\omega_L}{m}\right)^6\left(\frac{\Omega}{\omega_L}\right)^3 \lambda\!\!\!^{-2}_{c}. \tag{140}$$

The cross-section is a Lorentz-invariant. Thus, using Eq. (140) in the Lab frame gives the number of γ-photons scattered off the laser wave

$$N_\gamma \sim \alpha^3(m\tau)\left(\frac{\omega_L}{m}\right)^2\left(\frac{E}{E_c}\right)^2\left(\frac{\Omega}{m}\right)^3\frac{\varepsilon_\gamma}{\Omega}. \tag{141}$$

When the process is stimulated by another beam of laser radiation, the number of scattered γ-photons in the stimulated process equals

$$N_\gamma^{(st)} \sim N_\gamma\frac{\varepsilon_L}{\Omega}, \tag{142}$$

with ε_γ the energy of the stimulating γ-beam.

Now let us estimate the photon splitting probabilities. The lowest-order Feynman diagram for γ-photon splitting in the laser field is of order 6 (see Fig. 72(b)). We proceed to estimate the cross-section using the same arguments as above. In the case of one laser photon and two γ-photons in the final state, the final phase space of the emitted γ-photons is $d^3k_1d^3k_2 \sim \omega^6$. A factor $N_L = E^2/\omega_L$ (the laser photon density) in the probability corresponds to each laser photon in the diagram. Then the probability per unit time of split photons in the c.m. may be estimated from

$$W'_{split} \sim \alpha^3 m\left(\frac{\omega'}{m}\right)^5\left(\frac{E'}{E_c}\right)^6. \tag{143}$$

In the Lab frame, the probability per unit time transforms as $W = W'/\gamma$ because of the time Lorentz-transformation. Then expressing the probability via parameters of the Lab frame ($E' = \gamma E$ and Eq. (139)) results in

$$W_{\rm split} \sim \alpha^3 m \left(\frac{\Omega}{m}\right)^5 \left(\frac{E}{E_{\rm c}}\right)^6. \tag{144}$$

Explicit calculations give for the coefficient of proportionality in Eq. (144) the value $4107/(396900 \times \pi^2) \approx 0.001$ [400]. The number of split γ-photons during the interaction with a laser pulse of duration τ may be estimated from

$$N_{\rm split} \sim \alpha^3 m \tau \left(\frac{\Omega}{m}\right)^5 \left(\frac{E}{E_{\rm c}}\right)^6 \frac{\varepsilon_\gamma}{\Omega}. \tag{145}$$

The splitting can also be stimulated by an additional beam of γ-radiation. The number of split γ-photons in the stimulated process $N_\gamma^{(\rm st)} = N_{\rm split}\varepsilon_\gamma/\Omega$ is derived by multiplying Eq. (144) by the number of photons in the additional γ-beam.

The number of events of γ-photon splitting given by Eq. (141) may be compared to that of γ-photon scattering in Eq. (145) via

$$\frac{N_{\rm split}}{N_\gamma} \sim \left(\frac{\Omega}{\omega_L}\right)^2 \left(\frac{I}{I_{\rm c}}\right)^2, \tag{146}$$

where I and $I_{\rm c} = 4.6 \times 10^{29}\,{\rm W/cm^2}$ are the laser and critical intensities, respectively. Thus, we can draw the conclusion that in the laser field of $I = 5 \times 10^{20}\,{\rm W/cm^2}$, splitting is more favorable than scattering when the γ photon energy exceeds 1 GeV.

Next we make some numerical estimates pertaining to the process of stimulated photon–photon scattering in laser beams on the basis of Eq. (138).

One hundred scattering events per laser shot can be achieved in a laser pulse of energy 10 J and duration 100 fs, focused to an intensity of $I = 10^{22}\,{\rm W/cm^2}$. The number of scattering events is very small because it is proportional to some powers of the very small parameters $E/E_{\rm cr}$ and ω/m. The light-by-light scattering cross-section significantly increases with increasing frequency. As an example, using an UV laser pulse of energy 10 J (photon energy 100 eV), pulse duration 100 as, and an intensity of $10^{25}\,{\rm W/cm^2}$, produces 10^8 scattering events per laser shot. Similar estimates may be obtained for γ-photon splitting in a laser field on the basis of Eq. (145). For the same laser parameters as in the last example above, 10^3 splitting events of a γ-photon of 10 GeV energy may be observed.

A more accurate feasibility analysis for the experimental observation of photon–photon scattering, employing the currently available or near-future laser technology may be found in [406]. As an indicator, the minimum laser power $P_{L,\rm min}$ is estimated at which at least one scattering event is possible during the interaction, i.e.,

$$P_{L,\rm min} \simeq 33.5 \left(\frac{\lambda_L}{1\,{\rm nm}}\right) \left(\frac{\sigma_L}{1\,{\rm nm}}\right)^{2/3} \left(\frac{1\,{\rm fs}}{\tau}\right)^{1/3} \left(\frac{1\,{\rm fs}}{\tau_{\rm c}}\right)^{2/3} {\rm GW}. \tag{147}$$

By substituting the laser parameters of a typical focused optical laser: $\sigma_L = \lambda_L = 1\,\mu{\rm m}$ and $\tau = \tau_c = 100\,{\rm fs}$, we obtain $P_{L,\rm min} \simeq 30\,{\rm TW}$, a value that is available today. From this point of view assisted photon–photon scattering could be observed today. Finally, by substituting in Eq. (147) the laser parameters of a focused X-ray-free-electron laser [389]: $\sigma_L = \lambda_L = 0.4\,{\rm nm}$, $\tau = 100\,{\rm fs}$, with a coherence time of $\tau_{\rm c} = 80\,{\rm fs}$ [as given in the "goal" column in Table 1 of [389]], we obtain $P_{L,\rm min} \simeq 1.2\,{\rm GW}$, which is slightly larger than the power 1.1 GW of the planned X-ray-free-electron laser SASE-5 at DESY [389]. Thus, the feasibility analysis, for observation of the scattering of two counter-propagating laser beams in this regime using X-FELs, shows that the requirements are much less restrictive than would be to observe electron–positron pair creation.

Experimental feasibility for observation of photon–photon scattering, employing UV photons from a free-electron laser, and then transforming them into γ-photons via Compton scattering off the electron beam, has been discussed in [404]. Another proposal to detect QED vacuum nonlinearities has been advanced [405] using waveguide modes. In a waveguide, it is possible to achieve a resonant coupling between co-propagating modes of different frequencies, which, due to the QED vacuum nonlinearity, give rise to excitation of a third wave.

Another issue pertaining to the nonlinearity of vacuum electrodynamics concerns vacuum dispersion. The photon polarization tensor, describing refraction indices of a weak probe in a strong laser field, has been calculated in [407].

Birefringence of vacuum in a strong oscillating electric field has been investigated in [408]. In weak fields ($E \ll E_c$), the vacuum refractive index is proportional to the amplitude of the four-wave interaction responsible for light-by-light scattering, expressed by the *box* diagram. Let us show this relationship explicitly. To estimate the refractive index of a probe wave in the field of strong crossed laser beams, we write down an equation for the probe evolution and compare it with the photon–photon scattering amplitude. The evolution equation for the probe amplitude E_p as a result of the four-wave interaction may be written at the phase synchronism as [413]

$$\frac{dE_p}{dt} = i\omega\chi E_1 E_2 E_3, \tag{148}$$

where E_1, E_2, and E_3 are the amplitudes of the interacting waves. When the wave E_3 coincides with the probe and $E_1 = E_2 \equiv E$ are the fields of the crossed laser beams, then the susceptibility, χ, determines the refractive index of the probe through

$$n_v - 1 = \chi E^2. \tag{149}$$

From Eq. (148) the probe wave amplitude may be estimated as $E_p \sim \omega\chi E_1 E_2 E_3 t$. Then the probability of the probe photon scattering per unit time may be expressed as

$$W \sim \frac{E_p^2}{\omega}\frac{V}{t}(V d^3k) \sim \omega^2\chi^2\frac{E_1^2}{\omega}N_2 N_3, \tag{150}$$

with ω the probe frequency, t and V the interaction time and volume, respectively, and $N_{2,3}$ the number of photons in the waves $E_{2,3}$. In Eq. (150) $V d^3k$ stands for the phase space volume. Besides, in the derivation of Eq. (150) $t \to \delta$-function for energy conservation is used. The same probability may be expressed via the cross-section Eq. (136)

$$W \sim \sigma\frac{E_1^2}{\omega}N_2 N_3. \tag{151}$$

Comparing Eq. (150) with Eq. (151) gives the relationship between the light-by-light scattering cross-section and the vacuum refractive index

$$\chi \sim \frac{\sqrt{\sigma}}{\omega^3}E^2 \sim \frac{\alpha^2}{m^4}E^2. \tag{152}$$

Finally, an estimate of the vacuum refractive index can be made from

$$|n_v - 1| \sim \alpha\left(\frac{E}{E_c}\right)^2. \tag{153}$$

In the case of counter-propagating laser waves, the refractive index, for mutually parallel polarizations, is given by Eq. (153) with a proportionality coefficient equal to 16/45. For perpendicular polarization, on the other hand, the corresponding proportionality coefficient is 28/45 [408]. Further, one needs an estimate of the de-phasing $\Delta\phi = (\omega/c)(n_v - 1)L$ on the optical path L due to vacuum dispersion, in order to obtain an order-of-magnitude value for the effect. In a laser field of intensity $10^{20}\,\mathrm{W/cm^2}$ ($\lambda = 1\,\mu\mathrm{m}$) the de-phasing is $\Delta\phi = 10^{-9}$ on the optical path of $L = 100\,\mu\mathrm{m}$. Whereas using an X-ray probe of keV photon energy, the de-phasing value can be increased up to 10^{-6}. The above mentioned de-phasing in an appropriate experimental setup can be observed as a rotation of polarization. In [409] is shown that, in a conventional experimental situation with tightly-focused laser beams and X-ray probe, the probe observation is carried out in the diffraction far zone where influence of the diffraction effects on the polarization rotation cannot be neglected. Quantitative estimates for observation of vacuum birefringence taking into account diffraction effects have shown that it can be nowadays measurable.

Experimental observation of the vacuum polarization effects has been successful so far only for the Delbrück scattering of γ-rays on a heavy nucleus [410] and for the related process of the γ-photon splitting in the field of a heavy nucleus [411]. Experiments on photon–photon scattering at optical energies [412] and stimulated photon–photon scattering [413] have been able to determine only an upper limit on the cross-sections. We should also mention the PVLAS project currently underway for the experimental investigation of vacuum nonlinearities in a constant magnetic field [414].

Harmonic generation in vacuum in the strong field of counter-propagating laser waves has been considered in [406]. Photon–photon scattering would be the lowest order process in which two laser photons simply interact giving rise to another pair of photons with similar frequencies but propagating in different directions. Adiabatic perturbation theory has been used, which is valid when the laser frequency ω_L is much smaller than the characteristic energy m and the characteristic frequency ω of the emitted photons. Typical electric field strengths needed to observe the vacuum high order harmonics are larger than the critical field E_c. In this ultra-strong field regime, n photons from each laser wave can be absorbed (merged) to generate two counter-propagating high energy photons, $\omega_n = n\omega_L$. In this view harmonic generation is the inverse process of photon-splitting in vacuum. The harmonic spectrum shows a wide plateau followed by a cutoff. The cutoff starts approximately at photon energies $\hbar\omega_M \sim \sqrt{\hbar ecE}$, with E the amplitude of the laser field. In the weak laser field regime, $E \ll E_{cr}$, which still corresponds to the electric fields of the strongest available lasers, the vacuum HHG spectra have a perturbative nature.

The discussion above on light-by-light scattering effects strictly covers coherent fields. Another area in nonlinear QED research concerns interaction of a strong coherent radiation field with a photon gas of high energy density [415,416], which necessarily overlaps with the field of radiation hydrodynamics. In [415] the nonlinear coupling between the coherent radiation field and the excitations of the photon gas is discussed. Radiation pressure of the strong incident pulse excites acoustic waves in the photon gas which modulate its energy density. The latter has back-reaction on the incident radiation pulse which, in the case of extremely strong pulses and high gas energy density, may lead to the pulse focusing and collapse. In [415] a rough estimate of the collapse criterion is given, namely

$$k_p^2 r_p^2 |E_p|^2 |E_{gas}|^2 > |E_{char}|^2 \tag{154}$$

with $E_{char} \approx 2.6 \times 10^{18}$ V/cm the characteristic field strength for this type of processes, r_p the pulse width, and k_p the wavenumber. As for the cosmic microwave background, $|E_{gas}| \approx 2 \times 10^2$ V/cm, the criterion (154) requires rather strong incident radiation pulses, not currently available experimentally.

7.2. Laser-induced nuclear reactions

7.2.1. Nuclear reactions in plasmas

The possibility of application of laser radiation in nuclear physics has been a matter of scrutiny for a long time. The review [417] summarizes work in which not so highly-intense visible or UV laser radiation has influence on the low-energy nuclear phenomena mediated by the radiation coupling to electronic shells. For more on the new experiments in this area of investigation, see Ref. [418].

At laser intensities corresponding to $q \gtrsim 1$, the energy acquired by an electron in the laser field during one period is of the order of its rest energy, i.e., in the MeV range. This kind of energy belongs in the realm of nuclear physics and the question immediately arises as to whether *direct* high-energy nuclear physics may be done employing high-intensity laser fields [419]. Thoughts of this nature must have been around since the early nineteen seventies in connection with inertial-confinement fusion research. High-power, large-scale laser facilities of energies exceeding 10 kJ and ns-pulse durations have been used at the Lawrence Livermore National Laboratory (LLNL) to initiate nuclear fusion with a high yield of fusion neutrons [420]. A typical rate for the yield in this kind of experiments is 10^5 fusion neutrons per joule of laser energy. For instance, in Ref. [421] it is reported that 5×10^9 neutrons in a deuterium fusion experiment have been observed using the Nova laser of 30 kJ energy at LLNL. Inertial fusion will not be considered here any further. The reader may find details of new developments in this field, including fast ignition, in [422]. Nowadays, with the development of ultrashort chirped-pulse-amplification (CPA) lasers of about 100 fs pulse-duration, the same laser intensity range of 10^{18} W/cm^2 ($q \sim 1$) can be built with a device energy in the 100 mJ range. This allows for use of terawatt (TW) lasers instead of petawatt ones and for a significant increase in the repetition rate (from 1 shot/h in the case of a large facility to 10 Hz in a table-top system), while at the same time decreasing cost significantly.

The new laser techniques continue to stimulate investigations in the field of relativistic femtosecond laser–plasma interactions and to lead them to reach new frontiers. In particular, the relativistic effects of self-focusing and self-channeling have been discovered. The electron relativistic effective mass increase in a laser field and, consequently, intensity-dependence of the plasma frequency and refractive index, are responsible for the relativistic self-focusing effect. With further increase in laser intensity, the relativistic electron drift in the laser propagation direction, and with it

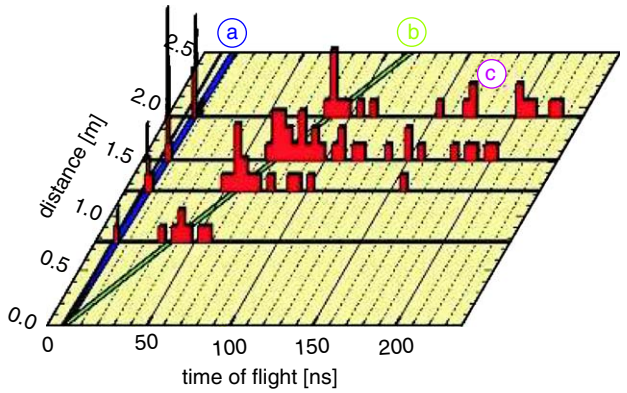

Fig. 73. Temporal distribution of the number of detected pulses at several distances of the detector from the target. The expected delays for neutrons with two different energies are indicated by the two straight lines. The second peak in each readout represents 2.45 MeV D–D fusion neutrons (adapted from [432] by its authors). Reprinted with permission from [432]; Copyright 1998 by the American Physical Society.

the strong magnetic field generation, give rise to the self-channeling effect. These effects cause the laser-beam energy to be concentrated in narrow channels with diameters of a few laser wavelengths [231]. The hot plasma channel provides a medium for high-energy experiments with a few TW laser. This can be done via a cascade process using hot electrons or in a direct process using hot ions.

Thus, in Ref. [423] a cascade process has been proposed for inducing nuclear reactions with lasers: electron beams of MeV energy from a plasma channel to produce γ-quanta via Bremsstrahlung in a high-Z material, for further production of positrons or fission neutrons. Positron production from a hot plasma channel in the cascade process using a high-Z converter is demonstrated in Ref. [424]. A total number of $\sim 2 \times 10^7$ positrons were obtained per laser shot (790 nm, 220 mJ, 130 fs, 10 Hz). This source of positrons exhibits a very favorable scaling for higher laser intensities. A cascade process showing neutron production is realized in Ref. [295]. Hot electrons, ejected from a tantalum surface irradiated by a strong laser beam of intensity 5×10^{18} W/cm^2, emit Bremsstrahlung penetrating into the bulk of the target, and further Bremsstrahlung γ-radiation of MeV energy induces the photonuclear reaction $^9\mathrm{Be} + \gamma \rightarrow 2\alpha + n$. Photonuclear reactions have been used to diagnose γ-radiation in high-intensity laser interaction experiments [291,425] as well as for the characterization of relativistic electron beams produced by the laser wakefield accelerators [426]. In [427] photonuclear reactions $^{181}\mathrm{Ta}(\gamma, \mathrm{n})^{180}\mathrm{Ta}$ and $^{181}\mathrm{Ta}(\gamma, 3\mathrm{n})^{178}\mathrm{Ta}$ on Ta targets produced by γ-rays, has been registered. The laser-induced fission via cascade processes has been demonstrated for ^{238}U in [291,428] and for ^{232}Th in [429]. A very important application of the laser-generated γ-rays has been proposed in [430,431] to dispose of high-level radioactive waste without the need for nuclear reactors or particle accelerators. The idea is to use laser-generated Bremsstrahlung γ-rays to drive photo-transmutation of long lived ^{129}I, with a half-life of 15.7 million years, to ^{128}I, with a half-life of only 25 min, via a (γ, n) reaction.

More interesting, it seems, are experiments on the direct usage of the hot laser channel for nuclear reactions that has been demonstrated in the results of Ref. [432]. The fusion reaction

$$D + D \rightarrow {}^3\mathrm{He} + n, \tag{155}$$

has been realized with the production of high energy neutrons (2.45 MeV) in a laser channel of a deuterium plasma. The experiments were carried out at the Max-Planck Institut für Quantenoptik in Garching (Germany) using the ATLAS Ti:Sapphire laser at a wavelength of 790 nm, a pulse-duration of 160 fs, and an energy of 200 mJ focused down to a 4.5 μm diameter. The peak intensity of the laser system used is of the order of 10^{18} W/cm^2. The target, coated with a pressed deuterated polyethylene powder, was irradiated by a pre-pulse of 30 mJ energy for pre-plasma formation to prepare conditions for the main pulse self-channeling. The detected 4.5 MeV neutrons were attributed to the fusion reaction of accelerated deuterium ions, because other channels of the deuterium disintegration by γ-rays or by fast electrons would produce very low-energy neutrons with much lower cross-sections (see Fig. 73). The deuterium acceleration scenario, confirmed by PIC simulations, looks as follows. The laser energy gets transformed initially into electron longitudinal drift energy. The hot electrons give rise to strong space-charge fields that act to accelerate the

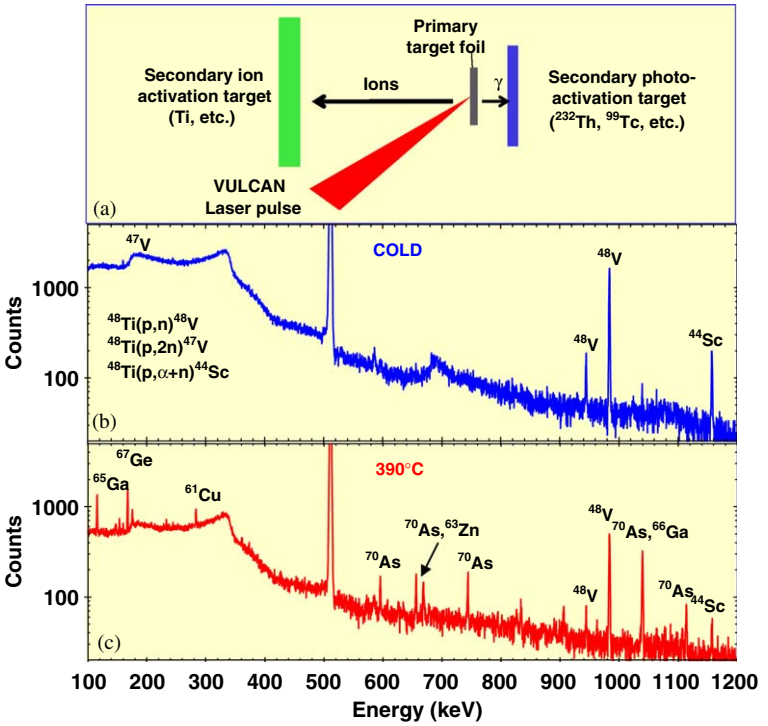

Fig. 74. (a) Typical arrangement for experiment on ion-induced reactions and photonuclear activation. Characteristic γ peaks from a ^{48}Ti secondary target when exposed to ions from a ^{27}Al primary target, which was (b) unheated and (c) heated to 390 °C are shown [438]. Reprinted with permission from [438]; Copyright 2003 by the AAAS.

deuterium ions radially outward from the plasma channel. Then, the accelerated ions collide with cold deuterium ions at the edge of the plasma channel, driving the fusion reactions. The experiment is table-top with focus parameters close to the threshold of self-channeling. Nevertheless, the rate of neutron yield, in such a small-scale facility, is rather low (about 140 neutrons per shot, i.e., around 700 neutrons/J of energy).

A similar experiment, using subpicosecond laser pulses of intensity of a few times 10^{19} W/cm^2 and focused on a deuterated polyethylene target, has been carried out [433]. A large number of neutrons, 10^7, was detected. The emission of neutrons along the laser propagation direction prevails over emission in the transverse direction, which indicates ion acceleration along the laser beam in this experiment. Neutron energy spectra from the fusion reaction (155) induced by the interaction of 50 fs laser pulses of intensity 2×10^{18} W/cm^2 in a solid $(CD_2)_n$ target have been reported and discussed in [434]. The maximum yield was 10^4 neutrons per pulse. The energy spectra were measured in the direction of the laser beam and approximately perpendicular to it. The spectra had a width of 700 keV and an energy shift of about 300 keV between the peaks, corresponding to the two angles. The maximum neutron energy was 4 MeV, indicating that deuterons were accelerated up to 1 MeV. The spectra assume isotropic deuteron acceleration and a reduction of the reaction probability by 30% for deuterons emitted from the front of the target. There were deuterons moving both into and out of the front of the target.

When an intense laser radiation pulse interacts with the surface of a thin target foil, multi-MeV proton [435] and MeV ion beams [436] are produced due to the positive ion and negative electron sheets at the back surface of the target. The energetic heavy ions have been used to induce nuclear reactions in a secondary target when they collide with the stationary atoms of the target and create compound nuclei in excited states [437,438]. The latter de-excite through the evaporation of protons, neutrons, and alpha-particles. Characteristic γ-radiation from nuclei in activated materials are measured, which can serve to diagnose heavy ion acceleration. Thus, Fig. 74 shows spectra of nuclei in an experiment in which an Al target foil was hit by laser radiation of 5×10^{19} W/cm^2, generating protons and ions. Protons and ions hit a Ti secondary target in which ^{48}V, ^{47}V, and ^{44}Sc radioactive nuclei are created via (p, n), $(p, 2n)$, and $(p, \alpha + n)$ reactions on ^{48}Ti, identified by their characteristic γ-emission. It was shown that heating of the target increases the energy of the heavy ions. Further results [439] show how to generate the intense, short-lived isotopes ^{11}C and ^{18}F for

positron emission tomography, using the VULKAN Nd:glass laser at the Rutherford Appleton Laboratory in the UK (pulse duration 750 fs, energy on target 220–300 J, intensity of the order of $2 \times 10^{20}\,\mathrm{W/cm^2}$) and also, for the first time, the synthesis of 2-[^{18}F]-fluorodeoxy glucose, the workhorse of positron emission tomography.

An interesting application of a beam of MeV protons from a laser-irradiated thin foil target has been demonstrated in an experiment [440] using the petawatt VULKAN, with energy of 400 J, average duration 0.7 ps, and a peak intensity of $4 \times 10^{20}\,\mathrm{W/cm^2}$. It was shown that the laser-generated proton beam has a broad energy distribution, quite similar to the spectrum of evaporative protons below 50 MeV energy produced in the GeV-proton-induced spallation reaction. Using this fact and from the experimental results of the investigation of the residual nuclide production on a Pb target, due to its bombardment by a laser-produced proton beam, the data is recovered for the residual nuclide production due to evaporated protons in a GeV spallation reaction on Pb. Moreover, as the energy spectrum of accelerated protons can be tailored by controlling the laser-irradiated target parameters [441], it is possible to apply the proposed method for the intranuclear cascade and other spallation reactions.

A fusion reaction can be also driven in an underdense deuterium plasma, as was shown in [442], where the laser ponderomotive force is able to accelerate the ions to keV energies. Fusion neutrons provide information about ion kinetics, showing that the Coulomb explosion of ions cannot explain solely the ions' observed energies. Non-collisional heating plays a significant role in the heating of ions to thermonuclear fusion energy.

7.2.2. Nuclear reactions with clusters

Laser interactions with clusters offers a unique opportunity to achieve efficient fusion neutron production employing table-top femtosecond lasers, so far observed only in large-scale facilities. In the case of clusters the neutron production is debris-free in contrast to the laser–solid interaction. Experiments on photoionization of atomic clusters with high intensity femtosecond lasers, intensities in excess of $10^{16}\,\mathrm{W/cm^2}$, have shown that ions of up to MeV energies can be created [233]. In Ref. [288] this effect is used for the realization of deuterium fusion in a cluster jet with very high efficiency. A cluster constitutes a form of matter intermediate between a bulk solid and a gaseous atomic medium. The solid density of atoms inside a cluster and their finite microscopic size make exceptional features.

When clusters are exposed to a strong laser radiation, the rapid ionization creates a micro-plasma in the cluster. When the laser radiation is very strong and the cluster size R is rather small, namely when $eE/m\omega^2 \ll R$, with the laser field strength and frequency E and ω, respectively, the laser field can remove the electrons from the cluster directly. Otherwise, the cluster of more than 1000 atoms undergoes fast collisional heating, up to many keVs, during a timescale less than one picosecond, before the electrons escape because their mean free path becomes larger than the cluster size. Then a Coulomb explosion occurs which accelerates the ions up to tens of keV energies, allowing fast energy transfer from the electrons to the ions and an efficient laser energy deposition in the created plasma (nearly 90% of the laser energy). Fast ions created in this process can be used to initiate nuclear fusion reactions with deuterium clusters. Details of the cluster heating mechanisms leading to the nuclear reactions can be found in the review [443].

This kind of process has been investigated Ditmire and his coworkers [288]. A table-top laser of 120 mJ energy, a wavelength of 820 nm, a pulse duration of 35 fs, and a repetition rate of 10 Hz, has been used in this experiment.

In the experiment laser radiation is focused into a deuterium gas jet, cooled to -170° to create large clusters of deuterium with a size of 50 Å (see Fig. 75). The average deuterium ion energy was inferred to be about 2.5 keV, which suffices for the fusion reaction to have significant probability. Deuterium-fusion neutrons were registered by time-of-flight spectrometry. Neutrons with energy 2.45 MeV were identified as a well known signature of the fusion process in Eq. (155), (see Fig. 76).

A laser spot size of 200 μm (intensity at focus $2 \times 10^{16}\,\mathrm{W/cm^2}$) optimizes the fusion neutron yield to 10^4 neutrons per laser shot (10^5 neutrons per joule of incident laser energy). The fusion neutrons disappeared if the gas jet temperature was not low enough to clusterize the gas, underlining the role of clusters in the process. Comparable results have been also obtained in the investigation of fusion neutrons from deuterium and deuterated methane clusters in a strong laser field [285–287].

To increase the efficiency of the ion acceleration via the Coulomb explosion of clusters, one has to increase the cluster electrostatic potential energy. An obvious way to do that is to increase the cluster size, while keeping the size small enough to allow the electrons to escape and the Coulomb explosion to take place. A more interesting, and nontrivial, way of increasing efficiency of the Coulomb explosion of a cluster using clusters formed from heteronuclear molecules (HI, NH_3, and pyradine) has been advanced in Ref. [444]. Fully stripped heteronuclear molecular clusters contain ions with higher Z. That increases the electrostatic potential energy of the stripped cluster and, therefore, increases the

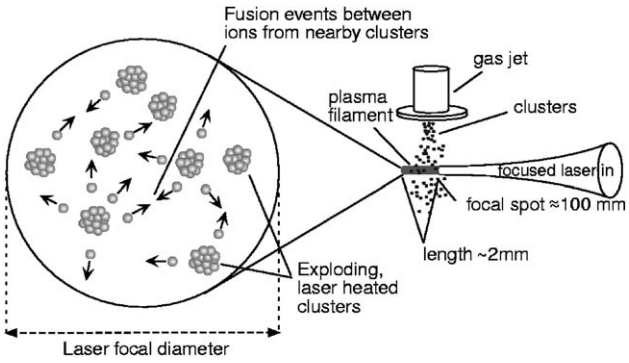

Fig. 75. Layout of the deuterium cluster fusion experiment [288]. Reprinted with permission from [288]; Copyright 1999 by the Macmillan Publishers Ltd.

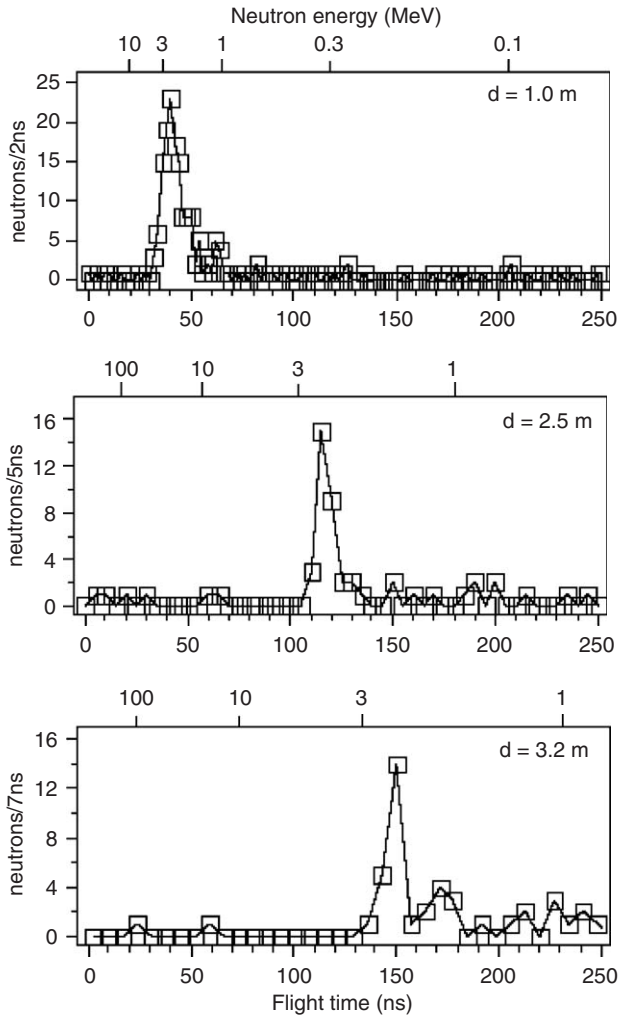

Fig. 76. The time-of-flight spectrum of particles detected on the neutron detectors for three plasma-detector separations (1, 2.5 and 3.2 m). Particle flight time is shown along the top axes. The presence of 2.45 MeV neutrons is clearly visible in all these spectra [288]. Reprinted with permission from [288]; Copyright 1999 by the Macmillan Publishers Ltd.

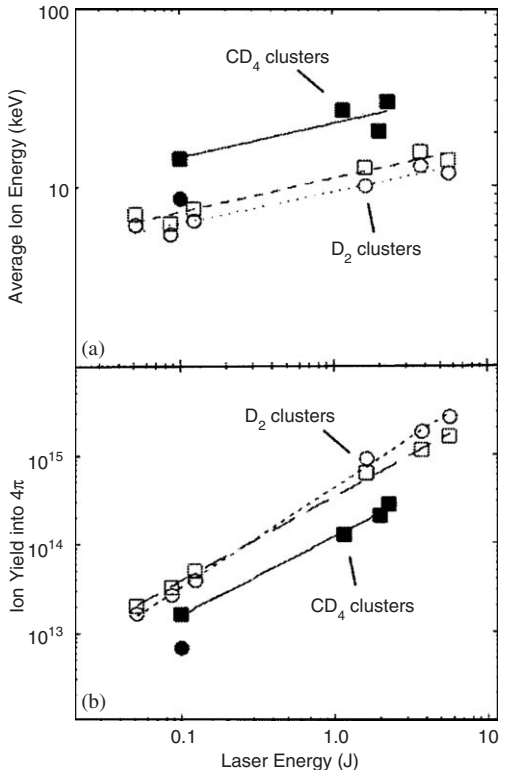

Fig. 77. Average deuterium ion energy (a) and total ion yield (b) as a function of laser energy for both D_2 (open circles and squares) and CD_4 (filled circles and squares) cluster plasmas. The ion number and energy dependence on pulse energy were each fit to a power law dependence (shown by lines) [23]. Reprinted with permission from [23]; Copyright 2004 by the American Institute of Physics.

energy of the deuterons which get ejected as a result of the Coulomb explosion. Moreover, because of the difference in charge to mass ratio, the Coulomb explosion energy does not get distributed uniformly between the deuterium and the heavier high-Z ions, as has been pointed out in Ref. [445]. Let m_B and q_B be the mass and charge of a heavy ion, respectively, and let m_D denote the deuterium mass. If the parameter

$$\eta = \frac{m_B}{q_B m_D}, \tag{156}$$

is greater than unity, the deuterium ions explode in an outer shell and acquire more energy than the ions. Enhancement of the ejected proton energy, from HI clusters irradiated with 100 fs laser pulses, has been confirmed in Ref. [446]. Observation of nuclear fusion from heteronuclear molecular clusters has first been reported in Ref. [286] using 800 mJ, 35 fs laser pulses at an 820 nm wavelength, focused to an intensity above 10^{17} W/cm^2 in deuterated methane clusters. The reported yield is 10^4 neutrons per shot. More comprehensive investigations of nuclear fusion in heteronuclear cluster plums has been reported in Ref. [23]. By measuring the cluster plum parameters and the ejected ion emission characteristics, for deuterium and deuterated methane cluster plasmas under similar conditions, the same investigators [23] proved that deuterated methane clusters yield higher ion energies and result in more efficient fusion reactions than the neat deuterium clusters. The cluster size in the case of deuterium (D_2) and deuterated methane (CD_4) has been measured employing a Rayleigh scattering method, and the ion yield and energy distribution have been found from time-of-flight ion spectroscopy. Furthermore, the fusion neutron yield (with 2.45 MeV energy) has been registered. The Lawrence Livermore National Laboratory JanUSP laser has been used, delivering up to 10 J of energy per pulse of 100 fs duration at 800 nm wavelength (focused intensity of up to 10^{20} W/cm^2). Although, at these experimental conditions, the methane cluster size appears to be about half that of the D_2 cluster, yet the energy of the deuterium ions produced from methane via Coulomb explosion is almost twice as high as that from D_2, for a laser pulse energy of 100 mJ (see Fig. 77).

This is mainly due to highly-charged carbon ions (C^{+6}) present in the methane cluster which increase the electrostatic potential energy of the Coulomb explosion. The kinematic parameter is $\eta \approx 1$, in this experiment, and separation of exploding deuterium and carbon shells does not play a significant role. The fusion neutron yield at 100 mJ of laser energy is twice as large for CD_4 as it is for D_2 (see Fig. 78).

In a recent experiment [25] fusion neutrons were produced by laser irradiation of a heavy-water (D_2O) spray target. Heavy-water droplets, 150 nm in diameter, are 10–15 times larger than the usual cluster size. Due to this, deuterons were accelerated to significantly higher energies (up to 1 MeV) (see Fig. 79), yielding much higher neutron outcome per accelerated deuteron, compared to the cases of other cluster sources obtained before. A laser pulse, of 35 fs duration and a $1 \times 10^{19}\,W/cm^2$ intensity, was used. At the pulse energy of 0.6 J, 6×10^3 neutrons were produced by 10^{11} deuterons. The D(d,n) reaction probability was estimated to be 6×10^{-8}, which is two orders of magnitude larger than in cluster targets.

The work of Ref. [447] is devoted to the experimental and computational investigation of laser–cluster interactions for peak laser intensities above $10^{18}\,W/cm^2$. It studies the resultant fusion yield as a function of the laser and target parameters to find optimal conditions for performance. The experiment used the JanUSP laser of LLNL. The maximum pulse energy was 10 J and the pulse duration was varied from 100 fs to 1 ps. The work explains a feature of the laser–cluster experiments in which the neutron yield follows a quadratic power law dependence on pulse energy. This is mainly due to the increase of ion yield with increasing laser pulse energy. What is more important is that it was shown, experimentally and numerically, that the ion energies vary only weakly by changing pulse energy at a given pulse duration (see Fig. 80). This suggests that the cluster explosion mechanism in this regime is unaffected by the peak laser intensity, even in the domain of relativistic intensities. Moreover, the ion energies, due to the cluster explosion, are determined only by the ratio of the cluster ionization time to its expansion time due to Coulomb explosion (see Fig. 81). The ionization time is defined as the time during which the laser intensity rises from the value of the atomic ionization threshold up to the second threshold value for the complete ion charge uncovering, i.e. when the laser electric field exceeds the space charge field of the fully stripped cluster. When the ionization time is shorter than the cluster expansion time then in the rising edge of the laser pulse the cluster will be completely stripped, after which a Coulomb explosion will occur. While in the opposite case, the cluster ionization process will continue during expansion, which will result in lower kinetic energy for the ions. The ionization time depends on the laser pulse duration (see Fig. 82). Consequently, the cluster explosion energy strongly depends on the pulse duration. Fig. 81 indicates also that the explosion energy is only weakly enhanced by the pulse duration reduction below 200 fs, when the cluster's complete ionization occurs instantaneously. Meanwhile, the cluster explosion energy is rather insensitive to changes of the laser intensity above

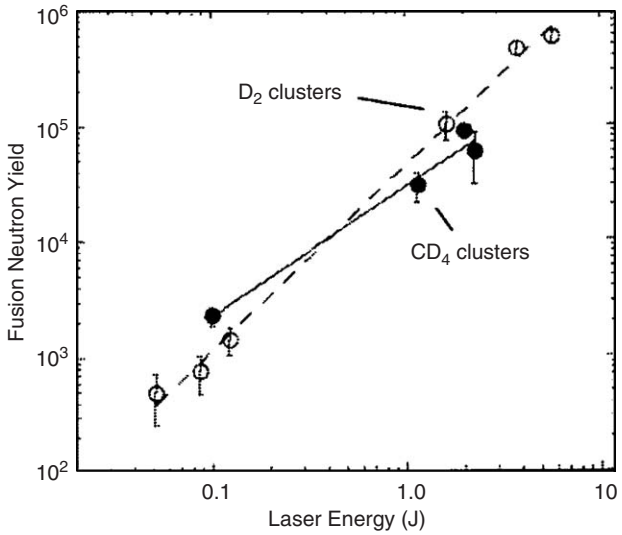

Fig. 78. Fusion neutron yield from exploding D_2 (open circles) and CD_4 cluster (filled circles) plasmas as a function of pulse energy. The solid lines are the least mean squares fit to a power law dependence of the yield on pulse energy [23]. Reprinted with permission from [23]; Copyright 2004 by the American Institute of Physics.

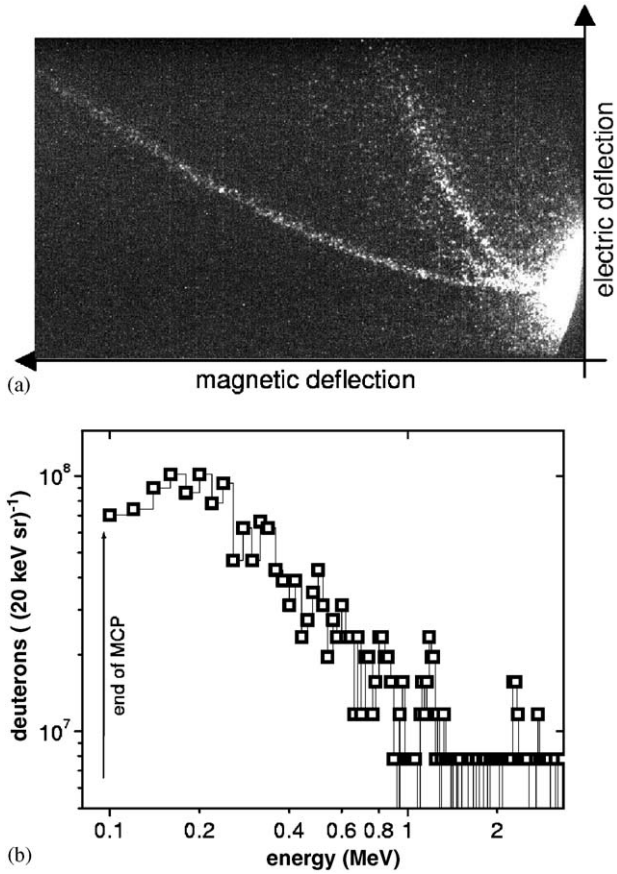

Fig. 79. (a) Single-shot ion spectrum registered on a microchannel-plate (Thomson parabola spectrometer) from a heavy-water D_2O spray of submicron droplets at 135° emission direction. Blob at the right: zero-point and spectrometer axis; blurred O^+ and O^{2+} traces due to propagation through ambient target material, and deuteron trace. (b) Determined deuteron spectrum. The low-energy cut for $E < 0.1$ MeV is due to limited size of the microchannel-plate [25]. Reprinted with permission from [25]; Copyright 2005 by the American Institute of Physics.

10^{18} W/cm^2 (this intensity exceeds the second threshold value of the field for nm size clusters). This is because the change of the laser intensity at a given pulse duration does not change the ionization time significantly. The conclusion that may be drawn is that the process at laser intensity above 10^{18} W/cm^2 is governed by the pure Coulomb explosion of the cluster. That is why the observed fusion yield scales primarily as a plasma volume effect.

The high and efficient yield of neutrons as a result of the laser-driven nuclear fusion reaction can be used to diagnose ion energies [26], as well as to develop compact, high-flux, ultra-fast, and pulsed neutron sources for time-resolved material damage studies. The neutron yields in Table 1 are taken from Table 1 of Ref. [447], where other parameters of some available table-top and medium-scale laser-driven fusion neutron sources are gathered. The neutron flux of a source has to be upgraded to 10^9 neutrons per shot to fulfil the requirements of an application.

Another target for possible laser-induced nuclear reactions, namely aerogels, has been proposed in [443]. The aerogel is a system similar to a cluster and characterized by the correlation radius R_c. At $r > R_c$, the aerogel has a homogeneous structure and a fractal structure for $r < R_c$. As is shown in [443], a laser-created plasma in this kind of target can be suitable for nuclear reactions and can serve as a source of neutrons with alternative parameters.

7.2.3. Nuclear reactions with single atomic systems

Recently, a couple of proposals have been advanced which prove that an elegant process of initiation of nuclear reactions, via interaction of a single ion with a strong laser field, is feasible with present day laser technology. In [317] feasibility of a new effect of fast re-collision in the MeV energy range has been established. The effect

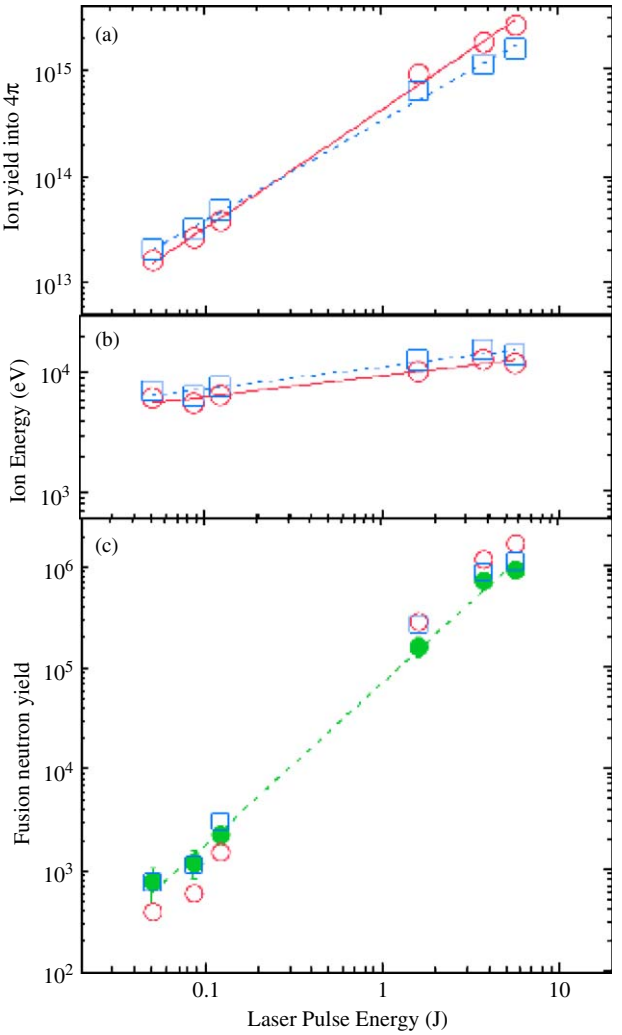

Fig. 80. Ion yield (a), average ion energy (b), and fusion neutron yield (c) as a function of laser energy for 100 fs pulse duration. The ion yield and energies, as well as the expected fusion neutron yield, were determined from two Faraday cup signals: cup A 0.52 m behind the laser focus and aligned 15° from the laser propagation axis (open circles) and cup B 0.36 m from the laser focus and aligned 15° from the polarization axis and 90° from cup A (open squares). The measured fusion neutron yield (Y) at each energy (E) is also shown (filled circles) and fitted to a power law dependence (dotted line) with $Y = QE^{\alpha}$ where $Q = 7.1 \times 10^4$ and $\alpha = 1.6$ [447]. Reprinted with permission from [447]; Copyright 2004 by the American Physical Society.

appears when a multiply-charged hydrogen-like ion counter-propagates at high energy with respect to an applied very intense laser pulse. The laser wavelength in the rest frame of the ion becomes smaller than the ground state's radius, which allows to accelerate the electron to MeV energies within a very short time, corresponding to the quarter of a wavelength. Then a fraction of the wave packet acquires MeV energy before leaving and passing close to the nucleus (see Fig. 83). Using a KrF laser system with an intensity of 1.5×10^{20} W/cm^2, and accelerating the ions up to a gamma-factor of $\gamma \approx 3300$, partial re-collisions in the MeV range can be achieved. It has been shown that an average electron momentum $p \simeq 410.5$ a.u. can be reached using the above-mentioned parameters. The momentum magnitude close to the core is just above 387.6 a.u. (1.022 MeV/c) and the momentum flow passes straight through the core. The current density has its maximum at a location somewhat away from the core, but, with a magnitude of 602.0 a.u., it should be large enough to give a substantial probability for nuclear reactions. This renders nuclear reactions possible with single laser-driven ions.

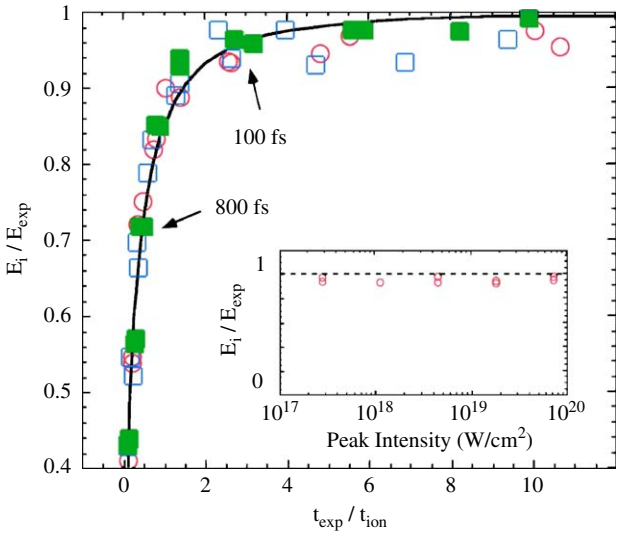

Fig. 81. Average ion energy from a cluster explosion plotted against the ratio $g = t_{exp}/t_{ion}$. The cluster expansion time $t_{exp} \sim 10.7$ fs, and the cluster ionization time was calculated at various pulse durations between 25 and 3200 fs (the results at 100 and 800 fs are marked) for clusters of sizes $N = 100$ (empty circles and squares) and $N = 1000$ (filled circles and squares). The peak laser intensities were 2.8×10^{17} (circles) and 1.12×10^{18} W/cm^2 (squares). The inset shows a calculation of the final explosion energy for a cluster of size $N = 100$, a pulse duration of 100 fs, and various peak laser intensities [447]. Reprinted with permission from [447]; Copyright 2004 by the American Physical Society.

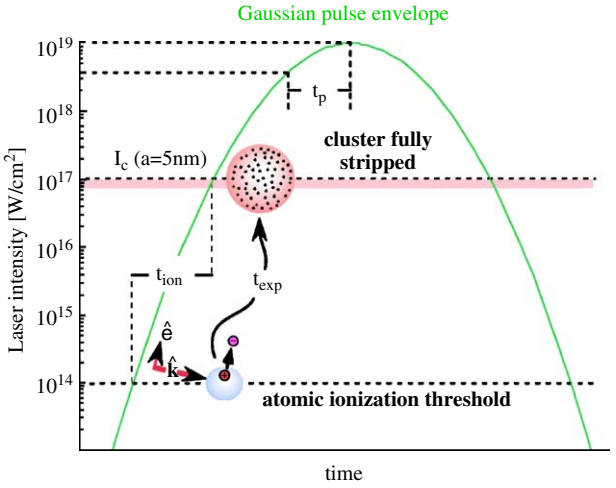

Fig. 82. Schematic of cluster ionization and expansion dynamics during the laser pulse. The ionization time t_{ion} is determined by the time required for the laser intensity to rise from the first threshold, at which atomic ionization begins, to the second threshold, at which the electric field of the laser exceeds the threshold for complete ion charge uncovering (approximately when the laser electric field exceeds the space charge electric field of the fully stripped cluster). The second threshold, which is shown for a cluster of radius $a = 5$ nm, depends on the size and density of the cluster and will fall from its initial value as the cluster expands. Because of the finite duration of the cluster ionization time, the cluster will explode more slowly than its characteristic expansion time t_{exp} resulting in a final kinetic energy below the characteristic energy of the expansion [447]. Reprinted with permission from [447]; Copyright 2004 by the American Physical Society.

A more exotic proposal has been advanced in [451] to initiate nuclear reactions during interaction of a muonic molecule (e.g. $dd\mu^-$) with a strong laser field. After bond breaking of the muonic molecule, the strong laser field accelerates the deuteron by further recollision with the $d\mu^-$ atom. The recollision energy can be high enough to initiate a fusion reaction. In fact, in a situation like that, the muonic molecule survives much stronger laser fields than does an

Table 1
Neutron yield from recent table-top and medium-scaled fusion sources [447]

Target	Neutron yield (into 4π)	Ref.
C_8D_8 and D_2 solid	7×10^7	[448]
C_2D_4 solid	1×10^2	[432]
CD_2 solid	1×10^7	[433]
CD_2 solid	1×10^4	[434]
C_8D_8 solid	9×10^5	[449]
CD_2 solid	5×10^4	[450]
D_2 gas	1×10^6	[442]
D_2 clusters	1×10^4	[288]
D_2 clusters	2×10^6	[287]
CD_4 clusters	7×10^3	[286]
CD_4 clusters	1×10^5	[447]

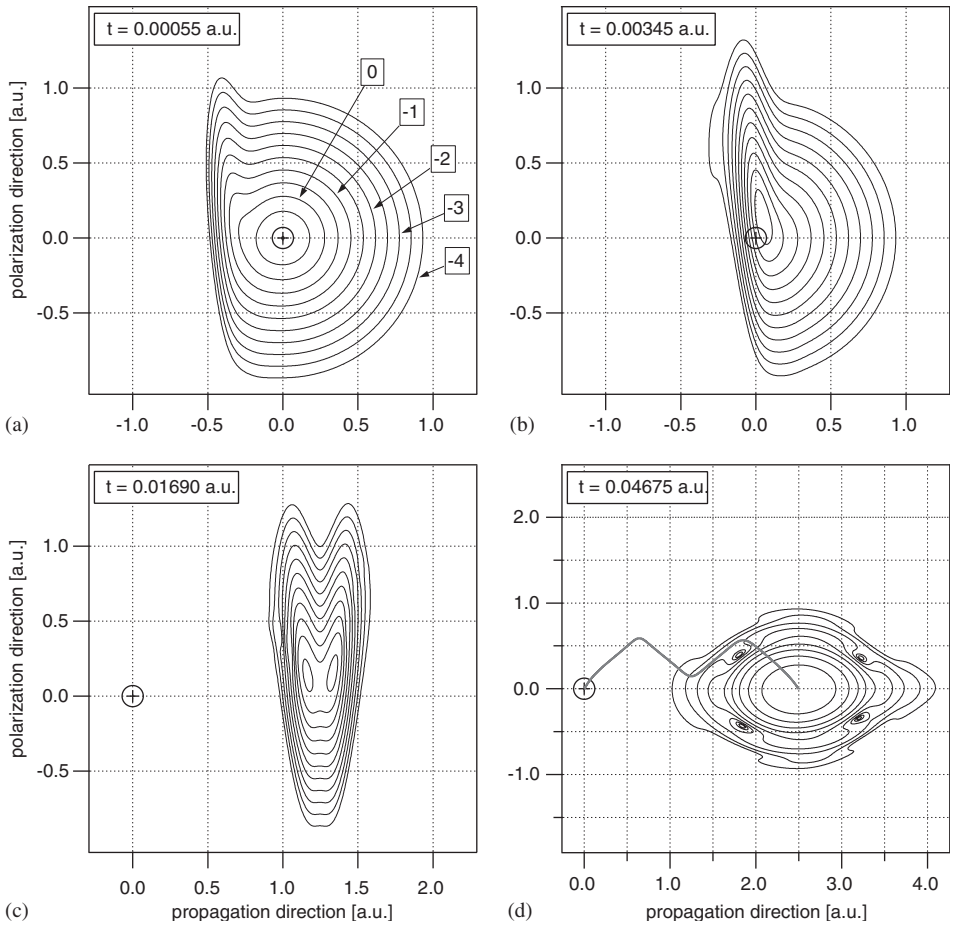

Fig. 83. Snapshots of the electron wavepacket taken at four different times t from 0.00055 to 0.04675 a.u. the contour lines indicate the logarithm of the probability density as shown by the labels in (a). In (d) the thick line which starts at the origin marks the trajectory of the position operator's expectation value. The marker '+' indicates the position of the ionic core with the charge $Z = 8$. The Lorentz transformed amplitude and frequency of the laser field are $E_0 = 4.334 \times 10^5$ a.u. and $\omega_0 = 1208.5$ a.u., respectively [317]. Reprinted with permission from [317]; Copyright 2004 by the IOP Publishing Limited.

ordinary molecule. This is due to the large mass of the muon (about 200 times that of the electron). Accordingly, the Bohr radius of a muonic atom is 200 times smaller than that of a normal atom. The ionization potential of a muonic atom and the potential well of a muonic molecule are 200 times larger than those of a normal atom or molecule. Therefore, ionization and bond softening occur at larger laser field strengths than for a normal atom. For example, ionization and bond braking in a $dd\mu^-$ take place at an intensity of $10^{22}\,\mathrm{W/cm^2}$. Moreover, as is shown in [451], the bond softening channel can dominate over the ionization one. Thus at an intensity of $10^{22}\,\mathrm{W/cm^2}$ the dissociation rate is $10^{14}\,\mathrm{s^{-1}}$ while the $d\mu^-$ ionization rate is $10^4\,\mathrm{s^{-1}}$. Therefore, the muonic molecule disintegrates in the strong laser field into a muonic atom and a deuteron. The latter is accelerated by the laser field to as large as 0.1–1 MeV energy before its re-collision with $d\mu^-$. The laser-induced fusion reaction rate has been estimated to be $R_{\mathrm{laser}} = 1.2 \times 10^5\,\mathrm{s^{-1}}$ at the above-mentioned laser intensity. Although this rate is small compared with the large background fusion signal, the fragments of the laser-induced fusion reaction can be distinguished by their larger energy compared to the low energy fragments of the background fusion reaction.

So far we have considered only indirect involvement of the laser radiation in nuclear reactions. Laser radiation is used only to accelerate particles, incoherently or coherently, up to energies appropriate for nuclear reactions. Finally we note that *direct* and appreciable nuclear multi-photon couplings are also feasible. The conditions for that involve moderately pre-accelerated particles and intense X-FEL laser light [452].

In conclusion, present-day table-top laser facilities are capable of driving nuclear fusion reactions. These facilities use laser self-guiding channels, foils or gas clusters and achieve rates approaching those previously achievable only in large-scale facilities of the type used in inertial confinement fusion research, and with significantly enhanced repetition rates.

7.3. Laser-induced particle physics

The earliest indications that laser fields may have a role to play in particle physics research go back to the work of Ritus and others [453–455], where influence of laser radiation on the muon decay $\mu \to e\nu\bar{\nu}$, pion decay $\pi \to \pi^0 e\nu$ and $\pi \to \mu\nu$ or $e\nu$, and neutrino radiation of the electron $e \to e\nu\bar{\nu}$ due to the weak interaction, have all been considered. Nuclear beta decay in a laser field has also been studied [456]. Modern-day achievements and the visible prospects of techniques involving lasers indicate that there are clear possibilities for doing *high-energy* particle physics with lasers. The strong interaction of particle physics comes into play at distances of order $r \sim 1\,\mathrm{fm} = 10^{-13}\,\mathrm{cm}$ and below. The corresponding energies involved are of the order $\varepsilon \sim c\hbar/r \sim 1\,\mathrm{GeV}$. A concept for an optical electron–positron collider in the high-energy regime has been advanced in [457]. Rather than improving the characteristics of current laser-accelerator schemes, *an alternate type of* laser-driven electron–positron collider has been proposed which employs positronium atoms instead of electron and positron beams. In contrast to conventional electron–positron colliders, it unites in one single stage the electron and positron acceleration and focusing, and provides *microscopic* head-on-head collisions with a significant enhancement of the luminosity. This is because, in conventional colliders, bunches of accelerated electrons and positrons are focused to collide head-on-head *incoherently*, i.e., bunches collide head-on-head but electrons and positrons in the bunch do not. In the situation with laser fields, electrons and positrons originating from positronium may collide head-on-head *coherently* (the mean impact parameter for the coherent re-collision is microscopic, of the order of the Bohr radius).

Single laser pulses are not suitable for realizing a laser-driven collider, because the main part of the laser energy is misused to accelerate the created particles along the laser beam direction and the spreading of the electron (or positron) wavepacket is usually large, hence diminishing the advantage of coherent collisions [458]. Adding an extra static magnetic field to the laser pulse helps to avoid laser energy waste. In the magnetically-assisted collision setup, electrons and positrons acquire longitudinal momentum from the laser field, then the magnetic kick turns the particles' longitudinal momenta into the transversal direction, boosting electron and positron scattering energy in their center-of-mass. Using a spatially-confined magnetic field of $10^4\,\mathrm{T}$ and the laser intensity of $10^{25}\,\mathrm{W/cm^2}$, a total scattering energy of 100 GeV is achievable, being almost 35 times larger than without the magnetic field and sufficient to produce a Z^0 boson. Nevertheless, the re-collision time, and with it the electron (positron) wave packet spreading, is so large it diminishes the advantage of microscopic collisions. Replacing the magnetic field by a second counter-propagating laser pulse of the same intensity cancels the electron drift and with this the large acceleration (wave packet spreading) time. Moreover, if the laser beams are circularly polarized and equal-handed, the resulting magnetic field, being directed along the electric field, induces a focusing force and the wave-packet spreading is substantially reduced [256,457].

Suppression of the electron drift induces rapid head-on-head re-collisions during one laser period in the lab frame. Total c.m. energy of 3.2 GeV can be reached while keeping the impact parameter below approximately 10 Å and allowing to fulfill the coherent collision condition.

The coherent collider concept considered in [457] may enable initiation of particle reactions in the GeV regime, provided that a dense gas of positronium atoms (alternatively, a Bose–Einstein condensate of positronium atoms) or an electron–positron plasma, would be available [459,460].

8. Conclusions and outlook

Recent progress in the study of phenomena in laser–matter interactions, which require a non-dipole or relativistic description, has been reviewed in this article. Following are some final thoughts, conclusions and hints at plausible future developments.

The relativistic dynamics of simple basic atomic systems has been investigated both classically and quantum mechanically. Subtle quantum effects, such as spin-induced dynamics and quantum interferences in laser-driven electrons and atoms were shown to alter the dynamics in a characteristic manner. Most still await experimental confirmation in the relativistic regime because of clear challenges in their detection.

In the field of laser acceleration, the most successful experimental activity is directed at plasma-based laser accelerator schemes [461]. In addition to that, we have demonstrated that the numerous proposals of laser acceleration in vacuum have considerable potential as well. They include ultrashort laser pulse interactions, crossed-beam geometries and the inclusion of auxiliary static fields. We emphasize the recent efforts in that direction [219–222] which report on proof-of-principle experiments.

For ATI and HHG from laser-driven multiply-charged ions at relativistic intensities, we stressed both the advantages, in reaching enormous energies by the released electrons and emitted photons, and the difficulties, in controlling the relativistic quantum dynamics allowing for the re-collisions. We stressed especially the importance of various investigations aimed at devising schemes in which some additional effects counteract the relativistic drift of the electron in ATI and HHG at relativistic intensities. In particular, the use of special laser geometries or atomic systems turned out to be promising. Finally, relativistic multi-photon physics was discussed at length and shown to be suitable for high-frequency generation.

The complex quantum dynamics of systems ranging from few-electron atoms and few-ion ensembles to clusters and thin crystals was investigated and will continue to remain a challenging topic. In thin-layer-laser interactions, e.g., idealized considerations have suggested promising X-ray yields, for experimentally less demanding situations collective effects and plasma instabilities remain to be investigated. Apart from the indicated few exceptions based on rather restricted models, many-particle relativistic quantum dynamics is virtually unexplored.

Despite significant progress in laser-mediated quantum electrodynamics, conditions for the experimental observation of vacuum instabilities and vacuum polarization effects remain challenging. Further practical ideas in this field are very desirable. We would also like to point out that open questions still exist in the theoretical treatment, such as concerning vacuum instabilities in inhomogeneous fields, particularly in extremely strong Coulomb and strong laser fields. Laser-induced nuclear reactions have been demonstrated in impressive manners and further ideas for nuclear spectroscopy are put forward. Finally, there are clear prospects for particle physics based on strong lasers rather than conventional accelerators and colliders.

Significant advances in laser technology are likely to continue to be achieved for some years to come, hopefully leading to further enhancements in extremely short and high-frequency pulses and a sizeable jump in the achieved power. These developments will surely stimulate the emergence of novel ideas for measuring some of the effects alluded to above, and others not even thought of today. Theoretical calculations, on the other hand, stand to benefit significantly from more advanced software development, utilizing the continued progress made in CPU speed and parallel-programming capabilities. All of this is guaranteed to open up new research areas, push currently active ones to new frontiers, and generate further excitement in the field of laser–matter physics.

Acknowledgments

We would like to thank all the people whose work has been reviewed in this article and who have been supportive and willing to send us figures and other relevant material at short notice. We have benefited in this field from numerous

fruitful discussions over the years with former collaborators, colleagues and mentors: Hamlet Avetissian, Wilhelm Becker, John S. Briggs, Keith Burnett, Lee Collins, Todd Ditmire, Farhad Faisal, Michael Fedorov, Rainer Grobe, Charles Joachain, Peter L. Knight, Gagik Kryuchkyan, Alfred Maquet, Jon Marangos, Guido Mocken, Peter Mulser, Jens Prager, Georg Pretzler, Howard Reiss, Luis Roso, Jan-Michael Rost, Wolfgang Sandner, Roland Sauerbrey, Tony Starace, Andreas Staudt, Charles Su, Carsten Szymanowski, Joachim Ullrich, Markus Walser, Oswald Willi. Special thanks go to Guido Mocken for crucial help on Section 2.2.2(a). Y.I.S. received support for this work from the Alexander von Humboldt Foundation, from the Max-Planck-Institute for Nuclear Physics in Heidelberg, and from the American University of Sharjah in the United Arab Emirates through a Faculty Research Grant. S.X.H. is supported by the US Department of Energy through the Los Alamos National Laboratory under the LDRD program. K.Z.H. acknowledges support from the Alexander von Humboldt Foundation and ISTC grant No. A-353. C.H.K. is funded by DFG project KE-721/1 beyond support by the Max-Planck Society.

References

[1] M.D. Perry, G. Mourou, Science 264 (1994) 917.
[2] P. Gibbon, E. Forster, Plas. Phys. Cont. Fus. 38 (1996) 769.
[3] V.P. Silin, Quant. El. 26 (1999) 11.
[4] D. Giuletti, L.A. Gizzi, Riv. Nuovo Cim. 21 (1998) 1.
[5] A. Pukhov, Rep. Prog. Phys. 66 (2003) 47.
[6] M. Protopapas, C.H. Keitel, P.L. Knight, Rep. Progr. Phys. 60 (1997) 389.
[7] T. Brabec, F. Krausz, Rev. Mod. Phys. 72 (2000) 545.
[8] M. Drescher, M. Hentschel, R. Kienberger, G. Tempea, C. Spielmann, G.A. Reider, P.B. Corkum, F. Krausz, Science 291 (2001) 1923.
[9] W. Becker, F. Grasbon, R. Kopold, D.B. Milošević, G.G. Paulus, H. Walther, Adv. At. Mol. Opt. Phys. 48 (2002).
[10] D.B. Milošević, F. Ehlotzky, Adv. At. Mol. Opt. Phys. 49 (2003) 373.
[11] C.J. Joachain, in: V. Bell et al. (Eds.), Supercomputing, Collision Processes, and Applications, Kluwer/Plenum Publishing, New York, 1999, p. 77.
[12] C.J. Joachain, M. Dörr, N. Kylstra, Adv. At. Mol. Phys. 42 (2000) 225.
[13] C.H. Keitel, Contemp. Phys. 42 (2001) 353.
[14] A. Maquet, R. Grobe, J. Mod. Opt. 49 (2002) 2001.
[15] D. Strickland, G. Mourou, Opt. Commun. 56 (1985) 219;
A. Dubeis, et al., Opt. Commun. 88 (1992) 437;
G.A. Mourou, C.P.J. Barty, M.D. Perry, Phys. Today 51 (1) (1998) 22.
[16] R. Jung, et al., Phys. Rev. Lett. 94 (2005) 195001.
[17] J. Tassart, Nucl. Fusion 44 (2004) S134;
R. Kodama, et al., Nucl. Fusion 44 (2004) S276;
C. Cavailler, et al., Plasma Phys. Contr. Fusion 46 (2004) B135;
J. Hein, et al., Appl. Phys. B 79 (2004) 419.
[18] S. Bahk, P. Rousseau, T. Planchon, V. Chvykov, G. Kalinchenko, A. Maksimchuk, G. Mourou, V. Yanovsky, Opt. Lett. 29 (2004) 2837.
[19] S.P.D. Mangles, et al., Nature 431 (2004) 535.
[20] C.G.R. Geddes, et al., Nature 431 (2004) 538.
[21] J. Faure, et al., Nature 431 (2004) 541.
[22] R. Kodama, et al., Nature 418 (2002) 933.
[23] K.W. Madison, P.K. Patel, D. Price, A. Edens, M. Allen, T.E. Cowan, J. Zweiback, T. Ditmire, Phys. Plasmas 11 (2004) 270.
[24] H. Popescu, et al., Phys. Plasmas 12 (2005) 063106.
[25] S. Ter-Avetisyan, et al., Phys. Plasmas 12 (2005) 012702.
[26] S. Karsch, et al., Phys. Rev. Lett. 91 (2003) 015001.
[27] S. Dobosz, et al., Phys. Rev. Lett. 95 (2005) 025001.
[28] S.B. Hansen, et al., Phys. Rev. E 71 (2005) 016408.
[29] U. Teubner, et al., Phys. Rev. Lett. 92 (2004) 185001.
[30] O. Albert, H. Wang, D. Liu, Z. Chang, G. Mourou, et al., Opt. Lett. 25 (2000) 1125.
[31] R. Dorn, S. Quabis, G. Leuchs, Phys. Rev. Lett. 91 (2003) 233901.
[32] R. Dorn, S. Quabis, G. Leuchs, J. Mod. Opt. 50 (2003) 1917.
[33] M.Y. Shverdin, D.R. Walker, D.D. Yavuz, G.Y. Yin, S.E. Harris, Phys. Rev. Lett. 94 (2005) 033904.
[34] U. Keller, Nature 424 (2003) 831.
[35] T. Tajima, G. Mourou, Phys. Rev. ST AB 5 (2002) 031301.
[36] S.V. Bulanov, T. Esirkepov, T. Tajima, Phys. Rev. Lett. 91 (2003) 085001.
[37] J. Nees, N. Naumova, E. Power, V. Yanovsky, I. Sokolov, A. Maksimchuk, S.-W. Bahk, V. Chvykov, G. Kalinchenko, B. Hou, G. Mourou, J. Mod. Opt. 52 (2005) 305;
N.M. Naumova, et al., Phys. Rev. Lett. 92 (2004) 063902.

[38] N.M. Naumova, et al., Phys. Rev. Lett. 93 (2004) 195003.
[39] S. Gordienko, A. Pukhov, O. Shorokhov, T. Baeva, Phys. Rev. Lett. 94 (2005) 103903;
A. Scrinzi, M. Yu. Ivanov, R. Kienberger, D.M. Villeneuve, J. Phys. B 39 (2006) R1.
[40] P. Agostini, L.F. DiMauro, Rep. Prog. Phys. 67 (2004) 813;
A. Scrinzi, M.Yu. Ivanov, R. Kienberger, D.M. Villeneuve, J. Phys. B 39 (2006) R1.
[41] M. Hentschel, R. Kienberger, C. Spielmann, G.A. Reider, N. Milošević, T. Brabec, P.B. Corkum, U. Heinzmann, M. Drescher, F. Krausz, Nature 414 (2001) 509.
[42] R. Kienberger, E. Goulielmakis, M. Uiberacker, A. Baltuska, V. Yakovlev, F. Bammer, A. Scrinzi, Th. Westerwalbesloh, U. Kleinberger, U. Heinzmann, M. Drescher, F. Krausz, Nature 427 (2004) 817.
[43] E. Goulielmakis, M. Uiberacker, R. Kienberger, A. Baltuska, V. Yakovlev, A. Scrinzi, Th. Westerwalbesloh, U. Kleinberger, U. Heinzmann, M. Drescher, F. Krausz, Science 305 (2004) 1267.
[44] http://www-ssrl.slac.stanford.edu/lcls/science.html
[45] TESLA Technical Design Report. See http://tesla.desy.de/new_pages/TDR_CD/start.html
[46] J. Andruszkow, et al., Phys. Rev. Lett. 85 (2000) 3825.
[47] Th. Tschentscher, Chem. Phys. 299 (2004) 271.
[48] P. Chen, C. Pellegrini, in: P. Chen (Ed.), Quantum aspects of beam physics, Proceedings of the 15th Advanced ICFA Beam Dynamics Workshop, Monterey, CA, World Scientific, Singapore, 1998, p. 564.
[49] P.H. Mokler, Th. Stöhlker, Adv. At. Mol. Opt. Phys. 37 (1996) 297.
[50] S.X. Hu, A.F. Starace, Phys. Rev. Lett. 88 (2002) 245003.
[51] A. Maltsev, T. Ditmire, Phys. Rev. Lett. 90 (2003) 053002.
[52] Th. Stöhlker, et al., Phys. Rev. Lett. 86 (2001) 983.
[53] R.E. Marrs, S.R. Elliott, D.A. Knapp, Phys. Rev. Lett. 72 (1994) 8042.
[54] J.R. Crespo López-Urrtia, et al., J. Phys.: Conf. Ser. 2 (2004) 42.
[55] W. Quint, et al., Hyp. Int. 132 (2001) 457 http://www.gsi.de/documents/DOC-2003-Dec-69.html.
[56] L.V. Keldysh, Sov. Phys. JETP 20 (1965) 1307.
[57] F.H.M. Faisal, J. Phys. B 6 (1973) L312.
[58] H.R. Reiss, Phys. Rev. A 22 (1980) 1786.
[59] W. Gordon, Z. Phys. 40 (1926) 117;
D.M. Volkov, Z. Phys. 94 (1935) 250.
[60] See H. R. Reiss, Progr. Quant. El. 16 (1992) 1 and references therein.
[61] A.M. Perelomov, V.S. Popov, M.V. Terentyev, Zh. Exp. Theor. Fiz. 50 (1966) 1393;
A.M. Perelomov, V.S. Popov, M.V. Terentyev, Zh. Exp. Theor. Fiz. 51 (1966) 309 [Sov. Phys. JETP 23 (1966) 924];
A.M. Perelomov, V.S. Popov, M.V. Terentyev, Sov. Phys. JETP 24 (1967) 207.
[62] V.S. Popov, Phys. Uspekhi 47 (2004) 855.
[63] A.M. Perelomov, V.S. Popov, Zh. Exp. Theor. Fiz. 52 (1967) 514 [Sov. Phys. JETP 25 (1967) 336];
A.I. Nikishov, V.I. Ritus, Sov. Phys. JETP 52 (1967) 223.
[64] V.S. Popov, V.P. Kuznetsov, A.M. Perelomov, Zh. Exp. Theor. Fiz. 53 (1967) 331 [Sov. Phys. JETP 26 (1967) 222].
[65] M.V. Ammosov, N.B. Delone, V.P. Krainov, Zh. Exp. Theor. Fiz. 91 (1986) 2008.
[66] A.M. Dykhne, Zh. Exp. Theor. Fiz. 38 (1960) 570;
N.B. Delone, V.P. Krainov, J. Opt. Soc. Am. 8 (1991) 1207;
N.B. Delone, V.P. Krainov, J. Opt. Soc. Am. 14 (1997) 425;
V.P. Krainov, V.M. Ristich, Zh. Exp. Theor. Fiz. 101 (1992) 1479.
[67] V.S. Popov, B.M. Karnakov, V.D. Mur, Phys. Lett. A 229 (1997) 306;
V.S. Popov, B.M. Karnakov, V.D. Mur, Zh. Exp. Theor. Fiz. 113 (1998) 1579.
[68] Y.I. Salamin, Phys. Rev. A 56 (1997) 4910.
[69] H.R. Reiss, V.P. Krainov, Phys. Rev. 50 (1994) R910;
M.H. Mittleman, Phys. Rev. 50 (1994) 3249;
M.V. Fedorov, J. Phys. B 27 (1994) 4145;
J.H. Eberly, M. Kalinski, Institute of Physics Conference Series, vol. 154, 1997, p. 29.
[70] M. Jain, N. Tzoar, Phys. Rev. A 18 (1978) 538.
[71] V.P. Krainov, J. Opt. Soc. Am. B 14 (1997) 425;
H.R. Reiss, V.P. Krainov, SPIE 2796 (1996) 39.
[72] A. Becker, F.H.M. Faisal, J. Phys. B 29 (1996) L197.
[73] J.Z. Kaminski, F. Ehlotzky, Phys. Rev. A 55 (1997) 4625;
D.B. Milošević, F. Ehlotzky Phys. Rev. A 57 (1998) 2859;
Shu-Min Li, et al., Phys. Rev. A 58 (1998) 2615;
A. Jaron, J.Z. Kaminski, F. Ehlotzky, Phys. Rev. A 61 (2000) 023404;
G. Duchateau, E. Cormier, H. Bachau, R. Gayet, Phys. Rev. A 63 (2001) 053411;
G. Duchateau, R. Gayet, Phys. Rev. A 65 (2002) 013405;
G. Duchateau, E. Cormier, R. Gayet, Phys. Rev. A 66 (2002) 023412;
P.A. Macri, J.E. Miraglia, M.S. Gravielle, J. Opt. Soc. Am. B 20 (2003) 1801;
V.D. Rodríguez, E. Cormier, R. Gayet, Phys. Rev. A 69 (2004) 053402.

[74] J. Bauer, Phys. Rev. A 71 (2005) 067401.
[75] A. Becker, L. Plaja, P. Moreno, M. Nurhuda, F.H.M. Faisal, Phys. Rev. A 64 (2001) 023408.
[76] P. Agostini, F. Fabre, G. Mainfray, G. Petite, N.K. Rahman, Phys. Rev. Lett. 42 (1979) 1127.
[77] G.G. Paulus, W. Nicklich, Huale Xu, P. Lambropoulos, H. Walther, Phys. Rev. Lett. 72 (1994) 2851;
G.G. Paulus, W. Nicklich, H. Walther, Europhys. Lett. 27 (1994) 267.
[78] K.C. Kulander, K.J. Schafer, J.L. Krause, in: B. Piraux, A. L'Huillier, K. Rzazewski (Eds.), Super-Intense Laser-Atom Physics, NATO Advanced Study Institutes, Ser. B, vol. 316, Plenum, New York, 1993, p. 95.
[79] P.B. Corkum, Phys. Rev. Lett. 71 (1993) 1994.
[80] W. Becker, A. Lohr, M. Kleber, J. Phys. B 27 (1994) L325;
G.G. Paulus, W. Becker, W. Nicklich, H. Walther, J. Phys. B 27 (1994) L703.
[81] M. Lewenstein, K.C. Kulander, K.J. Schafer, P.H. Bucksbaum, Phys. Rev. A 51 (1995) 1495.
[82] A. Lohr, M. Kleber, R. Kopold, W. Becker, Phys. Rev. A 55 (1997) R4003.
[83] M. Lewenstein, P. Salieres, A. L'Huillier, P. Antoine, Adv. At. Mol. Opt. Phys. 41 (1999) 83;
R. Kopold, D.B. Milošević, W. Becker, Phys. Rev. Lett. 84 (2000) 3831.
[84] P. Salieres, et al., Science 292 (2001) 902.
[85] T. Brabec, M.Y. Ivanov, P.B. Corkum, Phys. Rev. A 54 (1996) R2551.
[86] F.H.M. Faisal, A. Becker, J. Muth-Böhm, Laser Phys. 9 (1999) 115;
A. Becker, F.H.M. Faisal, Phys. Rev. A 59 (1999) R1742;
A. Becker, F.H.M. Faisal, Phys. Rev. A 59 (1999) R3182;
A. Becker, F.H.M. Faisal, Phys. Rev. Lett. 84 (2000) 3546.
[87] R. Panifili, J.H. Eberly, S.L. Haan, Opt. Express 8 (2000) 431;
P.J. Ho, R. Panifili, S.L. Haan, J.H. Eberly, Phys. Rev. Lett. 94 (2005) 093002;
P.J. Ho, J.H. Eberly, Phys. Rev. Lett. 95 (2005) 193002;
P.J. Ho, Phys. Rev. A 72 (2005) 045401.
[88] R. Kopold, W. Becker, H. Rottke, W. Sandner, Phys. Rev. Lett. 85 (2000) 3781;
S.V. Popruzhenko, S.P. Goreslavskii, J. Phys. B 34 (2001) L239;
S.P. Goreslavskii, S.V. Popruzhenko, R. Kopold, W. Becker, Phys. Rev. A 64 (2001) 053402;
C. Figueira de Morisson Faria, X. Liu, W. Becker, H. Schomerus, Phys. Rev. A 69 (2004) R043405;
C. Figueira de Morisson Faria, X. Liu, A. Sanpera, M. Lewenstein, Phys. Rev. A 70 (2005) 043406.
[89] D. Bauer, F. Ceccherini, Opt. Express 8 (2001) 377.
[90] N.L. Manakov, Pis'ma Zh. Exp. Teor. Fiz. 74 (2000) 426;
B. Borca, et al., Phys. Rev. Lett. 88 (2002) 193001.
[91] N.L. Manakov, M.V. Frolov, A.F. Starace, I.I. Fabrikant, J. Phys. B 33 (2000) R141;
N.L. Manakov, M.V. Frolov, A.F. Starace, I.I. Fabrikant, J. Phys. B 36 (2003) R49.
[92] H.R. Reiss, Phys. Rev. A 42 (1990) 1476.
[93] H.R. Reiss, J. Opt. Soc. Am. B 7 (1990) 574.
[94] D.P. Crawford, H. Reiss, Phys. Rev. A 50 (1994) 1844;
D.P. Crawford, H. Reiss, Opt. Expr. 2 (1998) 289.
[95] F.H.M. Faisal, S. Bhattacharyya, Phys. Rev. Lett. 93 (2004) 053002.
[96] V.P. Krainov, J. Phys. B 32 (1999) 1607;
V.P. Krainov, J. Phys. B 36 (2003) L169;
V.P. Krainov, A.V. Sofronov, Phys. Rev. A 69 (2004) 015401;
J. Ortner, V.M. Rylyuk, Phys. Rev. A 61 (2000) 033403;
J. Ortner, J. Phys. B 33 (2000) 383.
[97] V.S. Popov, V.D. Mur, B.M. Karnakov, JETP Lett. 66 (1997) 229;
V.S. Popov, V.D. Mur, B.M. Karnakov, Phys. Lett. A 250 (1998) 20;
V.D. Mur, B.M. Karnakov, V.S. Popov, JETP 87 (1998) 433.
[98] N. Milošević, V.P. Krainov, T. Brabec, Phys. Rev. Lett. 89 (2002) 193001;
N. Milošević, V.P. Krainov, T. Brabec, J. Phys. B 35 (2002) 3515.
[99] V.S. Popov, B.M. Karnakov, V.D. Mur, JETP Lett. 79 (2004) 262.
[100] H.K. Avetissian, A.G. Markossian, G.F. Mkrtchian, Phys. Rev. A 64 (2001) 053404.
[101] H.K. Avetissian, K.Z. Hatsagortsian, A.G. Markossian, S.V. Movsissian, Phys. Rev. A 59 (1999) 549.
[102] F.H.M. Faisal, Radożycki, Phys. Rev. A 47 (1993) 4464;
F.H.M. Faisal, Radożycki, Phys. Rev. A 48 (1994) 554.
[103] D.B. Milošević, S.X. Hu, W. Becker, Phys. Rev. A 63 (2001) R011403.
[104] M.W. Walser, C.H. Keitel, A. Scrinzi, T. Brabec, Phys. Rev. Lett. 85 (2000) 5082.
[105] N.J. Kylstra, R.M. Potvliege, C.J. Joachain, J. Phys. B 34 (2001) L55.
[106] C.C. Chirila, N.J. Kylstra, R.M. Potvliege, C.J. Joachain, Phys. Rev. A 66 (2002) 063411.
[107] C.C. Chirila, C.J. Joachain, N.J. Kylstra, R.M. Potvliege, Phys. Rev. Lett. 93 (2004) 243603.
[108] M. Klaiber, K.Z. Hatsagortsyan, C.H. Keitel, Phys. Rev. A 71 (2005) 033408.
[109] M. Dammasch, M. Dörr, U. Eichmann, E. Lenz, W. Sandner, Phys. Rev. A 64 (2001) R061402.
[110] J. Prager, C.H. Keitel, J. Phys. B 35 (2002) L167.

[111] B. Henrich, K.Z. Hatsagortsyan, C.H. Keitel, Phys. Rev. Lett. 93 (2004) 13601.
[112] K.C. Kulander, T.N. Rescigno, Comput. Phys. Commun. 63 (1991) 523;
K.C. Kulander, K.J. Schafer, J.L. Krause, Phys. Rev. Lett. 66 (1991) 2601.
[113] J.H. Eberly, J. Javanainen, K. Rzazewski, Physics Reports 204 (1991) 331;
Q. Su, J.H. Eberly, Phys. Rev. A 43 (1991) 2474;
R. Grobe, J.H. Eberly, Phys. Rev. Lett. 68 (1992) 2905.
[114] P. Moreno, L. Plaja, L. Roso, Europhys. Lett. 28 (1994) 629;
L. Roso, Phys. Scr. T 58 (1995) 5.
[115] J.L. Krause, K.J. Schafer, K.C. Kulander, Phys. Rev. A 45 (1992) 4998.
[116] Q. Su, J.H. Eberly, Phys. Rev. A 44 (1991) 5997.
[117] V.C. Reed, K. Burnett, Phys. Rev. A 46 (1992) 424.
[118] K.J. Schafer, K.C. Kulander, Phys. Rev. A 42 (1990) 5794.
[119] M.D. Feit, J.A. Fleck Jr., A. Steiger, J. Comput. Phys. 47 (1982) 412.
[120] A.D. Bandrauk, H. Shen, Chem. Phys. Lett. 176 (1991) 428;
A.D. Bandrauk, H. Shen, J. Phys. A 27 (1994) 7147.
[121] S.X. Hu, Z.Z. Xu, Phys. Rev. A 56 (1997) 3916;
S.X. Hu, W.X. Qu, Z.Z. Xu, Phys. Rev. A 57 (1998) 3770;
S.X. Hu, W.X. Qu, Z.Z. Xu, Appl. Phys. Lett. 73 (1998) 2552.
[122] M. Suziki, J. Math. Phys. 26 (1985) 601;
M. Suziki, J. Math. Phys. 32 (1991) 400.
[123] S. Goedecker, Comput. Phys. Commun. 76 (1993) 294.
[125] J.W. Braun, Q. Su, R. Grobe, Phys. Rev. A 59 (1999) 604.
[126] R. Taieb, V. Veniard, A. Maquet, J. Mod. Opt. 50 (2003) 365.
[127] O. Latinne, C.J. Joachain, M. Dörr, Europhys. Lett. 26 (1994) 333.
[128] U.W. Rathe, C.H. Keitel, M. Protopapas, P.L. Knight, J. Phys. B 30 (1997) L531.
[129] L.N. Gaier, C.H. Keitel, Phys. Rev. A 65 (2002) 023406.
[130] See Ref. [5] and references therein.
[131] X.M. Tong, S.I. Chu, Chem. Phys. 217 (1997) 119.
[132] J. Parker, K.T. Taylor, Comput. Phys. Commun. 88 (1995) 217;
K.T. Taylor, Phil. Tran. Royal Soc. London A 360 (2002) 1135.
[133] G.R. Mocken, C.H. Keitel, J. Comput. Phys. 199 (2004) 558.
[134] V. Alonso, S.D. Vincenzo, L. Mondino, Eur. J. Phys. 18 (1997) 315.
[135] A. Maquet, R. Grobe, J. Mod. Opt. 49 (2002) 2001.
[136] L. Susskind, Phys. Rev. D 16 (1977) 3031.
[137] C. Müller, N. Grün, W. Scheid, Phys. Lett. A 242 (1998) 245.
[138] M. Frigo, S.G. Johnson, in: Proceedings of the IEEE International Conference on Acoustics Speech and Signal Processing, vol. 3, 1998, pp. 1381–1384.
[139] J. San Roman, L. Roso, H.R. Reiss, J. Phys. B: At. Mol. Opt. Phys. 33 (2000) 1869.
[140] P. Krekora, Q. Su, R. Grobe, Phys. Rev. A 63 (2001) 032107.
[141] J.D. Jackson, Electrodynamics, second ed., Wiley, New York, 1975.
[142] T.W.B. Kibble, Phys. Rev. 138 (1965) B740.
[143] E.S. Sarachik, G.T. Schappert, Phys. Rev. D 1 (1970) 2738.
[144] F.V. Hartemann, S.N. Fochs, G.P. Le Sage, N.C. Luhmann Jr., J.G. Woodworth, M.D. Perry, Y.J. Chen, A.K. Kerman, Phys. Rev. E 51 (1995) 4833.
[145] F.V. Hartemann, A.K. Kerman, Phys. Rev. Lett. 76 (1996) 624.
[146] A.L. Troha, J.R. Van Meter, E.C. Landahl, R.M. Alvis, Z.A. Unterberg, K. Li, N.C. Luhmann Jr., A.K. Kerman, F.V. Hartemann, Phys. Rev. E 60 (1999) 926.
[147] S.K. Ride, E. Esarey, M. Baine, Phys. Rev. E 52 (1995) 5425;
E. Esarey, S.K. Ride, M. Baine, A. Ting, P. Sprangle, Nucl. Inst. Meth. Phys. Res. 375 (1996) 545.
[148] Y.I. Salamin, F.H.M. Faisal, Phys. Rev. A 54 (1996) 4383;
Y.I. Salamin, F.H.M. Faisal, Phys. Rev. A 55 (1997) 3964;
Y.I. Salamin, F.H.M. Faisal, J. Phys. A 31 (1997) 3678.
[149] Y.I. Salamin, F.H.M. Faisal, Phys. Rev. A 61 (2000) 043801.
[150] Y.I. Salamin, F.H.M. Faisal, C.H. Keitel, Phys. Rev. A 62 (2000) 053809.
[151] M. Verschl, C.H. Keitel, Laser Phys. 15 (2005) 1.
[152] M. Mahmoudi, Y.I. Salamin, C.H. Keitel, Phys. Rev. A 72 (2005) 033402.
[153] G.R. Mocken, C.H. Keitel, Comput. Phys. Commun. 166 (2005) 171.
[154] M.W. Walser, C. Szymanowski, C.H. Keitel, Europhys. Lett. 48 (1999) 533.
[155] M.W. Walser, C.H. Keitel, J. Phys. B 33 (2000) L221.
[156] M.W. Walser, D.J. Urbach, K.Z. Hatsagortsyan, S.X. Hu, C.H. Keitel, Phys. Rev. A 65 (2002) 043410.
[157] J. Frenkel, Z. Phys. 32 (1925) 518;
J. Frenkel, Z. Phys. 37 (1926) 243;

J. Weysenhoff, Acta Phys. Pol. 9 (1947) 8;
H.C. Corben, Phys. Rev. 121 (1961) 1833;
V. Bargmann, L. Michel, V.L. Telegdi, Phys. Rev. Lett. 2 (1959) 435.
[158] M. Ivanov, et al., Phys. Rev. Lett. 74 (1995) 2933.
[159] Ph. Antoine, et al., Phys. Rev. A 54 (1996) R1761.
[160] S. Long, W. Becker, J.K. McIver, Phys. Rev. A 52 (1995) 2262;
D.B. Milošević, B. Piraux, Phys. Rev. A 54 (1996) 1522;
M.B. Gaarde, A. L'Huillier, M. Lewenstein, Phys. Rev. A 54 (1996) 4236.
[161] T. Zuo, et al., Phys. Rev. A 51 (1995) 3991;
T. Zuo, A.D. Bandrauk, J. Nonlinear Opt. Phys. Mater. 4 (1995) 533;
A.D. Bandrauk, et al., Int. J. Quantum Chem. 64 (1997) 613.
[162] J.-P. Connerade, C.H. Keitel, Phys. Rev. A 53 (1996) 2748.
[163] D.B. Milošević, A.F. Starace, Phys. Rev. Lett. 82 (1999) 2653.
[164] M.Q. Bao, A.F. Starace, Phys. Rev. A 53 (1996) R3723;
A. Lohr, W. Becker, M. Kleber, Laser Phys. 7 (1997) 615;
B. Wang, X. Li, P. Fu, J. Phys. B 31 (1998) 1961.
[165] Yu.B. Kudasov, et al., JETP Lett. 68 (1998) 350.
[166] R.E. Wagner, Q. Su, R. Grobe, Phys. Rev. Lett. 84 (2000) 3282;
R.E. Wagner, Q. Su, R. Grobe, Phys. Rev. Lett. 84 (2000) 5682;
P.J. Peverly, R.E. Wagner, Q. Su, R. Grobe, Laser Phys. 10 (1999) 303.
[167] P. Krekora, R.E. Wagner, Q. Su, R. Grobe, Phys. Rev. A 63 (2001) 025404.
[168] http://www.phy.ilstu.edu/∼ilp/movies/camovie/mcapca.html
[169] R.E. Wagner, S. Radovich, J. Gillispie, Q. Su, R. Grobe, Phys. Rev. A 66 (2002) 043412.
[170] W.P. Leemans, E. Esarey, in: W. Lawson, C. Bellamy, D. Brosius (Eds.), Advanced Accelerator Concepts: Eighth Workshop, AIP Conf. Proc. No. 472, AIP, New York, 1999, p. 174.
[171] W.D. Kimura, et al., Phys. Rev. Lett. 86 (2001) 4041.
[172] W.D. Kimura, et al., Phys. Rev. ST Accel. Beams 4 (2001) 101301.
[173] A. Pukhov, J. Meyer-ter-Vehn, Appl. Phys. B: Laser. Opt. 74 (2002) 355.
[174] R. Bingham, J.T. Mendonca, P.K. Shukla, Plasma Phys. Cont. Fus. 46 (2004) R1.
[175] R.B. Palmer, J. Appl. Phys. 43 (1973) 3014;
P. Sprangle, C.M. Tang, IEEE Trans. Nucl. Sci. NS 28 (1981) 3346;
E.D. Courant, C. Pellegrini, W. Zakowicz, Phys. Rev. A 32 (1985) 2813;
P. Musumeci, C. Pellegrini, J.B. Rosenzweig, Phys. Rev. E 72 (2005) 016501.
[176] J.D. Lawson, Eur. J. Phys. 5 (1984) 104.
[177] J.X. Wang, W. Scheid, M. Hoeless, Y.K. Ho, Phys. Rev. E 65 (2002) 028501.
[178] A.L. Troha, F.V. Hartemann, Phys. Rev. E 65 (2002) 028502.
[179] Y.I. Salamin, C.H. Keitel, Phys. Rev. Lett. 88 (2002) 095005.
[180] Y.I. Salamin, G.R. Mocken, C.H. Keitel, Phys. Rev. ST Accel. Beams 5 (2002) 101301.
[181] Y.I. Salamin, G.R. Mocken, C.H. Keitel, Phys. Rev. E 67 (2003) 016501.
[182] Y.I. Salamin, C.H. Keitel, Laser Phys. 13 (2003) 407.
[183] Y.I. Salamin, Phys. Lett. A 335 (2005) 289.
[184] Y.I. Salamin, J. Phys. B: At. Mol. Opt. Phys. 38 (2005) 4095.
[185] K.T. McDonald, http://www.hep.princeton.edu/∼mcdonald/accel/gaussian.ps; http://www.hep.princeton.edu/∼mcdonald/accel/gaussian2.ps
[186] J. Pang, et al., Phys. Rev. E 66 (2002) 066501.
[187] Y.J. Xie, et al., Phys. Lett. A 318 (2003) 15.
[188] Q. Kong, Y.K. Ho, N. Cao, J. Pang, P.X. Wang, L. Shao, Appl. Phys. B 74 (2002) 517.
[189] P.X. Wang, et al., Appl. Phys. Lett. 78 (2001) 2253.
[190] J.X. Wang, et al., Phys. Rev. E 60 (1999) 7473;
J.X. Wang, W. Scheid, M. Höless, Y.K. Ho, Phys. Lett. A 280 (2001) 121.
[191] C.M. Haaland, Opt. Commun. 114 (1995) 280.
[192] E. Esarey, P. Sprangle, J. Krall, Phys. Rev. E 52 (1995) 5443.
[193] Y.C. Huang, D. Zheng, W.M. Tulloch, R.L. Beyer, Appl. Phys. Lett. 68 (1996) 753;
Y.C. Huang, R.L. Beyer, Appl. Phys. Lett. 69 (1996) 2175;
Y.C. Huang, R.L. Beyer, Nucl. Instr. Meth. Phys. Res. A 407 (1998) 316;
Y.C. Huang, R.L. Beyer, Rev. Sci. Instrum. 69 (1998) 2629;
Y.C. Huang, Opt. Commun. 157 (1998) 145.
[194] Y. Cheng, Z. Xu, J. Phys. D: Appl. Phys. 31 (1998) 3229.
[195] Y.I. Salamin, C.H. Keitel, Appl. Phys. Lett. 77 (2000) 1082.
[196] Y.I. Salamin, C.H. Keitel, J. Phys. B: At. Mol. Opt. Phys. 33 (2000) 5057.
[197] B. Hafizi, A. Ting, E. Esarey, P. Sprangle, J. Krall, Phys. Rev. E 55 (1997) 5924.
[198] B. Hafizi, A.K. Ganguly, A. Ting, C.I. Moore, P. Sprangle, Phys. Rev. E 60 (1999) 4779.
[199] V.M. Haroutunian, H.K. Avetissian, Phys. Lett. A 59 (1976) 115;
H.K. Avetissian, H.A. Jivanian, R.G. Petrossian, Phys. Lett. A 66 (1978) 161.

[200] H.K. Avetissian, G.F. Mkrtchian, Phys. Rev. E 65 (2002) 016506.
[201] G.K. Avetisyan, A.A. Dzhivanyan, R.G. Petrosyan, JETP Lett. 34 (1981) 537.
[202] H.K. Avetissian, A.K. Avetissian, G.F. Mkrtchian, JETP Lett. 78 (2003) 615.
[203] Y.I. Salamin, J. Phys. B: At. Mol. Opt. Phys., 39 (2006) 1353.
[204] M.S. Hussein, M.P. Pato, Phys. Rev. Lett. 68 (1992) 1136.
[205] Y.I. Salamin, C.H. Keitel, F.H.M. Faisal, J. Phys. A 34 (2001) 2819.
[206] Y.I. Salamin, Phys. Lett. A 283 (2001) 37.
[207] A.A. Kolomenskii, A.N. Lebedev, Dokl. Akad. Nauk SSSR 145 (1962) 1259 [Sov. Phys. Dokl. 7 (1962) 492];
A.A. Kolomenskii, A.N. Lebedev, Sov. Phys. JETP 17 (1963) 179.
[208] A. Loeb, L. Friedland, S. Eliezer, Phys. Rev. A 35 (1987) 1692.
[209] L. Friedland, Phys. Plasmas 1 (1994) 421.
[210] M.A. Lapointe, et al., Phys. Rev. Lett. 76 (1996) 2718.
[211] J.L. Hirshfield, et al., Phys. Plasmas 3 (1996) 2163;
C.B. Wang, J.L. Hirshfield, Phys. Rev. E 57 (1998) 7184.
[212] Y.I. Salamin, F.H.M. Faisal, Phys. Rev. A 58 (1998) 3221.
[213] F.H.M. Faisal, Y.I. Salamin, Phys. Rev. A 60 (1999) 2505.
[214] W.E. Baylis, Y. Yao, Phys. Rev. A 60 (1999) 785.
[215] Q. Kong, et al., Phys. Rev. E 69 (2004) 056502.
[216] N. Cao, et al., Appl. Phys.: Lasers Opt. 78 (2004) 781.
[217] S.J. Huang, C.X. Tang, P.X. Pang, J. Appl. Phys. 95 (2004) 2163.
[218] H.K. Avetissian, G.F. Mkrtchian, M.G. Poghosyan, JETP 99 (2004) 290.
[219] T. Plettner, R.L. Byer, R.H. Siemann, J. Phys. B: At. Mol. Opt. Phys. 38 (2005) S741.
[220] T. Plettner, R.L. Byer, E. Colby, B. Cowan, C.M.S. Sears, J.E. Spencer, R.H. Siemann, Phys. Rev. Lett. 95 (2005) 134801.
[221] C.M.S. Sears, E.R. Colby, B.M. Cowan, R.H. Siemann, J.E. Spencer, R.L. Byer, T. Plettner, Phys. Rev. Lett. 95 (2005) 194801.
[222] T. Plettner, R.L. Byer, E. Colby, B. Cowan, C.M.S. Sears, J.E. Spencer, R.H. Siemann, Phys. Rev. ST Accel. Beams 8 (2005) 121301.
[223] L.F. DiMauro, P. Agostini, Adv. At. Mol. Opt. Phys. 35 (1995) 79.
[224] B. Walker, B. Sheehy, K.C. Kulander, L.F. DiMauro, Phys. Rev. Lett. 77 (1996) 5031.
[225] H.G. Muller, Phys. Rev. Lett. 83 (1999) 3158.
[226] W. Becker, A. Lohr, M. Kleber, Quant. Semiclass. Opt. 7 (1995) 423;
W. Becker, M. Kleber, A. Lohr, G.G. Paulus, H. Walther, F. Zacher, Laser Phys. 8 (1998) 56.
[227] B.R. Yang, K.J. Schafer, B. Walker, K.C. Kulander, P. Agostini, L.F. DiMauro, Phys. Rev. Lett. 71 (1993) 3770;
see also Ref. [224].
[228] R. Taieb, V. Veniard, A. Maquet, Phys. Rev. Lett. 87 (2001) 053002.
[229] D.D. Meyerhofer, J.P. Knauer, S.J. McNaught, C.I. Moore, J. Opt. Soc. Am. B 13 (1996) 113.
[230] C.I. Moore, J.P. Knauer, D.D. Meyerhofer, Phys. Rev. Lett. 74 (1995) 2439;
S.J. McNaught, J.P. Knauer, D.D. Meyerhofer, Phys. Rev. Lett. 78 (1997) 626;
S.J. McNaught, J.P. Knauer, D.D. Meyerhofer, Phys. Rev. A 58 (1999) 1399.
[231] D. Umstadter, et al., IEEE J. Quant. El. 33 (1997) 1878;
D. Umstadter, Phys. Plasmas 8 (2001) 1774;
D. Umstadter, J. Phys. D 36 (2003) R151.
[232] Y.Y. Lau, F. He, D. Umsadter, R.R. Kowalczyk, Phys. Plasmas 10 (2003) 2155.
[233] T. Ditmire, et al., Nature (London) 386 (1997) 54;
T. Ditmire, et al., Phys. Rev. A 57 (1998) 369.
[234] J.D. Gillaspy, J. Phys. B 34 (2001) R93.
[235] S.X. Hu, C.H. Keitel, Europhys. Lett. 47 (1999) 318.
[236] C.H. Keitel, J. Phys. B 29 (1996) L873.
[237] M. Gavrila, J. Phys. B 35 (2002) R147 and references therein.
[238] M. Pont, M. Gavrila, Phys. Rev. Lett. 65 (1990) 2362.
[239] Q. Su, J.H. Eberly, J. Javanainen, Phys. Rev. Lett. 64 (1990) 862.
[240] M.V. Fedorov, O.V. Tikhonova, Phys. Rev. A 58 1322 (1998) ;
M.V. Fedorov, M.Yu. Ivanov, J. Opt. Soc. Am. B 7 (1990) 569 and references therein.
[241] H.R. Reiss, J. Opt. Soc. Am. B 13 (1996) 355;
H.R. Reiss, Phys. Rev. A 46 (1992) 391.
[242] R.M. Potvliege, P.H.G. Smith, Phys. Rev. A 48 (1993) 46;
A. Scrinzi, N. Elander, B. Piraux, Phys. Rev. A 48 (1993) R2527.
[243] K. Burnett, P.L. Knight, B.R.M. Piraux, V.C. Reed, Phys. Rev. Lett. 66 (1991) 301;
V.C. Reed, P.L. Knight, K. Burnett, Phys. Rev. Lett. 67 (1991) 001415.
[244] J. Parker, C.R. Stroud Jr., Phys. Rev. A 41 (1990) 1602.
[245] M.P. deBoer, et al., Phys. Rev. Lett. 73 (1993) 3263;
J.H. Hoogenraad, et al., Phys. Rev. A 50 (1994) 4133;
N.J. van Druten, et al., Phys. Rev. A 55 (1997) 622.
[246] M. Dondera, H.G. Müller, M. Gavrila, Phys. Rev. A 65 (2002) 031405.

[247] M. Protopapas, C.H. Keitel, P.L. Knight, J. Phys. B 29 (1996) L591.
[248] L.N. Gaier, C.H. Keitel, Phys. Rev. A 65 (2002) 023406.
[249] M. Lewenstein, K. Rzazewski, P. Salieres, NATO Adv. Sci. Ins. Ser. B 316 (1993) 425.
[250] K. Rzazewski, M. Lewenstein, P. Salieres, Phys. Rev. A 49 (1994) 1196.
[251] A. Staudt, C.H. Keitel, J. Phys. B 36 (2003) L203.
[252] C.H. Keitel, S.X. Hu, Appl. Phys. Lett. 80 (2002) 541.
[253] M. Casu, C.H. Keitel, Europhys. Lett. 58 (2002) 496.
[254] S.X. Hu, C.H. Keitel, Phys. Rev. A 63 (2001) 053402.
[255] S.X. Hu, A.F. Starace, W. Becker, W. Sandner, D.B. Milošević, J. Phys. B 35 (2002) 627.
[256] N. Milosevic, P.B. Corkum, T. Brabec, Phys. Rev. Lett. 92 (2004) 013002.
[257] G.R. Mocken, C.H. Keitel, Phys. Rev. Lett. 91 (2003) 173202.
[258] H.K. Avetissian, G.F. Mkrtchian, Phys. Rev. A 66 (2002) 033403.
[259] J.R. Vazquez de Aldana, L. Roso, J. Phys. B 33 (2000) 3701;
M.W. Walser, C.H. Keitel, Opt. Commun. 199 (2001) 447;
R. Arvieu, P. Rozmej, M. Turek, Phys. Rev. A 62 (2000) 022514.
[260] S.X. Hu, C.H. Keitel, Phys. Rev. Lett. 83 (1999) 4709.
[261] L.L. Foldy, S.A. Wouthuysen, Phys. Rev. 78 (1950) 29.
[262] J.H. Eberly, Q. Su, J. Javanainen, Phys. Rev. Lett. 62 (1989) 881.
[263] A. l'Huillier, L.A. Lompre, G. Mainfray, C. Manus, Phys. Rev. A 27 (1983) 2503.
[264] D. Fittinghoff, P. Bolton, B. Chang, K. Kulander, Phys. Rev. Lett. 69 (1992) 2642;
B. Walker, B. Sheehy, L.Df. DiMauro, P. Agostini, K.J. Schafer, K. Kulander, Phys. Rev. Lett. 73 (1994) 1227;
S. Larochelle, A. Talebpour, S.L. Chin, J. Phys. B 31 (1998) 1201.
[265] D.N. Fittinghoff, Phys. Rev. A 49 (1994) 2174.
[266] U. Eichmann, M. Dörr, H. Maeda, W. Becker, W. Sandner, Phys. Rev. Lett. 84 (2000) 3550.
[267] R. Dörner, et al., Adv. Atom. Mol. Opt. Phys. 48 (2002) 1.
[268] M. Schulz, R. Moshammer, W. Schmitt, H. Kollmus, B. Feuerstein, R. Mann, S. Hagmann, J. Ullrich, Phys. Rev. Lett. 84 (2000) 863;
B. Feuerstein, R. Moshammer, D. Fischer, A. Dorn, C.D. Schröter, J. Deipenwisch, J.R. CrespoLopez-Urrutia, C. Höhr, P. Neumayer, J. Ullrich, H. Rottke, C. Trump, M. Wittmann, G. Korn, W. Sandner, Phys. Rev. Lett. 87 (2001) 043003;
E. Eremina, X. Liu, H. Rottke, W. Sandner, M.G. Schätzel, A. Dreischuh, G.G. Paulus, H. Walther, R. Moshammer, J. Ullrich, Phys. Rev. Lett. 92 (2004) 173001;
A. Rudenko, K. Zrost, B. Feuerstein, V.L.B. de Jesus, C.D. Schröter, R. Moshammer, J. Ullrich, Phys. Rev. Lett. 93 (2004) 253001.
[269] E.A. Chowdhury, C.P.J. Barty, B.C. Walker, Phys. Rev. A 63 (2001) 042712.
[270] M. Maeda, M. Dammasch, U. Eichmann, W. Becker, W. Sandner, Phys. Rev. A 63 (2001) 025401.
[271] A. Staudt, J. Prager, C.H. Keitel, Europhys. Lett. 62 (2003) 691.
[272] N. Sarukura, K. Hata, T. Adachi, R. Nodomi, Watanabe, S. Watanabe, Phys. Rev. A 43 (1991) 1669.
[273] J.S. Briggs, V. Schmidt, J. Phys. B 33 (2000) R1.
[274] J.B. Watson, A. Sanpera, D.G. Lappas, P.L. Knight, K. Burnett, Phys. Rev. Lett. 78 (1997) 1884.
[275] J.L. Krause, K.J. Schafer, K.C. Kulander, Phys. Rev. Lett. 68 (1992) 3535;
A. Sanpera, P. Jönsson, J.B. Watson, K. Burnett, Phys. Rev. A 51 (1995) 3148;
H. Xu, X. Tang, P. Lambropoulos, Phys. Rev. A 46 (1992) R2225.
[276] X.M. Tong, S.I. Chu, Phys. Rev. A 57 (1998) 452.
[277] N. Moiseyev, F. Weinhold, Phys. Rev. Lett. 78 (1997) 2100.
[278] D.G. Lappas, A. Sanpera, J.B. Watson, K. Burnett, P.L. Knight, R. Grobe, J.H. Eberly, J. Phys. B 29 (1996) L619.
[279] K.T. Taylor, J.S. Parker, D. Dundas, E. Smyth, S. Vivirito, in Multiphoton Processes 1996, Institute of Physics, Bristol, 1997, p. 56.
[280] J. Prager, S.X. Hu, C.H. Keitel, Phys. Rev. A 64 (2001) 045402.
[281] A.D. Bandrauk, Molecules in Laser Fields, Dekker, New York, 1993.
[282] A. Becker, F.H.M. Faisal, J. Phys. B 38 (2005) R1.
[283] J.H. Posthumus, Rep. Prog. Phys. 67 (2004) 623.
[284] A. McPherson, et al., Nature (London) 370 (1994) 631.
[285] J. Zweiback, et al., Phys. Rev. Lett. 84 (2000) 2634;
J. Zweiback, et al., Phys. Rev. Lett. 85 (2000) 3640;
Y. Kishimoto, T. Masaki, T. Tajima, Phys. Plasmas 9 (2002) 589.
[286] G. Grillon, Ph. Balcou, J.-P. Chambaret, D. Hulin, J. Martino, S. Moustaizis, L. Notebaert, M. Pittman, Th. Pussieux, A. Rousse, J.-Ph. Rousseau, S. Sebban, O. Sublemontier, M. Schmidt, Phys. Rev. Lett. 89 (2002) 065005.
[287] K.W. Madison, et al., J. Opt. Soc. Am. B 20 (2003) 113.
[288] T. Ditmire, J. Zweiback, V.P. Yanovsky, T.E. Cowan, G. Hays, K.B. Wharton, Nature 398 (1999) 489.
[289] L. Plaja, L. Roso-Franco, Phys. Rev. A 45 (1992) 8334;
S. Huller, J. Meyer-ter-Vehn, Phys. Rev. A 48 (1993) 3906;
F.H.M. Faisal, J.Z. Kaminski, Phys. Rev. A 56 (1997) 748.
[290] P. Gibbon, IEEE J. Quant. Electron. 33 (1997) 11.
[291] K.W.D. Ledingham, et al., Phys. Rev. Lett. 84 (2000) 899.
[292] J. Denavit, Phys. Rev. Lett. 69 (1992) 3052.

[293] S.C. Wilks, W.L. Kruer, M. Tabak, A.B. Langdon, Phys. Rev. Lett. 69 (1992) 1383.
[294] M. Schnürer, et al., Phys. Plasmas 2 (1995) 3106;
A. Zhidkov, et al., Phys. Rev. E 62 (2000) 7232;
T. Feurer, et al., Appl. Phys. B 72 (2001) 15.
[295] H. Schwörer, et al., Phys. Rev. Lett. 86 (2001) 2317.
[296] K.Z. Hatsagortsyan, C.H. Keitel, Phys. Rev. Lett. 86 (2001) 2277.
[297] K.Z. Hatsagortsyan, C.H. Keitel, J. Phys. B 35 (2002) L175.
[298] K.Z. Hatsagortsyan, C.H. Keitel, Phys. Rev. A 72 (2005) 023812.
[299] J.P. Verboncoeur, et al., Comput. Phys. Commun. 87 (1995) 199;
D. Bruhwiler, et al., Phys. Rev. ST. AB. 4 (2001) 101302.
[300] J.C. Solem, G.C. Baldwin, Science 218 (1982) 229.
[301] M.H. Vos, J.-L. Martin, Annu. Rev. Biophys. Biomol. Struct. 21 (1992) 199.
[302] K. Boyer, J.C. Solem, J.W. Longworth, A.B. Borisov, C.K. Rhodes, Nat. Med. (N.Y.) 2 (1996) 939.
[303] C. Rose-Petruck, et al., Nature (London) 398 (1999) 310.
[304] G. Bandarage, A. Maquet, J. Cooper, Phys. Rev. A 41 (1990) 1744;
G. Bandarage, A. Maquet, T. Menis, R. Taieb, V. Veniard, J. Cooper, Phys. Rev. A 46 (1992) 380.
[305] W. Becker, S. Long, J.K. McIver, Phys. Rev. A 41 (1990) 4112;
W. Becker, S. Long, J.K. McIver, Phys. Rev. A 50 (1994) 1540;
W. Becker, A. Lohr, M. Kleber, M. Lewenstein, Phys. Rev. A 56 (1997) 645.
[306] M. Lewenstein, Ph. Balcou, M. Yu Ivanov, A. L'Huillier, P.B. Corkum, Phys. Rev. A 49 (1994) 2117.
[307] Z. Chang, et al., Phys. Rev. Lett. 79 (1997) 2967.
[308] C. Spielmann, et al., Science 278 (1997) 661.
[309] P.M. Paul, E.S. Toma, P. Breger, G. Mullot, F. Auge, P. Balcou, H.G. Müller, P. Agostini, Science 292 (2001) 1689.
[310] M. Casu, C. Szymanowski, S.X. Hu, C.H. Keitel, J. Phys. B 33 (2000) L411.
[311] R. Numico, D. Giulietti, A. Giulietti, L.A. Gizzi, L. Roso, J. Phys. B 33 (2000) 2605.
[312] R.M. Potvliege, N.J. Kylstra, C.J. Joachain, J. Phys. B 33 (2000) L743.
[313] N.J. Kylstra, R.M. Potvliege, C.J. Joachain, Laser Phys. 12 (2002) 409.
[314] D.B. Milošević, S.X. Hu, W. Becker, Laser Phys. 12 (2002) 389.
[315] N.J. Kylstra, R.A. Worthington, A. Patel, P.L. Knight, J.R.V. de Aldana, L. Roso, Phys. Rev. Lett. 85 (2000) 1835.
[316] S. Augst, D. Strickland, D.D. Meyerhofer, S.L. Chin, J.H. Eberly, Phys. Rev. Lett. 63 (1989) 2212.
[317] G. Mocken, C.H. Keitel, J. Phys. B 37 (2004) L275 see also Ref. [133].
[318] S.X. Hu, L.A. Collins, Phys. Rev. A 69 (2004) 033405.
[319] S.X. Hu, D.B. Milošević, W. Becker, W. Sandner, Phys. Rev. A 64 (2001) 013410.
[320] N.B. Delone, V.P. Krainov, Uspekhi Fizicheskikh Nauk 168 (1998) 531 [Eng. Transl. Physics—Uspekhi 41 (1998) 469].
[321] S.C. Rae, K. Burnett, J. Cooper, Phys. Rev. A 50 (1994) 3438.
[322] M. Yu Ivanov, P.B. Corkum, Phys. Rev. A 48 (1993) 580;
T. Zuo, S. Chelkowski, A.D. Bandrauk, Phys. Rev. A 48 (1993) 3837.
[323] E.A. Chowdhury, I. Ghebregziabher, J. MacDonald, B. Walker, Opt. Expr. 12 (2004) 3911.
[324] E.A. Chowdhury, I. Ghebregziabher, B. Walker, J. Phys. B 38 (2005) 517.
[325] D.B. Milošević, W. Becker, Phys. Rev. A 66 (2002) 063417.
[326] V.B. Berestetski, E.M. Lifshitz, L.P. Pitaevski, Relativistic Quantum Theory, Pergamon Press, New York, 1971.
[327] M.H. Mittleman, Phys. Rev. A 33 (1986) 2840.
[328] L.A. Rivlin, Quantum Electron. 6 (1976) 1313.
[329] H.R. Reiss, J. Math. Phys. 3 (1962) 59.
[330] J.-M. Ortega, Proceedings of the International Symposium on IR FELs and Applications, Noda, Chiba, Japan, 2002.
[331] J. Estrada, et al., Phys. Rev. Lett. 84 (2000) 859.
[332] L.A. Rivlin, Sov. Kvant. El. 1 (1974) 2066;
L.A. Rivlin, Sov. Kvant. El. 3 (1976) 2413;
L.A. Rivlin, Sov. Kvant. El. 5 (1978) 2497;
Winterberg, Phys. Rev. A 19 (1979) 1356;
M. Bertolotti, C. Sibilia, Appl. Phys. 19 (1979) 127;
Liang, Dermer, Opt. Commun. 65 (1988) 419.
[333] A.I. Nikishov, V.I. Ritus, Sov. Phys. JETP 19 (1964) 529;
A.I. Nikishov, V.I. Ritus, Sov. Phys. JETP 19 (1964) 1191;
A.I. Nikishov, V.I. Ritus, Sov. Phys. JETP 20 (1965) 757;
A.I. Nikishov, V.I. Ritus, Sov. Phys. JETP 25 (1967) 1135.
[334] C.B. Collins, J.J. Caroll, Laser Phys. 5 (1995) 209;
G.C. Baldwin, J.C. Solem, Laser Phys. 5 (1995) 231 [see also other references in a special issue on Grasers Laser Phys. 5(2) (1995)].
[335] D. von der Linde, et al., Phys. Rev. A 52 (1995) R25;
S. Kohlweyer, et al., Opt. Commun. 117 (1995) 431;
P.A. Norreys, et al., Phys. Rev. Lett. 76 (1996) 1832;
M. Zepf, et al., Phys. Rev. E 58 (1998) 5253;

A. Tarasevich, et al., Phys. Rev. A 62 (2000) 023816;
I. Watts, et al., Phys. Rev. Lett. 88 (2002) 155001;
U. Teubner, et al., Phys. Rev. A 67 (2003) 013816.
[336] S.V. Bulanov, et al., Phys. Plasmas 1 (1994) 745;
R. Lichters, J. Meyer-ter-Vehn, X. Pukhov, Phys. Plasmas 3 (1996) 3425;
D. von der Linde, K. Rzazewski, Appl. Phys. B 63 (1996) 499;
P. Gibbon, Phys. Rev. Lett. 76 (1996) 50;
L. Plaja, et al., J. Opt. Soc. Am. B 7 (1999) 1904;
A. Macchi, et al., Phys. Rev. Lett. 87 (2001) 205004;
S. Gordienko, et al., Phys. Rev. Lett. 93 (2004) 115002.
[337] C.W. Roberson, P. Sprangle, Phys. Fluids B 1 (1979) 3.
[338] P. Sprangle, E. Esarey, Phys. Rev. Lett. 67 (1991) 2021;
P. Sprangle, Phys. Rev. A 45 (1992) 5872.
[339] M.V. Fedorov, Zh. Exp. Theor. Fiz. 51 (1966) 795.
[340] R.C. Elton, X-ray Lasers, Academic Press, London, 1990;
B. Rus, et al., Phys. Rev. A 55 (1997) 3858;
S. Sebban, et al., Phys. Rev. A 61 (2000) 043810.
[342] J. Eberly, Prog. in Optics 7 (1969) 359.
[343] F. Ehlotzky, Can. J. Phys. 63 (1985) 907.
[344] W. Becker, Laser Part. Beams 9 (1991) 603.
[345] V.I. Ritus, Proc. Lebedev Inst. 111 (1979) 5.
[346] E.S. Fradkin, D.M. Gitman, Sh.M. Shvartsman, Quantum Electrodynamics with Unstable Vacuum, Springer, Berlin, 1991.
[347] A.A. Grib, S.G. Mamaev, V.M. Mostepanenko, Quantum Effects in Strong External Fields, Atomizdat, Moscow, 1980.
[348] F.V. Bunkin, M.V. Fedorov, Sov. Phys. Uspekhi 15 (1973) 416.
[349] M. Mittleman, Introduction to the Theory of Laser–Atom Interactions, Plenum Press, New York, 1982.
[350] A. Friedman, A. Gover, G. Kurizki, S. Ruschin, A. Yariv, Rev. Mod. Phys. 60 (1988) 471.
[351] M.V. Fedorov, Atomic and Free Electrons in a Strong Light Field, World Scientific, Singapore, 1997.
[352] C. Bula, K.T. McDonald, E.J. Prebys, C. Bamber, S. Boege, T. Kotseroglou, A.C. Melissions, D.D. Meyerhofer, W. Ragg, D.L. Burke, R.C. Field, G. Horton-Smith, A.C. Odian, J.E. Spencer, D. Walz, S.C. Berridge, W.M. Bugg, K. Shmakov, A.W. Weidemann, Phys. Rev. Lett. 76 (1996) 3116.
[353] D.L. Burke, R.C. Field, G. Horton-Smith, J.E. Spencer, D. Walz, S.C. Berridge, W.M. Bugg, K. Shmakov, A.W. Weidemann, C. Bula, K.T. McDonald, E.J. Prebys, C. Bamber, S. Boege, T. Kotseroglou, A.C. Melissions, D.D. Meyerhofer, W. Ragg, Phys. Rev. Lett. 79 (1997) 1626.
[354] I.I. Gol'dman, Sov. Phys. JETP 19 (1964) 954;
I.I. Gol'dman, Phys. Lett. 8 (1964) 103.
[355] L.S. Brown, T.W.B. Kibble, Phys. Rev. 133 (1964) A705.
[356] W.J. Brown, et al., Phys. Rev. STAB 7 (2004) 060702;
W.J. Brown, et al., Phys. Rev. STAB 7 (2004) 060703.
[357] F.V. Hartemann, et al., Phys. Rev. STAB 8 (2005) 100702.
[358] T.J. Englert, E.A. Rinehart, Phys. Rev. A 28 (1983) 1539.
[359] S. Chen, A. Maksimchuk, D. Umstadter, Nature 396 (1998) 653.
[360] S-Y. Chen, et al., Phys. Rev. Lett. 84 (2000) 5528.
[361] S. Banerjee, et al., J. Opt. Soc. Am. B 20 (2003) 182.
[362] K. TaPhuoc, A. Rousse, M. Pitman, J.P. Rousseau, V. Malka, S. Fritzler, D. Umstadter, D. Hulin, Phys. Rev. Lett. 91 (2003) 195001.
[363] C. Bamber, S. Boege, T. Koffas, T. Kotseroglou, A.C. Melissions, D.D. Meyerhofer, D.A. Reis, W. Ragg, C. Bula, K.T. McDonald, E.J. Prebys, D.L. Burke, R.C. Field, G. Horton-Smith, J.E. Spencer, D. Walz, S.C. Berridge, W.M. Bugg, K. Shmakov, A.W. Weidemann, Phys. Rev. D 60 (1999) 092004.
[364] N.B. Narozhny, et al., Sov. Phys. JETP 20 (1965) 622.
[365] J. Koga, T.Zh. Esirkepov, S.V. Bulanov, Phys. Plasmas 12 (2005) 093106.
[366] M. Abraham, Theorie der Elektizität, vol.II: Elektromagnetische Theorie der Strahlung, Teubner, Leipzig, 1905.
[367] H.A. Lorentz, The Theory of Electrons, Teubner, Leipzig, 1909.
[368] F. Rohlrich, Classical Charged Particles, Addison-Wesley, Reading, MA, 1965.
[369] A.A. Sokolov, I.M. Ternov, Radiation from Relativistic Electrons, AIP, New York, 1986.
[370] P.A.M. Dirac, Proc. Roy. Soc. (London) A 167 (1938) 148.
[371] L.D. Landau, E.M. Lifshits, The Classical Theory of Fields, Pergamon, Oxford, 1951.
[373] C.H. Keitel, C. Szymanowski, P.L. Knight, A. Maquet, J. Phys. B 31 (1998) L75.
[374] C.H. Keitel, P.L. Knight, Phys. Rev. A 51 (1995) 1420.
[375] F. Sauter, Z. Phys. 69 (1931) 742;
W. Heisenberg, H. Euler, Z. Phys. 98 (1936) 714;
J. Schwinger, Phys. Rev. 82 (1951) 664.
[376] G. Breit, J.A. Wheeler, Phys. Rev. 46 (1934) 1087.
[377] H.A. Bethe, W. Heitler, Proc. Roy. Soc. London A 146 (1934) 83.
[378] V.P. Yakovlev, Zh. Exp. Theor. Fiz. (Sov.) 49 (1965) 318.

[379] M.H. Mittleman, Phys. Rev. A 35 (1987) 4624.
[380] C. Müller, A.B. Voitkiv, N. Grün, Phys. Rev. A 67 (2003) 063407.
[381] C. Müller, A.B. Voitkiv, N. Grün, Phys. Rev. Lett. 91 (2003) 223601;
C. Müller, A.B. Voitkiv, N. Grün, Phys. Rev. A 70 (2004) 023412.
[382] E. Brezin, C. Itzikson, Phys. Rev. D 2 (1970) 1191.
[383] V.S. Popov, Zh. Exp. Theor. Fiz. (Sov.) 61 (1971) 1334;
V.S. Popov, Zh. Exp. Theor. Fiz. (Sov.) 63 (1972) 1586;
V.S. Popov, Yad. Fiz. (Sov.) 19 (1974) 1140.
[384] V.M. Mostepanenko, V.M. Frolov, Yad. Fiz. (Sov.) 19 (1974) 885.
[385] H.K. Avetissian, et al., Phys. Rev. E 66 (2002) 016502.
[386] H.M. Fried, et al., Phys. Rev. D 63 (2001) 125001.
[387] A.A. Grib, S.G. Mamayev, V.M. Mostepanenko, Vacuum Quantum Effects in Strong Fields, Friedmann, St. Petersburg, 1994.
[388] V.S. Popov, JETP Lett. 74 (2001) 133;
V.S. Popov, JETP Lett. 94 (2002) 1057;
N.B. Narozhny, et al., Phys. Lett. A 330 (2004) 19;
A. DiPiazza, Phys. Rev. D 70 (2004) 053013.
[389] A. Ringwald, Phys. Lett. B 510 (2001) 107.
[390] H.K. Avetissian, et al., Sov. Phys. JETP 67 (1988) 660;
H.K. Avetissian, et al., Sov. Phys. JETP 72 (1991) 26;
H.K. Avetissian, et al., Sov. Phys. JETP 73 (1991) 44;
H.K. Avetissian, et al., Phys. Rev. D 54 (1996) 5509;
S.S. Bulanov, Phys. Rev. E 69 (2004) 036408.
[391] S.S. Bulanov, A.M. Fedotov, F. Pegoraro, JETP Lett. 80 (2004) 734;
S.S. Bulanov, A.M. Fedotov, F. Pegoraro, Phys. Rev. E 71 (2005) 016404.
[392] Y. Kluger, et al., Phys. Rev. D 45 (1992) 4659;
Y. Kluger, E. Mottola, Phys. Rev. D 58 (1998) 125015;
S. Schmidt, et al., Int. J. Mod. Phys. E 7 (1998) 709;
S. Schmidt, et al., Phys. Rev. D 59 (1999) 094005;
J.C.R. Bloch, et al., Phys. Rev. D 60 (1999) 116011.
[393] R. Alkofer, M.B. Hecht, C.D. Roberts, S.M. Schmidt, D.V. Vinnik, Phys. Rev. Lett. 87 (2001) 193902.
[394] C.D. Roberts, S.M. Schmidt, D.V. Vinnik, Phys. Rev. Lett. 89 (2002) 153901.
[395] A.I. Akhiezer, V.B. Berestetskii, Kvantovaya elektrodinamika, Nauka, Moscow, 1969.
[396] H. Euler, Ann. Physik 26 (1936) 398;
A.I. Ackiezer, Phys. Z. 11 (1937) 263.
[397] M. Delbrück, Z. Phys. 84 (1933) 144.
[398] W. Dittrich, M. Reuter, Effective Lagrangians in Quantum Electrodynamics, Springer, Berlin, 1985;
W. Dittrich, H. Gies, Probing the Quantum Vacuum, Springer, Berlin, 2000.
[399] S.L. Adler, et al., Phys. Rev. Lett. 25 (1970) 1061;
S.L. Adler, Ann. Phys. (N. Y.) 67 (1971) 599.
[400] I. Affleck, L. Kruglyak, Phys. Rev. Lett. 59 (1987) 1065.
[401] N.N. Rozanov, Sov. Phys. JETP 76 (1993) 991.
[402] W. Heisenberg, H. Euler, Z. Phys. 98 (1936) 714.
[404] W. Becker, J.K. McIver, R.R. Schlicher, Phys. Rev. A 38 (1988) 4891;
W. Becker, J.K. McIver, R.R. Schlicher, J. Opt. Soc. Am. B 6 (1988) 1083.
[405] G. Brodin, M. Marklund, L. Stenflo, Phys. Rev. Lett. 87 (2001) 171801.
[406] A. Di Piazza, K.Z. Hatsagortsyan, C.H. Keitel, Phys. Rev. D 72 (2005) 085005.
[407] W. Becker, H. Mitter, J. Phys. A 8 (1975) 1638.
[408] Z. Bialynicka-Birula, I. Bialynicki-Birula, Phys. Rev. D 2 (1971) 2341;
E. Brezin, C. Itzikson, Phys. Rev. D 3 (1971) 618;
E.B. Aleksandrov, A.A. Ansel'm, A.N. Moskalev, Sov. Phys. JETP 62 (1985) 680;
J.S. Heyl, L. Hernquist, J. Phys. A 30 (1997) 6485.
[409] A. Di Piazza, K.Z. Hatsagortsyan, C.H. Keitel, arXiv.org: hep-ph/0602039.
[410] G. Jarlskog, et al., Phys. Rev. D 8 (1973) 3813;
M. Schumacher, et al., Phys. Rev. C 13 (1976) 2318;
Sh.Zh. Akhmadaliev, et al., Phys. Rev. C 58 (1998) 2844.
[411] Sh.Zh. Akhmadaliev, et al., Phys. Rev. Lett. 89 (2002) 061802.
[412] F. Moulin, D. Bernard, F. Amiranoff, Z. Phys. C 72 (1996) 607.
[413] D. Bernard, et al., Eur. Phys. J. 10 (2000) 141.
[414] D. Bakalov, et al., Nuclear Physics B 35 180 (1994) See also http://www.ts.infn.it/experiments/pvlas/pvlas.html.
[415] M. Marklund, G. Brodin, L. Stenflo, Phys. Rev. Lett. 91 (2003) 163601.
[416] P.K. Shukla, B. Eliasson, Phys. Rev. Lett. 92 (2004) 073601;
M. Marklund, B. Eliasson, P.K. Shukla, JETP Lett. 79 (2004) 262;

P.K. Shukla, M. Marklund, D.D. Tskhakaya, B. Eliasson, Phys. Plasmas 11 (2004) 3767;
M. Marklund, P.K. Shukla, B. Eliasson, Europhys. Lett. 70 (2005) 327.
[417] S. Matinyan, Physics Reports 298 (1998) 199.
[418] A.V. Andreev, et al., J. Exp. Theor. Phys. 91 (2000) 1163;
A.V. Andreev, et al., Quant. Electron. 31 (2001) 941;
J.J. Carol, et al., Hyperfine Interactions 135 (2001) 3.
[419] D. Umstadter, Nature 404 (2000) 239.
[420] J. Lindl, Phys. Plasmas 2 (1995) 3933.
[421] T.R. Dietrich, et al., Phys. Rev. Lett. 73 (1994) 2324.
[422] M. Tabak, et al., Phys. Plasmas 12 (2005) 057305;
M. Keith Matzen, et al., Phys. Plasmas 12 (2005) 055503.
[423] P.L. Shkolnikov, A.E. Kaplan, A. Pukhov, M. Meyer-ter-Vehn, Appl. Phys. Lett. 71 (1997) 3471.
[424] C. Gahn, et al., Appl. Phys. Lett. 77 (2000) 2662.
[425] M.I. Santala, et al., Phys. Rev. Lett. 84 (2000) 1459.
[426] M.I.K. Santala, et al., Phys. Rev. Lett. 86 (2001) 1227;
W.P. Leemans, et al., Phys. Plasmas 8 (2001) 2510.
[427] I. Spencer, et al., Rev. Sci. Instrum. 73 (2002) 3801.
[428] T.E. Cowan, et al., Phys. Rev. Lett. 84 (2000) 903.
[429] H. Schwoerer, et al., Europhys. Lett. 84 (2002) 47.
[430] K.W.D. Ledingham, et al., J. Phys. D 36 (2003) L79.
[431] J. Magill, et al., Appl. Phys. B 77 (2003) 397.
[432] G. Pretzler, et al., Phys. Rev. E 58 (1998) 1165.
[433] L. Disdier, J-P. Garçonnet, G. Malka, J-L. Miquel, Phys. Rev. Lett. 82 (1999) 1454.
[434] D. Hilscher, et al., Phys. Rev. E 64 (2001) 016414.
[435] E.L. Clark, et al., Phys. Rev. Lett. 84 (2000) 670;
R.A. Snavly, et al., Phys. Rev. Lett. 85 (2000) 2945;
S.P. Hatchett, et al., Phys. Plasmas 7 (2000) 2076.
[436] E.L. Clark, et al., Phys. Rev. Lett. 85 (2000) 1654;
K. Krushelnick, et al., IEEE Trans. Plasma Sci. 28 (2000) 1184;
M. Hegelich, et al., Phys. Rev. Lett. 89 (2002) 085002.
[437] P. McKenna, et al., Phys. Rev. Lett. 91 (2003) 075006.
[438] K.W.D. Ledingham, P. McKenna, R.P. Singhal, Science 300 (2003) 1107.
[439] K.W.D. Ledingham, et al., J. Phys. D 37 (2004) 2341.
[440] P. McKenna, et al., Phys. Rev. Lett. 94 (2005) 084801.
[441] T.Z. Esirkepov, et al., Phys. Rev. Lett. 89 (2002) 175003.
[442] S. Fritzler, et al., Phys. Rev. Lett. 89 (2002) 165004.
[443] V.P. Krainov, M.B. Smirnov, Physics Reports 370 (2002) 237.
[444] S. Wei, J. Purnel, S.A. Buzza, R.J. Stanley, A.W. Castleman Jr., Chem. Phys. 97 (1992) 9480.
[445] I. Last, J. Jortner, Phys. Rev. Lett. 87 (2001) 033401.
[446] J.W.G. Tisch, N. Hay, E. Springate, E.T. Gumbrell, M.H.R. Hutchinson, J.P. Marangos, Phys. Rev. A 60 (1999) 3076.
[447] K.W. Madison, P.K. Patel, M. Allen, D. Price, R. Fitzpatrick, T. Ditmire, Phys. Rev. A 70 (2004) 053201.
[448] P.A. Norreys, et al., Plasma Phys. Contr. Fusion 40 (1998) 175.
[449] N. Izumi, et al., Phys. Rev. E 65 (2002) 036413.
[450] V.S. Belyaev, et al., JETP 98 (2004) 1133.
[451] S. Chelkowski, A.D. Bandrauk, P.B. Corkum, Phys. Rev. Lett. 93 (2004) 083602.
[452] T. Bürvenich, J. Evers, C.H. Keitel, arXiv.org: nucl-th/0601077.
[453] V.I. Ritus, Zh. Exp. Theor. Fiz. 56 (1969) 986 [Sov. Phys. JETP 19 (1964) 1191].
[454] V.A. Lyulka, Zh. Exp. Theor. Fiz. 69 (1975) 800 [Sov. Phys. JETP 42 (1975) 408].
[455] I.M. Ternov, et al., Sov. J. Nucl. Phys. 28 (1978) 747.
[456] W. Becker, W.H. Louisell, J.D. McCullen, M.O. Scully, Phys. Rev. Lett. 47 (1981) 1262;
H.R. Reiss, Phys. Rev. C 27 (1983) 1199.
[457] K.Z. Hatsagortsyan, C. Müller, C.H. Keitel, arXiv.org: physics/0602093.
[458] C. Müller, K.Z. Hatsagortsyan, C.H. Keitel, arXiv.org: physics/0602106.
[459] C.M. Surko, R.G. Greaves, Phys. Plasmas 11 (2004) 2333.
[460] S.C. Wilks, et al., Astroph. Space Sci. 298 (2005) 347.
[461] S.P.D. Mangles, et al., Phys. Rev. Lett. 94 (2005) 245001.
[462] M. Gajda, J. Grochmalicki, M. Lewenstein, Phys. Rev. A 46 (1992) 1638;
J. Grochmalicki, M. Lewenstein, K. Rzazewski, Phys. Rev. Lett. 66 (1991) 1038.